The Comprehensive study of Titanium oxide doped Conducting polymers nanocomposites for Photovoltaic applications

Bhagyashri U. Tale, K. R. Nemade & P. V. Tekade

Published online: 31 May 2021.

Submit your article to this journal

Article views: 2

View related articles

View Crossmark data

Taylor & Francis
Taylor & Francis Group

Check for updates

The Comprehensive study of Titanium oxide doped Conducting polymers nanocomposites for Photovoltaic applications

Bhagyashri U. Tale[a], K. R. Nemade[b], and P. V. Tekade[a]

[a]Department of Chemistry, Bajaj College of Science, Wardha, India; [b]Department of Physics, Indira Mahavidyalaya, Kalamb, India

ABSTRACT

To make the effective use of renewable energy, high performance, low-cost, and eco-friendly energy conversion devices are topic of intense research. Effect of addition of TiO_2 on photovoltaic performance of polymers was studied. The significant enhancement in % η was observed after addition of TiO_2 in Polyaniline. The Titanium dioxide (TiO_2) is n-type semiconductor with mechanical flexibility, and its conductivity can be modified by doping with PANi (*p*-type) to obtain high current by exciton separation at TiO_2/PANi interface. The value of % η (10.47%) for TiO_2-Polyaniline composite is found to be highest.

1. Introduction

The energy requirement of world is rising day by day and it is estimated that energy requirement will be double by 2050.[1] A photovoltaic or solar cell is used to convert the light energy into electrical energy. The electric power generation from renewable energy sources is the need of time. Among renewable energy resources used for generation of electricity, solar photovoltaic technology is rapidly growing.[2,3]

The interesting characteristics for the replacement of traditional energy sources by photovoltaic technology are

- Fossil fuels are limited and their cost is increasing day by day on the other hand solar energy is abundant & free.
- Fossil-fuels pollute the environment & solar PV's does not release pollutants.
- Fossil-fuels create global warming & solar PV's does not.
- As compared to other renewable energy sources, solar PV's provide the highest power density.
- Solar PV's has low operational costs & maintenance.
- There are more than 100 countries in the world where the work on solar PV technology is topic of intense research.[4–10]

1.1. Metal oxide/polymer composites

Polymer solar cells work in the following four stages for photocurrent generation:

(1) Excitons formation by absorption of light by the activated layer.
(2) Free charges formation by excitons at electron donor/acceptor interface.
(3) Transfer of the charged species in presence of electric field.
(4) Collection of charge by electrodes.[11]

One of the popular methods for charge separation in organic films is the addition of electron acceptors like TiO_2 nanomaterial.[12,13] Polymer/inorganic composite is topic of interest in research due to the synergetic effects which lead to better electrical properties. The direct interfacial interaction of the polymers & inorganic component in composite improves electronic properties. In composite, the polymeric material acts as donors and inorganic component are acceptors.

In this study, Titanium dioxide (TiO_2) is n-type semiconductor with mechanical flexibility, and its conductivity can be modified by doping with PANi (*p*-type) to obtain high current by exciton separation at TiO_2/PANi interface.[14–17] Polyaniline is one of the most studied material because of its eco-friendliness, good electrical conductivity, low cost, rigidity, unique reversible protonic dupability etc. PANI is widely used in nanoelectronic devices.

The high efficiency of composites of PANi & TiO_2 in photovoltaic devices can be explained on the basis of following:

1. The band-gap energies of PANI (2.8 eV) & TiO_2 (3.2 eV) are nearly same which facilitates the separation of charges and the transfer of electrons.

---

2. The photo-generated electrons get excited by light which increases the conductivity as well as photoelectrochemical response.

Another reason for enhanced photosensitivity of PANI/TiO$_2$ film depends on energy level. When PANI/TiO$_2$film irradiates withlight, boththeTiO$_2$ and PANI shows absorption of photons & charge separation. As the conduction band of TiO$_2$ and the LUMO level of the PANI are nearer to each other, it facilitates the charge transfer.[18,19]

2. Experimental

In present work, Polyaniline (PANi) was prepared by Chemical oxidative method by Ammonium persulfate as oxidant. Both aniline and oxidant in stoichiometric ratio were dissolved in aqueous medium. The greenish black ppt was obtained and it was kept for 24 hours at room temperature to achieve complete polymerization. The product was washed with distilled water and then dried in an oven.[20] For preparation of Polypyrrole(PPy), FeCl$_3$ was used as oxidizing agent. The suspension was kept at room temperature for 24 hours to get complete polymerization. Finally, the black ppt. of polypyrrole was washed with Acetone and dried in an oven.[21]

Polyindole(PIn) was synthesized by Chemical oxidative method using FeCl$_3$ as an oxidizing agent and 0.1 M Hydrogen peroxide was added to enhance the rate of reaction. The reaction mixture was stirred for 12 hours at 30°C.[22] Polythiophene (PTh) was obtained by mixing thiophene with ferric chloride. Hydrogen peroxide was added to increase the rate of reaction. The complete polymerization was obtained by constant stirring for 24 hours at 30°C. Then, concentrated sodium hydroxide solution was added to get the product. The product was washed with distilled water and dried in oven.[23]

The Titanium dioxide (TiO$_2$) was obtained using 10% titanium chloride (TiCl$_3$), 15% HCl and ammonia solution in aqueous solution at alkaline pH. 3% H$_2$O$_2$was added to increase oxidation rate. The resulting solution was kept at room temperature for 24 hours and probe sonicated. The product was washed with distilled water and dried in oven.[24]The Polymer/Metal oxide composites were prepared by ex-situ approach. During preparation of composite, Polymer (1 g) and Metal oxide (0.1 g) were added to the organic media.

The X-ray diffraction (XRD) patterns of as prepared materials were recorded on Rigaku Miniflex-II X-Ray Diffractometer. The morphology of samples was investigated using scanning electron microscope (SEM) images obtained from JEOL JSM-7500 F. The ultraviolet–visible (UV–VIS) absorption spectra of composites were acquired using Agilent Cary 60 UV–VIS
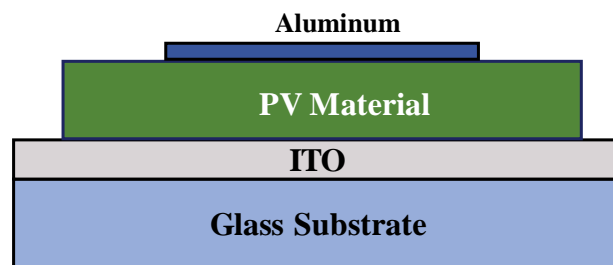

Figure 1. Side face of fabricated PV cell.

spectrophotometer. The Bruker RFS 27 Raman spectrometer was used for Raman analysis. Electrochemical study of prepared samples was carried out using three-electrode cell systems (CHI 660 D, CH Instruments). As-prepared materials were used as the working electrode, platinum wire as counter electrode and Ag/AgCl as the reference electrode. Photoluminescence (PL) spectra recorded using fluorescence spectroscopy (FL spectrophotometer model F-7000; Hitachi).

2.1. Fabrication of photovoltaic cell

The PV cells were prepared by doctor blade technique. The composite material was present as sandwich between ITO layer of plate and aluminum (Figure 1). The foil of aluminum acts as metallic electrode. The temporary binder was used to deposit the composite material on ITO coated plate and on that layer aluminum foil was kept. Then, it was dried at 40°C in order to remove the volatile organic components. The thickness of deposited layer was controlled by using transparency in doctor blade technique.

The current-voltage, that is, I–Vstudy of Photovoltaic cell was done by using an incandescent light bulb having power 0.2956 Watt/m^2. The parameters like short circuit current (I$_{SC}$), fill factor (FF), power conversion efficiency (η) & open-circuit voltage (V$_{OC}$) were measured using these conditions. The Fill Factor of Photovoltaic cell was measured using following equation,

$$FF = \frac{I_{MAX} \times V_{MAX}}{I_{SC} \times V_{OC}}$$

The power conversion efficiency, that is, %η of Photovoltaic cell was calculated by following relation,

$$\%\eta = \left(\frac{I_{SC} \times V_{OC} \times FF}{P_{in}} \right) \times 100$$

The FF and %η are the very important parameters for study of any PV cell. By using these parameters, it is possible to study any photovoltaic cell and its performance.
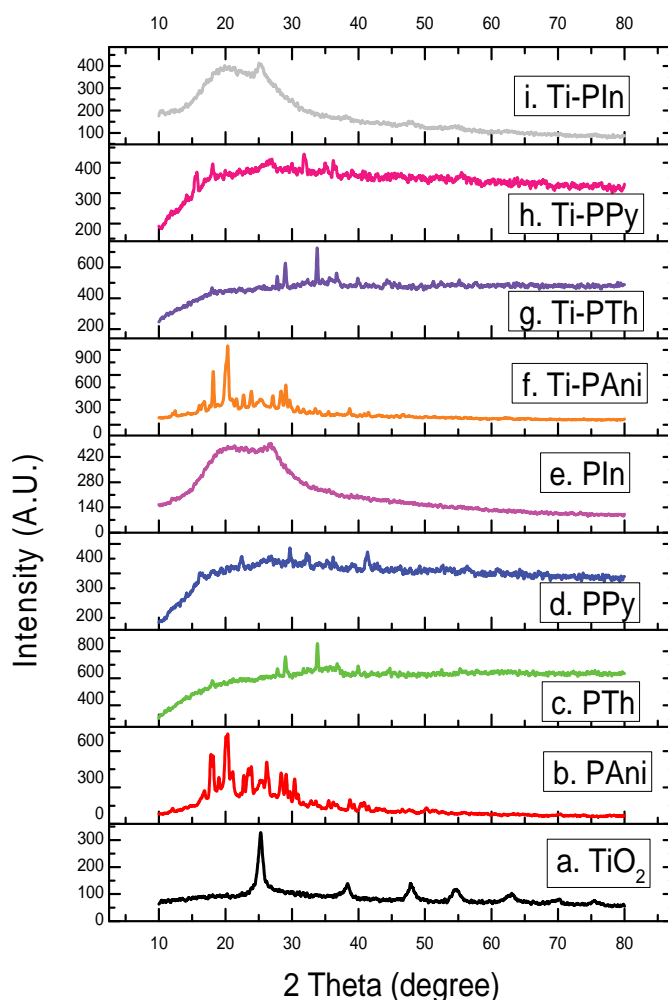
3. Result & discussion

3.1. XRD

Figure 2 indicates XRD pattern of (a) TiO_2, (b) Polyaniline (PANi), (c) Polythiophene (PTh), (d) Polypyrrole (PPy), (e) Polyindole (Pin), (f) TiO_2-Polyaniline composite (Ti-PANi), (g) TiO_2-Polythiophene composite (Ti-PTh), (h) TiO_2-Polypyrrole composite (Ti-PPy) and (i) TiO_2-Polyindole composite (Ti-Pin).

The experimental XRD pattern of TiO_2 matches with the JCPDS card no. 21–1272 (anatase TiO_2). Strong diffraction peaks at 25°,38°, 48°, and 54° indicates TiO_2 in the anatase phase. The intensity of XRD peaks indicates that the formed nanoparticles are crystalline.[25,26] X-ray diffraction of PANI shows peaks in the 2θ range 15° to 30°. The sharp and well-defined peaks indicate semi-crystalline nature of PANI. The crystalline nature of PANI is because of its nano fibrous nature and planarity of Benzenoid and Quinoid functional groups.[27]

XRD spectra of Polythiophene with only one broad peak centered at near 2θ value of 35°. This diffraction peak is due to π-π stacking structure in polythiophene chains. Thus, spectrum indicates the semi-crystalline nature of polythiophene.[28] The XRD pattern of Polyindole (PIn) shows a broad hump which indicates an amorphous structure which is the characteristic of Polyindole.[22] It is observed from the XRD of polypyrrole indicates its amorphous nature, as there is no sharp peak in the diffraction pattern. But a broad peak at about 24° of 2θ value is the characteristics peak of amorphous PPy polymer.[29]

Further the absence of broad diffraction peak of PANi at $2\theta = 25°$ in the PANi/TiO_2 composite is due to the presence of PANi in the polymerization system which strongly affects the degree of crystallinity of TiO_2.[30] Similarly, crystalline behavior is found to be decrease with composite formation. Thus, the XRD pattern of TiO_2-Polyaniline composite (Ti-PANi), TiO_2-Polyindole composite(Ti-PIn), TiO_2-Polypyrrole

Figure 2. XRD pattern of (a) TiO_2, (b) Polyaniline (PANi), (c) Polythiophene (PTh), (d) Polypyrrole (PPy), (e) Polyindole (Pin), (f) TiO_2-Polyaniline composite (Ti-PANi), (g) TiO_2-Polythiophene composite (Ti-PTh), (h) TiO_2-Polypyrrole composite (Ti-PPy) and (i) TiO_2-Polyindole composite (Ti-Pin).

composite(Ti-PPy) and TiO$_2$-Polythiophene composite (Ti-PTh) indicates amorphous nature as there is no sharp peak.

Particle size of TiO$_2$, Polymers and their composites calculated by Scherrer equation are shown in Table 1.

Table 1. Particle size of TiO$_2$, polymers and their composites.

Compound	Observed particle size calculated by Scherrer equation D(nm) = Kλ/βCosθ[31]
1. TiO$_2$,	92.74
2. Polyaniline(PANi),	84
3. Polythiophene(PTh),	108.51
4. Polypyrrole (PPy),	108.13
5. Polyindole(Pin),	10.28
6. TiO$_2$-Polyaniline composite(Ti-PANi),	165
7. TiO$_2$-Polythiophene composite(Ti-PTh),	90.67
8. TiO$_2$-Polypyrrole composite(Ti-PPy) and	50.67
9. TiO$_2$-Polyindole composite(Ti-Pin).	8

3.2. SEM

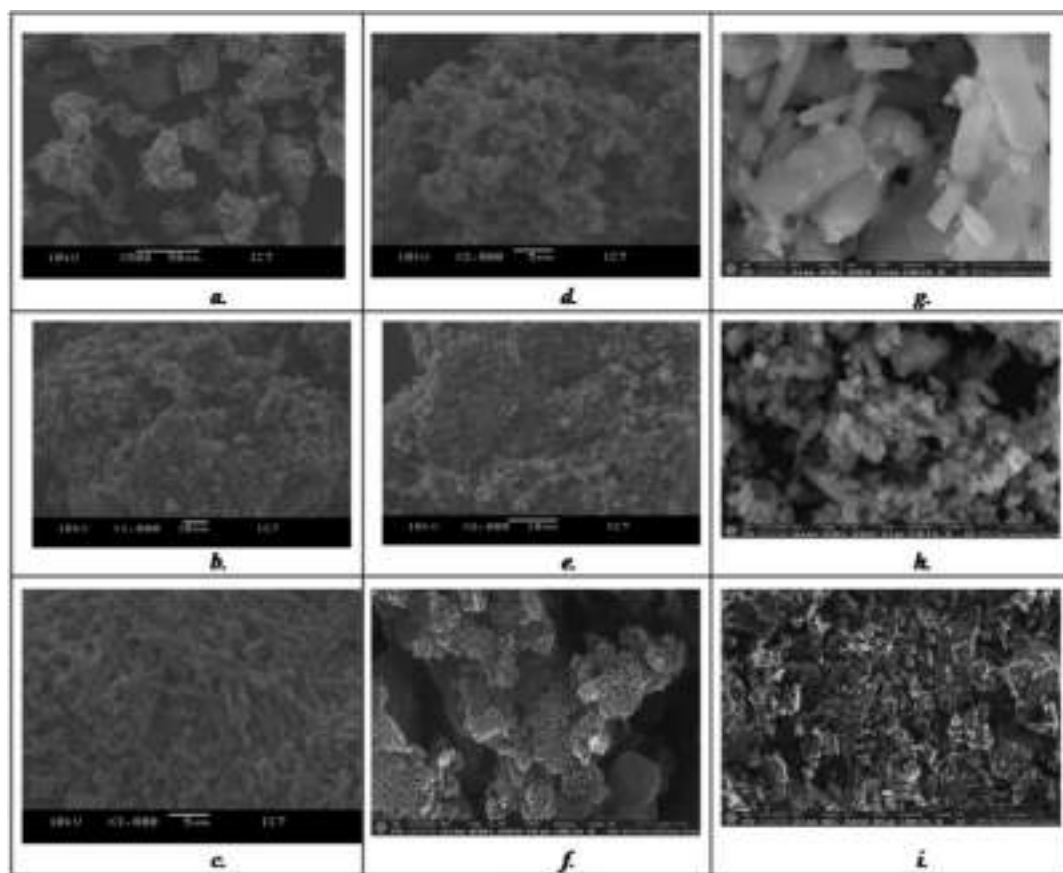SEM images of (a) TiO$_2$, (b) Polyaniline (PANi), (c) Polythiophene (PTh), (d) Polypyrrole (PPy), (e) Polyindole (Pin), (f) TiO$_2$-Polyaniline composite (Ti-PANi), (g) TiO$_2$-Polythiophene composite (Ti-PTh), (h) TiO$_2$-Polypyrrole composite (Ti-PPy) and (i) TiO$_2$-Polyindole composite (Ti-Pin) are shown in Figure 3.

3.3. Raman spectroscopy

Raman Spectra of(a) TiO$_2$, (b) Polyaniline (PANi), (c) Polythiophene (PTh), (d) Polypyrrole (PPy), (e) Polyindole (Pin), (f) TiO$_2$-Polyaniline composite (Ti-PANi), (g) TiO$_2$-Polythiophene composite (Ti-PTh), (h) TiO$_2$-Polypyrrole composite (Ti-PPy) and (i) TiO$_2$-Polyindole composite (Ti-PIn) are shown in Figure 4.

TiO$_2$ peak at 235 is due to rutile phase.[32,33] Raman spectra of Polyaniline indicates signal at 1140, 1230,1500 and 1582 cm^{-1}. 1100–1210 cm^{-1} region is due to C–H bending vibrations of benzene or quinone type rings. 1210–1520 cm^{-1} region indicates C-N stretching vibrations and 1520–1650 cm^{-1} region denotes C–C stretching vibration of benzene and quinone type rings.[34]

Polythiophene shows sharp signal at 1209,1379 and 1651 cm^{-1}. Peak near 1600 cm^{-1} indicates unquestionably frequency dispersion with increasing chain length. Signal

Figure 3. SEM images of(a) TiO$_2$, (b) Polyaniline(PANi), (c) Polythiophene (PTh), (d) Polypyrrole (PPy), (e) Polyindole (Pin), (f) TiO$_2$-Polyaniline composite (Ti-PANi), (g) TiO$_2$-Polythiophene composite (Ti-PTh), (h) TiO$_2$-Polypyrrole composite (Ti-PPy) and (i) TiO$_2$-Polyindole composite (Ti-Pin).

Figure 4. Raman Spectra of (a) TiO$_2$, (b) Polyaniline(PANi), (c) Polythiophene (PTh), (d) Polypyrrole (PPy), (e) Polyindole (Pin), (f) TiO$_2$-Polyaniline composite (Ti-PANi), (g) TiO$_2$-Polythiophene composite (Ti-PTh), (h) TiO$_2$-Polypyrrole composite (Ti-PPy) and (i) TiO$_2$-Polyindole composite (Ti-PIn).
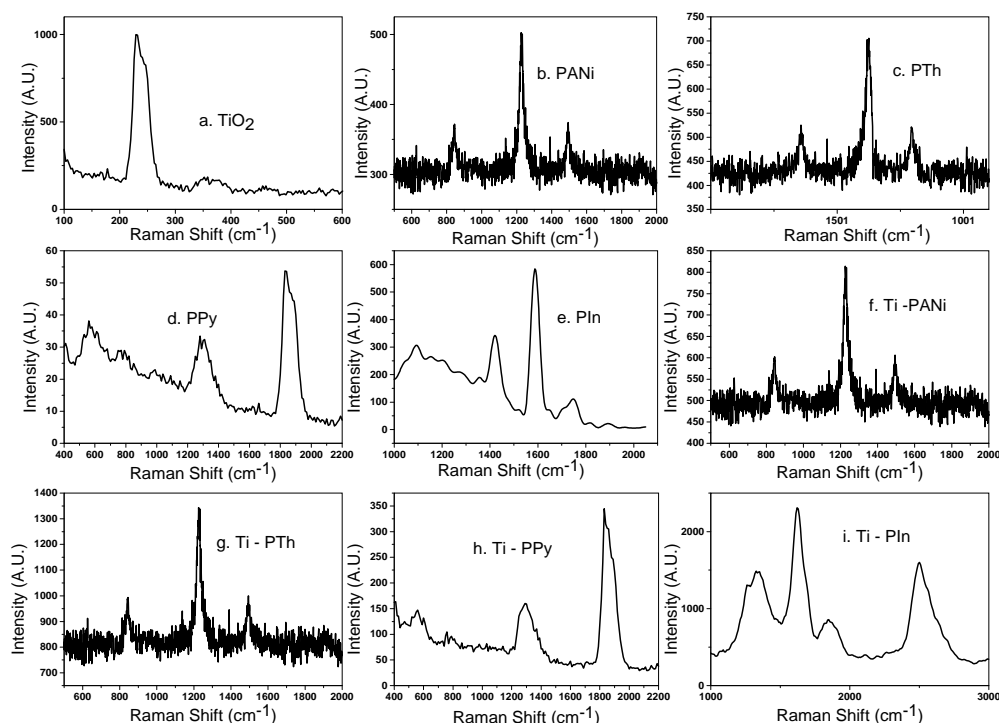
near 1500 cm^{-1} is a characteristic feature of the Raman spectra of aromatic and heteroaromatic systems. It is reported as very strong and dominating in the whole Raman spectrum. While it shifts toward lower frequencies with an increase in chain length. It shows somewhat variation in frequencies from one chemical series to another within the class of oligo and polythiophenes, but within individual class it is almost invariably strong and unshifted. Some signals appearing at the lower frequency side shows intensity enhancement with increase in chain length.[35]

Polypyrrole signal at 1330 cm^{-1} corresponds to C–C stretching in ring and antisymmetric C–N stretching.[36] Polyindole signal 1102 is due to out-of-plane as well as in-plane deformation of N-H, peak near 1594 is because of C = C backbone stretching and peak at 1414 correspond to ring stretching.[37,38] Ti-PANi and Ti-PPy composites show the same peak as polymer. Ti-PIn and Ti-PTh show shifting of peaks. Peaks observed in composites indicate strong interaction between TiO$_2$ and polymers.

3.4. UV spectroscopy

Figure 5 shows UV-Visible spectra of (a) TiO$_2$, (b) Polyaniline (PANi), (c) Polythiophene (PTh), (d) Polypyrrole (PPy), (e) Polyindole (Pin), (f) TiO$_2$-Polyaniline composite (Ti-PANi), (g) TiO$_2$-Polythiophene composite (Ti-PTh), (h) TiO$_2$-Polypyrrole composite (Ti-PPy) and (i) TiO$_2$-Polyindole composite (Ti-Pin). Band gap and absorption peak values for TiO$_2$, Polymers and their composites are shown in Table 2.

In the present work, UV-VIS technique was used to study the absorption wavelengths of materials and band gap. The absorption study of samples under study was recorded using Agilent Cary 60 UV–VIS spectrophotometer.

The energy band gap of sample can be calculated using relations: E = hc/λ [39]

Where Energy (E) = Band gap, Planks constant (h) = 6.626 × 10^{-34} Joules sec,

Velocity of Light (c) = 2.99 × 10^8 meter/sec and Wavelength (λ) = Absorption peak value. Also, 1 eV = 1.6 × 10^{-19} Joules (Conversion factor)

3.5. Photo luminescence

Figure 6 shows Photoluminescence (PL) spectra of (a) TiO$_2$, (b) Polyaniline(PANi), (c) Polythiophene (PTh), (d) Polypyrrole (PPy), (e) Polyindole (Pin), (f) TiO$_2$-Polyaniline composite (Ti-PANi), (g) TiO$_2$-Polythiophene composite (Ti-PTh), (h) TiO$_2$-Polypyrrole composite (Ti-PPy) and (i) TiO$_2$-Polyindole composite (Ti-Pin).
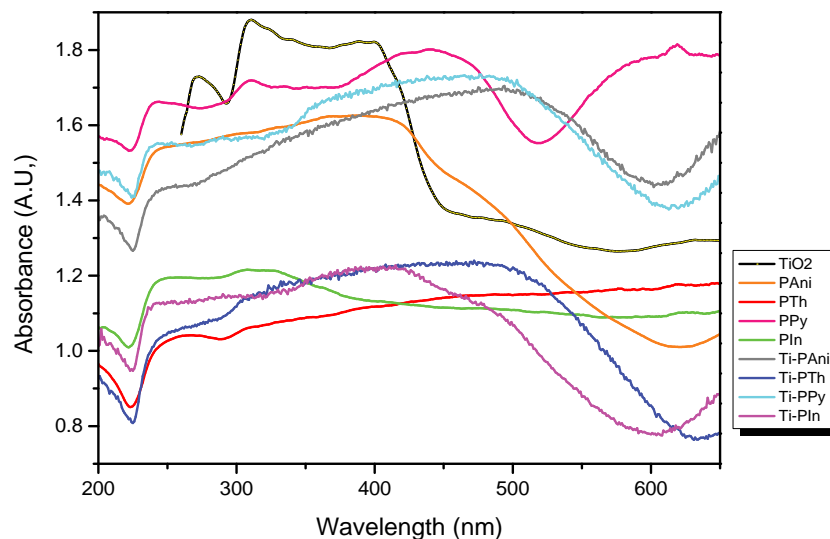
Figure 5. UV-Visible spectra of (a) TiO_2, (b) Polyaniline(PANi), (c) Polythiophene (PTh), (d) Polypyrrole (PPy), (e) Polyindole (Pin), (f) TiO_2-Polyaniline composite (Ti-PANi), (g) TiO_2-Polythiophene composite (Ti-PTh), (h) TiO_2-Polypyrrole composite (Ti-PPy) and (i) TiO_2-Polyindole composite (Ti-Pin).

Table 2. Band gap and absorption peak values for TiO_2, polymers and their composites.

| Compound	Absorption peak value (Wavelength in nm)	Band gap (eV)
1. TiO_2	350	3.54
2. Polyaniline(PANi)	310	3.99
4. Polythiophene(PTh)	265	4.67
3. Polypyrrole (PPy)	440	2.82
5. Polyindole(Pin)	249	4.98
6. TiO_2-Polyaniline composite(Ti-PANi)	450	2.8
8. TiO_2-Polythiophene composite(Ti-PTh)	400	3.1
7. TiO_2-Polypyrrole composite(Ti-PPy)	450	2.8
9. TiO_2-Polyindole composite(Ti-Pin)	400	3.1

TiO_2 shows PL signal near 490 nm.[40–42] Polyaniline shows peak at 367 nm, due to $\pi \rightarrow \pi^*$ transition.[43] Polythiophene shows absorption peak near excitation wavelength 325 nm.[44] PL signal for polyindole comes from the recombination of electron in singly occupied oxygen vacancies with photo excited holes.[45,46] Polypyrrole shows PL emission peaks near 400 nm. However, agglomeration affects the PL intensity of the polymer.[47] This PL emission characteristics indicate the promise of the synthesized materials for practical applications in ultraviolet and visible light emission devices.
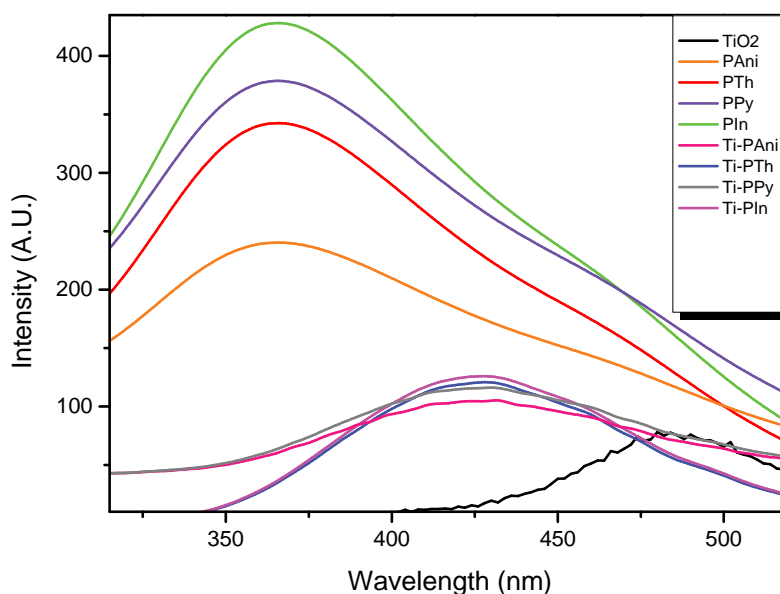
Figure 6. Photoluminescence(PL) spectra of (a) TiO_2, (b) Polyaniline(PANi), (c) Polythiophene (PTh), (d) Polypyrrole (PPy), (e) Polyindole (Pin), (f) TiO_2-Polyaniline composite (Ti-PANi), (g) TiO_2-Polythiophene composite (Ti-PTh), (h) TiO_2-Polypyrrole composite (Ti-PPy) and (i) TiO_2-Polyindole composite (Ti-Pin).
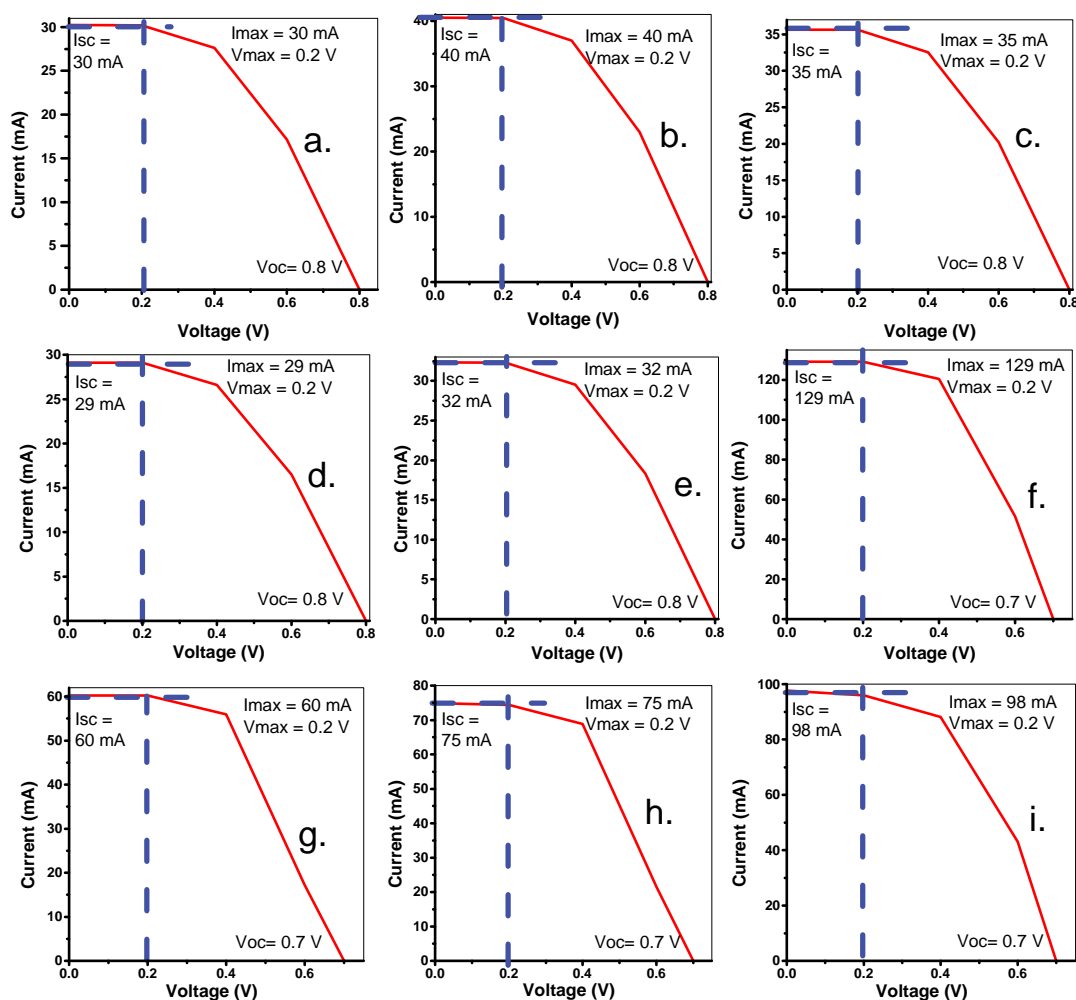
Figure 7. PV response of (a) TiO$_2$, (b) Polyaniline(PANi), (c) Polythiophene (PTh), (d) Polypyrrole (PPy), (e) Polyindole (PIn), (f) TiO$_2$-Polyaniline composite (Ti-PANi), (g) TiO$_2$-Polythiophene composite (Ti-PTh), (h) TiO$_2$-Polypyrrole composite (Ti-PPy) and (i) TiO$_2$-Polyindole composite (Ti-PIn).

Table 3. PV parameters (where Pin = 0.25 W/m^2).

Compound	Imax (mA)	Vmax (V)	Isc (mA)	Voc (V)	$FF = \frac{I_{MAX} \times V_{MAX}}{I_{SC} \times V_{OC}}$	$\%\eta = \left(\frac{I_{SC} \times V_{OC} \times FF}{P_{in}}\right) \times 100$
(a) TiO$_2$	30	0.2	30	0.8	0.25	2.4
(b) Polyaniline(PANi)	40	0.2	40	0.8	0.25	3.2
(c) Polythiophene (PTh)	35	0.2	35	0.8	0.25	2.8
(d) Polypyrrole (PPy)	29	0.2	29	0.8	0.25	2.32
(e) Polyindole (PIn)	32	0.2	32	0.8	0.25	2.56
(f) TiO$_2$-Polyaniline composite (Ti-PANi)	129	0.2	129	0.7	0.29	10.47
(g) TiO$_2$-Polythiophene composite (Ti-PTh)	60	0.2	60	0.7	0.29	4.872
(h) TiO$_2$-Polypyrrole composite (Ti-PPy)	75	0.2	75	0.7	0.29	6.09
(i) TiO$_2$-Polyindole composite (Ti-PIn)	98	0.2	98	0.7	0.29	7.957

3.6. Measurements of photovoltaic characteristics

Figure 7a–i represents Current-Voltage (IV) characteristics of fabricated photovoltaic cell (a) TiO$_2$, (b) Polyaniline(PANi), (c) Polythiophene (PTh), (d) Polypyrrole (PPy), (e) Polyindole (PIn), (f) TiO$_2$ Polyaniline composite (Ti-PANi), (g) TiO2-Polythiophene composite (Ti-PTh), (h) TiO2-Polypyrrole composite (Ti-PPy) and (i) TiO2-Polyindole composite (Ti-PIn) respectively. The photovoltaic parameters of these materials are listed in Table 3. It is observed that TiO2-Polyaniline composite (Ti-PANi) shows higher short

circuit current (Isc) ascomparred to all other mentioned materials.

The Current-Voltage (I–V) characteristics of PANI-TiO2 heterostructure diode show a nonlinear behavior. It indicates that a p–n heterostructure at PANI-TiO2 interface has been generated. The doping of TiO2 nanoparticles which facilitates the formation of a more efficient network for charge transport. Consequently, the conductivity of nanocomposites also increases with the addition of TiO2. It also facilitates interchain conduction due to the formation of conducting pathways between the chains. Thus, by the addition of TiO2, there becomes a more efficient network for charge transport in the PANI matrix which leads to higher conductivities. As a result, dispersion capacity of TiO2-Polyaniline composite (Ti-PANi) and charge transfer phenomenon are significantly enhancing due to synergistic effects in composite which leads to higher values of Isc.[48–51] The significant enhancement in the value of % η is due to the addition of TiO2 in PANi in composite. The maximum value of % η is found to be 10.47% for TiO2-Polyaniline composite (Ti-PANi).

4. Conclusion

In summary, TiO_2, four Polymers (Polyaniline, Polythiophene, Polypyrrole, Polyindole) and their four composites (TiO_2-Polyaniline composite, TiO_2-Polythiophene composite, TiO_2-Polypyrrole composite, TiO_2-Polyindole composite) were prepared. PV performance of all above compounds were studied. The significant enhancement in value of % η takes place by the addition of TiO_2 in PANi during preparation of composite. The value of % η is found to be highest for TiO_2-Polyaniline composite (Ti-PANi)i.e.10.47%.

Notes on contributors

Ms. Bhagyashri U.Tale is Ph.D. student, at department of chemistry, Bajaj College of Science, Dist.Wardha, Maharashtra, India.

Dr. K.R. Nemade is Assistant Professor, at department of physics, Indira Mahavidyalaya, Kalamb,Dist. yavatmal, Maharashtra, India.

Dr. P.V. Tekade is Associate Professor, at department of chemistry, Bajaj College of Science, Dist.Wardha, Maharashtra, India.

References

[1] Mahmood, N.; Zhang, C.; Yin, H.; Hou, Y. Graphene-based Nanocomposites for Energy Storage and Conversion in Lithium Batteries, Supercapacitors and Fuel Cells. *J. Mater. Chem. A* 2014, *2*(1), 15–32. DOI: 10.1039/C3TA13033A.

[2] Jordehi, A. R. Parameter Estimation of Solar Photovoltaic (PV) Cells: A Review. *Renewable Sustainable Energy Rev.* 2016, *61*, 354–371. DOI: 10.1016/j.rser.2016.03.049.

[3] Bai, J.; Liu, S.; Hao, Y.; Zhang, Z.; Jiang, M.; Zhang, Y. Development of a New Compound Method to Extract the Five Parameters of PV Modules. *Energy Conversion Manage.* 2014, *79*, 294–303. DOI: 10.1016/j.enconman.2013.12.041.

[4] Shafiee, S.; Topal, E. When Will Fossil Fuel Reserves Be Diminished? *Energy Policy.* 2009, *37*(1), 181–189. DOI: 10.1016/j.enpol.2008.08.016.

[5] Apergis, N.; Payne, J. E. Renewable Energy, Output, CO2 Emissions, and Fossil Fuel Prices in Central America: Evidence from a Nonlinear Panel Smooth Transition Vector Error Correction Model. *Energy Econ.* 2014, *42*, 226–232. DOI: 10.1016/j.eneco.2014.01.003.

[6] Shivalkar, R. S.; Jadhav, H. T.; Deo, P. Feasibility Study for the Net Metering Implementation in Rooftop Solar PV Installations across Reliance Energy Consumers. 2015 International Conference on Circuits, Power and Computing Technologies [ICCPCT-2015], IEEE: Nagercoil, India, Mar, 2015, pp 1–6.

[7] Wang, Y.; Zhou, S.; Huo, H. Cost and CO2 Reductions of Solar Photovoltaic Power Generation in China: Perspectives for 2020. *Renewable Sustainable Energy Rev.* 2014, *39*, 370–380. DOI: 10.1016/j.rser.2014.07.027.

[8] Sundareswaran, K.; Sankar, P.; Nayak, P. S. R.; Simon, S. P.; Palani, S. Enhanced Energy Output from a PV System under Partial Shaded Conditions through Artificial Bee Colony. *IEEE Trans. Sustainable Energy.* 2014, *6*(1), 198–209. DOI: 10.1109/TSTE.2014.2363521.

[9] Trifunović, M. Energy at the Crossroads. Synthesis 2015-International Scientific Conference of IT and Business-Related Research, Singidunum University: Serbia, 2015, pp 186–190.

[10] Hunt, T. *The Solar Singularity Is Nigh*; Greentech Media, (accessed 29, 2015).

[11] Liu, Z.; Zhou, J.; Xue, H.; Shen, L.; Zang, H.; Chen, W. Polyaniline/TiO2 Solar Cells. *Synth. Met.* 2006, *156*(9–10), 721–723. DOI: 10.1016/j.synthmet.2006.04.001.

[12] Breeze, A. J.; Schlesinger, Z.; Carter, S. A.; Brock, P. J. Charge Transport in TiO 2/M E H– P P V Polymer Photovoltaics. *Phys. Rev. B.* 2001, *64*(12), 125205. DOI: 10.1103/PhysRevB.64.125205.

[13] Arango, A. C.; Johnson, L. R.; Bliznyuk, V. N.; Schlesinger, Z.; Carter, S. A.; Hörhold, H. H. Efficient Titanium Oxide/conjugated Polymer Photovoltaics for Solar Energy Conversion. *Adv.Mate.* 2000, *12*(22), 1689–1692. DOI: 10.1002/1521-4095(200011)12:22<1689::AID-ADMA1689>3.0.CO;2-9.

[14] Kawata, K.; Gan, S. N.; Ang, D. T. C.; Sambasevam, K. P.; Phang, S. W.; Kuramoto, N. Preparation of polyaniline/TiO2 Nanocomposite Film with Good Adhesion Behavior for Dye-sensitized Solar Cell Application. *Polym. Compos.* 2013, *34*(11), 1884–1891. DOI: 10.1002/pc.22595.

[15] Bouclé, J.; Ravirajan, P.; Nelson, J. Hybrid Polymer–metal Oxide Thin Films for Photovoltaic Applications.

J. Mater. Chem. 2007, *17*(30), 3141–3153. DOI: 10.1039/b706547g.

[16] Çetin, H.; Boyarbay, B.; Akkaya, A.; Uygun, A.; andAyyildiz, E. N. İ. S. E. Electrical Characterization of Heterojunction between Polyaniline Titanium Dioxide Tetradecyltrimethylammonium Bromide and N-silicon. *Synth. Met.* 2011, *161*(21–22), 2384–2389. DOI: 10.1016/j.synthmet.2011.09.005.

[17] Ameen, S.; Akhtar, M. S.; Kim, Y. S.; Shin, H. S. *Fabrication, Doping and Characterization of Polyaniline and Metal Oxides: Dye Sensitized Solar Cells*; Solar cells-dye-sensitized devices, 2011.

[18] Bahramian, A.; Vashaee, D. In-situ Fabricated Transparent Conducting Nanofiber-shape Polyaniline/coral-like TiO2 Thin Film: Application in Bifacial Dye-sensitized Solar Cells. *Solar Energy Mater. Solar Cells.* 2015, *143*, 284–295. DOI: 10.1016/j.solmat.2015.07.011.

[19] Chung, I.; Lee, B.; He, J.; Chang, R. P.; Kanatzidis, M. G. All-solid-state Dye-sensitized Solar Cells with High Efficiency. *Nature.* 2012, *485*, 486. DOI: 10.1038/nature11067.

[20] Jing, X.; Wang, Y.; Wu, D.; Qiang, J. Sonochemical Synthesis of Polyaniline Nanofibers. *Ultrason. Sonochem.* 2007, *14*(1), 75–80. DOI: 10.1016/j.ultsonch.2006.02.001.

[21] Tat'yana, V. V.; Efimov, O. N. Polypyrrole: A Conducting Polymer; Its Synthesis, Properties and Applications. *Russ. Chem. Rev.* 1997, *66*(5), 443. DOI: 10.1070/RC1997v066n05ABEH000261.

[22] Wadatkar, N. S.; Waghuley, S. A. Complex Optical Studies on Conducting Polyindole As-synthesized through Chemical Route. *Egypt. J. Basic Appl. Sci.* 2015, *2*(1), 19–24. DOI: 10.1016/j.ejbas.2014.12.006.

[23] Wadatkar, N. S.; Waghuley, S. A. Studies on Properties of As-synthesized Conducting Polythiophene through Aqueous Chemical Route. *J. Mater. Sci.: Mater. Electron.* 2016, *27*(10), 10573–10581.

[24] Molea, A.; Popescu, V. The Obtaining of Titanium Dioxide Nanocrystalline Powders. *Optoelectron. Adv. Mater. Rapid Commun.* 2011, *5*(3–4), 242–246.

[25] Theivasanthi, T.; Alagar, M. Titanium Dioxide (Tio2) Nanoparticles XRD Analyses: An Insight. *arXiv preprint arXiv:1307*.1091. 2013.

[26] Rajakani, P.; Vedhi, C. Electrocatalytic Properties of polyaniline–TiO2 Nanocomposites. *Int. J. Ind. Chem.* 2015, *6*(4), 247–259. DOI: 10.1007/s40090-015-0046-8.

[27] Bhagwat, A. D.; Sawant, S. S.; Mahajan, C. M. *Facile Rapid Synthesis of Polyaniline (Pani) Nanofibers*, 2016.

[28] Sakthivel, S.; Boopathi, A. Synthesis and Preparation of Polythiophene Thin Film by Spin Coating Method. *Int. J. Sci. Res. Sec.* 2014, *141*, 97–100.

[29] Ma, C.; Sg, P.; Pr, G.; Shashwati, S. Synthesis and Characterization of Polypyrrole (Ppy) Thin Films. *Soft Nanosci. Lett.* 2011, *2011*,6–10.

[30] Sathiyanarayanan, S.; Azim, S. S.; Venkatachari, G. Preparation of polyaniline–TiO2 Composite and Its Comparative Corrosion Protection Performance with Polyaniline. *Synth. Met.* 2007, *157*(4–5), 205–213. DOI: 10.1016/j.synthmet.2007.01.012.

[31] Nemade, K. R.; Waghuley, S. A. Low Temperature Synthesis of Semiconducting α-Al2O3 Quantum Dots.

Ceram. Int. 2014, *40*(4), 6109–6113. DOI: 10.1016/j.ceramint.2013.11.062.

[32] Balachandran, U. G. E. N.; Eror, N. G. Raman Spectra of Titanium Dioxide. *J. Solid State Chem.* 1982, *42*(3), 276–282. DOI: 10.1016/0022-4596(82)90006-8.

[33] Frank, O.; Zukalova, M.; Laskova, B.; Kürti, J.; Koltai, J.; Kavan, L. Raman Spectra of Titanium Dioxide (Anatase, Rutile) with Identified Oxygen Isotopes (16, 17, 18). *Phys. Chem. Chem. Phys.* 2012, *14*(42), 14567–14572. DOI: 10.1039/c2cp42763j.

[34] Mažeikienė, R.; Tomkutė, V.; Kuodis, Z.; Niaura, G.; Malinauskas, A. Raman Spectroelectrochemical Study of Polyaniline and Sulfonated Polyaniline in Solutions of Different pH. *Vib. Spectrosc.* 2007, *44*(2), 201–208. DOI: 10.1016/j.vibspec.2006.09.005.

[35] Agosti, E.; Rivola, M.; Hernandez, V.; Del Zoppo, M.; Zerbi, G. Electronic and Dynamical Effects from the Unusual Features of the Raman Spectra of Oligo and Polythiophenes. *Synth. Met.* 1999, *100*(1), 101–112. DOI: 10.1016/S0379-6779(98)00167-2.

[36] Šetka, M.; Calavia, R.; Vojkůvka, L.; Llobet, E.; Drbohlavová, J.; Vallejos, S. Raman and XPS Studies of Ammonia Sensitive Polypyrrole Nanorods and Nanoparticles. *Sci. Rep.* 2019, *9*(1), 1–10. DOI: 10.1038/s41598-019-44900-1.

[37] Raj, R. P.; Ragupathy, P.; Mohan, S. Remarkable Capacitive Behavior of a Co3O 4–polyindole Composite as Electrode Material for Supercapacitor Applications. *J. Mater. Chem. A.* 2015, *3*(48), 24338–24348. DOI: 10.1039/C5TA07046E.

[38] Liu, Y. C.; Hwang, B. J.; Jian, W. J.; Santhanam, R. In Situ Cyclic Voltammetry-surface-enhanced Raman Spectroscopy: Studies on the Doping–undoping of Polypyrrole Film. *Thin Solid Films.* 2000, *374*(1), 85–91. DOI: 10.1016/S0040-6090(00)01061-0.

[39] Nemade, K. R.; Waghuley, S. A. UV–VIS Spectroscopic Study of One Pot Synthesized Strontium Oxide Quantum Dots. *Results Phys.* 2013, *3*, 52–54. DOI: 10.1016/j.rinp.2013.03.001.

[40] Brüninghoff, R.; Wenderich, K.; Korterik, J. P.; Mei, B. T.; Mul, G.; Huijser, A. Time-Dependent Photoluminescence of Nanostructured Anatase TiO2 and the Role of Bulk and Surface Processes. *J. Phys. Chem. C.* 2019, *123*(43), 26653–26661. DOI: 10.1021/acs.jpcc.9b06890.

[41] Xiao, Q.; Si, Z.; Yu, Z.; Qiu, G. Sol–gel Auto-combustion Synthesis of Samarium-doped TiO2 Nanoparticles and Their Photocatalytic Activity under Visible Light Irradiation. *Mater. Sci. Eng.* 2007, *137*(1–3), 189–194. DOI: 10.1016/j.mseb.2006.11.011.

[42] Haque, F. Z.; Nandanwar, R.; Singh, P. Evaluating Photodegradation Properties of Anatase and Rutile TiO2 Nanoparticles for Organic Compounds. *Optik.* 2017, *128*, 191–200. DOI: 10.1016/j.ijleo.2016.10.025.

[43] Chatterjee, M. J.; Ghosh, A.; Mondal, A.; Banerjee, D. Polyaniline–single Walled Carbon Nanotube Composite–a Photocatalyst to Degrade Rose Bengal and Methyl Orange Dyes under Visible-light Illumination. *RSC Adv.* 2017, *7*(58), 36403–36415. DOI: 10.1039/C7RA03855K.

[44] Tripathi, A.; Mishra, S. K.; Bahadur, I.; Shukla, R. K. Optical Properties of Regiorandom polythiophene/

Al2O3 Nanocomposites and Their Application to Ammonia Gas Sensing. *J. Mater. Sci.: Mater. Electron.* 2015, *26*(10), 7421–7430.

[45] Vanheusden, K.; Warren, W. L.; Seager, C. H.; Tallant, D. R.; Voigt, J. A.; Gnade, B. E. Mechanisms behind Green Photoluminescence in ZnO Phosphor Powders. *J. Appl. Phys.* 1996, *79*(10), 7983–7990. DOI: 10.1063/1.362349.

[46] Vanheusden, K.; Seager, C. H.; Warren, W. T.; Tallant, D. R.; Voigt, J. A. Correlation between Photoluminescence and Oxygen Vacancies in ZnO Phosphors. *Appl. Phys. Lett.* 1996, *68*(3), 403–405. DOI: 10.1063/1.116699.

[47] Dey, S.; Kar, A. K. Morphological and Optical Properties of Polypyrrole Nanoparticles Synthesized by Variation of Monomer to Oxidant Ratio. *Mater. Today Proc.* 2019, *18*, 1072–1076.

[48] Nemade, K.; Dudhe, P.; Tekade, P. Enhancement of Photovoltaic Performance of Polyaniline/graphene Composite-based Dye-sensitized Solar Cells by Adding TiO2 Nanoparticles. *Solid State Sci.* 2018, *83*, 99–106. DOI: 10.1016/j.solidstatesciences.2018.07.009.

[49] Zhang, X.; Yan, G.; Ding, H.; Shan, Y. Fabrication and Photovoltaic Properties of Self-assembled Sulfonated polyaniline/TiO2 Nanocomposite Ultrathin Films. *Mater. Chem. Phys.* 2007, *102*(2–3), 249–254. DOI: 10.1016/j.matchemphys.2006.12.013.

[50] Abaci, S.; Nessark, B.; Riahi, F. Preparation and Characterization of Polyaniline+ TiO 2 Composite Films. *Ionics.* 2014, *20*(12), 1693–1702. DOI: 10.1007/s11581-014-1129-9.

[51] Deivanayaki, S.; Ponnuswamy, V.; Ashokan, S.; Jayamurugan, P.; Mariappan, R. Synthesis and Characterization of TiO2-doped Polyaniline Nanocomposites by Chemical Oxidation Method. *Mater. Sci. Semicond. Process.* 2013, *16*(2), 554–559. DOI: 10.1016/j.mssp.2012.07.004.

CHEMICAL THERMODYNAMICS AND THERMOCHEMISTRY

Partial and Apparent Molar Volume of Azithromycin in Its Solutions in Ethanol, 1-Propanol, and 1-Butanol at 300.15, 305.15, 310.15 K and Ambient Pressure

Nita P. Mohabansi[a],*, Anita K. Satone[a], and Sonia N. Hirani[a]

[a] Department of Chemistry, Bajaj College of Science, Jamanalal Bajaj Marg, Civil Lines, Wardha, India
*e-mail: nitamohabansi15@gmail.com

Abstract—The densities and ultrasound velocities in azithromycin solutions in ethanol, 1-propanol and 1-butanol at various concentrations and at three different temperatures (T = 300.15, 305.15, and 310.15 K) have been measured. Based on the data obtained, various derived acoustical parameters viz, acoustic impedance (Z), adiabatic compressibility (β), intermolecular free length (L_f), free volume (V_f), Rao's constant (R), Wada's constant (W), partial molar volume (V_Φ), and hence apparent molar volume (V_Φ^0) of the solute have been calculated. The results are discussed on the basis of the nature of solute-solvent interactions.

INTRODUCTION

Studies of intermolecular interactions play an important role in understanding the interactions that take place in solutions. Changes in density, viscosity, ultrasound velocity and other parameters from temperature and concentration have been considered by many scientists and shed light on the structural changes occurring in solutions [1−5].

The choice of a suitable solvent is of primary scientific interest in order to obtain the required efficiency, selectivity and kinetics of a chemical process. The presence of hydrogen bonds in polar solvents has a significant effect on the dielectric, physicochemical and acoustic properties of mixtures. Alcohols are widely used as solvents in chemical and pharmaceutical industries, during extraction [6−8], as dispersing agents for nanomaterials [9−12] and for the synthesis of other organic compounds [13−16]. A large number of studies devoted to alcohols and their mixtures at various temperatures and pressures have been carried out using densimetry, viscometry, spectroscopy, and computer chemistry [17−29]. In clinical medicine, undesirable drug−alcohol interactions are of common concern [30]. Heavy drinking and its combined effect with the antibiotics resulted into deadly incidental and intentional poisoning. When a new drug is synthesized, drug-alcohol interactions should be thoroughly studied [30, 31].

Azithromycin (Fig. 1) is a macrolide antibiotic similar in structure to erythromycin. Azithromycin has increased activity against Gram-negative bacteria compared with erythromycin, while maintaining activity against Gram-positive organisms. Azithromycin is characterized by good oral bioavailability, excellent tissue penetration and persistence, and long elimination half-lives [32]. Azithromycin demonstrates good results in vitro against Zika and Ebola viruses [33] and severe respiratory diseases. Recently, the evaluation of azithromycin as a drug for the COVID-19 therapy has started [34−37].

Therefore, in the present article we report the experimental densities, ultrasonic velocities and the derived parameters of azithromycin solutions of various concentrations and at different temperatures: 300.15, 305.15, and 310.15 K in ethanol, 1-propanol, and 1-butanol.

EXPERIMENTAL

In the present study, the chemicals used are ethanol, 1-propanol, and 1-butanol, are of AR grade. These chemicals were used without any further purification. The details of these chemicals are given in Table 1. All the solutions were prepared gravimetrically and are kept hermetically sealed to prevent contact with moisture from the air and evaporation. Solutions were prepared using CONTECH CA 224 analytical balance (e ± 0.0001 g). The solutions of different
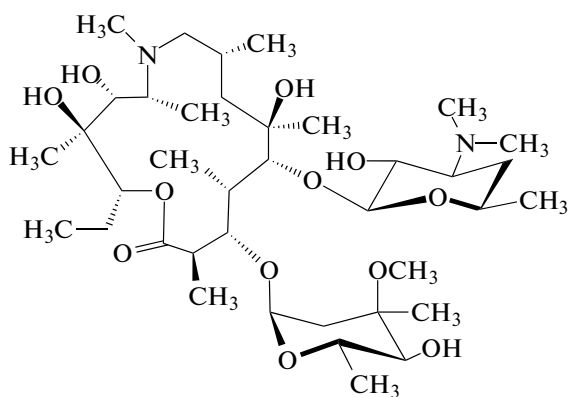
Fig. 1. Structure of azithromycin.

molality viz, 0.0144, 0.0275, 0.0394, 0.0503, 0.0602, 0.0694, 0.0779, 0.0858, 0.0931, and 0.1 of azithromycin were prepared in ethanol, 1-propanol, and 1-butanol. The solutions were gently stirred on a magnetic stirrer before measurements. Care was taken to avoid contamination during mixing. The estimated uncertainty of molality value is $u(m) = \pm 1 \times 10^{-3}$.

Densities were measured using calibrated pycnometer with nominal volume of 10 cm^3. The ultrasonic velocity (u) was measured on digital ultrasonic pulse echo velocity meter (Vi Microsystems Pvt. Ltd. model VCT-70) at 2 MHz with an accuracy of 0.1% (2 ± 0.0001 MHz). The estimated uncertainity of ultrasonic velocity is within $u(m) = \pm 1.09$ m s^{-1}. The instrument has a built-in thermostat to maintain the temperature (±0.1 K). Ultrasonic velocity meter was calibrated with triple distilled water and pure methanol at 300.15, 305.15, and 310.15 K.

RESULTS AND DISCUSSION

The comparison of experimentally obtained values of densities (ρ) and ultrasonic velocity (U) of pure liquids with literature values is presented in Table 2.

The experimentally determined values of density (ρ), ultrasonic velocity (u) for all solutions of the drug at different concentrations and at $T = 300.15$, 305.15, and 310.15 K are listed in Table 3. The data on density and ultrasonic velocity were used to calculate acoustical parameters [45] viz., acoustic impedance (Z), adiabatic

Table 1. Specification and mass fraction purity[a] of chemical samples

S.N.	Chemical name	Source	CAS no.	M, g/mol	Fraction purity
1	Ethanol	Merck	64-17-5	46.07	≥99.9%
2	1-Propanol	Merck	71-23-8	60.10	≥99.5%
3	1-Butanol	Merck	71-36-3	74.12	≥99.5%
4	Azithromycin	—	83905-01-5	749	

[a] Purity as provided by supplier.

Table 2. Comparison of experimental densities (ρ) and ultrasonic velocity (u) of pure liquids with interpolated literature values at 300.15, 305.15, and 310.15 K and atmospheric pressure

Liquids	$\rho \times 10^{-3}$, kg m^{-3}		u, m s^{-1}	
	exp.	literature	exp.	literature
300.15 K				
Ethanol	0.7810	0.7893 [38]	1128.2	1127.4 [39]
1-Propanol	0.7962	0.798 [39]	1188.1	1189.2 [38]
1-Butanol	0.8042	0.8069 [38]	1227.9	1225.8 [13]
305.15 K				
Ethanol	0.7875	0.7873 [38]	1108.9	1109.4 [38]
1-Propanol	0.7959	0.7955 [40]	1170.1	1169.7 [38]
1-Butanol	0.7942	0.7946 [42]	1203.2	1203 [44]
310.15 K				
Ethanol	0.7853	0.7855 [38]	1093.1	1092.9 [43]
1-Propanol	0.7879	0.7873 [41]	1098.3	1093 [41]
1-Butanol	0.7955	0.7945 [41]	1188.9	1189.5 [43]

Table 3. Molality (m), density (ρ), ultrasonic velocity (u), adiabatic compressibility (β), acoustic impedance (Z), intermolecular free length (L_f), free volume (V_f), Rao's constant (R), Wada's constant (W), and partial molar volume (V_Φ) for the solution of drug in ethanol, 1-propanol, and 1-butanol at 300.15, 305.15, 310.15 K and atmospheric pressure

m, mol kg^{-1}	ρ, kg/m^3	u, m s^{-1}	$Z \times 10^{-5}$, kg m^{-2} s^{-1}	$\beta \times 10^{10}$, m^2 N^{-1}	$L_f \times 10^{11}$, m	$V_f \times 10^6$, m^3 mol^{-1}	R	W	$V_\Phi \times 10^{-6}$, m^3 mol^{-1}
				Ethanol, $T = 300.15$ K					
0.014	772.63	1149.19	8.879	9.592	9.901	2.718	0.0393	1.407	55.123
0.028	780.02	1159.15	9.042	9.499	9.804	2.830	0.0390	1.411	54.191
0.039	791.74	1172.63	9.284	9.352	9.653	3.008	0.0384	1.412	53.958
0.050	800.31	1182.52	9.464	9.247	9.545	3.116	0.0380	1.412	53.755
0.060	805.45	1188.75	9.575	9.181	9.476	3.181	0.0378	1.413	53.58
0.069	817.74	1202.89	9.837	9.041	9.332	3.264	0.0372	1.414	53.392
0.078	824.88	1211.52	9.994	8.943	9.230	3.453	0.0369	1.416	53.25
0.086	830.31	1218.25	10.115	8.875	9.160	3.538	0.0367	1.417	53.128
0.093	836.14	1225.81	10.249	8.810	9.093	3.633	0.0365	1.419	52.994
0.102	842.88	1234.06	10.402	8.723	9.004	3.852	0.0362	1.421	52.842
				Ethanol, $T = 305.15$ K					
0.014	720.34	1077.28	7.760	10.289	10.619	2.534	0.0422	1.438	55.669
0.028	733.45	1092.57	8.013	10.102	10.426	2.661	0.0414	1.440	55.383
0.039	742.31	1103.04	8.188	9.975	10.296	2.820	0.0410	1.444	55.125
0.050	754.02	1116.44	8.418	9.815	10.131	2.935	0.0403	1.446	54.918
0.060	770.31	1135.21	8.745	9.600	9.909	3.042	0.0395	1.448	54.683
0.069	778.67	1145.35	8.918	9.495	9.800	3.108	0.0391	1.449	54.515
0.078	788.88	1157.86	9.134	9.351	9.651	3.302	0.0386	1.451	54.271
0.086	801.79	1172.74	9.403	9.190	9.486	3.416	0.0380	1.451	54.129
0.093	805.74	1178.53	9.496	9.142	9.436	3.501	0.0378	1.456	53.97
0.102	822.32	1197.20	9.845	8.941	9.229	3.758	0.0371	1.457	53.81
				Ethanol, $T = 310.15$ K					
0.014	715.46	1063.38	7.608	10.359	10.692	2.517	0.0425	1.351	56.163
0.028	728.62	1078.68	7.859	10.169	10.496	2.644	0.0417	1.353	55.856
0.039	740.31	1092.39	8.087	10.002	10.324	2.812	0.0411	1.355	55.559
0.050	748.89	1102.72	8.258	9.882	10.200	2.915	0.0406	1.357	55.335
0.060	756.89	1112.31	8.419	9.770	10.084	2.989	0.0402	1.359	55.056
0.069	768.76	1126.05	8.657	9.617	9.926	3.068	0.0396	1.361	54.843
0.078	777.74	1136.86	8.842	9.485	9.790	3.256	0.0392	1.363	54.604
0.086	784.61	1145.27	8.986	9.392	9.693	3.343	0.0389	1.365	54.43
0.093	794.89	1157.58	9.201	9.267	9.565	3.453	0.0384	1.367	54.253
0.102	802.94	1167.07	9.371	9.157	9.452	3.670	0.0380	1.369	54.043
				1-Propanol, $T = 300.15$ K					
0.014	796.27	1100.54	8.763	9.308	9.607	2.801	0.0382	1.472	71.532
0.028	806.27	1112.39	8.969	9.189	9.485	2.926	0.0377	1.473	71.271
0.039	815.13	1123.23	9.156	9.084	9.376	3.097	0.0373	1.475	71.053
0.050	825.99	1136.60	9.388	8.960	9.248	3.216	0.0368	1.477	70.794
0.060	830.84	1142.59	9.493	8.901	9.187	3.282	0.0366	1.478	70.606
0.069	836.27	1150.62	9.622	8.841	9.125	3.338	0.0364	1.483	70.433
0.078	843.99	1160.88	9.798	8.740	9.021	3.533	0.0361	1.487	70.212
0.086	855.99	1176.65	10.072	8.608	8.885	3.647	0.0356	1.492	69.986
0.093	862.56	1185.10	10.222	8.540	8.815	3.748	0.0353	1.494	69.851
0.102	868.27	1192.51	10.354	8.468	8.741	3.968	0.0351	1.496	69.636

Table 3. (Contd.)

m, mol kg^{-1}	ρ, kg/m^3	u, m s^{-1}	$Z \times 10^{-5}$, kg m^{-2} s^{-1}	$\beta \times 10^{10}$, m^2 N^{-1}	$L_f \times 10^{11}$, m	$V_f \times 10^6$, m^3 mol^{-1}	R	W	$V_\Phi \times 10^{-6}$, m^3 mol^{-1}
1-Propanol, $T = 305.15$ K
0.014	750.27	1035.71	7.771	9.878	10.196	2.639	0.0405	1.438	73.292
0.028	762.27	1049.98	8.004	9.720	10.032	2.766	0.0399	1.441	72.859
0.039	774.84	1065.72	8.258	9.556	9.864	2.943	0.0392	1.444	72.546
0.050	781.99	1074.59	8.403	9.464	9.768	3.044	0.0389	1.446	72.123
0.060	791.99	1086.49	8.605	9.337	9.637	3.128	0.0384	1.448	71.814
0.069	805.99	1103.06	8.891	9.173	9.468	3.217	0.0378	1.449	71.528
0.078	813.99	1112.72	9.057	9.062	9.354	3.407	0.0374	1.451	71.189
0.086	830.56	1131.67	9.399	8.872	9.157	3.539	0.0367	1.451	70.869
0.093	837.41	1141.19	9.556	8.797	9.080	3.638	0.0364	1.456	70.615
0.102	843.72	1148.94	9.694	8.715	8.995	3.856	0.0362	1.457	70.389
1-Propanol, $T = 310.15$ K
0.014	731.74	1005.29	7.356	7.356	10.454	2.574	0.0415	1.412	74.266
0.028	739.99	1015.03	7.511	7.511	10.334	2.685	0.0411	1.413	73.877
0.039	748.56	1025.61	7.677	7.677	10.210	2.844	0.0406	1.416	73.571
0.050	756.27	1034.85	7.826	7.826	10.100	2.944	0.0402	1.417	73.246
0.060	763.74	1043.73	7.971	7.971	9.994	3.016	0.0398	1.419	73.012
0.069	773.19	1054.69	8.155	8.155	9.869	3.086	0.0394	1.419	72.693
0.078	780.84	1063.78	8.306	8.306	9.751	3.269	0.0390	1.421	72.442
0.086	787.99	1072.19	8.449	8.449	9.652	3.358	0.0387	1.422	72.209
0.093	795.99	1082.02	8.613	8.613	9.552	3.458	0.0383	1.424	72.046
0.102	805.13	1092.87	8.799	8.799	9.426	3.680	0.0379	1.425	71.747
1-Butanol, $T = 300.15$ K
0.014	804.21	1198.42	9.638	9.216	9.512	2.829	0.0378	1.513	89.285
0.028	819.36	1216.20	9.965	9.042	9.333	2.973	0.0371	1.514	88.999
0.039	826.5	1224.86	10.123	8.959	9.247	3.140	0.0368	1.515	88.769
0.050	831.93	1231.50	10.245	8.896	9.182	3.239	0.0366	1.515	88.567
0.060	839.07	1240.28	10.407	8.813	9.097	3.314	0.0363	1.517	88.416
0.069	849.36	1252.39	10.637	8.704	8.984	3.390	0.0358	1.517	88.212
0.078	856.21	1261.75	10.803	8.615	8.892	3.584	0.0356	1.52	88.021
0.086	862.55	1269.79	10.953	8.543	8.818	3.675	0.0353	1.522	87.857
0.093	877.64	1287.62	11.301	8.393	8.663	3.813	0.0347	1.522	87.685
0.102	883.07	1295.15	11.437	8.326	8.594	4.036	0.0346	1.525	87.568
1-Butanol, $T = 305.15$ K
0.014	747.93	1113.51	8.328	9.909	10.228	2.631	0.0406	1.461	90.982
0.028	756.21	1125.16	8.509	9.798	10.113	2.744	0.0402	1.467	90.715
0.039	771.07	1143.34	8.816	9.603	9.912	2.929	0.0394	1.47	90.393
0.050	774.50	1148.27	8.893	9.555	9.863	3.015	0.0393	1.473	90.215
0.060	782.21	1158.57	9.062	9.454	9.758	3.089	0.0389	1.477	89.914
0.069	794.35	1173.72	9.323	9.307	9.607	3.171	0.0383	1.479	89.643
0.078	804.79	1188.08	9.562	9.166	9.461	3.369	0.0379	1.486	89.472
0.086	818.79	1204.94	9.866	8.999	9.289	3.489	0.0372	1.487	89.286
0.093	829.07	1217.33	10.093	8.885	9.171	3.602	0.0368	1.489	89.074
0.102	831.03	1222.19	10.157	8.848	9.132	3.798	0.0367	1.495	88.878

Table 3. (Contd.)

m, mol kg^{-1}	ρ, kg/m^3	u, m s^{-1}	$Z \times 10^{-5}$, kg m^{-2} s^{-1}	$\beta \times 10^{10}$, m^2 N^{-1}	$L_f \times 10^{11}$, m	$V_f \times 10^6$, m^3 mol^{-1}	R	W	$V_\Phi \times 10^{-6}$, m^3 mol^{-1}
				1-Butanol $T = 310.15$ K					
0.014	725.64	1012.28	7.346	10.213	10.542	2.553	0.0419	1.408	93.989
0.028	733.93	1025.17	7.524	10.095	10.420	2.663	0.0414	1.415	93.595
0.039	742.5	1036.39	7.695	9.973	10.293	2.820	0.0410	1.419	93.184
0.050	750.21	1048.69	7.867	9.865	10.182	2.920	0.0405	1.422	92.838
0.060	757.64	1063.40	8.057	9.760	10.074	2.992	0.0402	1.425	92.446
0.069	767.64	1075.82	8.258	9.631	9.941	3.064	0.0396	1.429	92.129
0.078	746.21	1088.35	8.121	9.885	10.203	3.124	0.0408	1.433	91.815
0.086	753.36	1099.19	8.281	9.781	10.096	3.210	0.0405	1.436	91.551
0.093	761.27	1112.05	8.466	9.676	9.988	3.307	0.0400	1.441	91.279
0.102	770.5	1124.77	8.666	9.543	9.850	3.521	0.0396	1.445	91.032

Table 4. The apparent molal volume of azithromycin drug in alcoholic solution at different temperature (T = 300.15, 305.15, and 310.15 K)

Sr. no.	Solvent	300.15 K			305.15 K			310.15 K		
		$V_\Phi^0 \times 10^{-6}$, m^3/mol	$-S_m$	R^2	$V_\Phi^0 \times 10^{-6}$, m^3/mol	$-S_m$	R^2	$V_\Phi^0 \times 10^{-6}$, m^3/mol	$-S_m$	R^2
1	Ethanol	296.2	183.6	0.999	309.8	216.7	0.999	315.3	246.4	0.999
2	1-Propanol	297.8	199.4	0.998	313.8	246.7	0.997	345.4	349.0	0.999
3	1-Butanol	318.9	219.1	0.996	338.3	342.4	0.997	346.9	289.1	0.998

compressibility (β), intermolecular free length (L_f), free volume (V_f), Rao's constant (R), Wada's constant (W), and partial molar volume (V_m) by the following equations:

$$\beta = 1/u^2\rho, \qquad (1)$$

$$Z = u\rho, \qquad (2)$$

$$L_f = K_T \sqrt{\beta}, \qquad (3)$$

where K_T is temperature dependent constant known as Jacobson's constant

$$K_T = (93.875 + 0.375T) \times 10^{-8},$$

where T is absolute temperature, free volume

$$V_f = [M_{eff} u/K\eta]^{1/2}, \qquad (4)$$

where M_{eff} is effective molecular weight, Rao's constant:

$$R = \left(\frac{M}{\rho}\right)(u)^{1/3}, \qquad (5)$$

Wada's constant:

$$W = \frac{M(B)^{-1/7}}{\rho}, \qquad (6)$$

where M is molecular weight of solute, partial molar volume of azithromycin:

$$V_\Phi = \frac{M_2}{\rho} + \frac{(\rho_0 - \rho)}{m\rho_0\rho}. \qquad (7)$$

It is observed from Table 3 that the densities and ultrasonic velocities increase with concentration. Same types of the trends are observed at T = 300.15, 305.15, and 310.15 K. The product of density and ultrasonic velocity is the acoustic impedance (Z). Z increases gradually with increase in concentration and decreases with increase in temperature. This reflects the structure making action through strong hydrogen bonding [46]. Adiabatic compressibility (β) varies inversely to ultrasonic velocity and density (Eq. (2)). With the increase in the molality of the solution, β decreases linearly at the studied temperature. Naik et al. also reported the same trend in the values of β [1]. This indicates the closer packing of the molecules [47]. Intermolecular free length (L_f) is the indicator of the interactions between the solute and solvent due to association between the molecules through H-bonding. With the increase in the concentration, the decrease in the L_f values reflects the strong solute-solvent interactions. From the Table 3, it is observed that the value of V_f increases with increase in the concen-

tration for all studied alcoholic solutions. This may be due to the dispersive forces of the component molecules. The decrease in the Rao's constant and the increase in the Wada's constant values confirms that these alcohols are associated in solution due to dipole−dipole interaction and hydrogen bonding.

The partial molar volume (V_φ) of the drug in ethanol, 1-propanol, and 1-butanol were calculated from the density measurements at the different temperatures by using Eq. (7). These V_φ values are listed in Table 3. By using the values of the partial molar volumes, the apparent molar volumes ($V^0\varphi$) of the drug were evaluated by using Masson's equation [48] given below:

$$V_\varphi = V^0\varphi + S_m. \tag{8}$$

When V_φ are plotted against molality, the intercept on Y axis and slope gives the values of the apparent molar volume, $V^0\varphi$ and S_m, respectively. The negative values of the S_m listed in Table 4 confirm the drug−solvent interactions [2].

CONCLUSION

In the present work, densities and ultrasonic velocity in the solutions of azitromycin in ethanol, 1-propanol, and 1-butanol were experimentally determined at various concentrations and temperatures (T = 300.15, 303.15, and 310.15 K). By using these values, acoustical parameters of the drug are calculated over the entire concentration range. The obtained data are interpreted in terms of molecular interactions between the drug and the alcohols. The negative values of the apparent molar volume of the solute confirmed the presence of strong H-bonding between the drug and alcohol [49]. The strength of H bonding increases with increase in the concentration and temperature. The extent intermolecular interactions is higher in 1-butanol than in other solvents. The temperature also play the major effect on these interactions.

ACKNOWLEDGMENTS

REFERENCES

1. R. R. Naik, S. V Bawankar, and S. D. Kukade, Russ. J. Phys. Chem. A **89**, 2149 (2015).
https://doi.org/10.1134/S003602441511014X

2. D. M. Bhattacharya, S. S. Dhondge, and S. P. Zodape, J. Chem. Thermodyn. **101**, 207 (2016).
https://doi.org/10.1016/j.jct.2016.05.025

3. A. D. Arsule, R. T. Sawale, and S. D. Deosarkar, J. Mol. Liq. **275**, 478 (2019).
https://doi.org/10.1016/j.molliq.2018.10.122

4. D. M. Makarov, G. I. Egorov and A. M. Kolker, J. Chem. Thermodyn. **151**, 106233 (2020).
https://doi.org/10.1016/j.jct.2020.106233

5. A. Dyshin and M. G. Kiselev, J. Chem. Eng. Data **64**, 2536 (2019).

6. Y. Marcus, Separations **5**, 1 (2018).
https://doi.org/10.3390/separations5010004

7. M. N. Rammunia, Th. U. Ariyadasaa, P. H. V. Nimarshanab, and R. A. Attalage, Food Chem. **277**, 128 (2019).
https://doi.org/10.1016/j.foodchem.2018.10.066

8. Q. Salamat, Y. Yamini, M. Moradi, A. Farahani, et al., J. Separ. Sci. **42** (8) (2019).
https://doi.org/10.1002/jssc.201801152

9. R. Kevin and D. Hinklei, J. Phys. Chem. C **121**, 41 (2017).
https://doi.org/10.1021/acs.jpcc.7b07769

10. A. A. Dyshin, O. V. Eliseeva, G. V. Bondarenko, et al., Russ. J. Phys. Chem. A **87**, 2068 (2013).
https://doi.org/10.1134/S0036024413120054

11. T. Liu, G. Xu, J. Zhang, H. Zhang, and J. Pang, Colloid Polym. Sci. **291**, 3 (2013).

12. A. A. Dyshin, O. V. Eliseeva, G. V. Bondarenko, et al., Russ. J. Phys. Chem. A **89**, 1628 (2015).
https://doi.org/10.1134/S0036024415090095

13. B. Ndaba, I. Chiyanzu, and S. Marx, Biotechnol. Rep. **8**, 1 (2015).
https://doi.org/10.1016/j.btre.2015.08.001

14. B. Gananprakasam, J. Zhang, and D. Milstein, Angew. Chem., Int. Ed. **49**, 8 (2010).
https://doi.org/10.1002/anie.200907018

15. L. U. Nordstrom, H. Vogt, and R. Madsen, J. Am. Chem. Soc. **130**, 52 (2008).

16. C. Gunanathan and D. Milstein, Angew. Chem. **47**, 45 (2008).
https://doi.org/10.1002/anie.200803229

17. K. A. Kurnia, M. I. A. Mutalib, T. Murugesan, and B. Ariwahjoedi, J. Solut. Chem. **40**, 818 (2011).
https://doi.org/10.1007/s10953-011-9680-8

18. S. J. Barlow, G. V. Bondarenko, Y. E. Gorbaty, T. Yamaguchi, and M. Poliakoff, J. Phys. Chem. A **106**, 10452 (2002).
https://doi.org/10.1021/jp0135095

19. A. A. Dyshin, R. D. Oparin, and M. G. Kiselev, Russ. J. Phys. Chem. B **6**, 868 (2012).
https://doi.org/10.1134/S1990793112080106

20. M. Sokolova, S. J. Barlow, G. V. Bondarenko, Y. E. Gorbaty, and M. Poliakoff, J. Phys. Chem. A **110**, 3882 (2006).
https://doi.org/10.1021/jp055931h

21. O. V. Eliseeva, A. A. Dyshin, and M. G. Kiselev, Russ. J. Phys. Chem. A **87**, 401 (2013).
https://doi.org/10.1134/S0036024413030096

22. M. Tomšič, A. Jamnik, G. F. Popovski, O. Glatter, and L. Vlček, J. Phys. Chem. B **111**, 1738 (2007).
https://doi.org/10.1021/jp066139z

23. A. M. Bala, W. G. Killian, C. Plascencia, J. A. Storer, A. T. Norfleet, and L. Peereboom, J. Phys. Chem. A **124**, 3077 (2020).
https://doi.org/10.1021/acs.jpca.9b11245

24. D. V. Ivlev, A. A. Dyshin, M. G. Kiselev, and A. M. Kolker, Russ. J. Phys. Chem. A **84**, 2077 (2010). https://doi.org/10.1134/S0036024410120125

25. G. S. Fanourgakis, Y. J. Shi, S. Consta, and R. H. Lipson, J. Chem. Phys. **119**, 6597 (2003). https://doi.org/10.1063/1.1605384

26. D. S. Bulgarevich, Y. Horikawa, and T. Sako, J. Supercrit. Fluids **46**, 206 (2008). https://doi.org/10.1016/j.supflu.2008.01.013

27. Y. E. Gorbaty and G. V. Bondarenko, Russ. J. Phys. Chem. B **6**, 873 (2012). https://doi.org/10.1134/S1990793112080118

28. J. M. Andanson, P. A. Bopp, and J. C. Soetens, J. Mol. Liq. **129**, 101 (2006). https://doi.org/10.1016/j.molliq.2006.08.019

29. A. A. Dyshin, O. V. Eliseeva, and M. G. Kiselev, Russ. J. Phys. Chem. A **86**, 563 (2012). https://doi.org/10.1134/S0036024412040073

30. T. Launiainen, E. Vuori, and I. Ojanpera, Int. J. Legal Med. **123**, 109 (2009).

31. H. J. Carson, Leg. Med. **10**, 92 (2008).

32. C. P. Digest, Am. J. Hospital Pharm. **49**, 686 (1992). https://doi.org/10.1093/ajhp/49.3.686

33. P. Gautret, J. C. Lagier, P. Parola, V. T. Hoang, L. Meddeb, M. Mailhe, B. Doudier, J. Courjon, V. Giordanengo, V. E. Vieira, H. Tissot Dupont, S. Honoré, P. Colson, E. Chabrière, B. la Scola, J. M. Rolain, P. Brouqui, and D. Raoult, Int. J. Antimicrob. Agents **56**, 105949 (2020). https://doi.org/10.1016/j.ijantimicag.2020.105949

34. N. Bleyzac, S. Goutelle, L. Bourguignon, and M. Tod, Clin. Drug Invest. **40**, 683 (2020). https://doi.org/10.1007/s40261-020-00933-3

35. J. M. Molina, C. Delaugerre, J. le Goff, B. Mela-Lima, D. Ponscarme, L. Goldwirt, and N. Castro, Med. Mal. Infect. **50**, 384 (2020). https://doi.org/10.1016/j.medmal.2020.03.006

36. A. Fanin, J. Calegari, A. Beverina, S. Tiraboschi, and G. A. Metodologica, Intern. Emerg. Med. **15**, 841 (2020). https://doi.org/10.1007/s11739-020-02388-y

37. B. Damle, M. Vourvahis, E. Wang, J. Leaney, and B. Corrigan, Clin. Pharm. Ther. **108**, 2 (2020).

38. S. Sreehari Sastry, S. Babu, T. Vishwam, K. Parvateesam, and H. Sie Tiong, Phys. B (Amsterdam, Neth.) **420**, 40 (2013). https://doi.org/10.1016/j.physb.2013.03.028

39. E. N. Rezanova and R. N. Lichtenthaler, Fluid Phase Equilib. **182**, 289 (2001).

40. G. Watson, C. K. Mikkelsen, A. Baylaucq, and C. Boned, J. Chem. Eng. Data **51**, 112 (2006).

41. A. Rodríguez, J. Canosa, and J. Tojo, J. Chem. Eng. Data **46**, 1476 (2001).

42. C. Valles, E. Pérez, M. Cardoso, M. Domínguez, and A. M. Mainar, J. Chem. Eng. Data **49**, 1460 (2004).

43. M. Dominguez, C. Lafuente, M. C. López, F. M. Royo, and J. S. Urieta, J. Chem. Thermodyn. **32**, 155 (2000).

44. J. A. Riddick, W. A. Bunger, and T. K. Sakano, *Organic Solvents: Physical Properties and Methods of Purification,* 4th ed. (Wiley, New York, 1986), Vol. 2.

45. N. Mohabansi, J. Sci. Res. **64**, 352 (2020). https://doi.org/10.37398/JSR.2020.640248

46. S. Chauhan, L. Pathania, and M. S. Chauhan, J. Mol. Liq. **221**, 755 (2016). https://doi.org/10.1016/j.molliq.2016.06.025

47. R. Roy, S. Mondal, S. Ghosh, and S. Jengathe, Russ. J. Phys. Chem. A **92**, 2606 (2018). https://doi.org/10.1134/S0036024418130253

48. S. Chauhan, L. Pathania, and M. S. Chauhan, J. Mol. Liq. **221**, 755 (2016). https://doi.org/10.1016/j.molliq.2016.06.025

49. P. V. Tekade, B. U. Tale, S. D. Bajaj, and N. Authankar, Russ. J. Phys.Chem. A **92**, 2488 (2018). https://doi.org/10.1134/S0036024418120415

Evaluation of *Ehretia Laevis Roxb.* (Khandu Chakka/Ajan Vruksha) in the Wound Healing Adjudged by Histological Examination of the Tissue

Rushikesh Thakre[1], Arvinda Bhake[2], Pradip Tekade[3], Ketaki Harne[4], Preeti Sujit Borkar[5]

[1]Assistant Professor , Department of Samhita Siddhant, MGACH & RC, Datta Meghe Institute Medical Sciences (DU) Wardha(MS) India, [2]Professor Department of Pathology,JNMC, Datta Meghe Institute Medical Sciences (DU) , Wardha(MS), India, [3]Associate Professor Department of Chemistry Bajaj College of Science(Formerly known as Jankidevi Bajaj College of Science), Wardha (MS), India, [4]PhD scholar(Chemistry), Rastra Santa Tukadoji Maharaj Nagpur University Nagpur (MS). India, [5]Professor & Head, Department of Samhita& Siddhant MGACH & RC, Datta Meghe Institute Medical Sciences (DU) Wardha(MS) India

Abstract

Many herbal plants are mentioned in Ayurveda for wound healing. Folklore medicine for various ailments including wound healing is being practiced in India. *Ehretia Laevis Roxb*. contains many such chemical compounds useful for promotion of healing & repair. Tissue renewal goes hand in hand with inflammation influenced by multiple processes. *Ehretia Laevis Roxb*. called Khandu Chakka & Ajan Vruksha and traditionally being used for wound healing, body pain & minor fractures in the form of local application by folklore in the state of Maharashtra India. Objectives of the present study is to know the effect of *Ehretia Laevis Roxb*. in the wound healing on the histological parameters in animal model. Phenytoin ointment as a control was used. The present study has found put that leaf extract paste of *Ehretia Laevis Roxb*. has enhanced the process of wound healing ascertained on histological parameters as compared to topical phenytoin application. *Ehretia Laevis Roxb*. paste is found to be immensely useful at wound healing as compared to Phenytoin. *Ehretia Laevis Roxb*. is concluded to promote the healing significantly as observed by feature of granulation, collagenisation & re epithelisation of the wounds suggesting early healing by primary intension

Key words*:- Ehretia Laevis Roxb., Phenytoin, Khandu Chakka, Ajan Vruksha, Wound healing , Histological study.*

Introduction

Many herbal plants are mentioned in Ayurveda for wound healing. Folklore medicine for various ailments including wound healing is being practiced in India. *Ehretia Laevis Roxb*. contains many such chemical compounds useful for promotion of healing & repair. These chemical compounds act as anti bacterial, anti fungal, anti viral, anti-inflammatory, anti parasite, analgesic, anti-oxidant, anti-apoptotic, clotting of blood plasma, improves immune responses, promotes collagen synthesis & regeneration of tissue. These properties are important for phenomenon of wound healing. Both of these processes can be mediated by external application of herbal extract of *Ehretia laevis Roxb*.[1]

Tissue renewal goes hand in hand with inflammation influenced by multiple processes. These processes includes the regeneration of cells by two underline processes such as wound healing by primary intension and wound healing by secondary intension.

Ehretia Laevis Roxb. called Khandu Chakka & Ajan Vruksha and traditionally being used for wound healing, body pain & minor fractures in the form of local application by folklore in the state of Maharashtra India.[1]

Infections, old age, local tissue stress, metabolic disorder, diabetics, chemotherapy drugs, obesity, alcohol, habits such as chronic smoking, mal

nourishment influenced wound healing. Such situations require bearing of high expenditure on modern medicine drugs like expensive antibiotics.

There are not many studies in literature that has proven the role of *Ehretia Laevis Roxb*. in the wound healing, by histological evidences gathered by time graded biopsies collected from the site of wound after application of *Ehretia Laevis Roxb*. leaves paste.

Modern medicine uses Phenytoin for local application at enhancement of wound healing. [3]. Most of the studies reviewed for the present work & compared the results of Phenytoin with that of *Ehretia Laevis Roxb*.[3-9]

Study has been planned to evaluate & address their research gap involving histological evaluation.

Objectives of the present study is to know the effect of *Ehretia Laevis Roxb*. in the wound healing on the following parameters, that unable to judge the processes of wound healing secondary experimental burn into the Albino Rabbits.

· Quantification of granulation tissue after application of Ehretia Laevis Roxb. compared to Phenytoin paste application.

· Gradation of inflammatory infiltrates after application of paste of Ehretia Laevis Roxb. compared to Phenytoin.

· Quantification & pattern of collagen after application of paste of *Ehretia Laevis Roxb*. compared to Phenytoin.

Review of Literature

Drug Review:-

Ehretia laevis Roxb. known as Khandu Chakka & referred to Sant Dnyaneshwar Alandi Maharashtra, India too called as Ajan Vruksha[10], when he took Sanjivan Samadhi. Folklore believes this plant for its plenty of medicinal healing properties. [1]

Plant Description:- Following is the binomial nomenclature for the plant in the botany.

(Figure 1 & Figure 2)

Planta   Tracheophyta   Magnoliopsida Boraginales   Boraginaceae

Ehretia   Ehretia Laevis (Roxb)

Figure 1   **Figure 2**

Ehretia Laevis Roxb. **plant shows anti microbial activity on salivary microflora , B.subtilis , S. aureus, E. Coli. Pseudomonas aeruginosa**[11-14]

Materials and Methods

Study Material:

• Healthy 10 Rabbits were selected from DMIMS animal house. Then they were divided into two groups of 5 in each group.

• Leaves paste was prepared under all aseptic precautions. Leaves paste was applied on wound in first group and considered as Group A.

• Phenytoin ointment as a control was used in second group and considered as Group B.

• Animals were anesthetized before creating wound

• The skin shaved, disinfected with 70% alcohol and injected with 1 ml of Lignocaine HCl (2%, 100 mg/5 ml).

• Approval from institutional animal ethical committee was taken.

External wound protocols

· Physically external wound was made by burn injury of 2X2cm. The edges of the wound was sampled by forcep biopsy.

· Daily leaves paste was applied in Group A and Phenytoin ointment in group B. Biopsies for assessment of healing & repair were taken on 7th and on 15th day.

Assessment of biopsy from wound site was done by following histological features.

• Epithelialization

• Leucocytic infiltration

• Vascularity

• Fibroblastic cell proliferation

• Appearance of granulation tissue

Parameters to calculate healing score [15]

Histological Parameter

The following histological parameters were used to calculate healing score.

1. Quantity of granulation tissue (profound -1, moderate – 2, scanty-3, absent-4)

2. Inflammatory infiltrate(plenty -1, moderate – 2, a few- 3)

3. Collagen fiber orientation (vertical -1, mixed -2, horizontal-3)

4. Pattern of collagen (reticular -1, mixed-2, fascicle-3)

5. Quantity of early collagen (profound-1, moderate -2, minimal-3, absent-4)

6. Quantity of mature collagen (profound-1, moderate -2, minimal-3)

Histological assessments of wound were Semi Quantitative and Quantitative methods as described below.

· Semi-quantitative method:- Wound reepithelialisation,Migration of keratinocytes, Bridging of cells, keratinisation, Inflammatory cells: absence/ Presence: (mild/ moderate/ marked), Fibroblasts: absence/presence(mild/moderate/marked),New vessels; absence/ presence(mild/ moderate/ marked),Collagen: absence/ presence(mild/ moderate/ marked)

· Quantitative method:- Polymorpho nuclear leucocytes/ tissue macrophages ratio, Percentage of reepithelialisation, Area of the granulation tissue

· Results

The following observations were made for healing score & other histological parameters in conclusion of process of healing.

Table 1 Shows the Healing score of comparison between *Ehretia Laevis Roxb*. and Phenytoin for comparison over the time grade of 0, 7th, 15th day

Table:-1 Histological Healing Score

Day	Date of burn injury 0 day		Biopsy done on 7th day		Biopsy done on 15th day	
Parameters	**Group A Ehretia Laevis Roxb.**	**Group B Phenytoin**	**Group A Ehretia laevis Roxb.**	**Group B Phenytoin**	**Group A Ehretia laevis Roxb.**	**Group B Phenytoin**
Quantity of granulation tissue (profound -1, moderate – 2, scanty-3, absent-4)	4	4	2	3	4	4
Inflammatory infiltrate(plenty -1, moderate – 2, a few- 3)	3	3	2	3	3	3
Collagen fibre orientation (vertical -1, mixed -2, horizontal-3)	-	-	2	2	3	2
Pattern of collagen (reticular -1, mixed-2, fascicle-3)	-	-	2	2	2	2
Quantity of early collagen (profound-1, moderate -2, minimal-3, absent-4)	-	-	1	2	1	1
Quantity of mature collagen (profound-1, moderate -2, minimal-3)	-	-	2	3	1	2

Description of Table-1

It is seen from table one, the *Ehretia Laevis Roxb*. as compared to Phenytoin application works well for the synthesis of collagen fibres & its orientation. The quantity however of mature collagen was high on the 15th day by Phenytoin as compared to the group of Albino Rabbits applied with *Ehretia Laves Roxb*. There are not many difference noted for scar on the day 7 of biopsy.

The semi quantitative & quantitative histological parameters assessed are shown in Table-2

Table-2 Assessment of other semi quantitative & quantitative histological parameters

Semi-quantitative method	Date of burn injury 0 day	Biopsy done on 7th day		Biopsy done on 15th day	
Parameters	**-**	**Group A Ehretia Laevis Roxb.**	**Group B Phenytoin**	**Group A Ehretia Laevis Roxb.**	**Group B Phenytoin**
Wound reepithelialisation;	-	Maximum	Minimum	Maximum	Maximum
Migration of keratinocytes,	-	Present	Present	Absent	Absent
Bridging of cells, keratin	-	Present	Present but feeble	Present	Present
Inflammatory cells: absence/ Presence: (mild/ moderate/ marked)	-	Mild	Moderate	Absent	Absent
Fibroblasts: absence/ presence	-	Present	Present	Rare	Absent
New vessels; absence/ presence	-	Present	Present	Absent	Absent
(mild/ moderate/ marked)	-	Moderate	Mild		
Collagen: absence/ presence (mild/ moderate/ marked)	-	Present Marked	Present Moderate	Present Moderate	Present Mild
Quantitative method					
Polymorpho nuclear leucocytes/ tissue macrophages ratio	-	Maintained Normal	Normal	-	-
Percentage of reepithelialisation	-	85%	80%	98%	92%
Area of the granulation tissue	-	Present	Occasional y present	Absent	Absent

The overall epithelisation on the 15th day is much better in group of *Ehretia Laevis Roxb.*(98%) as compared to application of Phenytoin (92%). The presence of collagen was moderate on 15th day in the group of rabbits receiving *Ehretia Laevis Roxb.* as compared to group B receiving Phenytoin.

Histological changes for comparison between *Ehretia Laevis Roxb.& Phenytoin on 7th day & 15th day have been shown in Figure- 3 A & B and Figure- 4 A & B. Figure- 4 A & B- Comparative Photographs of histology (15th day)

Figure 3:- Comparative photomicrographs of histology (7th day)

Group A:- Ehretia Laevis Roxb.   Group B:- Phenytoin

Figure 3-A (Ehretia Laevis Roxb).   Figure 3-B (Topical Phenytoin)
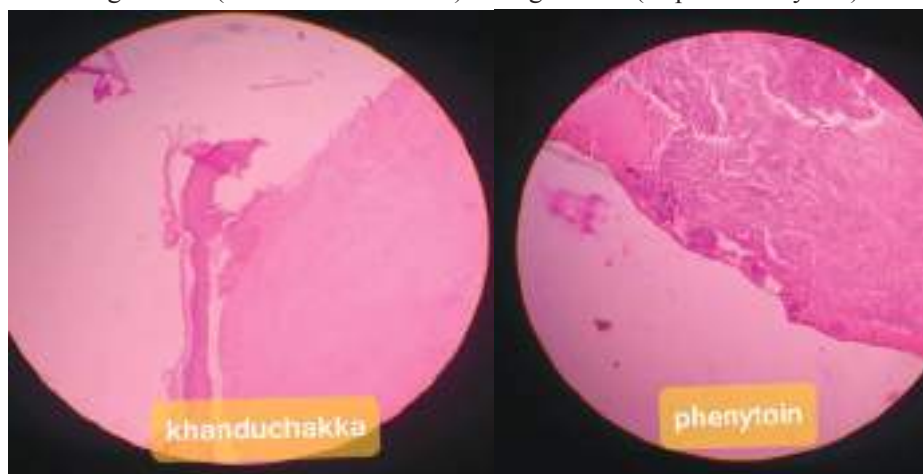
(H & E 10X)

Figure 3-A Shows early epithelisation & appearance of sub epithelial fibroblast

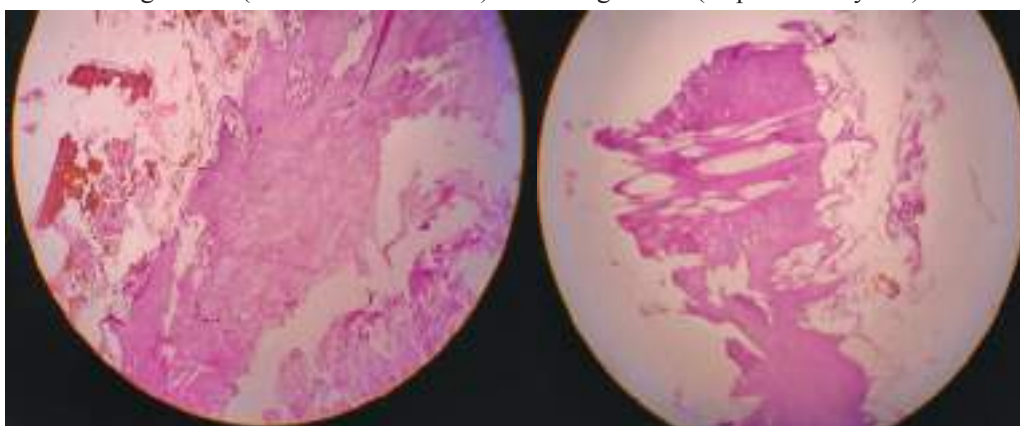Figure 3-B- Shows epithelisation & persistent granulation tissue.

Figure 4:- Comparative photomicrographs of histology (15th day)

Group A :- Ehretia Laevis Roxb.   Group B:- Phenytoin

Figure 4-A(Ehretia Laevis Roxb)   Figure 4-B(Topical Phenytoin)

(H & E 10X)

Figure 4-A- Complete epithelisation & proper organisation of mature collagen

Figure 4-B- Epithelisation marred incomplete dermal collagenosis.

Discussion

Part -I

The wound healing property has been documented. The similar observation were made in the studies but for the other drugs.

In another group Phenytoin ointment was taken, which promotes wound healing. Histological assessment was done on 7th and 15th day.

Granulation tissues were absent on date of injury and at fifteenth day from date of injury in both cases i.e. in group A and group B. Granulation tissues were

moderate in group A and scanty in group B on seventh day. Hence granulation enhances by *Ehretia Laevis Roxb.*plant compared to Phenytoin.

Inflammatory infiltrates were few at the date of injury and on fifteenth day from date of injury in both groups. Inflammatory infiltrate was few in group B and moderate in group A. Inflammatory infiltrate is more by *Ehretia Laevis Roxb.*plant as compared to Phenytoin.

Collagen fibre orientation was nil at date of injury in both groups, mixed on seventh day in both groups and on fifteenth day, horizontal in group A and mixed in group B.

Pattern of collagen was nil at the day of injury and mixed on the seventh and fifteenth day in both groups.

Quantity of early collagen was nil at the day of injury, profound in group A and moderate in group B on seventh day. Quantity of early collagen was profound in both groups on fifteenth day. Quantity of early collagen is significant by *Ehretia Laevis Roxb.*as compared to Phenytoin.

Quantity of mature collagen was nil at the day of injury, moderate in group A and minimum in group B on seventh day. Quantity of mature collagen is profound in group A and moderate in group B on fifteenth day. Quantity of mature collagen is significant by *Ehretia Laevis Roxb.*as compared to Phenytoin.

Part II: - As per semi-quantitative method and quantitative assessment:-

Wound reepithelialisation nil at the day of injury, maximum in group A and minimum in group B on seventh day and maximum in both groups on fifteenth day. Wound reepithelialisation is significant by *Ehretia Laevis Roxb.*as compared to Phenytoin.

Migration of keratinocytes nil at the day of injury, present in both groups on seventh day and absent in both groups on fifteenth day.

Bridging of cells keratin nil at the day of injury, present in group A and present but feeble in group B on seventh day and present in both groups on fifteenth day. Bridging of cells keratin is significant by *Ehretia Laevis Roxb.*as compared to Phenytoin.

Presence of inflammatory cells is nil at the day of injury, mild in group A and moderate in group B on seventh day and absent in both groups on fifteenth day. Presence of inflammatory cells is significant by *Ehretia Laevis Roxb.*as compared to Phenytoin.

Fibroblasts is nil at the day of injury, present in both groups on seventh day and rare in group A and absent in group B on fifteenth day.

New vessels is nil at the day of injury, moderate in group A and mild in group B on seventh day and absent in both groups on fifteenth day. Formation of new vessels is significant by *Ehretia Laevis Roxb.*as compared to Phenytoin.

Collagen is nil at the day of injury, present marked in group A and present moderate in group B and present moderate in group A and present mild in group B on fifteenth day. Formation of Collagen is significant by *Ehretia Laevis Roxb.*as compared to Phenytoin.

Part III- Quantitative assessment:-

Polymorpho nuclear leucocytes/ tissue macrophages ratio is nil at the day of injury, maintained normal in group A and normal in group B on seventh day and nil in both groups on fifteenth day.

Percentage of reepithelialisation is 85% in group A and 80% in group B on seventh day and is 98 % in group A and 92% in group B on fifteenth day. Percentage of reepithelialisation is significant by *Ehretia Laevis Roxb.* as compared to Phenytoin.

Area of the granulation tissue is present in group A and occasionally present in group B. And it is absent in both groups on fifteenth day. Area of the granulation is significant by *Ehretia Laevis Roxb.* as compared to Phenytoin.

Hence wound healed more significantly by *Ehretia Laevis Roxb.*Plant leaves paste as compared to application of Phenytoin ointment.

Anti microbial activity of plant useful in wound healing and promote healing. Anti oxidant activity plan promote the growth of tissue in wound healing. Hence both these activities help in wound healing.

The study of Sushma et al. has observed the role of natural medicine in wound healing on the basis of bio mechanical histological, biochemical, and molecular studies. However their studies included natural medicine of honey, ghee, Glycyrrhiza glabra, Nerium indicum. Histological analysis with all these application were found to have increase the rate of wound healing, rapid epithelisation, the normal collagenisation in dermis. The limited inflammatory cell response adjudged by *Interleukin*-1β & enhances activity of myo-fibroblast & small blood vessels. The study has concluded that these natural traditional medicine brings enhances wound healing activity as observed in histological material. However the study of Sushma et al did not have group of sample, those were treated by *Ehretia Laevis Roxb.* [4]

Al-Henhena N et al evaluated topical application of Strobilanthes crispus ethanolic extract on the rat of wound closer & histology of healed wound. It was observed that group 3 & group 4 were. Strobilanthes crispus was used in 100 mg/ml & 200 mg/ml of ethanolic extract were found to have mean healing time 14.80 ± 0.37 days and 13.00 ± 0.37 days respectively. Histological evaluation when compared to control group had average healing time of 20.6 ± 0.37a days. The study concluded that Strobilanthes crispus leaf extract enhances wound healing as ascertained by histological study. [5]

The present study has found put that leaf extract paste of *Ehretia Laevis Roxb.* has enhanced the process of wound healing ascertained on histological parameters as compared to topical phenytoin application. There are not many studies that have experimental with *Ehretia Laevis Roxb.* leaves paste for the objective assessment for its property of enhance wound healing.

Conclusion

Ehretia Laevis Roxb. paste is found to be immensely useful at wound healing as compared to Phenytoin. *Ehretia Laevis Roxb.* is concluded to promote the healing significantly as observed by feature of granulation, collagenisation & re epithelisation of the wounds suggesting early healing by primary intension.

References

1. Thakre R, Bhutada S, Chouragade B, Khobragde P, Harne K. Ethano Botanical botanical properties of unexplored plant khandu chakka (ehretia laevis roxb.). Int. J. Ayur. Pharma Research. 2016;4(7):68-73.

2. Rushikesh T, Bhutada S, Chouragade B, Khobragade P, Ketaki H. www. ijrap. net..

3. PENDSE AK, SHARMA A, SODANI A, HADA S. Topical phenytoin in wound healing. International journal of dermatology. 1993 Mar;32(3):214-7.

4. Sushma K, Kumar B, Sreedhara P, Jayakrishna N, Anne S, Karthik G, Divya P. The role of natural medicines on wound healing: a biomechanical, histological, biochemical and molecular study. Ethiopian journal of health sciences. 2018;28(6).

5. Al-Henhena N, Mahmood AA, Al-Magrami A, Syuhada AN, Zahra AA, Summaya MD, Suzi MS, Salmah I. Histological study of wound healing potential by ethanol leaf extract of Strobilanthes crispus in rats. Journal of Medicinal Plants Research. 2011 Aug 18;5(16):3660-6..

6. Anstead GM, Hart LM, Sunahara JF, Liter ME. Phenytoin in wound healing. Annals of Pharmacotherapy. 1996 Jul;30(7-8):768-75.

7. Bhatia A, Prakash S. Topical phenytoin for wound healing. Dermatology Online Journal. 2004;10(1).

8. Shaw J, Hughes CM, Lagan KM, Bell PM. The clinical effect of topical phenytoin on wound healing: a systematic review. British Journal of Dermatology. 2007 Nov;157(5):997-1004.

9. Talas G, Brown RA, McGrouther DA. Role of phenytoin in wound healing--a wound pharmacology perspective. Biochemical pharmacology. 1999 May;57(10):1085-94.

10. Admuthe N. B.Micropropagation for Ehretia laevis Roxb. A rare Indian medicinal plant. International Journal of Advanced Scientific and Technical Research. Issue 6 volume 3, May –June 2016.

11. Deshpandea RR, Kamatha A, Shepa S, Muthaa M, Methaa B, Patila D, Toraneb R, Deshpandeb N. The Journal for Dentistry..

12. N.Jyothirmai et al. Evaluation of anti-inflammatory and anti-bacterial activities of different solvent extracts of Ehretia laevis Roxb. ,J. Pharm. Sci. &

Res. Vol. 8(8), 2016, 715-720

13. Thakre R et al. Anti microbial activity of Ehretia Laevis Roxb. (Khandu Chakka) plant, wjpls, 4, (7) 2018, 112-116

14. Thakre R, Harne K. Comparative Antimicrobial Study Of Polar And Non Polar Extracts Of Ehretia Laevis Roxb.(Khandu Chakka) Plant.

15. Gupta A, Kumar P. Assessment of the histological state of the healing wound. Plast Aesthet Res. 2015 Sep 1;2(2):239-42.

Internal Use of Ajan Vruksha/ Khandu Chakka *(Ehretia Laevis Roxb)*. Plant Leaves Powder in Shoulder Pain Management. – Case Report

Rushikesh Thakre[1], Abhyuday Meghe[2], Ketaki Thakre[3], Pradip Tekade[4]

[1]Assistant Professor , Department of Samhita Siddhant, MGACH & RC, Datta Meghe Institute of Medical Sciences (DU) Wardha(MS) India, [2]Dean Science & Technology Datta Meghe Institute of Medical Sciences(DU) Wardha (MS) India, [3]PhD scholar(Chemistry), Rastra Santa Tukadoji Maharaj Nagpur University Nagpur (MS). India, [4]Associate Professor Department of Chemistry Bajaj College of Science(Formerly known as Jankidevi Bajaj College of Science), Wardha (MS), India

Abstract

Introduction— Shoulder pain and stiffness are common features among working women. It is affecting their day to day life style.

The main symptoms of the patient and the important clinical findings:- Patient was suffering from severe pain in right shoulder with restricted movement of right shoulder from 8 days. Patient was assessed by (SPADI) Shoulder Pain & Disability Index.

The main diagnoses, therapeutics interventions, and outcomes:- *Ehretia Laevis Roxb.* leaves powder capsules was made up of 250 mg. Patient was advised to take two capsules in morning and two capsules at night after food. Daily 1 gm powder was administered internally for 7 days

On the day zero pain score was 80%, on third day of treatment pain score was 54% and on seventh day pain score was 0. On the day zero disability score was 95%, on third day disability score was 55% and on seventh day score was 0.

Conclusion—. Patient cured from pain and shoulder disability by internal use of *Ehretia Laevis Roxb.* leaves powder within seven days.

Key Words: - Pain Management, Khandu Chakka, Ajan Vruksha, Ehretia Laevis Roxb. Shoulder Pain.

Introduction

Shoulder pain and stiffness are common features among working women. It is affecting their day to day life style. Musculo skeleton pain is major burden on individual and health care system

The prevalence of shoulder pain in the United Kingdom population was 7% [1].

1069 subjects were participated in the study, 245 (22.9%) reported with shoulder pain in Rohtak District of Northern India. [2]

Shoulder pain causes inability to do daily routine work. Prevalence of shoulder pain is as 67 percent for whole life. The incidence of shoulder pain is between 0.9%-2.5% and prevalence rate is from 6.9-26% for point prevalence to 6.7-66.7% for lifetime prevalence [3]

Shoulder pain may caused by bursitis & tendinitis, tear of tendon, arthritis, fracture, malignancy, infection, and neurotic problems.

Common treatment including avoiding overexertion or overdoing activities, involves rest. medications, surgeries.

Ricinus communis & Commiphora Mukul, Boswellia serrata, Withania somnifera,Dashamool,

Mahayograj Guggul, Vatavidhwansa, Yograj Guggul, Suvarna Bhasma commonly used for pain management in Ayurveda. *(4)*

Analgesic drugs act on the peripheral and central nervous systems. Painkillers include (NSAIDs) such as the salicylates, ibuprofen & COX-2 inhibitors, opioid drugs such as morphine and oxycodone, and acetaminophen.

Leaves and Bark of Ehretia Laevis Roxb. is being traditionally used for Pain Relief, wound healing and minor fracture.[5]

Ehretia Laevis Roxb. contains chemical compounds like Naphthoquinone derivative, Baurenol, ursolic acid, Rutin, Phytol, α and β amyrin, Betulin & Betulinic acid, Lupeol, β-sitosterol, Histidine, Hexadecanoic acid, Benzoic acid, Arachidonic acid show analgesic, antinociceptive and anti inflammatory activities.[6]

It has anti microbial properties [7-8] and its wound healing[9] property is also proven on scientific ground.

Patient Information:- Mrs. Archana Dilip Sawarkar Age-42, Sawangi(M) Wardha,(MS) India was reported at MGACH & RC Salod(Hi), Wardha(MS) with severe pain in right shoulder with stiffness.

Clinical Findings:- Patient was suffering from severe pain in right shoulder with restricted movement from 8 days. She has taken hot fomentation at her house but did not get any relief. There was no history of trauma, old injury, diabetes mellitus, and hyper tension.

Timeline: - Patient was suffering from severe pain in right shoulder from 8 days.

Diagnostic Assessment:- Patient was investigated for complete blood culture, Random Blood Sugar, Kidney Function Test, Liver Function Test, Lipid Profile, Serum Calcium, Rheumatic Arthritis. All tests were within normal limits.

Patient was assessed by (SPADI) Shoulder Pain & Disability Index [10]. on first, third and seventh day.

(SPADI) Shoulder Pain and Disability Index
Pain scale
0 = no pain to 10 = the worst pain imaginable
Table:- 1

	Day- 0	Day- 3rd	Day-7th
At its worst?	8	6	0
When lying on the involved side?	8	6	0
Reaching for something on a high shelf?	8	5	0
Touching the back of your neck?	8	5	0
Pushing with the involved arm?	8	5	0
Total Pain score	40/50X50= 80%	27/50X100= 54%	0%

Disability scale

0 = no difficulty to 10 = so difficult

Table:- 2

	Day-0	Day-3rd	Day-7th
0 = no difficulty and 10 = so difficult it requires help. Washing your hair?	8	5	0
Washing your back?	10	5	0
Putting on an undershirt or jumper?	10	5	0
Putting on a shirt that buttons down the front?	10	5	0
Putting on your pants?	9	5	0
Placing an object on a high shelf?	10	5	0
Carrying a heavy object of 10 pounds (4.5 kilograms)	10	7	0
Removing something from your back pocket?	9	7	0
Total Disability score	76/80X100= 95%	44/80X100= 55%	0%

Total SPADI Score

Table:- 3

	Day -0	Day-3rd	Day-7th
Total SPADI Score	89.23 %	54.61%	0 %

Therapeutic Intervention:- *Ehretia Laevis Roxb.* leaves were shed dried, powdered and filled in capsules in GMP And FDA approved Dattatrya Ayurved Rasashala Wardha(MS). Each capsules was of 250 mg. Patient was advised to take two capsules in morning and two capsules at night after food. Daily 1 gm powder was administered internally for 7 days.

Follow-up and Outcomes: - Patient's shoulder pain was assessed on the day of reporting, 3rd day and on seventh day by Shoulder Pain and Disability Index (SPADI). On day zero when treatment started SPADI was assessed. On the day zero pain score was 80%, on third day pain score was 54%. Within three days patient got significant pain relief. And on seventh day score was 0%. Patient got complete relief from pain.

On the day zero disability score was 95%, on third day disability score was 55%. Within three days patient got significant relief from disability. And on seventh day

disability score was 0%. Patient got complete relief from disability on seventh day along with complete relief from pain.

Patient cured from pain and shoulder disability by internal use of *Ehretia Laevis Roxb.* leaves powder within seven days.

Discussion

Ehretia Laevis Roxb. plant is a being used for various ailments traditionally. It is commonly used for pain relief, wound healing and minor fractures.

Velappan et al experimented methanolic extract (500 mg/kg) of the *Ehretia Laevis Roxb.* leaves in in mice,and found that it reduces paw volume by 56%, paw oedema to 60% [11].

N.Jyothirmai et al stated that the chloroform, methanolic and aqueous extract of Ehretia laevis reduces inflammation in animal model.[12]

Subodh et al shown anti arthritic activity of medicated oil of Ehretia Laevis Roxb. leaves by local application in human beings . [13]

Internal use of Ehretia Laevis Roxb. leaves powder is tested first time in this study for pain management in shoulder pain and assessed by(SPADI) Shoulder Pain & Disability Index And found very effective without any untoward side effects. Patient got near about 50% relief for his complaints within three days of administration and complete relief within seven days.

This study will pave the path for further study of internal use of *Ehretia Laveis Roxb.* in various ailment including pain management.

Also use of this herbal plant in pain management will minimise the side effects of modern medicine like Non-steroidal anti-inflammatory drugs.

Patient Perspective:- :- Patient was very happy as she got complete relief from pain and disability of her shoulder without using modern medicine and side effects of modern medicine was avoided.

Conflict of Interest:- Nil

Source of Funding:- Self

Consent of Patient:- Taken

References

1. Urwin M, Symmons D, Allison T et al. Estimating the burden of musculoskeletal disorders in the community: the comparative prevalence of symptoms at different anatomical sites, and the relation to social deprivation. Ann Rheum Dis 1998 1998, 57:649–55

2. Bhawna[1] NK, Kundu ZS. Prevalence of shoulder pain among adults in Northern India.

3. Luime JJ, Koer BW, Hendriksen IJ, Burdorf A, Verhagen AP, Micdema HS and Verhaar JA. Prevalence and incidence of shoulder pain in general population: a systematic review. Scand J Rheu. 2004; 33(2): 73-81.

4. Chopra A, Saluja M, Tillu G. Ayurveda–modern medicine interface: A critical appraisal of studies of Ayurvedic medicines to treat osteoarthritis and rheumatoid arthritis. Journal of Ayurveda and integrative medicine. 2010 Jul;1(3):190.)

5. Rushikesh *Thakre, Shyam B, Bharat C, Pramod K, Ketaki Ravindra H. ETHANO BOTANICAL PROPERTIES OF UNEXPLORED PLANT KHANDU CHAKKA (EHRETIA LAEVIS ROXB.). Int J Ayu Pharm Res [Internet]. 2016Aug.6 [cited 2020Oct.23];4(7).

6. Thakre R, Harne K, Tekade P, Parve S. Role of Ajan Vruksha/Khandu Chakka plant (Ehretia laevis roxb.) in COVID-19 pandemic. International Journal of Research in Pharmaceutical Sciences. 2020 Mar 11;11(Special Issue 1).

7. Thakre Rushikesh et al anti microbial activity of Ehretia Laevis Roxb. (Khandu Chakka) plant, wjpls, 2018, Vol. 4, Issue 7, 112-116

8. Thakre R, Harne K. Comparative Antimicrobial Study Of Polar And Non Polar Extracts Of Ehretia Laevis Roxb.(Khandu Chakka) Plant

9. Thakre, R., Bhutada, S., Chouragade, B., Khobragade, P., & Ketaki, H. (2016). UNEXPLORED WOUND HEALING PROPERTY OF EHTRETIA LAEVIS ROXB. (KHANDU CHAKKA) PLANT. *International journal of research in ayurveda and pharmacy, 7*, 54-57

10. Roach KE, Budiman-Mak E, Songsiridej N, Lertratanakul Y. Development of a shoulder pain and disability index. Arthritis & Rheumatism: Official Journal of the American College of Rheumatology.

1991 Dec;4(4):143-9.

11. Velappan S, Thangaraj P. Phytochemical Constituents and Antiarthritic Activity of E hretia laevis Roxb. Journal of Food Biochemistry. 2014 Aug;38(4):433-43.)

12. Jyothirmai N, Nagaraju B, Kumar JS. Evaluation of anti-inflammatory and anti-bacterial activities of different solvent extracts of Ehretia laevis Roxb. Journal of Pharmaceutical Sciences and Research. 2016 Aug 1;8(8):715.)

13. Subodh G. Karluke & Pramod Khobragade: Efficacy Of Folklore Plant Khanduchakka (Ehretia Laevis Roxb) Patra Siddha Tail In Sandhivata. International Ayurvedic Medical Journal {online} 2017.

Taylor & Francis
Taylor & Francis Group

Check for updates

Graphene based nano-composites for efficient energy conversion and storage in Solar cells and Supercapacitors : A Review.

Bhagyashri Tale[a], K. R. Nemade[b], and P. V. Tekade[a]

[a]Department of Chemistry, J. B. College of Science, Wardha, Maharashtra, India; [b]Department of Physics, Indira Mahavidyalaya Kalamb, District: Yavatmal, Maharashtra, India

ABSTRACT

Due to unique properties, ease of synthesis and functionalization, graphene-based nanocomposites show great potential in energy storage and conversion. These hybrid materials have excellent characteristics like high carrier mobility, faster recombination rate and long-time stability. In this review, the recent progresses in the synthesis and applications of graphene and its composites in the fields of energy storage (supercapacitors) and conversion (Solar cells) are summarized. This article highlights the challenges of the practical applications of graphene-based materials in supercapacitors and solar cells. Future research to develop new methodologies for the design and the synthesis of graphene-based nanocomposite are also proposed.

1. Introduction

The energy requirement of world is rising day by day and it is estimated that energy requirement will be double by 2050. Besides that, the energy production from conventional ways creates pollution of environment. So, renewable energy storage and conversion materials as well as their devices are topics of intense research.[1] To make the effective use of renewable energy, it is necessary to develop high-performance, low-cost and eco-friendly energy conversion and storage devices. Carbon materials are of great interest in research related to electrochemical devices due to their abundance, stability and eco-friendliness. Among different allotropes of carbon, graphene, is emerged as an excellent candidate for energy conversion and storage applications because of its unique properties, including high specific surface area $(2630 \ m^2/g)$, good chemical stability and excellent electrical conductivity.[2]

2. History of graphene

Graphene appears frequently in our day to day life and it is topic of intense research for more than six decades, but the pioneer efforts were of two scientists from the University of Manchester, Prof. Andre Geim and Prof. Kostya Novoselov who successfully carried out the cleavage of one atom thick single layer of graphene from graphite. This was a milestone discovery in history of nanotechnology as it practically demonstrates the concept of single atom components from theory closer to reality. The various events in the discovery of single-layer graphene are as follows[3]:
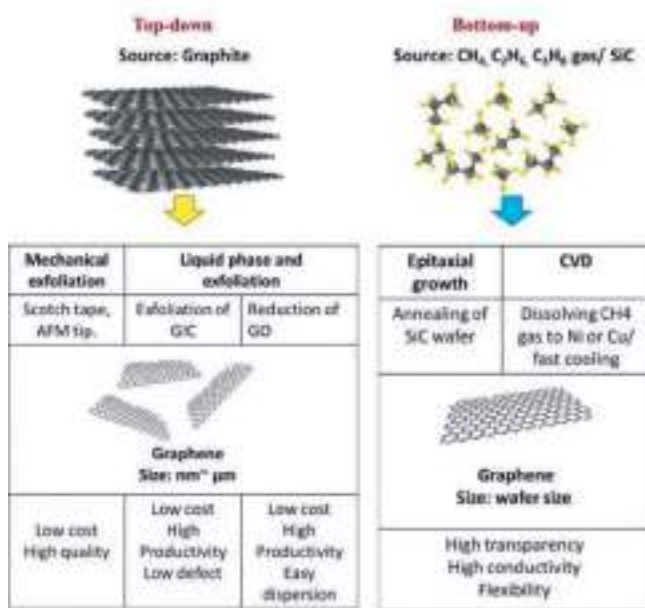
- Simonio and Lyndiana Bernacotti developed the first pencil in 1560.
- John Desmond Bernal described the layered structure of graphite in 1924.
- The theoretical study of electronic properties of a single graphite layer was initiated by Philip Wallace in 1947.

## 3. J. W. McClure proposed the equation of wave function for single graphite layer in 1956

- In 1987, S. Mouras used the term graphene for the first time as a virtual expression of unit structure in graphite instead of a realistic form of carbon nanomaterials.

In 2004, Andre Geim and Konstantin Novoselov published very first article about the synthesis of graphene by mechanical exfoliation method in Science magazine. For their groundbreaking experiments in the synthesis and characterization of this two-dimensional material Graphene, they received the Nobel Prize in Physics 2010.

CONTACT Bhagyashri Tale ✉ bhagyashritale@gmail.com 🖃 Bajaj College of Science, Wardha 442001, India.

Figure 1. Top-down and bottom-up graphene synthesis approaches[96] (Adopted from Mahmoudi, T., Wang, Y., and Hahn, Y. B. (2018). Graphene and its derivatives for solar cells application. Nano Energy, 47, 51–65).
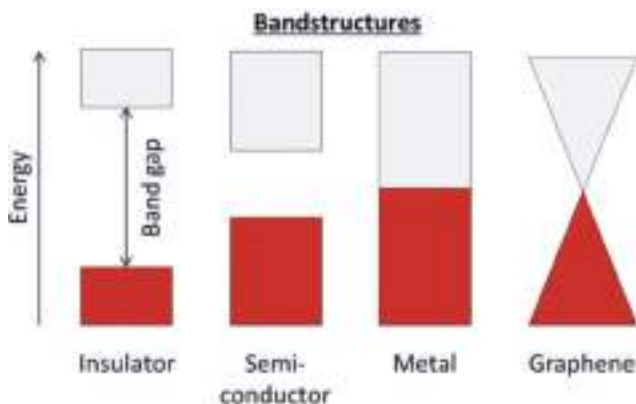

Figure 2. Band structure of different materials (Adopted from https://whitenoise.kinja.com/graphene-miracle-material -1575961841[97].

4. Synthesis of graphene

The amazing properties of graphene are mainly due to the defect of less pristine graphene. structural defects occur during growth and processing steps of graphene which alters their properties. Several scientists reported innovations in the mass and low-cost production of graphene with minimal defects for various applications. The approach for the synthesis of graphene is classified into two types:

(1) In top-down approach, the stack of graphene precursor (graphite) dissociates into individual atomic
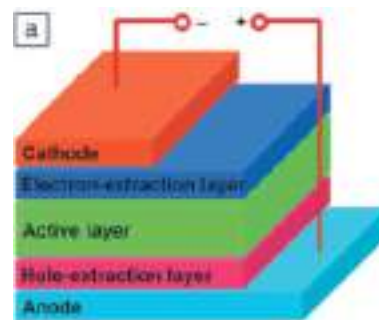
Figure 3. Device structure of polymer solar cell[73].

layer graphene sheet by overcoming Vander Waals forces of attraction.

(2) In bottom-up approach, carbon molecules obtained from various resources are used to develop the honeycomb structure of graphene sheet.

Various methods reported worldwide by many researchers for synthesis of graphene are given below:

4.1. Mechanical exfoliation

This is top-down approach to produce high-quality graphene with minimal defects and high electron mobility. It is a repeated peeling process used to break weak Vander Waals forces present between the stacked layers of graphite to produce individual graphene sheets.[4–7]

4.2. Chemical exfoliation

Using this technique, good quality graphene suspension can be obtained from graphite by using aqueous electrolyteThis technique can be used for the production of conductive inks, transparent conducting oxides and electrodes for batteries and supercapacitors but cannot be used to generate large sheets of graphene required for device applications.[8–10]

4.3. Hummer's method

Synthesis of graphene oxide is reported by placing graphite in concentrated acid in the presence of an oxidizing agent. In this process, potassium permanganate is used in a solution of graphite, sodium nitrate, and sulfuric acid to generate graphene oxide and the reaction is terminated with the help of hydrogen peroxide. Many modifications are reported to make it more efficient and environmentally friendly.[11–13]
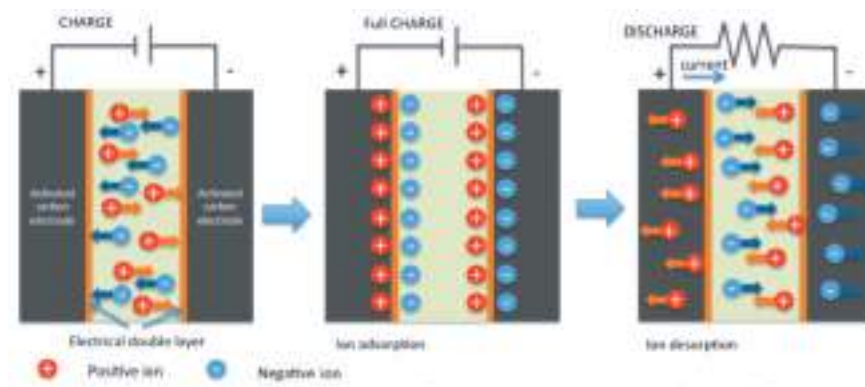
Figure 4. Charge and discharge processes of an EDLC.[98] (Adopted from Notarianni, M., Liu, J., Vernon, K., and Motta, N. (2016). Synthesis and applications of carbon nanomaterials for energy generation and storage. *Beilstein journal of nanotechnology, 7*(1), 149–196.).

4.4. Chemical vapor deposition(CVD)

It involves pyrolysis of the precursor material to form carbon which is used to form the structure of graphene. This process is carried out in an inert environment by passing the gases like N_2/Ar.[14,15]

5. Properties of graphene

Major properties of graphene are as follows.[3,16,17]

- Graphene is considered as the first two dimensional crystalline material developed in lab.
- Graphene is a zero-gap semiconductor and it shows conductivity higher than copper.
- Graphene is a highly transparent material with great flexibility and stretchability.
- Graphene can be stretch up to 120% of its length and can recover its original shape.
- At room temperature, the thermal conductivity of Graphene is found to be more than diamond, graphite and any other known material.

This is a thinnest material **and** it can transmit up to 98% of light.

- Graphene is very strong. Graphene is 200 times stronger as compared to steel.

Graphene is a two-dimensional atomic sheet with sp^2-hybridized carbon atoms arranged in a Hexagonal manner. The s, p_x and p_y orbitals involve in σ-bond formation with neighbouring carbon atoms while p_z orbital forms π-bond . This makes one electron free. The C-C bond length is reported as 0.142 nm and the thickness of single layer of graphene is found to be 0.35 nm. The graphene is stable due to strong interatomic bonds present in the material which helps to overcome the thermal fluctuations and does not create dislocations or other crystal defects even at high temperatures

5.1. Electrical and thermal properties of graphene

Graphene is a zero-gap semiconductor or semi-metal. Its conduction band and valence band are same as semiconductor with no band gap. Here, holes and electrons act as charge carrier which leads to a very high electrical conductivity (more than copper). The π-bonds have high mobile pi (π) electrons that overlap together to form bonding π (valence) and antibonding $π^*$ (conduction) bands. The free moving electrons show high mobility and hence travel sub-micrometer distances without any scattering (ballistic transport). The electron mobility in graphene is found to be 15,000 $cm^2 \cdot V^{-1} \cdot s^{-1}$ and its theoretical potential limits are 200,000 $cm^2 \cdot V^{-1} \cdot s^{-1}$ mainly due to the quality of graphene and the substrate. Graphene also shows the highest value of thermal conductivity because of the highly stable sp^2 bonding pattern and a two-dimensional nature. The experimental values are found to be in the range of 3000– 5000 $Wm^{-1}K^{-1}$.

5.2. Thermal and mechanical properties of graphene

The study of mechanical properties of single-layer graphene was done by atomic force microscopy technique and it is reported as strongest material ever tested. Thermal conductivity was found in the range of 3000–5000 $Wm^{-1}K^{-1}$. Graphene shows an extraordinary tensile strength, i.e.,130 GPa which is found to be higher than 0.4 GPa of A36 steel and 0.375 GPa of Kevlar (Aramid) fibers. The values of Spring constant and Young's modulus values were reported to be 1–5 Nm^{-1} and 1TPa respectively.

Table 1. Summary of Supercapacitor work based on graphene-based composite.

Material	Capacitance	Reference
Fluorographene	7 F g^{-1}	[99]
Cyanographene	97 F g^{-1}	[100]
Graphene acid	86 F g^{-1}	[100]
5-Ethynylpyrimidinegraphene	188 F g^{-1}	[101]
Graphene-dicarboxylic acid	326 F g^{-1}	[99]
Graphene-dicarboxylic acid conjugated with tetraaminophthalocyanine	936 F g^{-1}	[102]
Inkjet-printed graphene/PANI	82 Fg^{-1} @ 10 mVs1	[103]
PANI–GO	475 Fg^{-1} @ 0.4 Ag^{-1}	[104]
PANIGRAPHENE (PG100:1)	25 mF cm^{-2} @ 5 m Vs^{-1}	[105]
PANI–GO	25 mF cm^{-2} @ 5mVs^{-1}	[106]
PANI-GO	355 Fg^{-1} @ 0.5 Ag^{-1}	[107,108]
Graphene/PANI	408 Fg^{-1} from CV at a scan rate of 5 mVs^{-1}	[109]
Graphene/PANI	233 Fg^{-1}	[53]
GO/PANI RGO/PANI	GO/PANI: 827 Fg^{-1} from CV at a scan rate of 1 mVs^{-1} RGO/PANI: 1129 Fg^{-1} from CV at a scan rate of 1 mVs^{-1}	[110]
GO/PANI RGO/PANI	320 Fg^{-1} at 0.1 Ag^{-1} 480 Fg^{-1} at 0.1 Ag^{-1}	[111]
Graphene/PANI	1046 Fg^{-1} from CV at a scan rate of 1 mVs^{-1}	[112]
RGO/PANI	361 Fg^{-1} at 0.3 Ag^{-1}	[113]
Graphene/PANI Paper	763 Fg^{-1} at 1 Ag^{-1}	[114]
RGO/PANI	257 Fg^{-1} at 0.1 Ag^{-1}	[115]
GO/PANI	448 Fg^{-1} at 0.5 Ag^{-1}	[116]
Crumpled graphene/ CNT/PANI	456 Fg^{-1} at 0.1 Ag^{-1}	[117]
RGO/PANI	438.8 Fg^{-1} at 0.5 Ag^{-1}	[118]
Graphene/PPy	165 Fg^{-1} at 1 Ag^{-1} at end of 1000th cycle	[111]
GO/PPy	417 Fg^{-1} from CV (scan rate: 100 mVs^{-1}) 267 Fg^{-1} from CV (scan rate: 100 mVs^{-1})	[119]
RGO/PPy	249 Fg^{-1} at 0.3 Ag^{-1}	[120]
RGO/PPy	420 Fg^{-1} at 0.1 Ag^{-1} 240 Fg^{-1} at 5 Ag^{-1}	[121]
RGO/PPy nanowire	728 Fg^{-1} at 0.5 Ag^{-1} 675 Fg^{-1} at 2.5 Ag^{-1}	[122]
Exfoliated graphene/ PPy	351 Fg^{-1} at 1 Ag^{-1}	[123]
Graphene/PPy Nanotubes	514 Fg^{-1} at 0.2 Ag^{-1} 420 Fg^{-1} at 1 Ag^{-1}	[124]
RGO/PPy	440 mFcm^{-2} at 0.5 mAcm^{-2}	[125]
Sulfonated graphene/PPy	310 Fg^{-1} at 0.3 Ag^{-1}	[111]
Graphene/PEDOT	HCl: 304 Fg^{-1} from CV at a scan rate of 10 mVs^{-1} H$_2$SO$_4$: 261 Fg^{-1} from CV at a scan rate of 10 mVs^{-1}	[126]
RGO/PEDOT	108 Fg^{-1} at 0.3 Ag^{-1}	[127]
Graphene/PEDOT	270 Fg^{-1} at 1 Ag^{-1}	[128]
RGO/PEDOT	213 Fg^{-1} at 0.5 Ag^{-1}	[129]
Hallow RGO/PEDOT	304.5 mFcm^{-2} at 0.08 mAcm^{-2}	[130]
RGO/PEDOT:PSS	367 Fg^{-1} at 1 Ag^{-1}	[131]

5.3. Optical properties of graphene

In Graphene, there is no gap between the conduction and valence band and it touches each other at Dirac point which leads to strong interaction of Dirac Fermions with electromagnetic radiation. Pristine graphene layer has thickness equal to only one atom and it can absorb 2.3% of the white light. The wide range of spectral absorption of pristine graphene is due to the

Table 2. Performance summary of solar cells studied by different research groups.

Cell structure	Eff (%)	Reference
TiO_2– graphene	6.49%	[132]
TiO_2– graphene	6.49%	[133]
TiO_2– graphene	15.6%	[134]
TiO_2– graphene sulfide	1.68%	[135]
Silicon	17%	[136]
Organic molecules or polymers	5%	[136]
Hybrid solar cell	22–23%	[136]
Graphene nanoplatelets	5%	[137]
rGO–PANI	6.15%	[138]
TiO2/RGO	7.46	[81]
Dye-sensitized solar cells based on TiO_2 nanoparticles	4.81%	[139]
Dye-sensitized solar cells based on PANI/graphene	7.70	[140]
Dye-sensitized solar cells based on PANI-RGO	7.84	[141]
Dye-sensitized solar cells based on Ppy/RGO	6.45	[142]
Dye-sensitized solar cells based on PANI/graphene	6.09	[143]
dye-sensitized solar cells (DSSC) were fabricated using graphene-TiO2composite	4.28%	[144]
2D graphene	6.97%	[145]
Dye-Sensitized Solar Cells by using GrapheneTiO2 Composites	6.86%	[146]
A dye-sensitized solar cell (DSSC) based on graphene–TiO_2composite photoelectrode	4.28%	[147]
DSSC based on pure TiO_2 photoelectrode	3.11%	[147]
Dye-sensitized Solar Cell using Graphene-TiO_2	7.1%	[148]
. DSSCs based on TiO2@RGO hybrid photoanodes with a graphene content of 1.6 wt %	7.68%	[82]
DSSC based on Polyaniline/graphene (1 wt%) complex	6.71	[149]
DSSC based on Polyaniline/graphene (8 wt%) complex	7.78	[149]
DSSC based on Polyaniline/graphene (15 wt%) complex	6.89	[149]
DSSC based on Polyaniline-graphene (10 wt%)/GO n (n = 10)	7.88	[150]
DSSC based on Polyaniline-graphene (10 wt%)/GO n (n = 5)	6.61	[150]
DSSC based on Polyaniline-graphene (8 wt%)/GO n (n = 10)	7.83	[150]
DSSC based on Polyaniline-graphene (8 wt%)/GO n (n = 5)	6.03	[150]
DSSC based on Polyaniline-graphene (4 wt%)/GO n (n = 10)	6.38	[150]
DSSC based on Polyaniline-graphene (4 wt%)/GO n (n = 5)	4.21	[150]
DSSC based on Graphene/TiO_2	9.2	[151]
DSSC based on TiO2/graphene nanocomposite (0.5 wt%)	5.41	[152]
DSSC based on TiO_2 only	4.11	[152]
DSSC based on TiO2/graphene nanocomposite (1.6 wt%)	3.69	[152]
DSSC based on TiO2/graphene nanocomposite (0.4 wt%)	2.82	[152]
DSSC based on TiO_2 only	2.49	[152]
DSSC based on Graphene (1.5 wt%)/TiO_2	4.20	[153]
DSSC based on TiO_2 only	3.17	[153]
]DSSC based on TiO2/graphene composite	3.98	[153]
DSSC based on TiO_2 only	1.45	[153]

contribution from both interband and intraband optical transitions. The optical absorption of single-layer graphene in visible region takes place mainly due to interband transitions which are independent of frequency. The optical absorption in the far-infrared region is mainly due to intraband transitions or free carrier absorption.

Hence, graphene shows excellent thermal management applications especially in micro- and nano-electronics.

6. Solar cells

A solar cell, or photovoltaic cell, is an electrical device which is used to converts the energy of light into electricity. In electric power generation by use of renewable energy resources instead of conventional fossil-fuels is rapidly increasing. Among renewable energy resources which are used for electric power generation, solar photovoltaics (PVs) are the fastest growing resource.[18] After hydro and wind energy, solar energy is the third largest renewable energy resource of electric power generation in the world.[19]

The motivating factors for the replacement of conventional fossil-fuels by solar PVs for electric power generation are

Price of fossil fuels is increasing day by day and they are limited while the source of solar energy is free and abundant.[20,21]

Use of Fossil-fuels pollutes the environment while solar PV's does not release any pollutant.[22,23]

Use of fossil-fuels contribute to global warming while solar PV's mitigate this issue.

Solar PV's requires less maintenance and operational costs.[24]

Among renewable energy sources, solar PVs provide the highest power density.[25,26]

More than100 countries in the world are using solar PVs.[24]

In order to encourage investments, governments declared financial assistance for solar electricity generation.[27–31] PV cell is the basic component of PV systems. Basically, PV cell is a semiconductor diode in which P–N junction is exposed to the light.[32]

Despite all the above advantages of solar PV systems, there are some challenges.

PV systems do not create emissions during their operation, but these technologies are not completely emission-free. A lifecycle assessment (LCA) of solar PV cells is found to be divided into three phases; manufacturing, operation and recycling. It is observed that, Manufacturing phase is responsible for most of GHG emissions (around 90 percent) while recycling phase lowers GHG emissions[33]

Currently, the efficiency of solar PV cells is low, hence cost of electricity produced from them is high. Hence, researchers are taking effort to increase the efficiency of solar cells so as to reduce the cost of produced electricity .[19–22]

Another challenge of solar PV cells is their handling after end of their lifecycle. Research is going on to for recycling of solar modules and its different parts involved in manufacturing after the end of their life cycle. .[23] Once recycled, solar companies can use it again to build new modules so as to reduce their cost of manufacturing.[23]

The power generated by solar PV cells is depend on environmental parameters such as irradiation and temperature which are not controllable .[34–36] To overcome this issue, storage devices are integrated into PV systems.

6.1. Working principles of solar cells

6.1.1 Exciton formation
After the phenomenon of light absorption, Inorganic semiconductors immediately produce free carriers, while organic semiconductors require additional process known as exciton formation.[37]

6.1.2 Exciton transport
The next step is exciton transport, which is in competition with other decay process such as Luminescence or radiative recombinations to ground state.

6.1.3 Charge Separation
Creation of charge is one of the important steps in conversion of sunlight into electric energy. In most PV cells, charges are p**roduced by photoinduced e**lectron *transfer f*rom a donor (D) to acceptor (A) by using additional input energy of absorbed photon.

6.1.4 Charge transport
The next step is *c*harge transport phenomenon where charge carriers go towards electrodes.

6.1.5 Charge collection
The collection o*f* charge carriers at electrodes is done by a transparent conductive oxide (T*CO) such as ITO on* one side and a metal contact on another side.

Thus, A built-in-potential barrier in the cell activates the electrons to produce a voltage, to drive a current through a circuit.[38–40]

7. Supercapacitor

Electrochemical capacitors (ECs) are also known as "ultracapacitors" or "power capacitors" but currently the most recognized name is "supercapacitors". The term supercapacitor was proposed by NEC, since it was the first company to introduce a device with the name SupercapacitorTM in 1971.[41] Supercapacitors are under development since 1957 when Becker[42] first time used carbon flooded with a sulfuric acid electrolyte for charge storage at the interface of these two materials. However, in 1969 that the company SOHIO[43] first launched this technology into the market. The real success of supercapacitors research started in the 1990s when government programs in the United States donated funds for this technology to incorporate it into hybrid vehicles to provide necessary power for acceleration.[44] Supercapacitors show a higher power density but a smaller energy density compared to traditional batteries, which make them attractive for applications where instantaneous power is necessary. The other characteristics of supercapacitors are: ability to charge–discharge within seconds; a long lifetime of more than 106 cycles; ecofreindlyness and stability at various temperatures.[45] Thus, supercapacitors are electrochemical devices that can store energy and release it with high power capability and high current density within a short time interval.[46] So, supercapacitors are the perfect complement for batteries or fuel cells in various applications, such as automobiles and high-performance portable electronics.[47] Electrode materials which are intensively studied for supercapacitors are carbon, metal oxides, and conducting polymers, with a recent focus on CNTs and graphene.[48–50]

7.1. Working principles of supercapacitors

Supercapacitors are broadly divided into two types: electric double-layer capacitors (EDLCs) and pseudo-capacitors. One more subcategory known as hybrid capacitors can be identified if the EDLCs and the pseudo-capacitors are combined together into a single device. EDLCs store the energy at the electrode/electrolyte interface. During the charging, an external electric field is applied to the device responsible to move the ions at the electrode/electrolyte interface.[45,51]

Positive and negative ions are accumulated at this interface, typically on the order of 5–10 A^0 .[52]

The thickness (d) of the interface is very small (on the order of A^0), while the surface area (A) of the electrode usually varies due to the choice of porous structures with a large internal surface area. In this way, the capacitance can increase to a high value (>10 $\mu F/cm^2$).[53] In contrast, pseudo-capacitors are such a devices in which the charge is not stored electrostatically but electrochemically, as in conventional lithium ion batteries. Pseudocapacitive materials such as conducting polymers (e.g., polyaniline (PANI)) or metal oxides (e.g., ruthenium oxide (RuO_2)) can have 10–100 times larger capacitance as compared to EDLCs but they show poor stability, short lifetime and their synthesis is expensive.

Because of such drawbacks, they are generally combined with carbon materials which are known as hybrid supercapacitors.[54,55] In study the electrical properties of a supercapacitor, three electrochemical measurement techniques are generally used: cyclic voltammetry (CV), galvanostatic charging/discharging and electrochemical impedance measurements.[56]

Some important characteristics of an EDLC which should be considered to maximize the performance of the device are:

- The appropriate specific surface area of the electrodes so as to increase the capacitance
- The conductivity of the electrodes to minimize the power density losses
- The resistance to any oxidation/reduction at the surface of the electrode to achieve good stability and performance
- Sufficient size distribution of the pores so that it should match with the size of the electrolyte ions
- Good electrochemical stability of the electrolyte material in the voltage operating range of the device
- Low interconnected resistance of the electrolyte material
- Good wettability of the electrolyte material on the electrode.[52]

8. Challenges associated with manufacture and use of graphene

(i) Graphene is expensive and it is difficult to manufacture.
(ii) It is difficult to obtain monolayer graphene every time during synthesis of Graphene. If thickness of graphene is more than 10 layers of graphene, the properties resemble graphite more than graphene.
(iii) Because of above reasons, results of graphene synthesis are not very reproducible.
(iv) Graphene is not suitable for its application as a transistor since it does not have an off state and it cannot be switched off completely.
(v) Graphene is a hydrophobic material and hence it cannot be used in water-oriented applications like in humidity sensor, water filters.

9. Applications of graphene

Graphene has wide range of applications. During the last decade, graphene is a topic of interest in the field of research due to their exceptional electrical, optical and mechanical properties. Graphene can significantly improve the properties of existing products and to develop new materials with novel functionalities. Some of the applications are[5, 57–59]:

9.1. Graphene – metal oxide/graphene – polymer composites for supercapacitor study

Energy storage is the major topic of interest for researchers and scientists. Graphene has extremely high surface area of ~2600 m^2g^{-1} and it is an ideal material for electrostatic charge storage such as in supercapacitors. Supercapacitors are different from capacitors as charge storage is not done by the insulator material which is present in between the electrodes but by the electrodes which are dipped in the electrolytic solution. Graphene with high surface area and high porosity can store more ions as compared to activated carbon. The specific capacitance of a Graphene-based supercapacitor is found to be five times more than of the activated carbon-based supercapacitor. Researchers are working for lightweight, low-cost, elastic with high mechanical strength graphene-based supercapacitors to reduce and ultimately replace the use of fossil fuels for energy.

The performance of hybrid structures is found to be better than those of pure graphene, GO, rGO, or pure metal oxides due to synergistic effects of both graphene and Metal-oxides. The graphene in the hybrid-structure has various advantages such as high surface area, ultra-thin thickness, excellent electrical and thermal conductivity, mechanical flexibility, while metal oxides have high chemical functionality, and other electrochemical properties. Consequently, graphene can be an ideal 2D membrane for growing tiny nanoparticles with very distinct structures and precious morphologies for constituting a three-dimensional interconnected conductive porous network, with enhanced the electrical conductivity and the charge transport. The other advantages of using hybrid structures are:

It can prevent the volume change and particle agglomeration of metal-oxides during the process of charging–discharging;

2) Oxygen-containing functional groups on GO, rGO imparts good interfacial bonding and electrical contacts between graphene and metal oxides; and

3) Metal-oxide nanoparticles suppress the re-stacking of graphene layers to get continuous, porous, interconnected network structure is with highest achievable power density and capacitance in supercapacitors. Thus, graphene-metal oxide hybrid-materials with all remarkable

properties turn it into a more efficient material for super-capacitor electrode applications.[58]

Hybrid nanocomposites obtained from graphene and polymers also show excellent mechanical, electrical properties and large specific surface areas are particularly suitable for supercapacitor applications. Polymers with a good electrical conductivity and a high pseudo-capacitance are required to prepare such nanocomposites. Such hybrid materials show enhanced electrochemical performance in supercapacitor devices due to the synergetic effects of graphene and polymers which combines the unique properties of the individual components.[60,61] Thus Along with energy conversion, energy storage (as in supercapacitors and batteries) is also important and for many practical applications, high energy-storage capability, high power-delivery capability, and long cycle life are necessary. Due to the unique characteristics of graphene, much effort has been taken to study the applications of graphene in high-performance supercapacitors and batteries.[46,62–66] Metal oxide shows high specific capacitance and low resistance makes it simpler to construct supercapacitors with high energy and power. A special attention was toward manganese dioxide MnO_2 as an electrode material for supercapacitors because of their low cost, excellent capacitive performance in aqueous electrolytes and environmental benignity. Different conducting polymers are widely used as supercapacitor electrode material due to its ease of production and low cost. Conducting polymers shows a relatively high conductivity, capacitance and equivalent series resistance as compared to carbon-based electrode materials. In conducting polymers reduction-oxidation process stores and releases charge.[67] So, graphene – metal oxide/graphene – polymer composites are topic of interest for supercapacitor study.

> Researchers have been working on a pathway to improve the performance of supercapacitors, and meet that demand for increased storage capacity. Recently, Mojtaba et al suggested a new path to develop further miniaturized on-chip energy storage systems, which are compatible with silicon electronics and can support the power demand to operate integrated smart systems.[68]

9.2. Graphene-metal oxide/graphene-polymer composites for photovoltaic study

Inorganic semiconductor materials, such as amorphous silicon, gallium arsenide, and sulfide salts, have been widely used in conventional photovoltaic cells, where free electrons and holes are generated directly upon photon absorption. Although a power conversion efficiency (PCE) of more than 40% is achieved by using inorganic semiconductor materials in solar cells, the widespread use of inorganic solar cells is still limited due to difficulties in modifying the bandgap of inorganic semiconductors and high costs associated with the elaborate fabrication processes including elevated temperature and high vacuum. These inorganic solar cells are very much expensive than the conventional grid electricity. Alternative approaches with organic or polymer materials have gained considerable attention due to their low cost, light weight, flexibility, and solution processability.[61, 69–74]

9.3. Dye-sensitized solar cells (DSSCs)

As compared to other types of solar cells, DSSCs are different. They consist of a semiconducting material (e.g. TiO_2) with a photosensitive dye as the anode which is coupled with an electrolyte solution and a pure metal cathode (e.g. Platinum). Graphene has a number of favorable properties so that the loading efficiency of the dye molecules can be increased by increasing the interfacial area and enhancing the conductivity of the electrons. The proper ratio of graphene and TiO_2 is necessary for achieving an efficient system. The valence electrons from graphene get excited to the TiO_2 conduction band through the Graphene-TiO_2 interface, so as to separate the holes and the electrons. So, about 1% graphene is needed for this separation and the introduction of higher graphene concentrations into the matrix reduces the transmittance. The use of graphene in DSSCs increases the light scattering phenomenon at the photoanode, provides an efficiency that is 39% greater than that of pure TiO_2 electrodes and efficiently disperses the dye molecules.[74] In the photovoltaic study done by Morais et_al, the influence of different amounts of RGO in the TiO_2 film was investigated and it was compared to pristine TiO_2 films. The best solar cells made up of TiO_2/RGO films were obtained with 2.0 wt % RGO.[75] At the national level, several national laboratories and universities have been working on PV cell based on graphene-metal oxide nanocomposites.[76–86]

Thus, Dye-sensitized solar cells have gained attention in field of research because of their low production costs, ease of fabrication, lighter weight property, eco-friendliness and recyclable advantages, optical properties regardless of its low-efficiency output as compared to conventional silicon solar cell.[87] Dye-sensitized solar cells containing TiO2 are found to be more efficient. It consists of a dye-sensitized nanocrystalline TiO_2 film, an electrolyte with an I-/I3-redox couple and a Pt counter-

electrode. In addition to practical applications as an alternative energy source, these devices are also useful from a scientific point of view, as it converts light in to electrical energy through complex energy and charge transfer processes. The overall energy conversion efficiency depends on the individual properties of the constituents of the cell. To enhance their performance requires better understanding of processes in energy conversion and controlling the properties of each component.[88] ICPs are organic polymers which conduct electricity. It may have metallic conductivity or can be semiconductors. The advantage of ICPs is their processability, mainly by dispersion.[53, 89–94]So, Graphene – metal oxide/Graphene – Polymer composites are topic of interest for Photovoltaic study.

Typical efficiency of Polycrystalline silicon solar cells is 13% to 16%. Thin-Film solar cells (TFSC), are made by depositing one or several thin layers of photovoltaic material onto a substrate. Different types of TFSCs are categorized by which photovoltaic material is deposited onto the substrate: Amorphous silicon (a-Si), cadmium telluride (CdTe), copper indium gallium selenide (CIS/CIGS), polymer solar panels and organic photovoltaic cells (OPC). Thin-film modules have reached efficiencies of 7–13%. Recently, researchers have used graphene to develop a perovskite-silicon solar cell – a promising new solar technology – with an impressive conversion efficiency of 26.3%.[95]

10. Conclusion

As discussed herein, the extensive study of graphene-based nanocomposite with unique structure and properties offer a great opportunity to deal with challenges of energy conversion and storage. Many of fundamental properties of graphene are discovered, but there are still much new discoveries to be made in properties of graphene-based materials and in their applications. Due to unique properties, ease of synthesis and functionalization, graphene-based nanocomposites show great potential in energy storage and conversion. These hybrid materials have excellent characteristics like excellent mechanical, electrical properties and large specific surface areas and long-time stability. So, it is interesting to study the graphene to open up new possibilities to produce graphene-based nanocomposites and to better understand their properties as well as related phenomenon.

Disclosure statement

No potential conflict of interest was reported by the authors.

References

[1] Mahmood, N.; Zhang, C.; Yin, H.; Hou, Y. Graphene-based Nanocomposites for Energy Storage and Conversion in Lithium Batteries, Supercapacitors and Fuel Cells. *J. Mater. Chem. A.* 2014, *2*(1), 15–32.

[2] Choi, H. J.; Jung, S. M.; Seo, J. M.; Chang, D. W.; Dai, L.; Baek, J. B. Graphene for Energy Conversion and Storage in Fuel Cells and Supercapacitors. *Nano Energy.* 2012, *1* (4), 534–551.

[3] Module 29: ChemApplications: Graphene and Its Applications, Online Refresher Course in Chemistry for Higher Education Faculty. (2018). @swayam.gov.in

[4] Lee, X. J.; Hiew, B. Y. Z.; Lai, K. C.; Lee, L. Y.; Gan, S.; Thangalazhy-Gopakumar, S.; Rigby, S. Review on Graphene and Its Derivatives: Synthesis Methods and Potential Industrial Implementation. *J. Taiwan Inst. Chem. Eng.* 2019, *98*, 163–180.

[5] Shams, S. S.; Zhang, R.; Zhu, J. Graphene Synthesis: A Review. *Mater. Science-Poland.* 2015, *33*(3), 566–578.

[6] Choi, W.; Lahiri, I.; Seelaboyina, R.; Kang, Y. S. Synthesis of Graphene and Its Applications: A Review. *Crit. Rev. Solid State Mater. Sci.* 2010, *35*(1), 52–71.

[7] Yi, M.; Shen, Z. A Review on Mechanical Exfoliation for the Scalable Production of Graphene. *J. Mater. Chem. A.* 2015, *3*(22), 11700–11715.

[8] Jibrael, R. I.; Mohammed, M. K. Structural and the Optical Properties of Graphene Prepared by Electrochemical Exfoliation Technique. *Al-Nahrain J. Sci.* 2016, *19*(4), 71–77.

[9] Tripathi, P.; Patel, C.; Prakash, R.; Shaz, M. A.; Srivastava, O. N., 2013. Synthesis of High-quality Graphene through Electrochemical Exfoliation of Graphite in Alkaline Electrolyte. arXiv preprint arXiv:1310.7371.

[10] Parvez, K.; Yang, S.; Feng, X.; Müllen, K. Exfoliation of Graphene via Wet Chemical Routes. *Synth. Met.* 2015, *210*, 123–132.

[11] Narasimharao, K.; Venkata Ramana, G.; Sreedhar, D.; Vasudevarao, V. Synthesis of Graphene by Modified Hummers Method and Hydrothermal Synthesis of graphene-NiO Nano Composite for Supercapacitor Application. *J. Mater. Sci. Eng.* 2016, *5* (284), 2169–0022.

[12] Alam, S. N.; Sharma, N.; Kumar, L. Synthesis of Graphene Oxide (GO) by Modified Hummers Method and Its Thermal Reduction to Obtain Reduced Graphene Oxide (Rgo). *Graphene.* 2017, *6*(1), 1–18.

[13] Krane, N.;. *Preparation of Graphene*; Physics of Nanoscale Carbon: Selected Topics in Physics. 2011.

[14] Colombo, L.; Li, X.; Ruoff, R. S. *U.S. Patent No. 8,470,400*; U.S. Patent and Trademark Office: Washington, DC. 2013.

[15] https://investorintel.com/sectors/technology-metals/technology-metals-intel/understanding-graphene-part-3/

[16] Atif, R.; Shyha, I.; Inam, F. Mechanical, Thermal, and Electrical Properties of Graphene-epoxy nanocomposites—A Review. *Polymers.* 2016, *8*(8), 281.

[17] Gong, J. R.; ed.. *Graphene: Synthesis, Characterization, Properties and Applications*; BoD–Books on Demand, 2011.

[18] Jordehi, A. R.;. Parameter Estimation of Solar Photovoltaic (PV) Cells: A Review. *Renewable Sustainable Energy Rev.* 2016, *61*, 354–371.

[19] Bai, J.; Liu, S.; Hao, Y.; Zhang, Z.; Jiang, M.; Zhang, Y. Development of a New Compound Method to Extract the Five Parameters of PV Modules. *Energy Conversion Manage.* 2014, *79*, 294–303.

[20] Shafiee, S.; Topal, E. When Will Fossil Fuel Reserves Be Diminished? *Energy Policy.* 2009, *37*(1), 181–189.

[21] Apergis, N.; Payne, J. E. Renewable Energy, Output, CO2 Emissions, and Fossil Fuel Prices in Central America: Evidence from a Nonlinear Panel Smooth Transition Vector Error Correction Model. *Energy Econ.* 2014, *42*, 226–232.

[22] Shivalkar, R. S.; Jadhav, H. T.; Deo, P.; Feasibility Study for the Net Metering Implementation in Rooftop Solar PV Installations across Reliance Energy Consumers. In 2015 International Conference on Circuits, Power and Computing Technologies [ICCPCT-2015] 2015 March (pp. 1–6). IEEE.

[23] Wang, Y.; Zhou, S.; Huo, H. Cost and CO2 Reductions of Solar Photovoltaic Power Generation in China: Perspectives for 2020. *Renewable Sustainable Energy Rev.* 2014, *39*, 370–380.

[24] The Solar Singularity Is Nigh. 2015. http://www.greentechmedia.com/ articles.

[25] Sundareswaran, K.; Sankar, P.; Nayak, P. S. R.; Simon, S. P.; Palani, S. Enhanced Energy Output from a PV System under Partial Shaded Conditions through Artificial Bee Colony. *IEEE Trans. Sustainable Energy.* 2014, *6*(1), 198–209.

[26] Energyatthecrossroads;2015. http://home.cc.umanitoba.ca/_vsmil/pdf_pubs/oecd.pdf

[27] Dusonchet, L.; Telaretti, E. Economic Analysis of Different Supporting Policies for the Production of Electrical Energy by Solar Photovoltaics in Western European Union Countries. *Energy Policy.* 2010, *38*(7), 3297–3308.

[28] Solangi, K. H.; Islam, M. R.; Saidur, R.; Rahim, N. A.; Fayaz, H. A Review on Global Solar Energy Policy. *Renewable Sustainable Energy Rev.* 2011, *15*(4), 2149–2163.

[29] Branker, K.; Pearce, J. M. Financial Return for Government Support of Large-scale Thin-film Solar Photovoltaic Manufacturing in Canada. *Energy Policy.* 2010, *38*(8), 4291–4303.

[30] Campoccia, A.; Dusonchet, L.; Telaretti, E.; Zizzo, G. Comparative Analysis of Different Supporting Measures for the Production of Electrical Energy by Solar PV and Wind Systems: Four Representative European Cases. *Solar Energy.* 2009, *83*(3), 287–297.

[31] Timilsina, G. R.; Kurdgelashvili, L.; Narbel, P. A. Solar Energy: Markets, Economics and Policies. *Renewable Sustainable Energy Rev.* 2012, *16*(1), 449–465.

[32] Iwan, A.; Chuchmała, A. Perspectives of Applied Graphene: Polymer Solar Cells. *Prog. Polym. Sci.* 2012, *37*(12), 1805–1828.

[33] Where-is-solar-power-used-the-most. 2015. http://energyinformative.org

[34] Karaveli, A. B.; Soytas, U.; Akinoglu, B. G. Comparison of Large Scale Solar PV (Photovoltaic) and Nuclear Power Plant Investments in an Emerging Market. *Energy.* 2015, *84*, 656–665.

[35] Clò, S.; D'Adamo, G. The Dark Side of the Sun: How Solar Power Production Affects the Market Value of Solar and Gas Sources. *Energy Econ.* 2015, *49*, 523–530.

[36] Köberle, A. C.; Gernaat, D. E.; van Vuuren, D. P. Assessing Current and Future Techno-economic Potential of Concentrated Solar Power and Photovoltaic Electricity Generation. *Energy.* 2015, *89*, 739–756.

[37] Lungenschmied, C.; Dennler, G.; Neugebauer, H.; Sariciftci, S. N.; Glatthaar, M.; Meyer, T.; Meyer, A. Flexible, Long-lived, Large-area, Organic Solar Cells. *Solar Energy Mater. Solar Cells.* 2007, *91*(5), 379–384.

[38] Parida, B.; Iniyan, S.; Goic, R. A Review of Solar Photovoltaic Technologies. *Renewable Sustainable Energy Rev.* 2011, *15*(3), 1625–1636.

[39] Jannat, A.; Rahman, M. F.; Khan, M. S. H. A Review Study of Organic Photovoltaic Cell. *Int. J. Sci. Eng. Res.* 2013, *4*(1), 1–6.

[40] Savinije, T. J.; Delf ChemTech, Organic Solar Cells, Faculty of Applied sciencesDelf University of Technology.

[41] Lu, M.;. *Supercapacitors: Materials, Systems, and Applications*; John Wiley and Sons, 2013.

[42] Becker, H. I.; General Electric Co, 1957. Low Voltage Electrolytic Capacitor. U.S. Patent 2,800,616.

[43] Boos, D. L.; Standard Oil Co. 1970. Electrolytic Capacitor Having Carbon Paste Electrodes. U.S. Patent 3,536,963.

[44] Murphy, T. C.; Wright, R. B.; Sutula, R. A., 1997. US Department of Energy Electrochemical Capacitor Development and Testing Activities. In Proceedings of the Symposium on Electrochemical Capacitors II, (Vol.96, pp. 258–267). The Electrochemical Society, Inc.: Pennington, NJ.

[45] Notarianni, M.; Liu, J.; Vernon, K.; Motta, N. Synthesis and Applications of Carbon Nanomaterials for Energy Generation and Storage. *Beilstein J. Nanotechnol.* 2016, *7*(1), 149–196.

[46] Zhang, L. L.; Zhao, X. S. Carbon-based Materials as Supercapacitor Electrodes. *Chem. Soc. Rev.* 2009, *38*(9), 2520–2531.

[47] Birss, V. I.; Conway, B. E.; Wojtowicz, J.; 1997. The Role and Utilization of Pseudocapacitance for Energy Storage by Supercapacitors.

[48] Frackowiak, E.; Beguin, F.; Carbon Materials for the Electrochemical Storage of Energy in Capacitors. *Carbon.* 2001, *39*(6), 937–950.

[49] Zheng, J. P.; Cygan, P. J.; Jow, T. R.; Hydrous Ruthenium Oxide as an Electrode Material for Electrochemical Capacitors. *J. Electrochem. Soc.* 1995, *142*(8), 2699.

[50] Timperman, L.; Béguin, F.; Frackowiak, E.; Anouti, M. Comparative Study of Two Protic Ionic Liquids as Electrolyte for Electrical Double-layer Capacitors. *J. Electrochem. Soc.* 2013, *161*(3), A228.

[51] Elcap Supercapacitor. Wikipedia http://en.wikipedia.org/wiki/Supercapacitor (accessed Dec 12, 2015).

[52] McEvoy, A.; Castaner, L.; Markvart, T.; *Solar Cells: Materials, Manufacture and Operation*; Academic Press, 2012.

[53] Zhang, K.; Zhang, L. L.; Zhao, X. S.; Wu, J.; Graphene/polyaniline Nanofiber Composites as Supercapacitor Electrodes. *Chem. Mater.* 2010, *22*(4), 1392–1401.

[54] Sugimoto, W.; Yokoshima, K.; Murakami, Y.; Takasu, Y.; Charge Storage Mechanism of Nanostructured Anhydrous and Hydrous Ruthenium-based Oxides. *Electrochim. Acta.* 2006, *52*(4), 1742–1748.

[55] Wang, J.; Controlled-potential Techniques. In *Analytical Electrochemistry*, 2006; pp 67–114.

[56] Coroş, M.; Pogăcean, F.; Măgeruşan, L.; Socaci, C.; Pruneanu, S.; A Brief Overview on Synthesis and Applications of Graphene and Graphene-based Nanomaterials. *Front. Mater. Sci.* 2019, *13*(1), 23–32.

[57] Geim, A. K.; Novoselov, K. S. The Rise of Graphene, Nanoscience and Technology: A Collection of Reviews from Nature Journals. *World Sci.* 2010, 11–19.

[58] Mattevi, C.; Colléaux, F.; Kim, H.; Lin, Y. H.; Park, K. T.; Chhowalla, M.; Anthopoulos, T. D. Solution-processable Organic Dielectrics for Graphene Electronics. *Nanotechnology.* 2012, *23*(34), 344017.

[59] Khedekar, V. V.; Zaeem, S. M.; Das, S. Graphene-metal Oxide Nanocomposites for Supercapacitors: A Perspective Review. *Adv. Mater. Lett.* 2018, *9*, 02–19.

[60] Zhang, X.; Samorì, P.; Graphene/polymer Nanocomposites for Supercapacitors. *ChemNanoMat.* 2017, *3*(6), 362–372.

[61] Liu, J.; Xue, Y.; Zhang, M.; Dai, L.; Graphene-based Materials for Energy Applications. *Mrs Bull.* 2012, *37*(12), 1265–1272.

[62] Stoller, M. D.; Park, S.; Zhu, Y.; An, J.; Ruoff, R. S.; Graphene-based Ultracapacitors. *Nano Lett.* 2008, *8*(10), 3498–3502.

[63] Zhu, Y.; Murali, S.; Stoller, M. D.; Velamakanni, A.; Piner, R. D.; Ruoff, R. S.; Microwave Assisted Exfoliation and Reduction of Graphite Oxide for Ultracapacitors. *Carbon.* 2010, *48*(7), 2118–2122.

[64] Zhu, Y.; Stoller, M. D.; Cai, W.; Velamakanni, A.; Piner, R. D.; Chen, D.; Ruoff, R. S. Exfoliation of Graphite Oxide in Propylene Carbonate and Thermal Reduction of the Resulting Graphene Oxide Platelets. *ACS Nano.* 2010, *4*(2), 1227–1233.

[65] Wang, Y.; Shi, Z.; Huang, Y.; Ma, Y.; Wang, C.; Chen, M.; Chen, Y. Supercapacitor Devices Based on Graphene Materials. *J. Phys. Chem. C.* 2009, *113*(30), 13103–13107.

[66] Iro, Z. S.; Subramani, C.; Dash, S. S. A Brief Review on Electrode Materials for Supercapacitor. *Int. J. Electrochem. Sci.* 2016, *11*(12), 10628–10643.

[67] Seelajaroen, H.; Bakandritsos, A.; Otyepka, M.; Zbořil, R.; Sariciftci, N. S. Immobilized Enzymes on Graphene as Nanobiocatalyst. *ACS Appl. Mater. Interfaces.* 2019, *12*(1), 250–259.

[68] https://www.sciencedaily.com/releases/2020/08/200803092131.htm.

[69] Swanson, R. M.; *Photovoltaics Res. Appl.*. 2006, *14*, 443–453.

[70] Johnson, J.; *Chem. Eng. News.* 2004, *82*, 13.

[71] Krebs, F. C.;. *Polymer Photovoltaics: A Practical Approach*; SPIE-International Society for Optical Engineering, 2008.

[72] Sariciftci, N. S.; Sun, S. S. *Organic Photovoltaics: Mechanism, Materials, and Devices.* Taylor and Francis: New York, 2005.

[73] Morais, A.; Alves, J. P. C.; Lima, F. A. S.; Lira-Cantu, M.; Nogueira, A. F. Enhanced Photovoltaic Performance of Inverted Hybrid Bulk-heterojunction Solar Cells Using TiO2/reduced Graphene Oxide Films as Electron Transport Layers. *J. Photonics Energy.* 2015, *5*(1), 057408.

[74] Using Graphene Based Solar Cells for Solar Applications Saved from URL. https://www.azonano.com/article.aspx?ArticleID=4565

[75] Dutta, M.; Sarkar, S.; Ghosh, T.; Basak, D.; ZnO/graphene Quantum Dot Solid-state Solar Cell. *J. Phys. Chem. C.* 2012, *116*(38), 20127–20131.

[76] Chen, J.; Li, C.; Eda, G.; Zhang, Y.; Lei, W.; Chhowalla, M.; Milne, W. I.; Deng, W. Q.; Incorporation of Graphene in Quantum Dot Sensitized Solar Cells Based on ZnO Nanorods. *Chem. Commun.* 2011, *47*(21), 6084–6086.

[77] Hsu, Y. C.; Chen, G. L.; Lee, R. H.; Graphene Oxide Sheet-polyaniline Nanocomposite Prepared through In-situ Polymerization/deposition Method for Counter Electrode of Dye-sensitized Solar Cell. *J. Polym. Res.* 2014, *21*(5), 440.

[78] Wan, L.; Wang, B.; Wang, S.; Wang, X.; Guo, Z.; Xiong, H.; Dong, B.; Zhao, L.; Lu, H.; Xu, Z.; et al. Water-soluble Polyaniline/graphene Prepared by in Situ Polymerization in Graphene Dispersions and Use as Counter-electrode Materials for Dye-sensitized Solar Cells. *React. Funct. Polym.* 2014, *79*, 47–53.

[79] Jung, J. W.; Jo, J. W.; Jung, E. H.; Jo, W. H.; Recent Progress in High Efficiency Polymer Solar Cells by Rational Design and Energy Level Tuning of Low Bandgap Copolymers with Various Electron-withdrawing Units. *Org. Electron.* 2016, *31*, 149–170.

[80] Cong, H. P.; Chen, J. F.; Yu, S. H.; Graphene-based Macroscopic Assemblies and Architectures: An Emerging Material System. *Chem. Soc. Rev.* 2014, *43*(21), 7295–7325.

[81] He, B.; Tang, Q.; Wang, M.; Ma, C.; Yuan, S.; Complexation of Polyaniline and Graphene for Efficient Counter Electrodes in Dye-sensitized Solar Cells: Enhanced Charge Transfer Ability. *J. Power Sources.* 2014, *256*, 8–13.

[82] Wang, M.; Tang, Q.; Xu, P.; He, B.; Lin, L.; Chen, H.; Counter Electrodes from Polyaniline– Graphene Complex/graphene Oxide Multilayers for Dye–Sensitized Solar Cells. *Electrochim. Acta.* 2014, *137*, 175–182.

[83] Wang, M.; Tang, Q.; Chen, H.; He, B.; Counter Electrodes from Polyaniline– Carbon Nanotube Complex/graphene Oxide Multilayers for Dye-sensitized Solar Cell Application. *Electrochim. Acta.* 2014, *125*, 510–515.

[84] Cai, H.; Tang, Q.; He, B.; Wang, M.; Yuan, S.; Chen, H.; Self-assembly of Graphene Oxide/polyaniline Multilayer Counter Electrodes for Efficient Dye-sensitized Solar Cells. *Electrochim. Acta.* 2014, *121*, 136–142.

[85] Gong, J.; Sumathy, K.; Qiao, Q.; Zhou, Z.; Review on Dye-sensitized Solar Cells (Dsscs): Advanced Techniques and Research Trends. *Renewable Sustainable Energy Rev.* 2017, *68*, 234–246.

[86] Longo, C.; De Paoli, M. A.; Dye-sensitized Solar Cells: A Successful Combination of Materials. *J. Braz. Chem. Soc.* 2003, *14*(6), 898–901.

[87] Bavane, R. G.; 2014. Synthesis and Characterization of Thin Films of Conducting Polymers for Gas Sensing Applications.

[88] Tan, S.; Zhai, J.; Wan, M.; Meng, Q.; Li, Y.; Jiang, L.; Zhu, D.; Influence of Small Molecules in Conducting Polyaniline on the Photovoltaic Properties of Solid-state Dye-sensitized Solar Cells. *J. Phys. Chem. B.* 2004, *108* (48), 18693–18697.

[89] Tan, S.; Zhai, J.; Xue, B.; Wan, M.; Meng, Q.; Li, Y.; Jiang, L.; Zhu, D.; Property Influence of Polyanilines on Photovoltaic Behaviors of Dye-sensitized Solar Cells. *Langmuir.* 2004, *20*(7), 2934–2937.

[90] Wu, Q.; Xu, Y.; Yao, Z.; Liu, A.; Shi, G.; Supercapacitors Based on Flexible Graphene/polyaniline Nanofiber Composite Films. *ACS Nano.* 2010, *4*(4), 1963–1970.

[91] Inoue, M.; Navarro, R. E.; Inoue, M. B.; New Soluble Polyaniline: Synthesis, Electrical Properties and Solution Electronic Spectrum. *Synth. Met.* 1989, *30*(2), 199–207.

[92] Tahir, Z. M.; Alocilja, E. C.; Grooms, D. L.; Polyaniline Synthesis and Its Biosensor Application. *Biosens. Bioelectron.* 2005, *20*(8), 1690–1695.

[93] Zhu, P.; Nair, A. S.; Shengjie, P.; Shengyuan, Y.; Ramakrishna, S.; Facile Fabrication of TiO2–graphene Composite with Enhanced Photovoltaic and Photocatalytic Properties by Electrospinning. *ACS Appl. Mater. Interfaces.* 2012, *4*(2), 581–585.

[94] Zhang, H.; Wang, W.; Liu, H.; Wang, R.; Chen, Y.; Wang, Z.; Effects of TiO2 Film Thickness on Photovoltaic Properties of Dye-sensitized Solar Cell and Its Enhanced Performance by Graphene Combination. *Mater. Res. Bull.* 2014, *49*, 126–131.

[95] https://www.graphene-info.com/graphene-solar-panels

[96] Mahmoudi, T.; Wang, Y.; Hahn, Y. B.; Graphene and Its Derivatives for Solar Cells Application. *Nano Energy.* 2018, *47*, 51–65.

[97] https://whitenoise.kinja.com/graphene-miracle-material-1575961841

[98] Kötz, R.; Carlen, M. J. E. A. Principles and Applications of Electrochemical Capacitors. *Electrochim. Acta.* 2000, *45(15-16)*, 2483–2498.

[99] Chronopoulos, D. D.; Błoński, P.; Nováček, Z.; Jakubec, P.; Tomanec, O.; Bakandritsos, A.; Novotná, V.; Zbořil, R.; Otyepka, M.; Alkynylation of Graphene via the Sonogashira C–C Cross-coupling Reaction on Fluorographene. *Chem. Commun.* 2019, *55*(8), 1088–1091.

[100] Bakandritsos, A.; Jakubec, P.; Pykal, M.; Otyepka, M. Covalently Functionalized Graphene as a Supercapacitor Electrode Material. *FlatChem.* 2019, *13*, 25–33.

[101] Wang, Q.; Yan, J.; Fan, Z.; Wei, T.; Zhang, M.; Jing, X.; Mesoporous Polyaniline Film on Ultra-thin Graphene Sheets for High Performance Supercapacitors. *J. Power Sources.* 2014, *247*, 197–203.

[102] Zhang, Q.; Li, Y.; Feng, Y.; Feng, W.; Electropolymerization of Graphene Oxide/polyaniline Composite for High-performance Supercapacitor. *Electrochim. Acta.* 2013, *90*, 95–100.

[103] Channu, V. S. R.; Holze, R.; Rambabu, B.; Kalluru, R. R.; Synthesis and Characterization of PANI Nanostructures for Supercapacitors and Photoluminescence. *Iran. Polym. J.* 2012, *21*(7), 457–462.

[104] Luo, Z.; Zhu, L.; Zhang, H.; Tang, H.; Polyaniline Uniformly Coated on Graphene Oxide Sheets as Supercapacitor Material with Improved Capacitive Properties. *Mater. Chem. Phys.* 2013, *139*(2–3), 572–579.

[105] Liu, H.; Xu, B.; Jia, M.; Zhang, M.; Cao, B.; Zhao, X.; Wang, Y.; Polyaniline Nanofiber/large Mesoporous Carbon Composites as Electrode Materials for Supercapacitors. *Appl. Surf. Sci.* 2015, *332*, 40–46.

[106] Majumdar, D.;. Functionalized-graphene/polyaniline Nanocomposites as Proficient Energy Storage Material: An Overview. *Innov. Ener. Res.* 2016, *5*(145), 2.

[107] Murugan, A. V.; Muraliganth, T.; Manthiram, A.; Rapid, Facile Microwave-solvothermal Synthesis of Graphene Nanosheets and Their Polyaniline Nanocomposites for Energy Storage. *Chem. Mater.* 2009, *21*(21), 5004–5006.

[108] Wang, D. W.; Li, F.; Zhao, J.; Ren, W.; Chen, Z. G.; Tan, J.; Wu, Z. S.; Gentle, I.; Lu, G. Q.; Cheng, H. M.; Fabrication of Graphene/polyaniline Composite Paper via in Situ Anodic Electropolymerization for High-performance Flexible Electrode. *ACS Nano.* 2009, *3*(7), 1745–1752.

[109] Wang, H.; Hao, Q.; Yang, X.; Lu, L.; Wang, X.; A Nanostructured Graphene/polyaniline Hybrid Material for Supercapacitors. *Nanoscale.* 2010, *2*(10), 2164–2170.

[110] Yan, J.; Wei, T.; Shao, B.; Fan, Z.; Qian, W.; Zhang, M.; Wei, F.; Preparation of a Graphene Nanosheet/polyaniline Composite with High Specific Capacitance. *Carbon.* 2010, *48*(2), 487–493.

[111] Zhang, J.; Zhao, X. S. Conducting Polymers Directly Coated on Reduced Graphene Oxide Sheets as High-performance Supercapacitor Electrodes. *J. Phys. Chem. C.* 2012, *116*(9), 5420–5426.

[112] Cong, H. P.; Ren, X. C.; Wang, P.; Yu, S. H.; Flexible Graphene–polyaniline Composite Paper for High-performance Supercapacitor. *Energy Environ. Sci.* 2013, *6*(4), 1185–1191.

[113] Li, Z. F.; Zhang, H.; Liu, Q.; Sun, L.; Stanciu, L.; Xie, J.; Fabrication of High-surface-area Graphene/polyaniline Nanocomposites and Their Application in Supercapacitors. *ACS Appl. Mater. Interfaces.* 2013, *5* (7), 2685–2691.

[114] Hassan, M.; Reddy, K. R.; Haque, E.; Faisal, S. N.; Ghasemi, S.; Minett, A. I.; Gomes, V. G.; Hierarchical Assembly of Graphene/polyaniline Nanostructures to Synthesize Free-standing Supercapacitor Electrode. *Compos. Sci. Technol.* 2014, *98*, 1–8.

[115] Jo, E. H.; Jang, H. D.; Chang, H.; Kim, S. K.; Choi, J. H.; Lee, C. M.; 3 D Network-Structured Crumpled Graphene/Carbon Nanotube/Polyaniline Composites for Supercapacitors. *ChemSusChem.* 2017, *10*(10), 2210–2217.

[116] Hong, X.; Zhang, B.; Murphy, E.; Zou, J.; Kim, F.; Three-dimensional Reduced Graphene Oxide/polyaniline Nanocomposite Film Prepared by Diffusion Driven Layer-by-layer Assembly for High-performance Supercapacitors. *J. Power Sources.* 2017, *343*, 60–66.

[117] Biswas, S.; Drzal, L. T.; Multilayered Nanoarchitecture of Graphene Nanosheets and Polypyrrole Nanowires for High Performance Supercapacitor Electrodes. *Chem. Mater.* 2010, *22*(20), 5667–5671.

[118] Bose, S.; Kim, N. H.; Kuila, T.; Lau, K. T.; Lee, J. H.; Electrochemical Performance of a Graphene–polypyrrole Nanocomposite as a Supercapacitor Electrode. *Nanotechnology.* 2011, *22*(29), 295202.

[119] Liu, Y.; Zhang, Y.; Ma, G.; Wang, Z.; Liu, K.; Liu, H. Ethylene Glycol Reduced Graphene Oxide/polypyrrole Composite for Supercapacitor. *Electrochim. Acta.* 2013, *88*, 519–525.

[120] Li, J.; Xie, H.; Li, Y.; Fabrication of Graphene Oxide/polypyrrole Nanowire Composite for High Performance Supercapacitor Electrodes. *J. Power Sources.* 2013, *241*, 388–395.

[121] Song, Y.; Xu, J. L.; Liu, X. X.; Electrochemical Anchoring of Dual Doping Polypyrrole on Graphene Sheets Partially Exfoliated from Graphite Foil for High-performance Supercapacitor Electrode. *J. Power Sources.* 2014, *249*, 48–58.

[122] Kashani, H.; Chen, L.; Ito, Y.; Han, J.; Hirata, A.; Chen, M.; Bicontinuous Nanotubular Graphene–polypyrrole Hybrid for High Performance Flexible Supercapacitors. *Nano Energy.* 2016, *19*, 391–400.

[123] Shu, K.; Wang, C.; Zhao, C.; Ge, Y.; Wallace, G. G.; A Free-standing Graphene-polypyrrole Hybrid Paper via Electropolymerization with an Enhanced Areal Capacitance. *Electrochim. Acta.* 2016, *212*, 561–571.

[124] Zuo, X.; Zhang, Y.; Si, L.; Zhou, B.; Zhao, B.; Zhu, L.; Jiang, X.; One-step Electrochemical Preparation of Sulfonated Graphene/polypyrrole Composite and Its Application to Supercapacitor. *J. Alloys Compd.* 2016, *688*, 140–148.

[125] Alvi, F.; Ram, M. K.; Basnayaka, P. A.; Stefanakos, E.; Goswami, Y.; Kumar, A.; Graphene–polyethylenedioxythiophene Conducting Polymer Nanocomposite Based Supercapacitor. *Electrochim. Acta.* 2011, *56*(25), 9406–9412.

[126] Sun, D.; Jin, L.; Chen, Y.; Zhang, J. R.; Zhu, J. J.; Microwave-Assisted in Situ Synthesis of Graphene/PEDOT Hybrid and Its Application in Supercapacitors. *ChemPlusChem.* 2013, *78*(3), 227–234.

[127] Wen, J.; Jiang, Y.; Yang, Y.; Li, S.; Conducting Polymer and Reduced Graphene Oxide Langmuir–Blodgett Films: A Hybrid Nanostructure for High Performance Electrode Applications. *J. Mater. Sci.: Mater. Electron.* 2014, *25*(2), 1063–1071.

[128] Qu, G.; Cheng, J.; Li, X.; Yuan, D.; Chen, P.; Chen, X.; Wang, B.; Peng, H.; A Fiber Supercapacitor with High Energy Density Based on Hollow Graphene/conducting Polymer Fiber Electrode. *Adv.Mate.* 2016, *28*(19), 3646–3652.

[129] Islam, M. M.; Subramaniyam, C. M.; Akhter, T.; Faisal, S. N.; Minett, A. I.; Liu, H. K.; Konstantinov, K.; Dou, S. X.; Three Dimensional Cellular Architecture of Sulfur Doped Graphene: Self-standing Electrode for Flexible Supercapacitors, Lithium Ion and Sodium Ion Batteries. *J. Mater. Chem. A.* 2017, *5*(11), 5290–5302.

[130] Gao, Y.;. Graphene and Polymer Composites for Supercapacitor Applications: A Review. *Nanoscale Res. Lett.* 2017, *12*(1), 387.

[131] Bube, R. H.;. *Photoelectronic Properties of Semiconductors*; Cambridge University Press, 1992.

[132] Wang, J. T. W.; Ball, J. M.; Barea, E. M.; Abate, A.; Alexander-Webber, J. A.; Huang, J.; Saliba, M.; Mora-Sero, I.; Bisquert, J.; Snaith, H. J.; et al. Low-temperature Processed Electron Collection Layers of graphene/TiO2 Nanocomposites in Thin Film Perovskite Solar Cells. *Nano Lett.* 2014, *14*(2), 724–730.

[133] Tang, Y. B.; Lee, C. S.; Xu, J.; Liu, Z. T.; Chen, Z. H.; He, Z.; Cao, Y. L.; Yuan, G.; Song, H.; Chen, L.; et al. Incorporation of Graphenes in Nanostructured TiO2 Films via Molecular Grafting for Dye-sensitized Solar Cell Application. *ACS Nano.* 2010, *4*(6), 3482–3488.

[134] Orgil, K. 2018. Comparison of Organic and Inorganic Solar Photovoltaic Systems.

[135] Kavan, L.; Yum, J. H.; Grätzel, M. Optically Transparent Cathode for Dye-sensitized Solar Cells Based on Graphene Nanoplatelets. *Acs Nano.* 2011, *5*(1), 165–172.

[136] Das, S.; Sudhagar, P.; Kang, Y. S.; Choi, W. Graphene Synthesis and Application for Solar Cells. *J. Mater. Res.* 2014, *29*(3), 299–319.

[137] Zi, M.; Zhu, M.; Chen, L.; Wei, H.; Yang, X.; Cao, B. ZnO Photoanodes with Different Morphologies Grown by Electrochemical Deposition and Their Dye-sensitized Solar Cell Properties. *Ceram. Int.* 2014, *40*(6), 7965–7970.

[138] Sugathan, V.; John, E.; Sudhakar, K. Recent Improvements in Dye Sensitized Solar Cells: A Review. *Renewable Sustainable Energy Rev.* 2015, *52*, 54–64.

[139] Wang, Y. S.; Li, S. M.; Hsiao, S. T.; Yang, S. Y.; Tien, H. W.; Ma, C. C. M.; Hu, C. C. Thickness-self-controlled Synthesis of Porous Transparent Polyaniline-reduced Graphene Oxide Composites Towards Advanced Bifacial Dye-sensitized Solar Cells. *J. Power Sources.* 2014, *260*, 326–337.

[140] Liu, W.; Fang, Y.; Xu, P.; Lin, Y.; Yin, X.; Tang, G.; He, M. Two-step Electrochemical Synthesis of Polypyrrole/reduced Graphene Oxide Composites as Efficient Pt-free Counter Electrode for Plastic Dye-sensitized Solar Cells. *ACS Appl. Mater. Interfaces.* 2014, *6*(18), 16249–16256.

[141] Wang, G.; Xing, W.; Zhuo, S. The Production of Polyaniline/graphene Hybrids for Use as a Counter Electrode in Dye-sensitized Solar Cells. *Electrochim. Acta.* 2012, *66*, 151–157.

[142] Sun, S.; Gao, L.; Liu, Y. Enhanced Dye-sensitized Solar Cell Using graphene-TiO 2 Photoanode Prepared by Heterogeneous Coagulation. *Appl. Phys. Lett.* 2010, *96* (8), 083113.

[143] Yang, N.; Zhai, J.; Wang, D.; Chen, Y.; Jiang, L. Two-dimensional Graphene Bridges Enhanced Photoinduced Charge Transport in Dye-sensitized Solar Cells. *ACS Nano.* 2010, *4*(2), 887–894.

[144] Tsai, T. H.; Chiou, S. C.; Chen, S. M. Enhancement of Dye-sensitized Solar Cells by Using graphene-TiO2 Composites as Photoelectrochemical Working Electrode. *Int. J. Electrochem. Sci.* 2011, *6*(8), 3333–3343.

[145] Zhu, M.; Li, X.; Liu, W.; Cui, Y. An Investigation on the Photoelectrochemical Properties of Dye-sensitized

Solar Cells Based on graphene–TiO2 Composite Photoanodes. *J. Power Sources*. 2014, *262*, 349–355.

[146] Tu, W.; Zhou, Y.; Liu, Q.; Yan, S.; Bao, S.; Wang, X.; Xiao, M.; Zou, Z. An in Situ Simultaneous Reduction-hydrolysis Technique for Fabrication of TiO2-graphene 2D Sandwich-like Hybrid Nanosheets: Graphene-promoted Selectivity of Photocatalytic-driven Hydrogenation and Coupling of CO2 into Methane and Ethane. *Adv. Funct. Mater.* 2013, *23* (14), 1743–1749.

[147] Cheng, G.; Akhtar, M. S.; Yang, O. B.; Stadler, F. J. *ACS Appl. Mater. Interfaces*. 2013, *5*, 6635.

[148] He, B.; Tang, Q.; Wang, M.; Chen, H.; Yuan, S. Robust Polyaniline–graphene Complex Counter Electrodes for Efficient Dye-sensitized Solar Cells. *ACS Appl. Mater. Interfaces*. 2014, *6*(11), 8230–8236.

[149] Lee, D. H.; Song, D.; Kang, Y. S.; Park, W. I. Three-dimensional Monolayer Graphene and TiO2 Hybrid Architectures for High-efficiency Electrochemical Photovoltaic Cells. *J. Phys. Chem. C*. 2015, *119*(12), 6880–6885.

[150] Madhavan, A. A.; Ranjusha, R.; Daya, K. C.; Arun, T. A.; Praveen, P.; Sanosh, K. P.; Subramanian, K. R. V.; Nair, S. K. V.; Nair, A. S.; Balakrishnan, A. Molten Salt Synthesized TiO2-graphene Composites for Dye Sensitized Solar Cells Applications. *Sci. Adv. Mater.* 2014, *6*(4), 828–834.

[151] Zhu, G.; Pan, L.; Sun, H.; Liu, X.; Lv, T.; Zhou, N.; Sun, Z. Enhanced Performance of Dye-sensitized Solar Cells by Graphene-incorporated Nanocrystalline TiO2 Films. *Nanosci. Nanotech. Lett.* 2013, *5*(2), 154–158.

[152] Zhu, Y.; Meng, X.; Cui, H.; Jia, S.; Dong, J.; Zheng, J.; Zhao, J.; Wang, Z.; Li, L.; Zhang, L.; et al. Graphene Frameworks Promoted Electron Transport in Quantum Dot-sensitized Solar Cells. *ACS Appl. Mater. Interfaces*. 2014, *6*(16), 13833–13840.

[153] Zabihi, F.; Tebyetekerwa, M.; Xu, Z.; Ali, A.; Kumi, A. K.; Zhang, H.; Jose, R.; Ramakrishna, S.; Yang, S. Perovskite Solar Cell-hybrid Devices: Thermoelectrically, Electrochemically, and Piezoelectrically Connected Power Packs. *J. Mater. Chem. A*. 2019, *7*(47), 26661–26692.

The Effect of Exposure of EMF Radiations from Cell Phones on Percentage of Glucose, Cholesterol and Protein in Developing Chick Embryos

Mamata Chandrakar[*]

Department of Zoology, Shiksha Mandal's Bajaj College of Science, Wardha, Maharashtra (India)-442001
*Corresponding author: mrchandrakar@gmail.com

Abstract Electromagnetic field radiations have influenced the range of bodily functions. EMF had put a major public concern due to its widespread applications and capability of producing deleterious effects. The present study is aimed to evaluate the changes in percentage of glucose, cholesterol and protein in chick embryo tissues following exposure to EMF radiations emitted from a cell phone. Fertile hen eggs of RIR species (*Rhode Island Red)* were incubated in two groups in standard egg incubators (group A=16) (group B=16). Group A serves as control while Group B would be experimental and exposed to radiations emitted from a cell phone. On completion of 7th and 14th day of incubation, the embryos were sacrificed; tissues were dissected, centrifuged and samples thus obtained after centrifugation was taken and estimations of glucose, cholesterol and protein were performed. Glucose estimations had done by O-toluidine method. Cholesterol estimations were performed by Liebermann-Burchard method and protein conc. were estimated by Biuret method. Student's t-test had been applied to check the statistical significance among Group A and Group B. Exposure of EMF from cell phone didn't have considerable effect on cholesterol percentage on 7th day of incubation and on glucose percentage on 7th as well as 14th day of incubation in chick embryo tissues. In the present study, cholesterol percentage on 14th day of incubation (P = .001) and protein concentration on 7th and 14th day of incubation (P < .001) showed significant changes among group A and group B. Decrease in the percentage of cholesterol and protein showed that EMF radiations emitted from cell phone might affect metabolism directly or indirectly and thus it might be a factor that is responsible for increased mortality in chick embryos.

Keywords: *EMF, cell phone, exposure, chick embryo, incubation*

Cite This Article: Mamata Chandrakar, "The Effect of Exposure of EMF Radiations from Cell Phones on Percentage of Glucose, Cholesterol and Protein in Developing Chick Embryos." *Applied Ecology and Environmental Sciences*, vol. 8, no. 6 (2020): 422-427. doi: 10.12691/aees-8-6-14.

1. Introduction

In day-to-day life, we use technology to make our lives simply better. This technology brings electrification with it. The electrification is based on the principle of electromagnetic radiations. There are so many electrical appliances that operate on electromagnetic radiations to perform their action. These electromagnetic radiations are of non-ionizing type and they are categorised into Extremely low frequency electromagnetic field (ELF) that covers the frequency range of 3Hz to 3 KHz and radiofrequency radiations (RFR) that covers frequency range from 10 KHz to 300 GHz. various applications uses different frequencies of EMF radiations. Cell phone is among the basic need of human's life. The cell phone technology uses frequencies of up to 800 MHz to 3 GHz [1]. The constantly increased use of cell phones from last several years put a major public concern about the potential risk associated with it.

The World Health Organisation stated that "Cell phone radiations can possibly carcinogenic to humans" as it may represent a long term health risk and classified the cell phone in category 2B which ranks it alongside coffee and other possibly carcinogenic substances [2]. Numerous studies suggests that electromagnetic field affects on biological systems [3], it is associated with increased risk of childhood leukaemia, brain tumours, neurological effects, neurodegenerative diseases, breast cancer, miscarriage and some cardiovascular effects [4]. EMF had shown to interact with the biomolecular system by amplifying initial weak signals associated with binding of antibodies, neurotransmitters and hormones to their specific binding sites [5], it might have the capacity to alter cell structure from plasma membrane to different biomolecules present within a cell that might cause genotoxicity [6]. A study on effects of EMF exposure on birds had shown that there were behavioural, physiological changes, increased oxidative stress, changes in immune and endocrine functions and had an effect on growth and development in birds that were exposed to EMF from power lines [7]. It

was found that EMF might induced stress related behaviour and it might be responsible for elevated levels of hormone ACTH in male *wistar* rats [8]. As a result of EMF exposure, there were decrease in organ weight in newly hatched chicks [9], irreversible developmental alteration and external malformations [10], as well as high mortality and developmental disorders had been seen in chick embryos [11].

Conversely no any harmful effects were reported by others. EMF found to stimulate proliferation and differentiation of embryonic cells [12]. A scientific study on cultured human lymphocytes suggests that there were no genotoxic effects had been found after exposure of lymphocytes with EMF radiations [13]. While some researches had shown that low frequency pulsed Electromagnetic field could be beneficial for the treatment of varieties of musculoskeletal disorders [14], exerts anti-inflammatory action, alleviates pain in arthritis condition and helps in bone remodelling [15].

Considering all these reviews, the present work had been taken to investigate any changes caused by EMF exposure on biochemical measures such as percentage of glucose, cholesterol, and protein in chick embryos. Glucose plays an essential role of providing energy to the body. Cholesterol is the steroid lipid found in the plasma membranes of all tissues in the body and is responsible for several vital biochemical processes such as regulating immunity and defence mechanism, transportation of lipid and other vital fats to body and provides protection to arteries, veins and muscles of the body. Proteins are building blocks of body and it plays an essential role in normal growth and development of an individual and

cellular repair. All these biomolecules plays an essential role in metabolism. Hence the study had been carried out to observe changes if any, and either it would be beneficial or hazardous. For that purpose, chick embryo is used as an experimental model. Various researchers demonstrated that chick embryo as a role model for different studies as its development is external hence embryos were not compromised by changes in mother's biological systems [16,17,18].

2. Materials and Method

Two separate electrical incubators were used to kept control and experimental eggs. The incubators were sterilized with 70% ethanol before keeping eggs in incubators. The temperature 37.5□ and humidity 50±5 % was maintained till the 21 days of incubation.

Freshly laid fertile hen eggs of RIR species (*Rhode Island Red*) were obtained from Government Poultry Farm, Camp road, Amravati. The eggs were incubated in two batches. Each batch comprise of 32 eggs, out of which 16 eggs were incubated in standard egg incubator. They were treated as control group (Group A). The other 16 eggs were treated as experimental group (Group B). These experimental eggs were kept in a separate incubator where there had an arrangement of mounting cell phone on top of the egg tray. The approximate distance between the cell phone and eggs kept in the centre was 5.8 cm. Before keeping Group A and Group B eggs in incubators, they were weighed and numbered. The mean egg weight was 50.6 gm (Figure 1).

Figure 1. Showing Arrangement of eggs for Group A and Group B respectively in an incubator with normal incubating temperature and humidity

Figure 2. Showing Candling of eggs on 7th and 14th day of incubation respectively

During the period of incubation, all the eggs from both the groups were rotated manually in 45° angle at least thrice or four times a day. The egg candling takes place from 4th day of incubation so that growth of embryos within egg could be observed. The egg candling is the process of observing appearance and growth of an embryo inside the egg without breaking egg shell (Figure 2).

A popular brand cell phone with a frequency bandwidth of 900-1900 MHz and SAR value of 1.11W/kg. in head and 0.22W/kg in body measured by FCC was used for the present work to expose the experimental embryos. The SAR value (Specific Absorption Rate) is the measure at which energy is absorbed by tissues when exposed to Radiofrequency EMF radiations. The cell phone was placed in incubator continuously up to 21 days, in silent mode, rang up to four times for 15 minutes each daily from another cell phone with time interval of one hour.

On the 7th and 14th day of incubation, 6 eggs each from Group A as well as Group B were sacrificed. After breaking of egg shell, air sac had been removed and then embryo got extracted from egg. The mortality of all embryos from Group A and Group B was observed. Also morphological anomalies were seen if present. The extracted live embryos were kept in 0.9% saline solution to clean it then the embryos were transferred in a clear solution of 0.9% saline. The weight and length of all the embryos sacrificed were measured and all the embryos were photographed. All the embryos from Group A and Group B were dissected and the tissues of embryos were taken out and homogenized in mortar pestle with the addition of saline in it. The solution thus obtained after homogenization of each embryo tissue had been centrifuged in 8000 R.P.M. for 10 min. The supernatant thus obtained after centrifugation, serves as a test sample from each embryo for the estimation of glucose, cholesterol and protein concentration in the tissues.

2.1. Estimation of Glucose

Glucose estimation was done by O-Toluidine method. For glucose analysis from sample, O-Toluidine reagent had been used. In each test tube, 5 ml of O-Toluidine reagent had been taken. In the test tube marked as blank, 0.1 ml of distilled water was added. In the test tube marked as standard, 0.1 ml of glucose working standard (1 ml. of stock standard in 9 ml benzoic acid saturated.) was added which was prepared from glucose stock standard solution (glucose 1 gm., benzoic acid 250 mg. in 100 ml of distilled water) and in test tubes mark as test, 0.1 ml of test sample were added from each sample tube.

All the test tubes then kept in boiling water bath exactly for 8 minutes. After 8 min. all the test tubes were moved from water bath and kept in cold water in a beaker. Optical density was measured in 630 nm in UV spectrophotometer with blank set as zero. Calculations were done for percentage of glucose per 100 ml.

Formula used to calculate the percentage of glucose in tissues:

Optical density of test/optical density of standard $\times$ 100.

2.2. Estimation of Cholesterol

Cholesterol estimation was done by Liebermann Burchard method. For analysis of Cholesterol from tissues, glacial acetic acid Aldehyde free was used. In test tube marked as Blank, 6ml of glacial acetic acid had been added then 0.1 ml of distilled water was added followed by 4 ml colour reagent (10% $FeCl_3$ 0.5ml was taken in 50 ml measuring cylinder and volume was make up with H_2SO_4 to the mark).

In test tube marked as standard, 5 ml of glacial acetic acid aldehyde free was taken. 1 ml of cholesterol working standard (10 ml of cholesterol stock standard in 50 ml glacial acetic acid extra pure)was added in test tube which was prepared from cholesterol stock standard solution (1mg cholesterol in 1 ml distilled water)followed by 4 ml of colour reagent.

In test tubes marked with test, 5 ml of acetic acid aldehyde free was taken. 0.1 ml of test sample was added from each sample tube followed by 4 ml of colour reagent in each test tube. All the test tubes were allowed to cool at room temperature. Absorbance was measured in 630 nm in UV Spectrophotometer against the reagent Blank. Blank was set as zero. Calculations were done for percentage of cholesterol present per 100 ml.

Formula used to calculate the percentage of cholesterol in tissues:

Optical density of test/optical density of standard $\times$ 0.2$\times$100/0.1.

2.3. Estimation of Protein

Protein estimation was done by Biuret method. To each of the test tubes, we have added 5 ml of biuret reagent. To the test tube mark as blank, 1 ml of distilled water was added. To the test tube mark as standard, 1 ml of protein reference standard was added. To each test tube marked as test, 1ml each test sample were added in biuret reagent. Absorbance was measured in 540 nm in UV Spectrophotometer with Blank set as zero. Absorbance for various samples were recorded.

2.4. Statistical Analysis

Collected data were analysed and Student's t-Test (paired) was applied to find out level of significance among means of Group A and Group B. Significance was set at $p < 0.05$.

2.5. Observations

Graphs were plotted against percentage of glucose (Graph 1), cholesterol (Graph 2) and protein (Graph 3) on X-axis and calculated means for each on Y-axis.
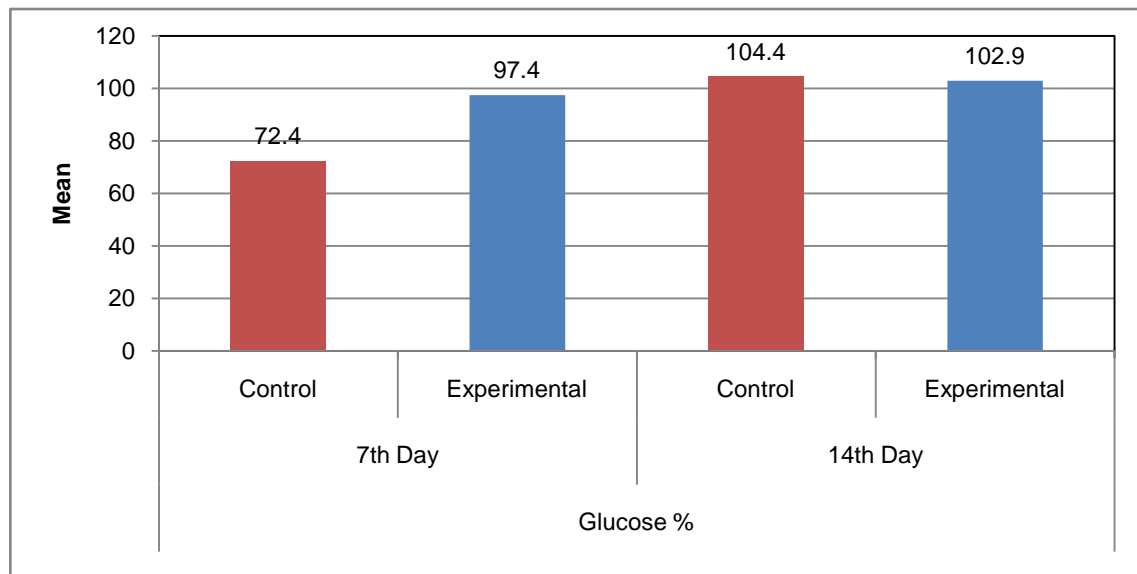
Graph 1. Percentage of glucose on 7th day and 14th day of incubation in Control and Experimental group embryos after EMF exposure
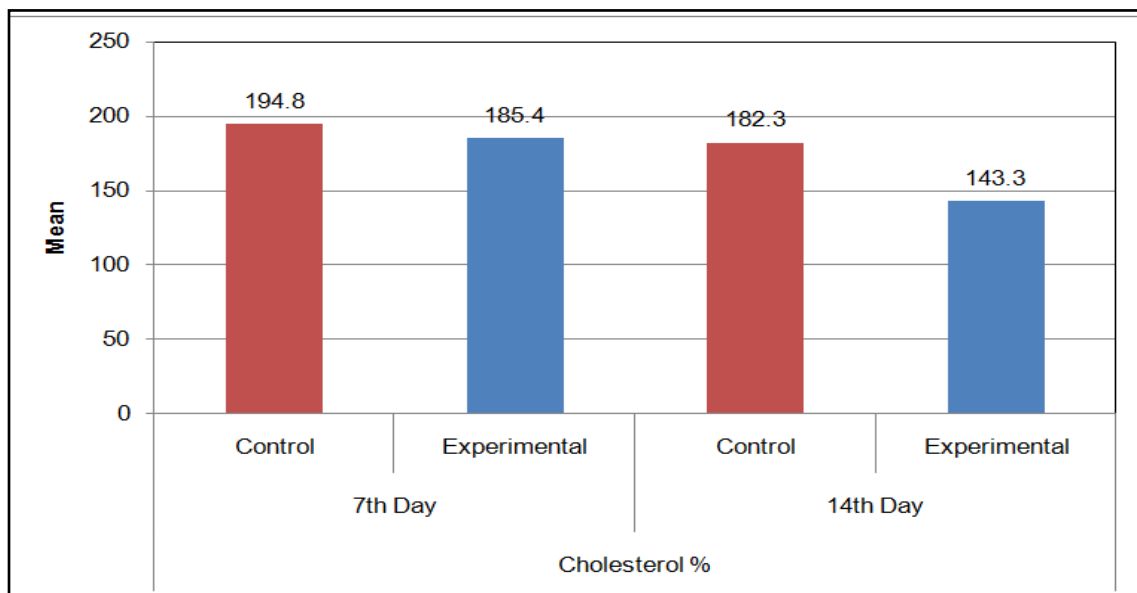
Graph 2. Percentage of Cholesterol in tissues on 7th day and 14th day of incubation in Control and Experimental group embryos after EMF exposure
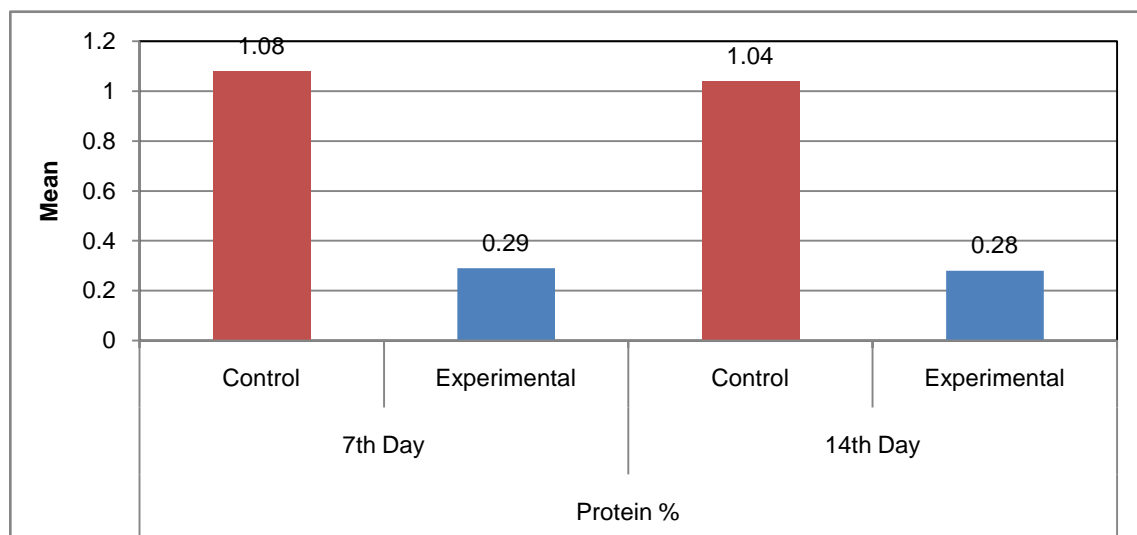
Graph 3. Concentration of protein in tissues on 7th day and 14th day of incubation in Control and Experimental group embryos after EMF exposure

Table 1. Showing t-Test, values are ± SD taken from control and experimental group, p-value of samples and interpretation of p-value indicating statistical significance

Parameter	Day	Group	Mean	±SD	Minimum	Maximum	t value	P Value	Interpretation of P Value
Glucose %	7th Day	Control	72.4	±45.4	5.9	108.0	-1.208	.294	Not Significant
		Experimental	97.4	±3.6	92.2	102.0			
	14th Day	Control	104.4	±12.2	96.1	125.5	0.890	.424	Not Significant
		Experimental	102.9	±10.0	94.1	119.6			
Cholesterol %	7th Day	Control	194.8	±16.2	173.5	213.3	0.865	.436	Not Significant
		Experimental	185.4	±12.9	165.3	200.0			
	14th Day	Control	182.3	±6.4	173.9	191.6	8.909	.001	Significant
		Experimental	143.3	±3.9	138.7	149.3			
Protein %	7th Day	Control	1.08	±0.08	1.00	1.20	23.729	.000	Significant
		Experimental	0.29	±0.05	0.20	0.35			
	14th Day	Control	1.04	±0.11	0.90	1.20	12.483	.000	Significant
		Experimental	0.28	±0.03	0.25	0.30			

3. Results

In day-to-day life, we use many electrical appliances that operate on electromagnetic radiations. Numerous studies suggests that electromagnetic field affects on biological systems [3], which is associated with increased risk of childhood leukaemia, brain tumours, neurological effects, neurodegenerative diseases, breast cancer, miscarriage and some cardiovascular effects [4]. EMF had shown to interact with the biomolecular system by amplifying initial weak signals associated with binding of antibodies, neurotransmitters and hormones to their specific binding sites [5], it might have the capacity to alter cell structure from plasma membrane to different biomolecules present within a cell that might cause genotoxicity [6]. As a result of EMF exposure, there were decrease in organ weight in newly hatched chicks [9], irreversible developmental alteration and external malformations [10], as well as high mortality and developmental disorders had been seen in chick embryos [11].

Considering all these reviews, the present work had been taken to investigate any changes caused by EMF exposure on biochemical measures such as percentage of glucose, cholesterol, and protein in developing chick embryos. All these biomolecules plays an essential role in metabolism. Hence the study had been carried out to observe changes if any, and either it would be beneficial or hazardous. For that purpose, chick embryo is used as an experimental model.

It had been found that there were increased rate of mortality in experimental embryos (Group B) as compared to control embryos (Group A). The morphological anomalies like deformation of limbs, beak were also seen in Group B. There were no significant differences found in percentage of glucose in tissues on both 7th and 14th day of incubation while percentage of cholesterol on 7th day of incubation is statistically not significant but on 14th day of incubation, there were decrease in cholesterol percentage in experimental group was found (Table 1). It means that there were significant differences had been found for cholesterol percentage in tissues amongst control and experimental group on 14th day of incubation (P = .001). The percentage of protein in tissues had been decreased in experimental embryos on both 7th and 14th day of incubation and highly significant differences had been found between control and experimental group (P < .001).

4. Conclusion and Discussion

Electromagnetic fields were, are and will be a very essential part of our life due to modern technological advances. The hazardous or beneficial effect of EMF radiation on living being is a topic of so many earlier researches [19].

There are many studies related to electromagnetic field and its impact on biosystem and ecosystem [20,21]. The present study on exposure of EMF radiations emitted from cell phone on chick embryos showed that there were increased mortality rate in experimental group, changes in the concentration of cholesterol and protein in chick embryo tissues. Some findings from our results also observed in other studies. A study on male *Wistar* rats concluded that there was reduction in the level of lipid peroxidise, Glutathione reductase and total cholesterol in different tissues of rats exposed to EMF base station [22], this study supports our obtained results. A study by [23] on Syrian Hamsters showed that cell phone radiations might be responsible for decrease in plasma cholesterol and triglycerides concentration in rodents for long term. In our study, there was decreased protein concentration in chick embryo tissues. One of the study also showed that there was decrease in total protein concentration in Swiss albino mice after exposed to 10 GHz microwaves [24]. Exposure to ELF-EMF decreases the total cholesterol of the liver in rats [25]. A study on effects of exposure of alternating magnetic field on rats concluded that there was decrease in level of total cholesterol in blood plasma of rats and showed that magnetic field might affect on hormonal system and slowed down metabolism [26]. [27] demonstrated that total cholesterol and triacylglycerols levels had been reduced in rats due to total body exposure to radiations. It had been found that EMF radiations might have effects on cholesterol in the biological membranes and it might have significant consequences for the structural and functional properties of cells [28]. Finally,

these all observations are consistent with an idea that, EMF radiations affects many biological systems by interacting with internal electrochemical environment of body and caused harmful as well as deleterious effects.

It had been concluded that EMF exposure from cell phone on chick embryos might increase mortality rate in chick embryos during incubation as well as it might be responsible for reduced level of cholesterol and protein in chick embryos. The alteration in concentration of cholesterol and protein suggest that there might be changes in metabolism. It would be suggested that use of cell phones during pregnancy should be minimized as it could affect the developing foetus.

Acknowledgements

References

[1] Henry Lai., Genetic Effects of Non-ionizing Electromagnetic Fields "International Workshop on Biological Effects of Ionizing Radiation, Electromagnetic Fields and Chemical Toxic Agents" in Sinaia, Romania, October 2-6, 2001.

[2] Kovvali, G. Cellphones are as carcinogenic as coffee. Journal of Carcinogenesis;10(1):18, 2011.

[3] Zenon Sienkiewicz., Biological effects of electromagnetic fields. POWER ENGINEERING JOURNAL, pp 131-139, 1998.

[4] Lennart Hardell, Cindy Sage., Biological effects from electromagnetic field exposure and public exposure standards. Biomedicine & Pharmacotherapy, pp-1-6, 2008.

[5] W. Ross Adey., Biological Effects of Electromagnetic Fields. Journal of Cellular Biochemistry 51:410-416; 1993.

[6] Fatma Al-Qudsi and Solafa Azzouz., Effect of Electromagnetic Mobile Radiation on Chick Embryo Development. Life Science Journal, 2012; 9(2)).

[7] Kim J. Fernie, S. James Reynolds., The Effects Of Electromagnetic Fields From Power Lines On Avian Reproductive Biology And Physiology: A Review., Journal of Toxicology and Environmental Health, Part B, 8:127–140, 2005.

[8] Seyed Mohammad Mahdavi, Hedayat Sahraei, Parichehreh Yaghmaei and Hassan Tavakoli. Effects of Electromagnetic Radiation Exposure on Stress-Related Behaviors and Stress Hormones in Male *Wistar* Rats. Biomol Ther 22(6), pp 570-576, 2014

[9] Alireza Lotfi, Habib Aghdam Shahryar, Jalil Dolgari Sharaf And Alireza Ashraafi., Effects of Exposure to 50 Hz, 0.5 mT Electromagnetic Fields during Incubation on Whole Body and Internal Organs Weight in Broiler Chicks. INTERNATIONAL JOURNAL OF AGRICULTURE & BIOLOGY; *Vol. 13, No. 6, 2011.*

[10] Maryam Shams Lahjini & Mahmoud Ghafoori., Teratogenic effects of sinusoidal extremely low frequency electromagnetic field on morphology of 24 hr chick embryo. Indian Journal of Experimental Biology, Vol.38, 2000, pp. 692-699.

[11] Miguel López-Soler, Olga Roda-Murillo, Mª Teresa Pascual Morenilla, Miguel Guirao Piñeyro, Indalecio Sanchez-Montesinos, José A. Roda Moreno. Development disorders and increased mortality in chick embryos exposed to electromagnetic fields of 10µT and 30 Hz. European Journal of Anatomy, 13 (2): 2009, pp. 67-69.

[12] Parivar, K., Kouchesfehani, M.H., Boojar, M.M., and Hayati, R.N., Organ culture studies on the development of mouse embryo limb buds under EMF influence; International Journal of Radiation Biology; 82 (7): 455-464, 2006.

[13] O Zeni, M B Lioi, A D'Alisa, M Sorrentino, F. Salvemini., Combined exposure to extremely low frequency (ELF) magnetic fields and chemical mutagens: Lack of genotoxic effects in human lymphocytes. Electro-and Magnetobiology., Vol. 20, issue 3, 2001.

[14] C. Andrew L. Bassett., Beneficial Effects of Electromagnetic Fields., Journal of Cellular Biochemistry 51, 1993, pp. 387-393.

[15] Kalaivani Ganesan, Akelayil Chandrapuram Gengadharan, Chidambaram Balachandran, Bhakthavatsalam Murali Manohar, Rengarajulu Puvanakrishnan., Low frequency pulsed electromagnetic field – A viable alternative therapy for arthritis., Indian journal of experimental biology., Vol. 47, 2009, pp. 939-948.

[16] M. Natalia Vergara, M. Valeria Canto-Soler., Rediscovering the chick embryo as a model to study retinal development. Neural Development, 2012, pp. 7-22.

[17] Kristin H. Kain, James W.I. Miller, Celestial R. Jones- Paris, Rebecca T. Thomason, John D. Lewis, David M. Bader, Joey V. Barnett, Andries Zijlstra. The chick embryo as an expanding experimental model for cancer and cardiovascular research. Dev Dyn. 243(2): 2014, pp. 216- 228.

[18] M.G. Davey a C. Tickle b. The chicken as a model for embryonic development., Cytogenet Genome Res 117: 2007, pp. 231–239,.

[19] Grzegorz Redlarski, Bogdan Lewczuk, Arkadiusz gak, Andrzej Koncicki, Marek Krawczuk, Janusz Piechocki, Kazimierz Jakubiuk, Piotr Tojza, Jacek Jaworski, Dominik Ambroziak, Aukasz Skarbek, DawidGradolewski. The Influence of Electromagnetic Pollution on Living Organisms: Historical Trends and Forecasting Changes. BioMed Research International; Volume 2015, Article ID 234098, pp. 1-18.

[20] Awn B. Rifai, Majed A. Hakami. Health Hazards of Electromagnetic Radiations. Journal of Biosciences and Medicines, (2), 2014. pp-1-12.

[21] S Sivani, D Sudarsanam. Impacts of radio-frequency electromagnetic field (RF-EMF) from cell phone towers and wireless devices on biosystem and ecosystem – a review. Biology and Medicine, 4 (4), 2012, pp. 202-216.

[22] AC Achudume, B Onibere, F Aina. Bioeffects of electromagnetic base station on glutathione reductase, lipid peroxidation and total cholesterol in different tissues of *Wistar* rats. Biology and Medicine, 1 (3): 2009, pp. 33-38.

[23] Alireza Lotfi and Habib Aghdam Shahryar., Effects of 900 MHz Electromagnetic Fields Emitted by Cellular Phone on Total Cholesterol and Triglyceride Levels of Plasma in Syrian Hamsters (*mesocricetus auratus*). Journal of Applied Biological Sciences 3(2), 2009, pp. 93-96.

[24] Faiza Rifat, Virender Kumar Saxena, Preeti Srivastava, Archana Sharma Rashmi Sisodia. Effects of 10 GHz MW exposure on hematological changes in Swiss albino mice and their modulation by Prunus domestica fruit extract. International Journal of Advanced Research, Volume 2, Issue 2, 2014, pp. 386-397.

[25] Patricia V Torres-Duran, Aldo Ferreira-Hermosillo, Marco A Juarez-Oropeza, David Elias-Viñas and Leticia Verdugo-Diaz. Effects of whole body exposure to extremely low frequency electromagnetic fields (ELF-EMF) on serum and liver lipid levels, in the rat. Lipids in Health and Disease, 2007, 6: 31.

[26] Isıl Öcal, Tunaya Kalkan and Ðsmail Günay. Effects of Alternating Magnetic Field on the Metabolism of the Healthy and Diabetic Organisms. Brazilian Archives of Biology and Technology: An International Journal. Vol. 51, no.3: 2008, pp. 523-530.

[27] CR Nwokocha1, MI Nwokocha, PPE Mounmbegna, DU Owu1, O Onyezuligbo, EH Olu-Osifo, E Okojie, E Asuquo, K Thaxter, C Ogunsalu. Serum Lipids, Proteins and Electrolyte Profiles in Rats Following Total Body Irradiation. West Indian med. journal, vol.61, no.2, 2012, pp. 117-121.

[28] Yurekli, Al. Ozkan, M., Kalkan, T., Saybasili, H. GSM base station electromagnetic radiation and oxidative stress in rats. Electromagnetic Biology and Medicine 25: 2006, pp. 177-188.

Studies on characterization and antifungal activity of plant growth promoting rhizobacteria isolated from semiarid soil against plant fungal pathogens.

S. S. Khandare, P. D. Bhoge, M. G. Ingale Dept. of Microbiology, Bajaj College of

Science, Wardha. 442001. :: ksuhas21@gmail.com

Abstract

Aim: Changes in global temperature leads to severe drought conditions that may hamper food production in some countries in arid and semiarid regions of the world. The chemical fungicides are toxic for soil health. This study deals with characterization and antifungal activity of plant growth promoting rhizobacteria (PGPR) from rhizosphere of wheat grown under semiarid soil (15.80% moisture).

Methodology: Out of 45 isolates, most potent PGPR were isolated, identified and studied for their different plant growth promoting traits. Isolates evaluated for antifungal activity against plant pathogenic fungi and zone of inhibition (ZOI) was taken as an indicator of antifungal property. PGPR were studied for the effect on seed germination of wheat.

Results: Among the five PGPR isolates *Pseudomonas fluorescens* was most potent antagonist with 35 mm of ZOI against *Aspergillus niger,* demonstrated maximum phosphate solubilization with phosphate solublization index 4.09, as well as showed highest rate of seed germination (80 %) compared to other PGPR. *Pseudomonas fluorescens* was found to be strong cyanide producing strain.

Keywords: Antifungal activity, Characterization, PGPR, Plant pathogenic fungi.

Introduction:

One of the foremost agricultural issues reducing crop yield is drought stress in arid and dry regions of the globe Changes in world air temperature are resulting in longer drought periods and a lot of severe drought conditions can hinder food production in some countries (Lau *et al*., 2012). Current methods to increase the ability of plants to tolerate drought stress involve the use of water-saving irrigation and genetic engineering of drought-tolerant transgenic plants. Sadly, the ways are effortful and highly technical and thus troublesome to apply in practice. Several plant growth promoting rhizobacteria (PGPR) are shown to boost drought stress effects in plants by reducing plant ethylene levels that are sometimes raised by unfavorable conditions (Arshad *et al*., 2008). Thus one alternative for growing plants beneath dry conditions is the use of PGPR. The rhizosphere is the slime zone of soil specifically influenced by the root system which provides an expensive supply of energy and nutrients for bacterium (Dobbelaere *et al*., 2003; Gray *et al*., 2005). The rhizosphere is inhabited by a diverse range of microorganisms and the bacteria colonizing this habitat are called rhizobacteria (Schroth *et al*., 1982).PGPR are a part of rhizobacterial community and occupy as much as 2 to 5% of total rhizobacterial population constituting a cardinal part of rhizosphere biota (Kevin-Vessey *et al*., 2003). Microorganisms are vital for agriculture in order to promote the circulation of plant nutrients and reduce the necessity of chemical fertilizers. The use of fertilizers, including chemical fertilizers and manures, to reinforce soil fertility and crop productivity has usually negatively affected the complex system of the biogeochemical cycles (Perrott *et al*., 1992; Steinshamn *et al*., 2004). PGPR affect plant growth in two different ways, indirectly or directly. The direct promotion of plant growth by PGPR entails either providing the plant with a compound that is synthesized by the bacterium, for example phytohormones, or facilitating the uptake of certain nutrients from the environment (Glick *et al*., 1995). The indirect promotion of plant growth occurs once PGPR reduce or forestall the harmful effects of one or more phytopathogenic organisms. This can

happen by manufacturing antagonistic substances or by inducing resistance to pathogens. Wheat *(Tritium aestivum L.)* is one in all the foremost cereal crop in India and worldwide. The quality of the nutritional components of this major cereal crop is of particular concern to producers and consumers throughout the globe (Walia *et al*.,2013). One of the main causative fungal diseases of wheat is *Fusarium graminearum* (Murray *et al*.,2009). The fungus, in addition to seedling blight and *Fusarium* head blight, causes different seed and soil-borne diseases of seedlings. Moreover, the pathogen also produces mycotoxins including trichothecenes such as deoxynivalenol (DON) which is potent inhibitor of eukaryotic protein biosynthesis and has involved in a number of human and animal mycotoxicoses (Obanora *et al*., 2013). Therefore, even low levels of these toxins in raw grain can make them unsuitable for human or animal consumption. Aspergillus spp. is storage mold responsible for production of aflatoxin (Hassan *et al*., 2009), Aspergillus flavus is a saprophytic soil fungus that infect and contaminates pre-harvest and post-harvest seed crops with the carcinogenic secondary metabolites aflatoxin (Amaike*et al*., 2011). In this work, we provide information on the isolation and identification of bacteria from the rhizospheric semiarid soil of wheat with potential to produce PGPR traits and antagonistic activity against *Aspergillus niger, Aspergillus flavus, Aspergillus glaucus, Aspergillus terreus, Fusarium oxysporum* and *Cladosporium*. The PGPR have the potential to be used in the biological control of these fungi and hence can be used as biofertilizers as well as biocontrol agent.

Materials and methods:
Collection of sample
Root samples of wheat (*Triticum aestivum*) plant from the semiarid soil (15.80% soil moisture) of Jamni region of Wardha district, Maharashtra during month of December, collected and placed in sterile plastic bag, stored at 4ºC in Laboratory of PG Department of Microbiology, Bajaj College of Science, Wardha for further analysis.

Isolation and Identification of Rhizobacteria:
The rhizosphere soil samples were processed within 24 hr for isolation of PGPR. Samples were serially diluted with sterile distilled water (10^{-1} to 10^{-7}) and each dilution was plated on peptone yeast extract dextrose agar, Pseudomonas isolation agar, King's B agar, Serratia differential medium, Jensen's medium and Nutrient agar respectively. After incubation for 24 h at 37°C, colonies were picked and maintained as pure cultures in nutrient agar slants with periodic transfer to fresh media (Aneja *et al*., 2001). The identification of isolates were done by cultural, morphological and biochemical characterization as described in Bergey's Manual of Systematic Bacteriology (Tein *et al*., 1979). Isolates were also evaluated for production of various enzymes like catalase, gelatinase, oxidase and amylase by using standard procedures. (Hsu *et al*., 1975; Berlemont *et al*., 1975).

Characterization of isolates for PGPR traits
Siderophore production
Siderophore production was determined on Chrome azurol S agar (CAS) by the method given by Schwyn and Neilands (1987). CAS agar plate divided into equal sectors and spot inoculated with PGPR isolates and incubated at 28^{0}C to 30^{0}C. Development of orange halos around the colonies indicates positive siderophore production (Schwyn *et al*., 1987).

Hydrogen Cyanide production (HCN)
Isolates were cultured on Nutrient agar medium supplemented with glycine (4 g l^{-1}). The production of HCN was detected after 48 hr by using whatman filter paper no. 1 soaked in 2 % sodium carbonate and 0.5% picric acid, fixed to the underside of the petri-dish lid which was sealed with parafilm before incubation at 28^{0}C to 30^{0}C. A change from yellow to orange, red, brown, or reddish brown was recorded as an indication of weak, moderate, or strongly cyanogenic potential, respectively (Lorck *et al*., 1948).

Assay for Indole acetic acid (IAA) Production

The isolates were freshly grown on their respective growth medium amended with tryptophan (500 μg/ ml) at 30^0C for 48 h. fully grown cultures were centrifuged at 8000 rpm for 10 min and were assayed for qualitative detection of IAA. 2 ml of supernatant of each isolate was mixed with two drops of orthophosphoric acid and 4 ml of salkowski reagent (1 ml of 0.5M $FeCl_3$ in 50 ml of 35 % $HClO_4$). Formation of pink colour indicates IAA production (Brick *et al*., 1991).

Production of Ammonia

The isolates were tested for the production of ammonia by inoculating in 10 ml peptone broth and incubated for 24 h at 30^0C. The test was performed by adding 0.5 ml of Nessler's reagent (Himedia) in tube. Development of brown to yellow colour was a positive test for ammonia production (Cappuccino *et al*., 1992).

Phosphate solubilization activity and Phosphate solubilizing index

For the study of phosphate solubilizing ability, the isolates were first screened on Pikovaskaya's agar for solubilization of insoluble inorganic phosphate. Cultures were inoculated on center of agar plate under aseptic condition. Plates were incubated for 3 days at 30°C. Presence of clear zone (halo zone) around the colony indicates presence of phosphate solubilization ability. Phosphate solubilization index was calculated by measuring the colony diameter and the halo zone diameter by using following formula.

Phosphate Solubilization Index (SI) = (colony diameter + clearing zone) / colony diameter (Karpagam*et al*., 2014).

Heavy metal tolerance

The isolates were studied for its heavy metal tolerance potential on Muller-Hinton agar supplemented with varying concentrations of four heavy metals Cu, Hg, Zn, Pb. Plates were incubated at 37°C for 24 hr to allow diffusion of the metal into the agar, after incubation the plates were observed for the growth of isolate (Hassen *et al*.1998).

Effect on Seed Germination

To evaluate the plant growth promoting efficiency of PGPR isolates, their *invitro* effect was observed on wheat seeds. Pot culture experiment was conducted to study seed germination efficiency for a period of 10 days. Twenty wheat seeds were surface-sterilized with $HgCl_2$ (0.1%) and successively washed several times with sterilized water. Then seeds were soaked overnight with culture of rhizobacterial isolates. Wheat seeds not soaked in PGPR isolates were used as control. Then all the seeds were sown in six separate plastic pots and filled with autoclaved soil. Pots sowed with inoculated seeds were labeled as experimental and pots sowed with un inoculated seeds were labeled as control. Pots were incubated for 10 days at 37° C. Then these six pots were observed for germination of seeds after regular interval of time (Noshin *et al*., 2010).

Antifungal activity of PGPR isolates against plant pathogenic fungi

All the PGPR isolates were screened for antagonistic activity against six plant pathogenic fungi viz; *Aspergillus flavus, Aspergillus niger, Aspergillus terreus, Aspergillus glaucus, Cladosporium* and *Fusarium oxysporum* by using agar diffusion assay. These fungi cultures were obtained from the P. G. Department of Botany, J.B. College of Science, Wardha and stored for the further experimental use at 4ºC. For the evaluation of antifungal activity, broth cultures of PGPR isolates were made and culture broth was centrifuged at 8000 rpm for 15 min. Czapek Dox agar medium was used to study the antifungal assay. After solidification of the medium, 0.01ml of each fungal broth culture was spread on the respective plates in uniform manner. Then by using the sterile borer, wells were prepared in each plate and 20 μl of supernatant of each PGPR isolates were added in each well and plates were incubated for 4-5 d at 30ºC. Amphotericin- B (AMB) was used as positive control. Inhibition of fungal mycelium around the well was noted as positive test and zone of inhibition was measured.

Cell wall degrading enzyme production:
Chitinase activity:
A minimal salt medium containing colloidal chitin as sole carbon and energy source was used. The medium consisted of Na2HPO$_4$ - 6 g, KH2PO$_4$ - 3.0 g, NH4Cl -1 g, NaCl- 0.5 g, yeast extract - 0.0 5 g, colloidal chitin -1.0 % (w/v), agar-15 g and distilled water-1000 ml and incubated at 30ºC. Colonies showing zones of clearance against the creamy background were recorded as chitinase producing PGPR (Hsu *et al*., 1975).

Cellulase activity:
A preliminary qualitative analysis for cellulolytic activity was conducted by using Congo red dye. The PGPR isolates were grown on Carboxy Methyl Cellulose agar (CMC) containing (g l-1) KH2PO$_4$ -1.0, MgSO$_4$.7H2O -0.5, NaCl -0.5, FeSO$_4$.7H2O - 0.01, MnSO$_4$.H2O - 0.01, NH$_4$NO$_3$ -0.3, CMC-10.0, Agar-12.0. The pH was adjusted to 7.0 with 1 M NaOH. The CMC agar plates were incubated at 37°C for 5 d to allow the secretion of cellulase. At the end of the incubation, to visualize the hydrolysis zone, the agar medium was flooded with an aqueous solution of congo red (1% w/v) for 15 min. The Congo red solution was then poured off, and the plates were further treated by flooding with 1 M NaCl for 15 min. Clear zone around the colony was indicative of cellulase enzyme production (Berlemont *et al*., 1975).

Results and Discussion
The rhizosphere of wheat plants fully grown underneath semi-arid soil (15.80% soil moisture) was tested to explore the diversity of plant growth promoting rhizobacteria. A total of 45 PGPR bacteria were isolated from the rhizosphere soil of the wheat plant. Five best potential bacterial isolates showing PGPR traits and demonstrating antifungal activities were selected for characterization. The isolates were identified as *Bacillus* spp.1, *Bacillus* spp. 2, *Azotobacter* spp., *Serratia marcescens* and *Pseudomonas fluorescens*. Among five isolates three were gram negative and two were gram positive and all were motile. *Bacillus* spp., *Azotobacter* spp. and *Serratia marcescens* were found to ferment glucose and sucrose with production of acid and gas. Only *Azotobacter* spp. could found to ferment lactose. Both *Azotobacter* spp. and *Serratia marcescens* were found to ferment mannitol also. *Bacillus* spp. 2 and *Pseudomonas fluorescens* did not found to ferment any sugar. The isolates were also found to produce catalase, oxidase, amylase, gelatinase, cellulase and chitinase enzymes. The results of morphological and biochemical characterization are depicted in Table 1. The isolates showed varied levels of PGPR traits such as siderophore production, phosphate solubilization, IAA, ammonia and HCN production. All PGPR bacterial isolates were found to produce indole-3-acetic acid (IAA), exerted ability for phosphate solubilization on the Pikovskaya medium with different efficacy. The maximum phosphate solubilization was found in *Pseudomonas fluorescens* with phosphate solubilization index 4.09. Less phosphate solubilizing activity was found in *Serratia marcescens* with phosphate solubilization index 3.1 (table 4). The production of ammonia and hydrogen cyanide observed in all the five isolates. Moderate cyanide production was observed in *Bacillus* spp., *Azotobacter* spp. And *Serratia marcescens* while *Pseudomonas fluorescens* were recorded as strong cyanide producing strain with brown colour of filter paper. In the present study all the bacterial isolates exhibited siderophore production on CAS medium. CAS assay is the universal assay for detection of siderophores. The principle of this assay is based on a color change of CAS from blue to orange resulting from siderophoral removal of Fe from the chrome azurol dye. Isolates were tested for their heavy metal tolerance ability. All the isolates were found to tolerate Cu, Zn and Pb at varying concentrations. *Bacillus spp.2* and *Azotobacter were* the only isolates that could tolerate Hg while rest of the isolates found to be very sensitive against Hg (Table 5). The important aspect of this investigation was to study the effect of PGPR isolates on seed germination of wheat plant *in vitro*. Our experiments showed that PGPR inoculation significantly enhanced seed germination of wheat over control. However, the speed of enhancement varied with bacterial strains. The results also indicate that the PGPR

strains initiate the germination of wheat seeds at the 3rd day of treatment connecting to active participation in germination system. The highest seedling height (18 ± 1.4 cm) was observed in seeds treated with *Pseudomonas fluorescens* then *S. marcescens* (14 ± 1.3) followed by *Azotobacter* spp. (13 ± 1.0), *Bacillus* spp.2 (10 ± 1.4) and *Bacillus* spp.1 (10 ± 1.5) after 7 d treatment as compared to 9 cm in control. These results were analyzed statistically by using Microsoft Excel tool and are depicted in Table 2. Similar experiment was done by Fatima *et al.,* (2009) supports our investigation. They reported the isolation of 3 PGPR strains ie. WPR-51, WPR-42 and WM-30 belonging to *Azotobacter* and *Azospirillum* from rhizosphere of wheat. These strains positively affected the germination of wheat as well as increased biomass and root shoot length when tested in pot experiments. Maximum root length was observed due to WPR-51 treatment (26.6 cm/plant) and mixture of three isolates (27.8 cm/plant). While shoot length was vice versa. A length of 39.4 cm per plant was observed due to treatment of WPR-51 while due to mixture shoot length was 36.1 cm plant. The WPR-42 and WM-3 treatments were not found so effective to increase root and shoot length as compared to control. The Rhizobacteria were screened for antifungal activity against *Aspergillus flavus, Aspergillus niger, Aspergillust erreus, Aspergillus glaucus, Cladosporium* and *Fusarium oxysporum* and zone of inhibition was taken as an indicator of antifungal property. On Czapek Dox agar medium all the five isolates were found to inhibit the growth of all plant pathogenic fungi. Among the six pathogens, *Aspergillus niger* was found to be most sensitive against PGPR isolates. *Pseudomonas fluorescens* was found to be most efficient antagonist against plant pathogenic fungi and showed zone of inhibition of 35 mm, 27 mm, 25 mm, 23 mm, 22 mm and 19 mm against *Aspergillus niger*, *Cladosporium*, *Fusarium, Aspergillus flavus*, *Aspergillus glaucus* and *Aspergillus terreus* respectively. Among the tested plant pathogenic fungi, highest antifungal activity of all the PGPR isolates was found to be against *Aspergillus niger* while *Aspergillus terreus* was found to be less sensitive plant pathogen against all the PGPR isolates. From this study it was found that *Pseudomonas fluorescens* was the most efficient plant growth promoting rhizobacteria and also the potent antagonist for plant pathogenic fungi. The detailed results of antifungal activity are depicted in table 3.

Conclusion

Present investigation elucidates the multifarious role of PGPR isolate *Pseudomonas fluorescens* obtained from semiarid soil of wheat rhizosphere, was found to exhibit different plant growth promoting traits which may be useful to promote the plant growth. The isolate demonstrated antifungal activity that may be useful in formulating new inoculants with combinations of different mechanisms of action, leading to a more efficient use for biocontrol of plant pathogenic fungi. This is efficient approach to replace chemical fertilizers and pesticides for sustainable agriculture. In view of these, PGPR as a biofertilizer and biocontrol agent could provide a means for reducing the plant disease incidences in addition to avoiding the use of chemical fertilizers and fungicides.

Table 1: Biochemical characterization and PGPR traits of isolates (+ means positive, - means negative)

Tests	*Bacillus* spp.1	*Bacillus* spp.2	*Azotobacter*	*S. marcescens*	*P. fluorescens*
Grams Reaction	+	+	-	-	-
Motility	Motile	Motile	Motile	Motile	Motile
Glucose fermentation	+	-	+	+	-
Sucrose fermentation	+	-	+	+	-
Lactose fermentation	-	-	+	-	-

Mannitol fermentation	-	-	+	+	-
H$_2$S Production	+	+	+	+	+
Indole test	-	-	+	-	-
Methyl red	+	+	+	+	+
Voges Proskaur test	-	-	+	-	+
Citrate test	+	+	+	+	+
Catalase	+	+	+	+	+
Oxidase	-	+	+	+	+
Amylase	-	+	+	+	-
Gelatinase	+	-	+	-	+
Cellulase	+	+	-	+	+
Chitinase	+	+	+	+	+
Ammonia	+	+	+	+	+
Siderophore	+	+	+	+	+
HCN	+	+	+	+	+
Phosphate solublization	+	+	+	+	+

Table 2: Effect of PGPR isolates on Seed Germination (Mean and Std. Error)

Pots no.	No. of Wheat seed Germinated out of 20	Wheat seeds soaked into	Length of the shoots measured in (cm)		
			3rd day	5th day	7th day
1	8	Control	1.2 ± 0.24	4 ± 0.26	9.3 ± 0.25
2	11	*Bacillus* spp.1	1.7 ± 0.22	5 ± 0.15	10 ± 1.5
3	9	*Bacillus* spp.2	1 ± 0.10	5.3 ± 0.29	10 ± 1.4
4	10	*Azotobacter* spp.	1.6 ± 0.21	5.6 ± 0.18	13 ± 1.0
5	11	Serratia marcescens.	2 ± 0.09	4.4 ± 0.20	14 ± 1.3
6	16	*Pseudomonas fluorescens*	3.6 ± 0.23	12 ± 1.3	18 ± 1.4

Table 3: Antifungal activity of PGPR isolates.

Fungi used	Zone of Inhibition (in mm)					
	AMB	*Bacillus* spp.1	*Bacillus* Spp.2	*Azotobacter*	*Serratia marcescens*	*Pseudomonas fluorescens*
Aspergillus flavus	11	12	11	14	16	23
Aspergillus niger	13	18	21	14	15	35
Aspergillus terreus	10	11	11	12	12	19
Aspergillus glaucus	12	12	11	12	11	22
Cladosporium	14	12	17	16	14	27
Fusarium oxysporum	18	13	11	12	13	25

Table 4: Phosphate solubilizing index of PGPR isolates.

Isolates	Days					
	1	**2**	**3**	**4**	**5**	**6**
	Phosphate solubilizing index					
Bacillus spp. 1	2.22	2.2	2.4	2.6	3	3.2
Bacillus spp. 2	2.5	2.5	3	3.3	3.7	3.8
Azotobacter	2.11	2.6	3	3.2	3.7	3.8
S. marcescens	2.25	2.33	2.4	2.6	2.69	3.1
P. fluorescens	2.5	3.0	3.8	3.9	4	4.09

Table 5: Heavy metal tolerance of PGPR isolates

Isolates	Heavy metals (mg/ml)			
	Cu	Hg	Zn	Pb
Bacillus spp.1	200	-	200	200
Bacillus spp.2	400	200	600	600
Azotobacter spp.	1000	200	1000	1000
S. marcescens	1000	-	1000	1000
P. fluorescens	600	-	400	400

References
1.   Amaike, S. and N. Keller: Aspergillus flavus. *Annual review of phytopathology*., 49, 107-133 (2011).
2.   Aneja, K.R.:Experiments in microbiology plant pathology tissue culture and Mushroom production technology, 3rd edn. *New Age International Publishers*.192 -195 (2001).
3.   Arshad, M. Shaharoona B. and Mahmood T: Inoculation with *Pseudomonas* spp. containing ACC-deaminase partially eliminates the effects of   drought stress on growth, yield, and ripening of pea (*Pisum sativum* L.). *Pedosphere.,* 18, 611–620 (2008).
4.   Berlemont, R., M. Delsaute, D. Pipers, S. D'amico, G. Feller, M. Galleni and P. Power: Insights into bacterial cellulose biosynthesis by functional metagenomics on Antarctica soil samples. *ISME J.,* 3, 1070-1081 (2009).
5.   Brick, J.M., R.M. Bostock and S. E. Silverstone: Rapid in situ assay for indole acetic acid production by bacteria immobilized on nitrocellulose membrane. *Appl Environ Microbiol.*, 57, 535–538 (1991).
6.   Cappuccino, J.C. and N. Sherman: In: *Microbiology: A Laboratory Manual*, New York. 125–179 (1992).
7.   Dobbelaere, S., J. Vanderleyden and Y. Okon: Plant growth promoting effects of diazotrophs in the rhizosphere. *CRC Crit Rev Plant Sci.,* 22, 107-149 (2003).
8.   Fatima, Z., M. Saleemi, M. Zia, T. Sultan, M. Gill and F. Chaudhary: Antifungal activity of plant growth-promoting rhizobacteria isolates against Rhizoctonia solani in wheat. *Afr. J. Biotechnol.,*8, 219-225(2009).
9.   Glick, B.R.: The enhancement of plant growth by free-living bacteria. *Can J Microbiol.,* 41, 109-117 (1995).
10.   Gray, E.J. and D.L. Smith: Intracellular and extracellular PGPR: Commonalities and distinctions in the plant-bacterium signaling processes. *Soil Biol Biochem.*, 37, 395-412 (2005)

11.   Hassan, A: Production of aflatoxins by Aspergillus flavus and Aspergillus niger strains isolated from seeds of pulses. *J. Food, Agric. Environ.,* 7, 33-39. (2009).

12.   Hassen, A., N. Saidi, M. Cherifh and A. Boudabous: Effects of heavy metals on Pseudomonas aeruginosa and Bacillus thuringiensis. *BioresourTechnol.,* 65, 73-82 (1998).

13.   Hsu, S.C. and J.L. Lockwood: Powdered chitin agar as selective medium for enumeration of actinomycetes in water and soil. *Appl. Microbiol.,* 29, 422-426 (1975).

14.   Karpagam, T and P. Nagalakshmi: Isolation and characterization of Phosphate Solubilizing Microbes from Agricultural soil. *Int.J.Curr.Microbiol.App.Sci*., 3, 601-614 (2014).

15.   Kevin-Vessey, J.: Plant growth promoting rhizobacteria as biofertilizers. *Plant Soil.,*255, 571-586 (2003).

16.   Lau, J. A. and J. T. Lennon: Rapid responses of soil microorganisms improve plant fitness in novel environments. *Proc. Natl. Acad. Sci. U.S.A.,* 109, 14058–14062. (2012).

17.   Lorck, H.: Production of hydrocyanic acid by bacteria. *Physiol. Plant.,* 1, 142-146 (1948).

18.   Murray, G. and J. Brennan: Estimating disease losses to the Australian wheat industry. *Australas. Plant Pathol*., 38, 558–570 (2009).

19.   Noshin, I. and A. Bano: Azospirillum strain s isolated from roots and rhizosphere soil of wheat grown under different soil moisture conditions. *Biol Fertilsoils*., 46, 393-406 (2010).

20.   Obanora, F., S. Neateb, S. Simpfendorferc, R. Sabburga, P. Wilsond and S. Chakrabortya: Fusarium graminearum and Fusarium pseudograminearum caused the 2010 head blight epidemics in Australia. *Plant Pathol*., 62, 79–91(2013).

21.   Perrott, K.W., S.U Sarathchandra and B.W. Dow: Seasonal and fertilizer effects on the organic cycle and microbial biomass in a hill country soil under pasture. *AUST J SOIL RES.,* 30, 383-394 (1992).

22.   Schroth, M. N. and J.G. Hancock: Disease-suppressive soil and root-colonizing bacteria. *Science.,*216, 1376-1381 (1982).

23.   Schwyn, B., and J.B. Neilands: Universal chemical assay for detection and determination of siderophores. *Anal Biochem.,*160, 47-56 (1987).

24.   Steinshamn, H., E. Thuen, M.A. Bleken, U.T. Brenoe, G. Ekerholt and C. Yri: Utilization of nitrogen (N) and phosphorus (P) in an organic dairy farming system in Norway. *AGR ECOSYST ENVIRON*, 104, 509-522 (2004).

25.   Tein, T.M., M.H Gaskins and D.H. Hubbell: Plant growth substances produced by *Azospirillum brasilense* and their effect on the growth of pearl millet (*Pennisetum americanum* L.). *Appl. Environ. Microbiol.,*37, 1016 – 1024 (1979).

26.   Walia, A., P. Mehta, A. Chauhan and C.K. Shirkot: Antagonistic Activity of Plant Growth Promoting Rhizobacteria Isolated from Tomato Rhizosphere Against Soil Borne Fungal Plant Pathogen. *IJAEB*., 6, 571-580 (2013).

FULL PAPER

In vitro Binding Interaction of Isoxazoline Derivative with BSA: Equilibrium, FT-IR, Acoustical and Molecular Modeling Study

Ajay Madhukarrao Pisudde, Pradip Vitthalrao Tekade[*], Shrikant Bandupant Thakare

Department of Chemistry, Jankidevi Bajaj College of Science, Jamnalal Bajaj Marg, Civil Lines, Wardha-442001, M. S., India.

Abstract:

The present study showed the binding interaction of 2-(4,5-Dihydro-1,2-oxazol-5-yl)-phenol-*N*-methylaniline (2DHOPNA) with BSA in 1,4-dioxane, DMSO and DMF by equilibrium dialysis, FT-IR, acoustical at physiological pH and its molecular modeling study. Findings were interpreted by scatchard plot which showed an increase in association constants with increasing temperature and concentrations of the 2DHOPNA. It is seen that, the binding supposed to be more significant in 1,4-dioxane than DMSO and DMF. Thermodynamic parameters are also determined for the binding interaction of 2DHOPNA with BSA. Values of Gibb's free energy (ΔG), enthalpy (ΔH) and entropy (ΔS) were calculated by using van't Hoff equation. The positive values of ΔH and ΔS showed exothermic interaction between 2DHOPNA and BSA. Similarly, negative ΔG showed the spontaneity of the binding process. ΔG becomes more negative with increase in temperature, indicated feasibility of the binding interaction at high temperature. Molecular modeling confirmed the binding interaction having energy of -210.13.
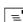
Keywords: Equilibrium dialysis; FT-IR; Scatchard analysis; association constants; BSA; thermodynamic parameters

1. Introduction

2-(4,5-Dihydro-1,2-oxazol-5-yl)-phenol-*N*-methylaniline (**1**, 2DHOPNA, Figure 1) is an important heterocyclic compounds shows various biological properties especially, herbicidal [1], antioxidant [2], antifungal [3], antibacterial [4], analgesic and antimicrobial [5] and anti-cancer properties [6]. Human serum albumin (HSA) is the most abundant protein in blood serum with the concentration of 0.63 mM. It is single polypeptide chain of 585 amino acids with a large helical triple domain structure that forms heart shaped molecule. Serum albumins are the most abundant proteins in the circulatory system of wide variety of organisms, being the major macromolecules contributing to the osmotic blood pressure [7]. A variation in temperature is found to be a key factor in binding affinities of HSA [8]. It is difficult to obtain HSA for experimental purposes. HSA and BSA exhibit similar chemical properties due to high percentage of sequence identities. BSA in lieu of HSA is used in this study because of low cost and easy availability. Various techniques are available to monitor the binding interactions of ligands to protein like U.V. visible absorbance [9], isothermal titration calorimetry [10], fluorescence [11], NMR [12], equilibrium and FT-IR spectroscopy [13]. These techniques are used to study the binding interaction of the various drugs with protein such as Phenformin [14], Ligustrazine [15], aspirin and vitamin C [16], Ciprofloxacin [17] and methotrexate [18]. Molecular modeling study is also an important aspect towards protein-drug interaction [19-20].

Present study proposed to evaluate the effect of ligand concentration, temperature, and polar/nonpolar solvent on binding interaction of 2DHOPNA with BSA at physiological pH. The study also involves the determination of

---
[*]Corresponding author. E-mail: ✉ pradiptekade@gmail.com

thermodynamic parameters like free energy, enthalpy, entropy and its molecular modeling.
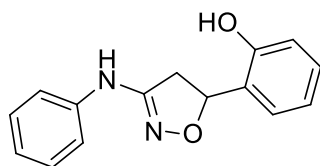
Figure 1. Structure of 2-(4, 5-Dihydro-1,2-oxazol-5-yl)-phenol-*N*-methylaniline (**1**, 2DHOPNA).

2. Results and Discussion

The binding interaction gives different absorbance values for BSA-2DHOPNA complexes in 1,4-dioxane, DMSO and DMF. The absorbance values for BSA-2DHOPNA complex solutions in 1,4-dioxane are 0.192, 0.227, 0.395, 0.412, 0.457 and 0.619 for the different concentrations of 2DHOPNA i.e. 1 mM, 1.5 mM, 2 mM, 2.5 mM, 3 mM and 3.5 mM respectively. Similarly, the absorbance values for BSA-2DHOPNA complexes in DMSO are 0.180, 0.191, 0.213, 0.325, 0.312, 0.497 and absorbance values in DMF are 0.162, 0.167, 0.198, 0.202, 0.258, 0.392 for the concentrations 1 mM, 1.5 mM, 2 mM, 2.5 mM, 3 mM and 3.5 mM, respectively. Figure 2 shows the graph of absorbance versus concentrations of 2DHOPNA in 1,4-dioxane, DMSO and DMF. Similarly, Figure 3 shows the graph for specific binding against concentrations of 2DHOPNA in 1,4-dioxane, DMSO and DMF. Figure 3 is the scatchard plot used to determine binding affinity of 2DHOPNA with BSA. The binding affinity of these complexes has been determined in terms of association constants. The association constants for BSA-2DHOPNA binding in 1,4-dioxane, DMSO and DMF are 0.6100, 0.5800, 0.5411, respectively. Table 1 gives the absorbances and specific binding for the interaction of 2DHOPNA with BSA in 1,4-dioxane, DMSO and DMF.

Table 1. Absorbance and specific binding values for BSA-2DHOPNA complex at different concentrations in 1,4-dioxane, DMSO and DMF.

Sr.No.	Concentra-tions of 2DHOPNA (mM)	BSA + 2DHOPNA in 1,4-dioxane		BSA + 2DHOPNA in DMSO		BSA + 2DHOPNA in DMF	
		Absorbance	Specific Binding	Absorbance	Specific Binding	Absorbance	Specific Binding
1	1	0.192	0.4752	0.180	0.4591	0.162	0.4331
2	1.5	0.227	0.5170	0.191	0.4739	0.167	0.4406
3	2	0.395	0.6507	0.213	0.4988	0.198	0.4829
4	2.5	0.412	0.6602	0.325	0.6052	0.202	0.4879
5	3	0.457	0.6831	0.312	0.5954	0.258	0.5489
6	3.5	0.619	0.7448	0.497	0.7009	0.392	0.6490
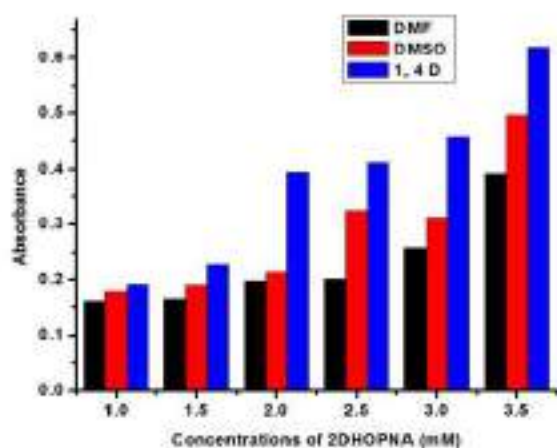
Figure 2. Graph of absorbance vs. conc. Of 2DHOPNA in 1,4-dioxane, DMSO and DMF.
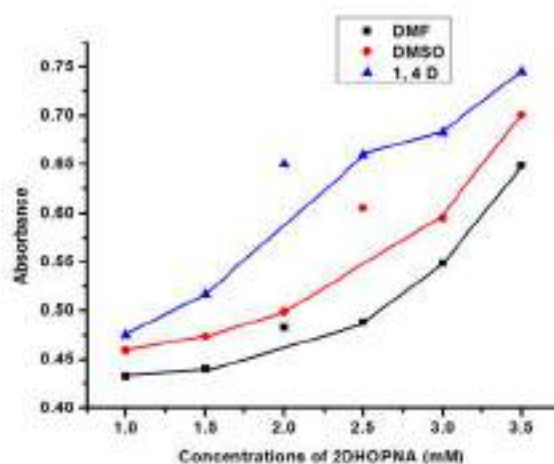
Figure 3. Graph of specific binding *vs.* conc. of 2DHOPNA in 1,4-dioxane, DMSO and DMF.

119

Orbital: Electron. J. Chem. 12 (3): 118-126, 2020

2.1 Effect of Arsenic and Mercury on Binding Interaction of 2DHOPNA with BSA

The effect of foreign particles viz. arsenic and mercury was studied on the binding interaction of 2DHOPNA with BSA. Different values of absorbance for BSA-2DHOPNA in 1,4-dioxane are obtained. Absorbances for BSA-2DHOPNA complex solutions in the presence of arsenic are 0.413, 0.427, 0.512, 0.601, 0.568 and 0.609 for different concentrations of 2DHOPNA 1 mM, 1.5 mM, 2 mM, 2.5 mM, 3 mM and 3.5 mM respectively. Similarly, the absorbances for complex solutions in the presence of mercury are 0.359, 0.359, 0.436, 0.493, 0.503 and 0.548 for the concentrations 1 mM, 1.5 mM, 2 mM, 2.5 mM, 3 mM and 3.5 mM, respectively. Figure 4 shows the graph of absorbance vs. concentrations of 2DHOPNA in 1,4-dioxane in presence of arsenic and mercury. Figure 5 shows the graph of specific binding against concentrations of 2DHOPNA in 1,4-dioxane in presence of arsenic and mercury. The scatchard plot gives the association constants for the interaction of 2DHOPNA with BSA. The association constants in presence of arsenic and mercury are 0.5943 and 0.5410 respectively. Table 2 gives the values of absorbance and specific binding for BSA-2DHOPNA complex in presence of arsenic and mercury.
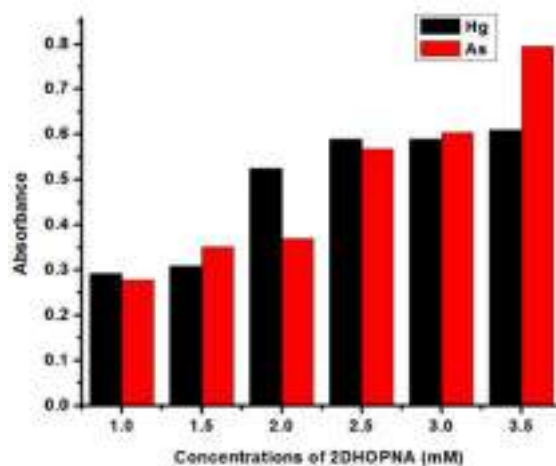
Figure 4. Graph of absorbance vs. conc. of 2DHOPNA in 1,4-dioxane in presence of arsenic and mercury.
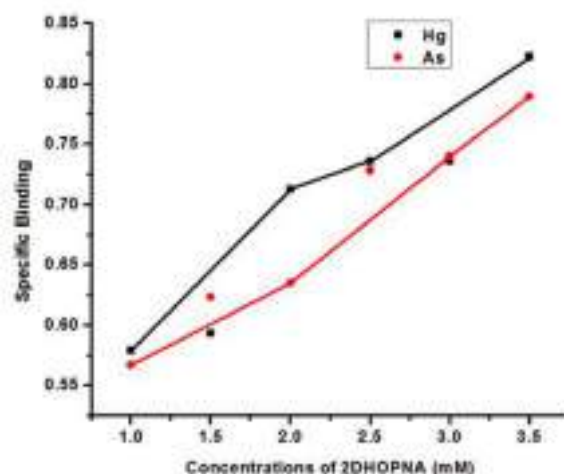
Figure 5. Graph of specific binding vs. conc. of 2DHOPNA in 1,4-dioxane in presence of arsenic and mercury.

Table 2. Absorbance and specific binding values for BSA-2DHOPNA complex in presence of arsenic and mercury at different concentrations of 2DHOPNA in 1,4-dioxane.

Sr.No.	Concentra-tions of 2DHOPNA (mM)	Hg + BSA+ 2DHOPNA in 1,4-dioxane		As + BSA+ 2DHOPNA in 1,4-dioxane	
		Absorbance	Specific Binding	Absorbance	Specific Binding
1	1	0.168	0.5000	0.212	0.4421
2	1.5	0.192	0.5479	0.257	0.4764
3	2	0.227	0.5867	0.301	0.5170
4	2.5	0.318	0.6524	0.398	0.6000
5	3	0.369	0.6547	0.402	0.6351
6	3.5	0.402	0.6886	0.469	0.6547

2.2 FT-IR Study

FT-IR spectroscopy analyzed the binding interaction of 2DHOPNA with BSA by the shifting in peak positions of amide bands in BSA. The amide I at 1635 cm^{-1} is due to C=O stretching and amide II at 1543 cm^{-1} is due to C-N stretch coupled with N-H bending. The changes in peak positions of these bands are observed on interaction of 2DHOPNA with BSA. It is seen that the peak position of amide I is shifted to greater extent, however, a very small change in the amide II has observed (Figures 6-8). Therefore, it is concluded that amide I band is more sensitive to

120

Orbital: Electron. J. Chem. 12 (3): 118-126, 2020

the changes of secondary structure of BSA than amide II. Figure 6 shows the changes in the peak positions of amide bands of BSA-2DHOPNA complex in 1,4-dioxane. Similarly, the shifting of amide bands in DMSO and DMF are shown in figure 7 and 8, respectively. In figures 6, 7 and 8, A shows spectrum of BSA and B, C, D, E, F, G shows the spectra of BSA-2DHOPNA complexes for the concentrations 1, 1.5, 2, 2.5, 3, 3.5 mM of 2DHOPNA respectively.
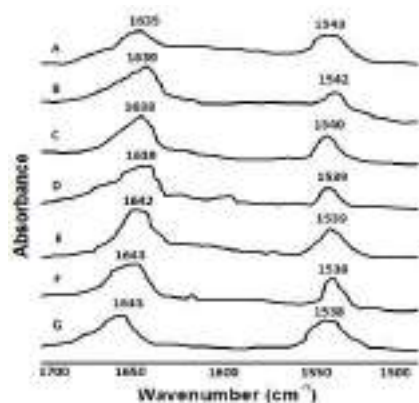
Figure 6. Stacked FT-IR spectra of BSA (A) and BSA-2DHOPNA (B-G) complexes in 1,4-dioxane.
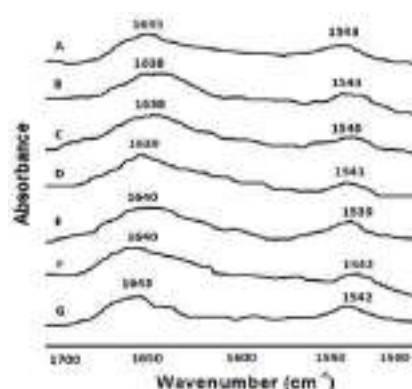
Figure 7. Stacked FT-IR spectra of BSA (A) and BSA-2DHOPNA (B-G) complexes in DMSO.
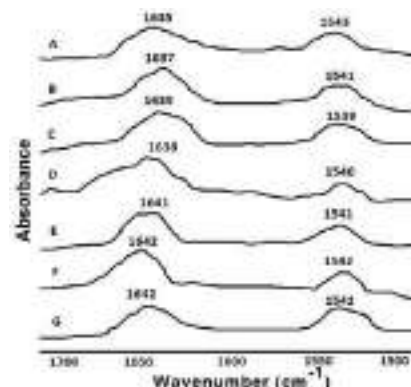
Figure 8. Stacked FT-IR spectra of BSA (A) and BSA-2DHOPNA (B-G) complexes in DMF.

2.3 Acoustical Study

Initially, ultrasonic velocities of BSA solution are measured at physiological pH. The ultrasonic velocities are 1482.192, 1483.157 and 1485.220 m/s at 298, 303 and 308K, respectively. Similarly, ultrasonic velocities of ligand 2DHOPNA-BSA complexes were measured at different concentrations and temperatures 298, 303 and 308K (Table 3). The scatchard graph is plotted for specific binding versus concentration of 2DHOPNA and from this plot binding constants have been determined. The Scatchard plot gives different association constants at different temperatures for 2DHOPNA-BSA binding interaction. The association constants in 1,4-dioxane are 0.5022, 0.5025, 0.5026 at 298, 303 and 308K respectively. Similar analysis was carried out in DMSO and DMF and association constants have been calculated. The association constants in DMSO are 0.5014, 0.5020, 0.5021 and in DMF are 0.5016, 0.5019, 0.5019 at 298, 303 and 308 K, respectively.

Table 3. Ultrasonic velocities of 2DHOPNA -BSA complexes at diff. conc. and temperature.

Temp. (K)	Ultrasonic velocities at temperatures 298, 303 and 308 K								
	298 K			303 K			308 K		
Conc (mM)	1,4-Dioxane	DMSO	DMF	1,4-Dioxane	DMSO	DMF	1,4-Dioxane	DMSO	DMF
1	1401.688	1395.301	1399.289	1405.266	1402.599	1403.413	1410.757	1408.209	1407.003
1.5	1401.509	1397.190	1399.921	1407.122	1404.806	1403.194	1413.499	1408.209	1407.614
2	1402.612	1397.612	1400.011	1410.381	1405.788	1405.805	1413.539	1409.211	1410.696
2.5	1403.499	1401.590	1401.499	1410.626	1407.048	1407.933	1415.870	1410.277	1412.959
3	1405.529	1402.554	1402.850	1412.637	1410.194	1408.416	1418.076	1413.191	1415.959
3.5	1407.720	1405.698	1403.492	1413.606	1410.513	1409.003	1418.892	1415.147	1415.512
BSA	1392.111	1392.111	1392.111	1395.172	1395.172	1395.172	1400.147	1400.147	1400.147

It is seen that the association constants increase with the increase in temperature and concentrations. Figures 9 to 11 shows the

121

Orbital: Electron. J. Chem. 12 (3): 118-126, 2020

scatchard plots of BSA-2DHOPNA binding interaction in 1,4-dioxane, DMSO and DMF respectively. The effect of temperature on BSA-2DHOPNA binding interaction is summarized in van't Hoff equation.
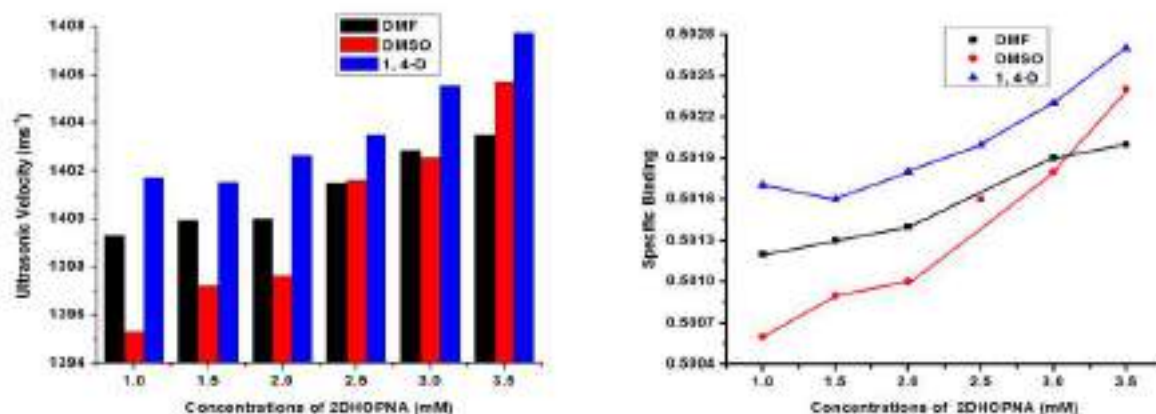
Figure 9. Scatchard plot of BSA-2DHOPNA complex in 1,4-dioxane, DMSO and DMF at 298 K.
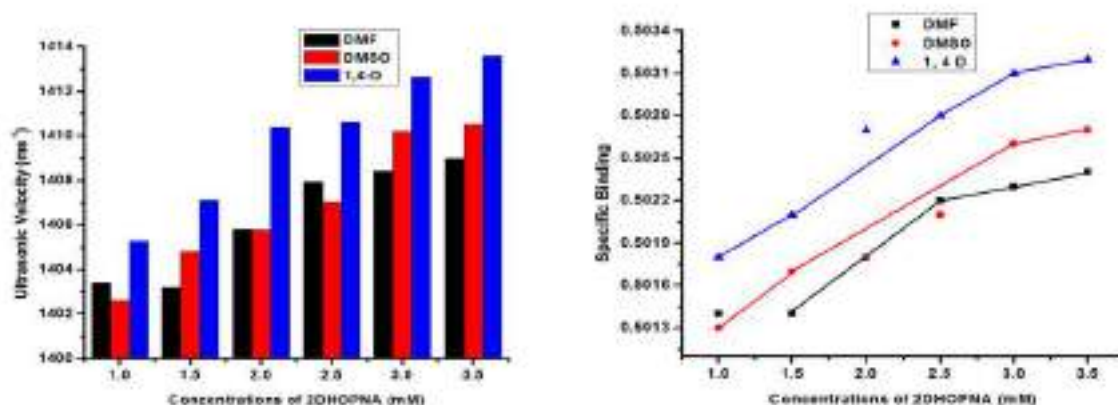
Figure 10. Scatchard plot of BSA-2DHOPNA complex in 1,4-dioxane, DMSO and DMF at 303 K
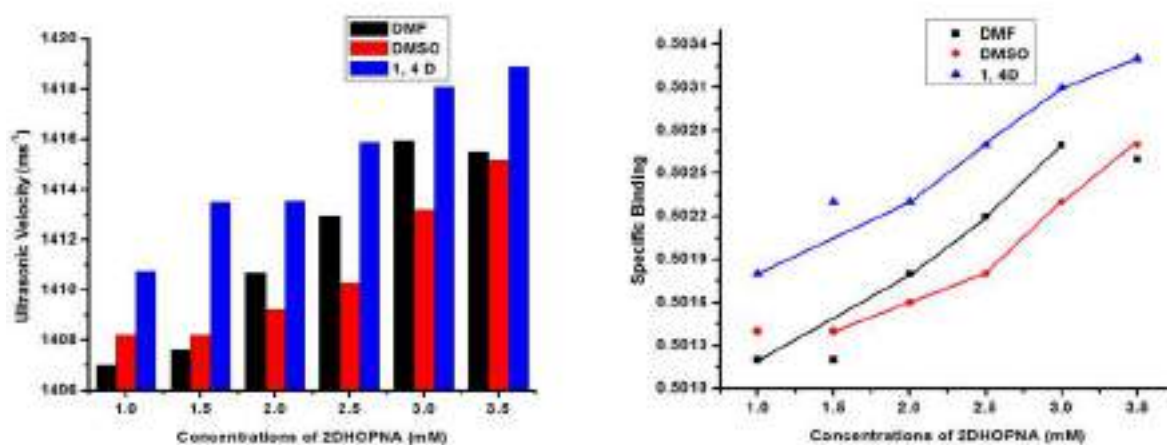
Figure 11. Scatchard plot of BSA-2DHOPNA complex in 1,4-dioxane, DMSO, DMF at 308 K.

2.4 Thermodynamic Study

In order to clarify the interaction of ligand 2DHOPNA with BSA, the thermodynamic parameters (ΔG, ΔH and ΔS) has been calculated by using van't Hoff equation at 298, 303 and 308

122

Orbital: Electron. J. Chem. 12 (3): 118-126, 2020

K (Table 4). The values of ∆H and ∆S were calculated from the slope & intercept of the plot of lnk vs 1/T respectively.

$$\ln k = -\frac{\Delta H}{RT} + \frac{\Delta S}{R} \quad \dots\dots\dots\dots (1)$$

Graph plotted between **lnk vs 1/T** shows straight line with negative slope, as shown in Figure 5.

Table 4. Thermodynamic parameters at different temperature of 2DHOPNA-BSA complex in 1,4-dioxane.

Sr. No.	Temp. (k)	ΔH J/mol	ΔG kJ/mol	ΔS J/mol
1	298 k		-14.573	
2	303 k	75.57	-14.819	49.16
3	308 k		-15.065	
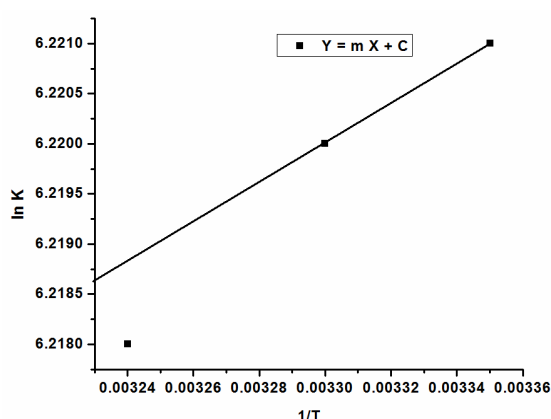
Figure 12. Graph of lnk vs 1/T in 1,4-dioxane for 2DHOPNA-BSA complex.

Positive value of ∆S and ∆H indicate that drug interaction with BSA are enthalpy and entropic driven. Positive value of entropy also shows that there is unfolding of BSA (Table 2). The specific electrostatic interaction is also characterized by the values of enthalpy and entropy. The negative value of ∆G supports the 2DHOPNA-BSA complexation is feasible process at high temperature. Thus, the overall stability of the complexes is indicated by Gibbs free energy. So, the hydrogen bonding, electrostatic and hydrophobic interactions are supposed to be possible factors contributing binding 2DHOPNA with BSA. The thermodynamic parameters in DMSO & DMF are not significant as that of 1,4-dioxane.

2.5 Molecular Modeling Study

Molecular modeling is also an efficient method for measurement of interaction between protein and drug. Furthermore, the binding interaction between BSA and 2DHOPNA is studied by molecular modeling. The energy obtained is the measure of binding interaction of ligand 2DHOPNA with BSA. The value of energy is -210.13, which shows efficient binding interaction of 2DHOPNA with BSA. Diagrammatic representation for the interaction of 2DHOPNA with BSA is shown in Figure 13.
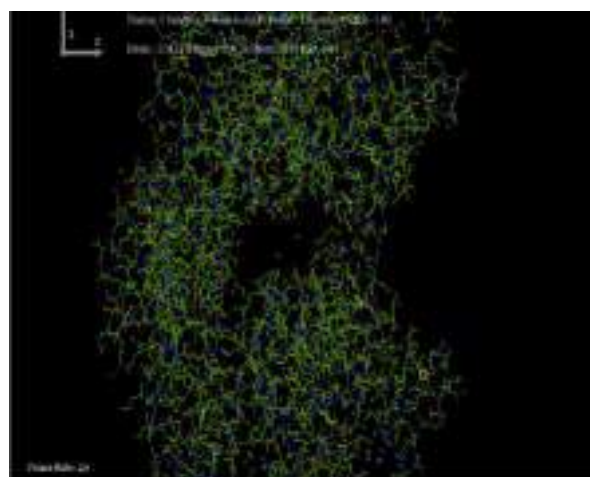
Figure 13. Molecular modeling interaction between BSA and 2DHOPNA.

3. Materials and Methods

Multi-frequency ultrasonic interferometer (VI microsystem, Chennai, India), FT-IR measurements were taken at room temperature on a Bruker's FT-IR spectrophotometer (Alpha model, Germany) equipped with Zn-Se attenuated total reflection (ATR) accessory. UV-VIS spectrophotometer (UV-1800, Shimadzu, Japan) and metabolic shaking incubator (REMI RS-24AC) used in the experiment. BSA (essential fatty acid free) purchased from Chemsworth Chemicals Ltd (India) and used without further purification. (USA). Basic buffer selected to maintain the physiological pH. For the synthesis, all the chemicals used are of A.R. grade of Merck India Limited and purchased from commercial suppliers.

3.1 Optimization Study

2DHOPNA is insoluble in basic buffer at

123

Orbital: Electron. J. Chem. 12 (3): 118-126, 2020

physiological pH. Hence mixture of buffer with non aqueous solvent such as 1,4-dioxane, DMSO and DMF were used to dissolve 2DHOPNA. Different ratio of buffer: non-aqueous solvents were tried, but the complete solubility of 2DHOPNA was obtained at optimum ratio 30:70: non-aqueous solvent: buffer.

3.2 Preparation of 2DHOPNA

2-(4,5-dihydro-1,2-oxazol-5-yl)-phenol-*N*-methylaniline (**1**) was synthesized by known method [21]. The mixture of purified 3-(2-hydroxyphenyl)-*N*-phenylprop-2-enamide (**2**) (0.01 mol), hydroxylamine hydrochloride (0.01 mol), K-10 Montmorillonite and a solution of NaOH (10%) in dry ethanol (10 mL) by using microwave irradiation for a period of 80 seconds (Scheme 1). After completion of the reaction the resultant mass was poured into ice water (10 mL) with constant stirring. It was kept in cool overnight. The resultant solid product was filtered, washed with sufficient cold water, dried and purified by recrystallization from acetone.

Scheme 1. Synthesis of 2-(4, 5-dihydro-1,2-oxazol-5-yl)phenol-*N*-methylaniline (**1**, 2DHOPNA).

2.3 Measurement of Binding Affinity

The binding interaction of 2DHOPNA with BSA is expressed as binding constant or association constant, which is derived from the law of mass action. BSA (B) interacts with the 2DHOPNA (L) to form the complex is given as
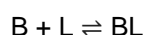
$$B + L \rightleftharpoons BL$$

Hence, association constant $K_a = \frac{[BL]}{[BL]+[B]}$

Binding strength of the ligand 2DHOPNA with BSA is a measure of association constants.

2.4 Equilibrium Dialysis

The solutions of 2DHOPNA of different concentrations 1 mM, 1.5 mM, 2 mM, 2.5 mM, 3 mM, 3.5 mM in 1, 4-dioxane, DMSO, DMF (30:70:: solvent: buffer) and 0.15 µM BSA were prepared. These solutions were mixed in 1:1 proportion and allowed to stand for maximum binding interaction. Each 3.5 mL complex solution poured into previously prepared semi-permeable membrane and both the ends were sealed properly. The BSA-2DHOPNA complex solutions tubes immersed in 100 mL conical flask containing 40 mL buffer. These conical flasks placed on a metabolic shaker for dialysis for 12 hrs at room temperature. On complete dialysis absorbance of bound fraction of 2DHOPNA with BSA was measured on UV spectrophotometer at 520 nm.

2.5 Effect of Foreign Particles

The binding interaction of 2DHOPNA with BSA was studied in presence of foreign particles. 0.1M solutions of arsenic and mercury salts were prepared and mixed with 2DHOPNA-BSA complex solutions. To study the effect of foreign particles on binding interaction these ternary complex solutions were kept for some time. On complete dialysis absorbance of bound fraction in presence of foreign particles was also measured.

2.6 FT-IR Study

FT-IR measurements were carried out on Bruker's FT-IR spectrophotometer equipped with Zn-Se attenuated total reflection (ATR) method. Different concentrations of 2DHOPNA and BSA were mixed and allowed to stand at room temperature for maximum interaction. On maximum binding interaction absorbances of BSA-2DHOPNA complexes were measured.

2.7 Acoustical Study

The binding interaction of 2DHOPNA with BSA was also studied by acoustical study. Initially multifrequency ultrasonic interferometer is set at

124

Orbital: Electron. J. Chem. 12 (3): 118-126, 2020

1MHz and different concentrations of ligand 2DHOPNA in 1,4-dioxane, DMSO, DMF has been prepared. 0.15μM BSA solution was prepared in basic buffer at physiological pH 7.4 and its ultrasonic velocity was measured. Concentrations of 2DHOPNA mixed with BSA at 298 K and allowed to stand for 1 hr for maximum binding. Then, ultrasonic velocities of these complex solutions were recorded. Similar steps are performed at 303 K and 308 K and specific binding along with association constants have been determined using Scatchard plot.

2.8 Molecular Modeling Study

Hex 8.0 gives the value of efficient energy for the binding interaction of ligand with BSA. The Molecular modeling study of 2DHOPNA with BSA is carried out on Hex 8.0 software. PDB file of the crystal structure of BSA is obtained from the RCSB data bank with ID 4F5S. Then 3D structure of 2DHOPNA was developed. The obtained 3D structure arranged in a minimized energy form. The PDB files of ligands and BSA runs together on Hex 8.0, which gives the energy value of the newly formed complex showing its stability.

4. Conclusions

In this study, the binding interaction of 2**-**(4,5-Dihydro-1,2-oxazol-5-yl)-phenol-*N*-methylaniline (**1**, 2DHOPNA) with BSA in 1,4-dioxane, DMSO and DMF BSA has been reported by equilibrium dialysis, FT-IR, acoustical study at physiological pH and its molecular modeling study. This study also involves determination of thermodynamic parameters. It is seen that association constants for BSA-2DHOPNA binding interaction increased with increase in temperatures, which clearly indicate exothermic nature of reaction. FT-IR spectroscopy shows the binding mainly through amide I site by hydrophobic interaction, which changes the secondary structure of BSA. The scatchard analysis provided a non-linear curve for binding of ligand 2DHOPNA with BSA, suggested the presence of at least two binding sites in BSA. The acoustical study at different temperatures clearly indicates that 2DHOPNA interact with BSA by means of Vander Waal's interactions and hydrogen bonds in the hydrophobic packet of binding sites. It is also observed that binding affinity increases with increased in the

concentrations and temperatures; this probably enhances the pharmacological activity of the 2DHOPNA. It is found that binding interaction is more significant in 1,4-dioxane than DMSO and DMF. It may be due to aprotic and nonpolar nature of the 1,4-dioxane. The thermodynamic parameters also indicated that the hydrogen bonding, electrostatic and hydrophobic interactions induce alterations in secondary structure of the BSA. Molecular docking is also used to confirm the binding of 2DHOPNA with BSA. The binding energy -210.13 indicates that the complex formed is stable concluding 2DHOPNA is successfully bound with BSA.

Acknowledgments

References and Notes

[1]   Hwang, I. T.; Kim, H. R.; Jeon, D. J.; Hong, K. S.; Song, J. H.; Cho, K. Y. *J. Agric. Food Chem.* **2005**, *53*, 8639.

[2]   Koo, S. J.; Hwang, K. H.; Jeon, M. S.; Kim, S. H.; Lim, J.; Lee, D. G.; Cho, N. G. *Pest Manage. Sci.* **2014**, *70*, 156.

[3]   Govindaraju, M.; Vasanth Kumar, G.; Ajay Kumar, K. *Int. J. ChemTech Res.* **2014**, *6*, 886.

[4]   Kumar, A.; Fernandes, J.; Kumar, P. *World J. Pharm. Pharm. Sci.* **2014**, *3*, 1267. [Crossref]

[5]   Sahu, S. K.; Banerjee, M.; Sahu, D.; Behera. C. C.; Pradhan G. C.; Azam, M.A. *Dhaka Univ. J. Pharm. Sci.* **2008**, *7*, 113. [Crossref]

[6]   Maksimovic-Ivanic, D.; Mijatovic, S.; Harhaji, L.; Miljkovic, D.; Dabideen, D.; Cheng, K. F.; Stosic-Grujicic, S. *Mol. Cancer Ther.* **2008**, *7*, 510. [Crossref]

[7]   Zhang, Q.; Yu, H.; Zhang, F. Z.; Shen, Z. C. *J. Zhejiang Univ., Sci., B* **2013**, *14*, 867. [Crossref]

[8]   Michalcová, L.; Glatz, Z. *J. Sep. Sci.* **2015**, *38*, 325. [Crossref]

[9]   Chaturvedi, S. K.; Ahmad, E.; Khan, J. M.; Alam, P.; Ishtikhar, M.; Khan, R. H. *Mol. BioSyst.* **2015**, *11*, 307. [Crossref]

[10] Li, X.; Wang, G.; Chen, D.; Lu. Y. *Mol. BioSyst.* **2014**, *10*, 326. [Crossref]

[11] Baroni, S.; Mattu, M.; Vannini, A.; Cipollone, R.; Aime, S.; Ascenzi, P.; Fasano, M. *Eur. J. Biochem.* **2001**, *268*, 6214. [Crossref]

[12] Skinner, A. L.; Laurence, J. S. *J. Pharm. Sci.* **2008**, *97*, 4670. [Crossref]

[13] Pisudde, A. M.; Tekade, P. V.; Bajaj, S. D.; Thakare, S. B. *Heterocycl. Lett.* **2016**, *6*, 679.

125

Orbital: Electron. J. Chem. 12 (3): 118-126, 2020

[14] Zhenbo, L.; Fengyan, J.; Ping, J.; Wang, X.; Liu, Y. *Spectrosc. Lett.* **2012**, *45*, 256. [Crossref]

[15] Shuai, L.; Chen, Z.; Tan, Z. *Spectrosc. Lett.* **2013**, *46*, 211. [Crossref]

[16] Nafisi, S.; Sadeghi, G. B.; PanahYab, A. *J. Photochem. Photobiol., B* **2011**, *105*, 198. [Crossref]

[17] Hu, Y. J.; Ou-Yang, Y.; Zhang, Y.; Liu, Y. *Protein J.* **2010**, *29*, 234. [Crossref]

[18] Paxton, J. W. *J. Pharmacol. Methods* **1981**, *5*, 203. [Crossref]

[19] Hartshorn, M. J.; Verdonk, M. L.; Chessari, G.; Brewerton, S. C.; Mooij, W. T.; Mortenson, P. N.; Murray, C. W. *J. Med. Chem.* **2007**, *50*, 726. [Crossref]

[20] Taufer, M.; Crowley, M.; Price, D. J.; Chien, A. A.; Brooks, C. L. *Concurrency and Computation: Practice and Experience* **2005**, *17*, 1627. [Crossref]

[21] Bajaj, S. D.; Mahodaya, O. A.; Tekade, P. V. *Heterocycl. Lett.* **2013**, *3*, 219.

126

Orbital: Electron. J. Chem. 12 (3): 118-126, 2020

Sensitization of Tb^{3+} and Dy^{3+} emission in $Li_4Ca(BO_3)_2$ via energy transfer from Ce^{3+} and study of energy transfer mechanism

Mangesh M. Yerpude[a,b], Govind B. Nair[c,*], S.J. Dhoble[b], SH Bagade[a], H.C. Swart[c,*]

[a] Department of Physics, Bajaj College of Science, Wardha, 442001, India
[b] Department of Physics, RTM Nagpur University, Nagpur, 440033, India
[c] Department of Physics, University of the Free State, P. O. Box 339, Bloemfontein 9300, South Africa

ABSTRACT

Different series of $Li_4Ca(BO_3)_2$ singly doped with Ce^{3+}, Tb^{3+} and Dy^{3+} as well as codoped with Ce^{3+}-Tb^{3+} and Ce^{3+}-Dy^{3+} pairs were prepared by a one-step solid state reaction method. Structural, optical and photoluminescence (PL) properties were studied in detail. The powder X-ray diffraction studies confirmed a single-phased structure with an orthorhombic structure ($Pnnm$). Vibrational modes of the BO_3 groups were determined using Fourier Transform Infrared spectra. The band gap value of 4.98 eV was determined from the UV–vis diffuse reflectance spectroscopy data. The PL of the single and codoped systems were investigated in detail. There was a significant quantitiy of spectral overlap between the emission spectrum of the Ce^{3+} and the excitation spectra of Tb^{3+}/Dy^{3+}, which showed the possibility of energy transfer from the Ce^{3+} to the Tb^{3+}/Dy^{3+}. Effective sensitization of the Tb^{3+} and Dy^{3+} emission was achieved via energy transfer from Ce^{3+} in the $Li_4Ca(BO_3)_2$. The energy transfer mechanism revealed that Ce → Tb energy transfer occured via an electric quadrupole-quadrupole interaction, whereas Ce → Dy energy transfer occured via amn electric dipole-dipole interaction. The prepared materials can act as a strong candidate for near-ultraviolet light emitting diodes and display applications.

1. Introduction

Easy and cheap availability of the raw materials, low synthesis temperatures as well as high chemical and thermal stability has defined borates as attractive materials for utilization in modern technological applications. Among borates, lithium-based materials have been reported for various applications such as cathode material in Li-ion batteries, neutron detectors, thermoluminescent dosimeters (TLD), magneto-optical material, nonlinear optical materials and phosphors [1–7]. In the past decade, extensive research interest has been developed on the synthesis and characterization of inorganic borates for their possible application as phosphor materials in white light emitting diodes (WLEDs) due to their high band gap and transparency to a wide range of wavelengths [8]. Several authors have reported borate materials for blue, green and red emitting phosphors for WLED application. The efficient blue emission and the effect of the addition of monovalent impurities in $YAl_3(BO_3)_4$ was reported by Satheesh Kumar et al. [9]. Yu *et al.* [10] reported peculiar green emission from Ce^{3+} doped $NaBaBO_3$, which is usually not observed in alkali (M) alkaline (N) earth borates having formula $MNBO_3$. The stronger crystal field produced due to the occupation of Ce^{3+} ions in a deformed BaO_9 polyhedron was deduced responsible for this green emission. Coexistence of red, green and blue emissions in a single-phased white-light-emitting $Ca_{11}(SiO_4)_4(BO_3)_2$:Ce^{3+},Eu^{2+},Eu^{3+} phosphor for WLED application was reported by Hou [11]. Many other researchers have

reported red, green, blue and white emissions from several other borate materials doped with different rare earth ions, *viz.* $YK_3B_6O_{12}:Eu^{3+}$, Tb^{3+}, Ce^{3+} [12], $Ba_3Sc(BO_3)_3:Tb^{3+}$ [13], $La_2CaB_8O_{16}:Eu^{3+},Tb^{3+}$ [14], $NaSr_4(BO_3)_3:Dy^{3+}$ [15], $(Sr/Ba)_2Mg$ $(BO_3)_2:Sm^{3+}$ [16] and $Li_6Y(BO_3)_3:Eu^{3+}$ [17].

In search of new birefringent and nonlinear optical crystals, researchers have found great potential in alkali alkaline earth borates. While searching for such materials, Wu et al investigated the phase relations in $Li_2O–CaO–B_2O_3$, and found several new ternary compounds [18]. One of them was $Li_4Ca(BO_3)_2$, which was synthesized through a solid-state reaction and reported the ab initio structural studies on $Li_4Ca(BO_3)_2$ for the first time. This compound belongs to the orthorhombic space group *Pnnm* having two molecules in a unit cell. In the unit cell of $Li_4Ca(BO_3)_2$, fundamental building units are isolated $[BO_3]^{3-}$ anionic groups, which are all parallel to the *a–b* plane stacked along the c-axis. The Ca atoms are coordinated by six O atoms to form octahedral coordination polyhedra, which are joined together through edges along the c-axis, forming infinitely long three-dimensional chains. The Li atoms have a four-fold and a five-fold coordination with O atoms that lead to complex Li–O–Li chains that also extend along the c-axis [18]. Recently, Neharika et al reported Dy^{3+} and Sm^{3+} doped $Li_4Ca(BO_3)_2$ nano phosphor prepared by combustion synthesis method for its possible application in solid state lighting (SSL) [19,20]. The energy transfer from sensitizer to activator in the phosphor has been used to enhance the desired emission from decades. The largely studied pairs for energy transfer are Ce-Tb and Ce-Dy, as Ce doped phosphors possess the allowed strong broadband 4f-5d absorption in the UV to near-UV (NUV) region and 5d-4f strong broadband emission in the NUV to blue region [9,11,12], whereas both Tb and Dy show forbidden but weak 4f-4f absorption in the NUV to blue region [6,21]. Thus, the energy emitted by Ce^{3+} ions inside the host can be absorbed by the Tb^{3+} or Dy^{3+} ion and their emissions can be enhanced significantly [22–26].

In the present work, the solid state synthesis of $Li_4Ca(BO_3)_2$ phosphors that were singly doped with Ce^{3+}, Tb^{3+}, Dy^{3+} and co-doped with Ce-Tb and Ce-Dy pairs for SSL application are reported. The luminescence energy transfer in Ce-Tb and Ce-Dy co-doped $Li_4Ca(BO_3)_2$ has been studied in detail. Also, a schematic energy-level diagram describing the energy transfer from Ce to Tb and Ce to Dy has been drawn with all possible transitions in the $Li_4Ca(BO_3)_2$ host.

2. Experimental

Different series of $Li_4Ca(BO_3)_2:Ce^{3+}$, $Li_4Ca(BO_3)_2:Tb^{3+}$, $Li_4Ca(BO_3)_2:Dy^{3+}$, $Li_4Ca(BO_3)_2:Ce^{3+},Tb^{3+}$ and $Li_4Ca(BO_3)_2:Ce^{3+},Dy^{3+}$ phosphors were prepared by the one-step solid-state synthesis route. Li_2CO_3 (Loba chemie), $CaCO_3$ (Merck), H_3BO_3 (Merck), $(NH_4)_2Ce(NO_3)_6$ (Merck), Tb_4O_7 (Himedia) and Dy_2O_3 (Himedia) were used as initial precursors. Stoichiometric proportions of precursors were homogeneously mixed by using a traditional hand milling process using a mortar pestle. The resultant mixture was heated at 650 °C for 4 h and then allowed to cool down up till room temperature. The finally obtained powder was pulverized and used for further characterization.

The phase purity and crystal structure of the as-synthesized phosphors were investigated by powder X-ray diffraction (XRD) with an X-ray Diffractometer (Panalytical's X'Pert Pro) using Cu-K$_\alpha$ radiation at 40 kV operating voltage and 25 mA current, equipped with a nickel filter. The XRD patterns were collected in the 2θ range of 10–80° with a step size of 0.02°. The Fourier transform infrared (FTIR) measurements were performed on an IRAffinity-1, Shimadzu, in ATR mode. For band gap measurement, diffuse reflectance spectra were collected on a JASCO V-670 fitted with an integrating sphere assembly. The excitation and emission spectra were measured by using a Shimadzu Instrument RF5301-PC spectrofluorophotometer. All the measurements were carried out at room temperature.

3. Results and discussion

3.1. Analysis of the phase and the crystal structure

The XRD pattern of the undoped; Ce^{3+}-doped; Ce^{3+},Tb^{3+}-codoped and Ce^{3+},Dy^{3+}-codoped samples of the $Li_4Ca(BO_3)_2$ phosphors are given in Fig. 1 **(a)**. $Li_4Ca(BO_3)_2$ is known to crystallize in an orthorhombic structure [space group: *Pnnm* (58)]. As demonstrated in Fig. 1 **(a),** the diffraction peaks of all the samples can be easily indexed as single-phase orthorhombic $Li_4Ca(BO_3)_2$ (ICDD card no. 01-074-4315). There are no traces of impurity phases arising from the doping of lanthanide ions in to the host. The raw XRD data of the undoped $Li_4Ca(BO_3)_2$ host was qualitatively analyzed using the Rietveld refinement technique *via* the Full Prof software package [27]. The XRD profiles derived from the Rietveld analysis are shown in Fig. 1 **(b)**. The refined lattice parameters were obtained as; $a = 9.2411$, $b = 8.0933$, and $c = 3.4821$ Å, and the corresponding volume was V = 260.4298 Å^3 which shows good agreement with a previous report [18]. As shown in Fig. 2, the B atoms are coordinated to three oxygen atoms forming BO_3 triangles, which are connected to Ca and Li polyhedrons through oxygen. The Ca atoms are six-coordinated by the oxygen atoms forming an octahedral polyhedron, while the Li atoms are seen to exhibit two kinds of coordination. The Li(1) atoms are coordinated with four oxygen atoms, forming a distorted tetrahedron. The Li(2) atoms are coordinated with five oxygen atoms, forming a distorted trigonal bipyramid. It is well known that an acceptable percentage difference in ion radii between the doped and substituted ions must not exceed 30%. Herein, it is known that the ionic radius of 6-coordinated Ca^{2+} is 1.00 Å, which is close to that of Ce^{3+} (1.01 Å) or Tb^{3+} (0.923 Å) or Dy^{3+} (0.912 Å), while the ionic radius of 4 or 5-coordinated Li^+ is below 0.9 Å, which is too small for Ce^{3+} or Tb^{3+} or Dy^{3+} to be substituted. Thus, it is expected that the Ce^{3+} or Tb^{3+} or Dy^{3+} ions substitute at the Ca^{2+} site. The charge imbalance can be compensated for by creating the Li^+ vacancy.
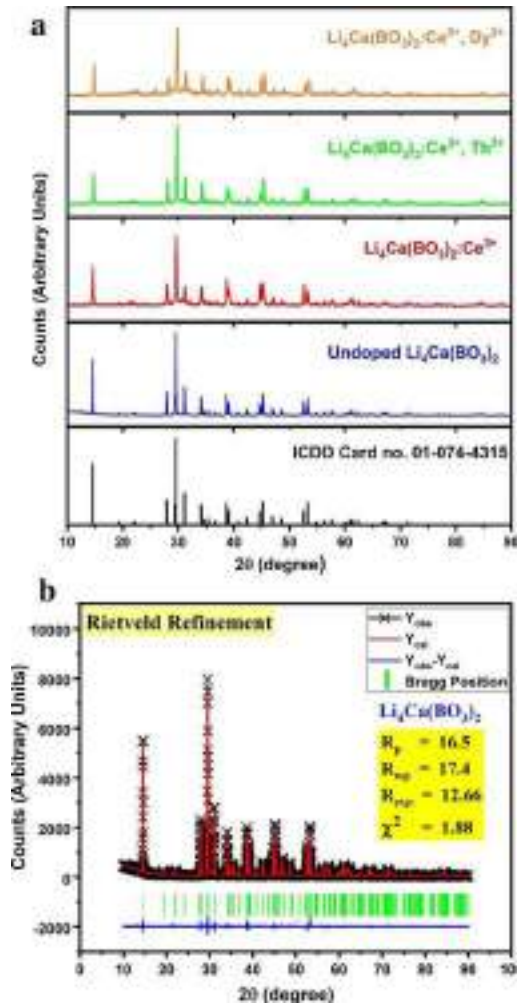
Fig. 1. (a) XRD patterns of undoped; Ce^{3+}-doped; Ce^{3+},Tb^{3+}-codoped and Ce^{3+},Dy^{3+}-codoped samples of $Li_4Ca(BO_3)_2$ phosphor compared with the standard ICDD pattern. **(b)** Observed (crosses), calculated (solid line), and difference (bottom) XRD profiles for the Rietveld refinement of undoped $Li_4Ca(BO_3)_2$.

3.2. FTIR analysis

To investigate the vibration modes of the different BO_3 groups, the FTIR spectra for $Li_4Ca(BO_3)_2$ was recorded at room temperature and presented in Fig. 3. The FTIR spectrum shows absorption lines from 400 to 1650 cm^{-1}. The bands in the region 1100 and 1600 cm^{-1} are due to B–O asymmetric stretching vibrations of triangular BO_3^{3-} units. The symmetric stretching bands of B–O bond in BO_3^{3-} units are observed in the region 800-1100 cm^{-1}. The bands in the range 650–770 cm^{-1} and 450–580 cm^{-1} assigned to the out-of-plane bending and in-plane bending of the BO_3 group, respectively. The vibrational frequencies below 450 cm^{-1} are attributed to lattice vibrations [4,28].

3.3. Bandgap measurements

Fig. 4 shows the diffuse reflectance spectrum of undoped and Ce^{3+}-doped $Li_4Ca(BO_3)_2$ phosphor. From Fig. 4, it can be seen that the prepared host lattice was transparent to a wide range of wavelengths which is characteristic of a good host material for the phosphor. The Ce^{3+}-doped sample clearly shows the absorption due to the 4f-5d transition of the Ce^{3+} ion. The diffuse reflectance spectrum was used to determine the band gap of the prepared material using the Kubelka-Munk theory [29]. The Diffuse reflectance spectrum was transformed into an absorption spectrum of the prepared material by using the Kubelka-Munk function [30] as in Eq. (1)

$$F(R) = \frac{(1 - R)^2}{2R} = \frac{K}{S} \tag{1}$$
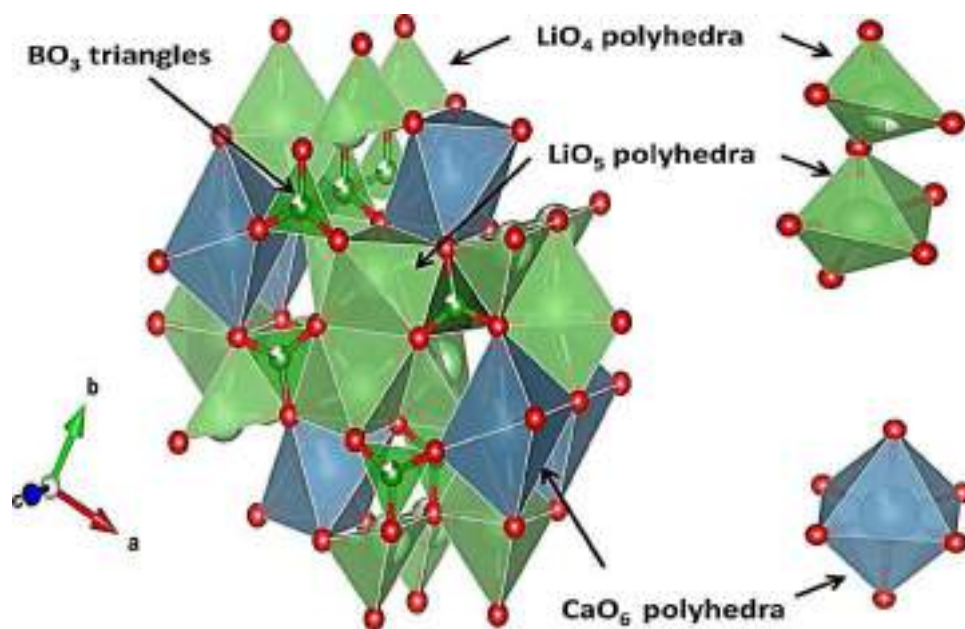
Fig. 2. Crystal structure of $Li_4Ca(BO_3)_2$ showing LiO_4, LiO_5 and CaO_6 polyhedra constructed using VESTA software.
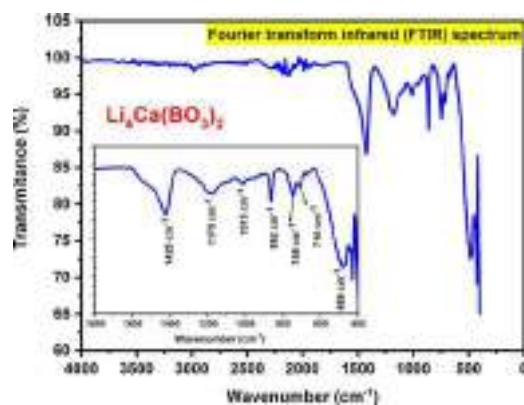
Fig. 3. FTIR spectrum of undoped $Li_4Ca(BO_3)_2$.
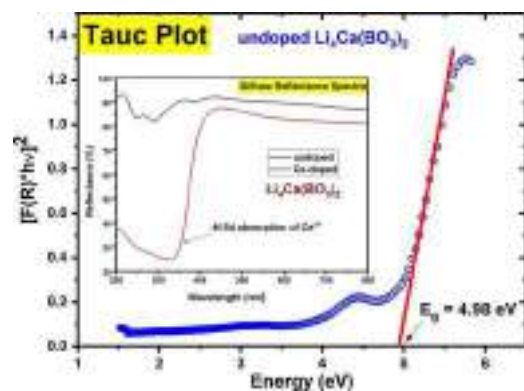
Fig. 4. Tauc plot showing the bandgap measurement of the $Li_4Ca(BO_3)_2$. The inset shows diffuse reflectance spectra of undoped and Ce-doped $Li_4Ca(BO_3)_2$.
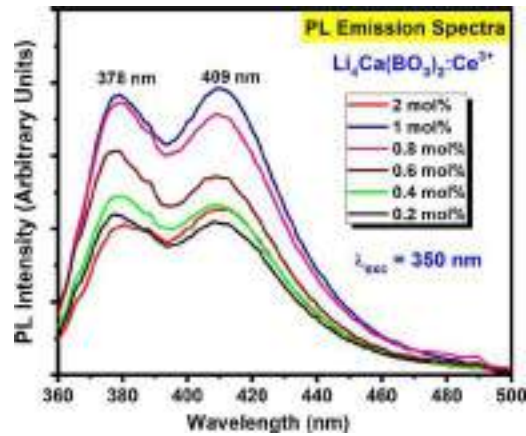
Fig. 5. PL emission spectra of the $Li_4Ca(BO_3)_2$:Ce^{3+} (0.2, 0.4, 0.6, 0.8, 1, 2 mol%) under 350 nm excitation.

Where R is the diffuse reflectance of the sample, K is an absorption coefficient and S is the scattering coefficient. The relation between the energy band gap E_g and absorption coefficient K of the material for a direct allowed transition is related through the Tauc relation [31] given by Eq. (2):

$$(Kh\vartheta)^2 = C(h\vartheta - E_g) \tag{2}$$

Where $h\vartheta$ is the energy of the photon and C is the constant of proportionality. The $F(R)$ is directly proportional to the absorption coefficient and thus, by comparing Eq.s (1) and (2) we get the following relation:

$$[F(R)h\vartheta]^2 = C(h\vartheta - E_g) \tag{3}$$

According to Equation (3), a graph can be plotted between $[F(R)h\vartheta]^2$ and $h\vartheta$ (Tauc's plot). Linear fitting is done in the linear region of the graph, upon extrapolating the linear line $[F(R)h\vartheta]^2 = 0$ as shown in the inset of Fig. 4. The point of the interception represents the value of the band gap E_g of the prepared material. The average electronic band gap of $Li_4Ca(BO_3)_2$ was estimated to be 4.98 eV which is comparable with previous studies [19,20].

3.4. Photoluminescence (PL)

3.4.1. Photoluminescence studies in $Li_4Ca(BO_3)_2$:Ce^{3+}

Fig. 5 shows the typical PL emission spectra of $Li_4Ca(BO_3)_2$:Ce^{3+} (0.2, 0.4, 0.6, 0.8, 1, 2 mol%) phosphors under excitation at 350 nm. From Fig. 5, it can be seen that the as-synthesized $Li_4Ca(BO_3)_2$:Ce^{3+} phosphor exhibits a NUV-blue emission band peaking at 378 nm and 409 nm, which corresponds to the Ce^{3+} 5d→4f transition. It is well known that Ce^{3+} ions show double-emission band corresponding to the splitting of its 4f ground state into the $^2F_{5/2}$ and the $^2F_{7/2}$ states due to the spin-orbit coupling [32]. This emission can be deconvoluted into two Gaussian bands corresponding to the 5d→$^2F_{5/2}$ and 5d→$^2F_{7/2}$ transitions, as shown in Fig. 6. The emission spectrum can be decomposed into two Gaussian components centered at 26,547 cm^{-1} (376 nm) and 24,450 cm^{-1} (409
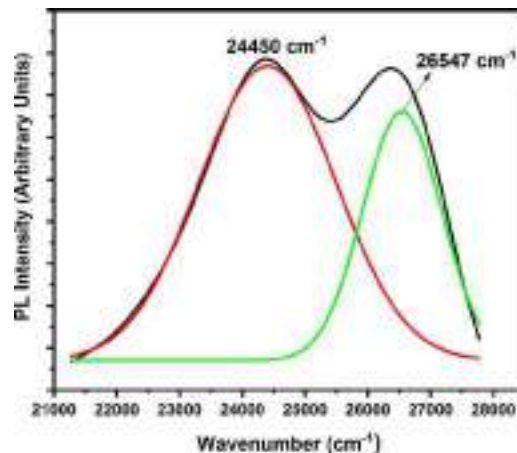
Fig. 6. Deconvoluted Gaussians peaks of the PL emission spectrum of the $Li_4Ca(BO_3)_2$:Ce^{3+} (1 mol%) showing two-band emission due to the 5d→4f ($^2F_{5/2}$,$^2F_{7/2}$) transition.
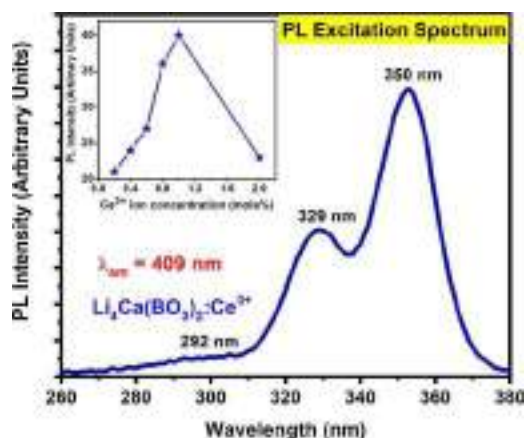
Fig. 7. PL excitation spectra of the $Li_4Ca(BO_3)_2$:Ce^{3+} (1 mol%) at 409 nm emission. Inset shows the variation of the PL excitation intensity with Ce^{3+}-concentration.

nm), which are corresponding to the transitions of 5d→$^2F_{5/2}$ and 5d→$^2F_{7/2}$, respectively (Fig. 6). The energy difference between these two bands is 2097 cm^{-1}. This value is consistent with the difference of about 2000 cm^{-1} between the two ground states $^2F_{5/2}$ and $^2F_{7/2}$ of Ce^{3+} [10]. This implies that there is only one type of Ce^{3+} luminescence site in the $Li_4Ca(BO_3)_2$ lattice, which is consistent with the fact that only a single crystallographic Ca site is available for Ce^{3+} substitution. This is in agreement with the reported structural data and also support our assumption that the rare earth dopant occupies the Ca-site in the crystal lattice. With the increasing Ce^{3+}-concentration, it can be seen that the intensity of 378 nm peak was slightly higher than the 409 nm peak at lower concentrations and as the concentration of Ce^{3+} was increased it reversed and the intensity of the 409 nm peak became higher than the 378 nm peak at higher concentrations. This indicates that the transition probability of the 5d→$^2F_{5/2}$ (378 nm) emission is higher at lower concentrations and, with the increasing concentration, the transition probability of the 5d→$^2F_{7/2}$ (409 nm) became higher.

The PL excitation spectrum of the $Li_4Ca(BO_3)_2$:Ce^{3+} (1 mol%) in Fig. 7 shows that the phosphor is excitable at different regions centered at 350, 329 and 292 nm, respectively. These excitation peaks are attributed to the electronic excitation from 4f ground state to 5d-multiplets of Ce^{3+}. All the peaks in the excitation and the emission spectra are characteristic of 5d-4f transitions of Ce^{3+}. The inset of Fig. 7 shows the dependence of the integrated intensity on the Ce^{3+}-doping concentration in the $Li_4Ca(BO_3)_2$:Ce^{3+} phosphor. Also, it can be found that the emission intensity enhanced with an increase in the Ce^{3+} concentration and it reached the maximum intensity at 1 mol%. Consequently, the concentration quenching occured as the concentration of Ce^{3+} ions went beyond 1 mol%. In other words, the emission intensity dramatically declined as the Ce^{3+}-concentration exceeded 1 mol%. This shows that the optimum doping concentration for Ce^{3+} ions in $Li_4Ca(BO_3)_2$ is 1 mol%.

3.4.2. Photoluminescence studies in $Li_4Ca(BO_3)_2$:Tb^{3+}

Fig. 8 shows the PL excitation spectrum of the $Li_4Ca(BO_3)_2$:Tb^{3+} phosphor for 1 mol% of Tb^{3+} ions by monitoring the emission wavelength at 545 nm. The excitation spectrum consists of two parts. The first part in the range from 200 to 300 nm is attributed to the $4f^8 \rightarrow 4f^75d^1$ transition of the Tb^{3+} ions. The first part of the PL excitation spectrum reveals two broad bands at 234 and 272 nm
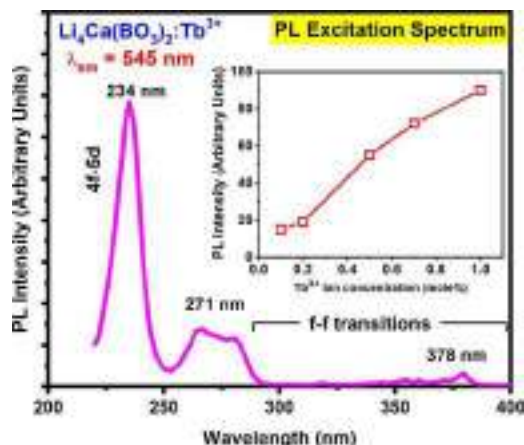
Fig. 8. PL excitation spectrum of the $Li_4Ca(BO_3)_2$:Tb^{3+} (1 mol%) phosphor at 545 nm emission wavelength. Inset shows the dependence of emission intensity on the Tb^{3+}-concentration.
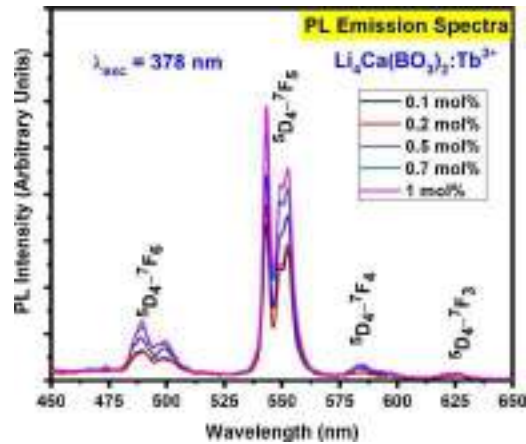
Fig. 9. PL emission spectra of the $Li_4Ca(BO_3)_2$:Tb^{3+} monitored at 378 nm excitation for different Tb^{3+}-concentrations.

due to spin-allowed $^7F_6 \rightarrow ^7DJ$ and spin-forbidden $^7F_6 \rightarrow ^9DJ$ transitions. The second and the weak part of the spectrum in the range 300–400 nm can be attributed to the $4f^8 \rightarrow 4f^8$ transition that contains several weak peaks at 319 nm, 353 nm, 361 nm and 378 nm corresponding to the parity-forbidden $^7F_6 \rightarrow ^5D_0$, $^7F_6 \rightarrow ^5D_2$, $^7F_6 \rightarrow ^5G_5$ and $^7F_6 \rightarrow ^5D_3$ transitions, respectively [14]. The PL emission spectra of the $Li_4Ca(BO_3)_2$:Tb^{3+} (Fig. 9), excited at 378 nm, consists of four Tb^{3+} emission peaks at around 490 nm, 545 nm, 586 nm, and 623 nm corresponding to the transitions from $^5D_4$ to $^7F_6$, $^7F_5$, $^7F_4$, and $^7F_3$, respectively. Among these, the emission intensity at 545 nm was the highest one. The Stark splitting of the Tb^{3+} emission peaks is attributed to the effect of the ligand field on the Tb^{3+} ion. The excitation and emission spectra showed that the $Li_4Ca(BO_3)_2$:Tb^{3+} is suitable for applications wherein green luminescence must be obtained by UV-excitation. The blue emissions from the $^5D_3$ level of the Tb^{3+} ion were not observed for the $Li_4Ca(BO_3)_2$ even at low Tb^{3+}-concentrations. This might be due to the cross relaxation process between $^5D_3$ and $^5D_4$ levels or the non-radiative relaxations that occur from the high energy lattice phonons of the host matrix [33]. No concentration quenching was observed up to 1 mol% of Tb^{3+} ions as shown in the inset of Fig. 8.

3.4.3. Photoluminescence studies in $Li_4Ca(BO_3)_2$:Dy^{3+}

The PL excitation spectrum of the $Li_4Ca(BO_3)_2$:Dy^{3+} (1 mol%) phosphor monitored at 577 nm, as shown in Fig. 10, shows several peaks at 325 nm, 350 nm, 364 nm, 388 nm, 426 nm, 455 nm and 476 nm that can be attributed to the transitions from the ground state $^6H_{15/2}$ to the excited states $[^4K_{15/2} + ^6P_{3/2}]$, $[^4M_{15/2} + ^6P_{7/2}]$, $[^4I_{11/2} + ^6P_{5/2}]$, $[^4I_{13/2} + ^4F_{7/2}]$, $^4G_{11/2}$, $^4I_{15/2}$, and $^4F_{9/2}$ respectively [34–36]. The excitation peaks at 350 nm and 455 nm due to $^6H_{15/2} \rightarrow [^4M_{15/2} + ^6P_{7/2}]$, $^6H_{15/2} \rightarrow ^4I_{15/2}$ respectively of the 4f→4f transition were seen to be dominant, and therefore, the emission spectra were recorded at 350 nm wavelength. The emission spectra recorded at 350 nm wavelength in Fig. 11 shows two peaks at 489 nm and 577 nm due to the transition from the $^4F_{9/2}$ excited state to the $^6H_{15/2}$ and $^6H_{13/2}$ states. The transitions at 489 nm and 577 nm correspond to blue and yellow color, respectively. The blue transition ($^4F_{9/2} \rightarrow ^6H_{15/2}$) is a magnetic dipole, allowed transition having moderate intensity, whereas the yellow transition ($^4F_{9/2} \rightarrow ^6H_{13/2}$) is hypersensitive, forced electric dipole $\Delta L = 2$ and $\Delta J = 2$ natured, which is strongly influenced by the host environment [6]. We could certainly observe that the yellow transition has slightly less intensity than that of the blue. The intensity of the blue band ($^4F_{9/2} \rightarrow ^6H_{15/2}$) is less sensitive to the environment. The integrated emission intensity ratios of $^4F_{9/2} \rightarrow ^6H_{13/2}$

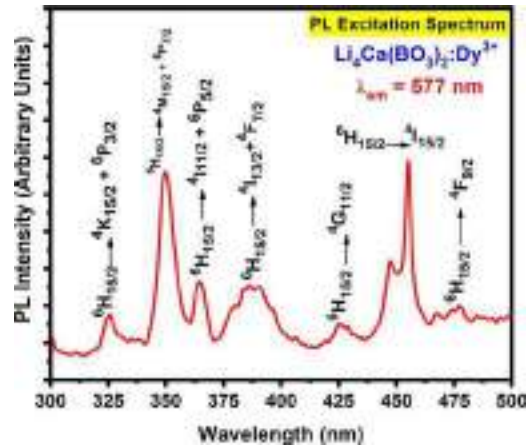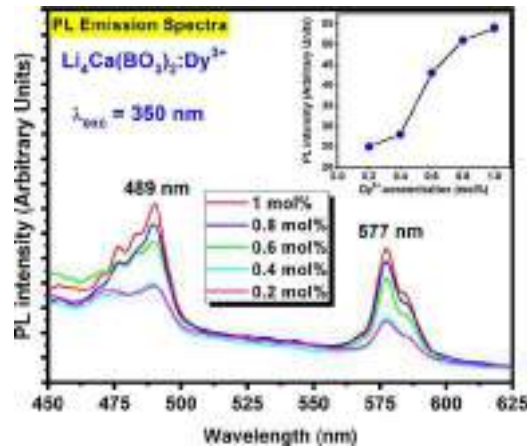**Fig. 10.** PL excitation spectrum showing all possible transitions in the $Li_4Ca(BO_3)_2$:Dy^{3+} (1 mol%) phosphor monitored at 577 nm emission.

Fig. 11. PL emission spectra of the $Li_4Ca(BO_3)_2:Dy^{3+}$ phosphor monitored at 350 nm excitation. The inset shows the variation of emission intensity as a function of Dy^{3+} concentration.

(yellow) to $^4F_{9/2} \rightarrow {}^6H_{15/2}$ (blue) was calculated for all samples and found to be constant, which demonstrates that the doping of Dy^{3+} does not alter the crystal structure and crystal field surrounding of Dy^{3+} [37]. The yellow/blue emission intensity ratio in case of the $Li_4Ca(BO_3)_2:Dy^{3+}$ phosphor is slightly less than unity, indicating that the Dy^{3+} ions occupied symmetry sites in the Li_4Ca $(BO_3)_2$ host lattice [38]. As the radius of Dy^{3+} and Ca^{2+} are nearly comparable, the Dy^{3+} ions will prefer to enter into the Ca^{2+} sites [19]. The concentration profile in the inset of Fig. 11 shows that the increase of the Dy^{3+} ion-concentration from 0.05 mol% led to an increase in the emission intensity and above 0.8 mol% it nearly saturated.

3.4.4. Photoluminescence studies and energy transfer in $Li_4Ca(BO_3)_2:Ce^{3+},Tb^{3+}$ and $Li_4Ca(BO_3)_2:Ce^{3+},Dy^{3+}$

It is well known that Ce^{3+} is an excellent sensitizer for Tb^{3+} ions. Cheng et al and Chen et al. studied the Ce-Tb energy transfer process in borate matrixes β-$Ba_3Y(BO_3)_3$ and $Sr_6YSc(BO_3)_6$, respectively [22,23]. We could predict the resonance type energy transfer from Ce^{3+} to Tb^{3+} (or Dy^{3+}) due to wide spectral overlap between the emission of Ce^{3+} and excitation of Tb^{3+} (or Dy^{3+}) in the $Li_4Ca(BO_3)_2$ matrix as depicted in Fig. 12. The emission spectrum monitored at 350 nm (Fig. 13) of the $Li_4Ca(BO_3)_2:0.01Ce^{3+},xTb^{3+}$ (x = 0.2, 0.4, 0.8, 1.2, 1.6 mol%) phosphor exhibited not only the obvious NUV-blue band from Ce^{3+}, but also a group of sharp characteristic green emission lines from Tb^{3+}. The excitation spectrum, recorded by monitoring the 545 nm emission of Tb^{3+}, consisted of both the excitation bands of the Ce^{3+} ions and that of the Tb^{3+} ions as shown in Fig. 14. The spectrum is similar to the singly doped $Li_4Ca(BO_3)_2:Tb^{3+}$ below 250 nm but have strong absorption in the range 250 to 375 nm due to energy transfer from Ce^{3+} to Tb^{3+} ions, thereby, making the phosphor more suitable for wider applications. Fig. 15(a) shows the effect of Tb^{3+}-concentration on the luminescence intensity of Ce^{3+} and Tb^{3+} ions. As the Tb^{3+}-concentration increased, the Ce^{3+} emission intensity decreased and Tb^{3+} emission increased up to 0.8 mol%; further increase in Tb^{3+} concentration resulted in a decrease of both Ce^{3+} and Tb^{3+} emission intensities due to concentration quenching effects. A similar effect was seen for the Tb^{3+} emission at 234 nm excitation. This suggests that the optimum concentration of Tb^{3+} ions for maximum luminescence intensity is 0.8 mol%.

Fig. 16 shows the emission spectra of the $Li_4Ca(BO_3)_2:1$ mol% Ce^{3+}/y mol% Dy^{3+} (y = 0, 0.05, 0.1, 0.2, 0.3, 0.4 and 0.8)
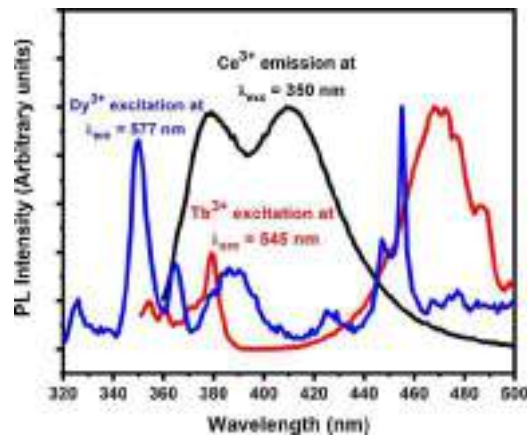
Fig. 12. Spectral overlap between the emission spectrum of the $Li_4Ca(BO_3)_2:Ce^{3+}$ phosphor and the excitation spectra of $Li_4Ca(BO_3)_2:Tb^{3+}$ and $Li_4Ca(BO_3)_2:Dy^{3+}$ phosphors.
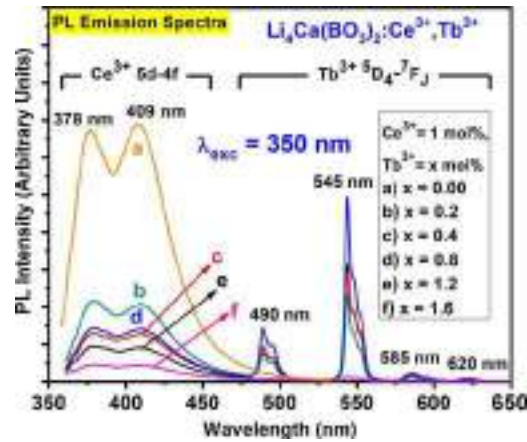
Fig. 13. PL emission spectra of the Li$_4$Ca(BO$_3$)$_3$:0.01Ce^{3+},xTb^{3+} phosphor monitored at 350 nm excitation.
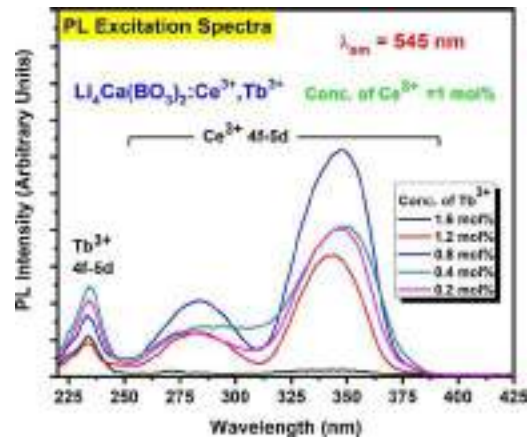
Fig. 14. PL excitation spectra of the Li$_4$Ca(BO$_3$)$_3$:0.01Ce^{3+},xTb^{3+} monitored at 545 nm emission.
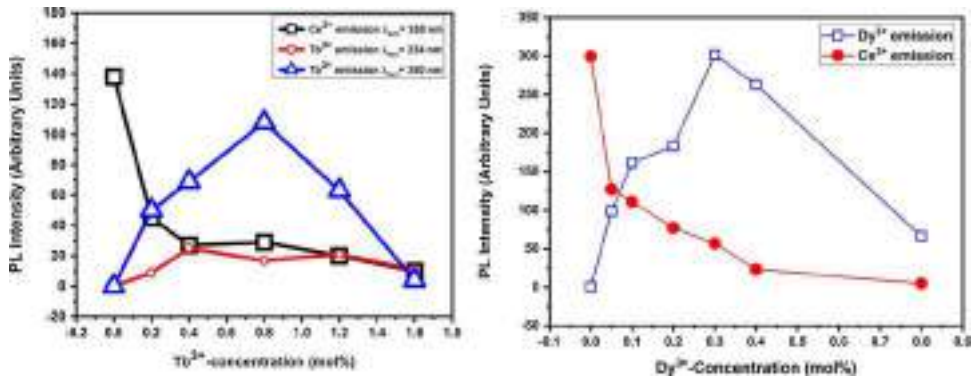
Fig. 15. (a) Variation of Ce^{3+} and Tb^{3+} emission intensity with Tb^{3+}-concentration in the Li$_4$Ca(BO$_3$)$_3$:0.01Ce^{3+},xTb^{3+} phosphor, (b) Variation of Ce^{3+} and Dy^{3+} emission intensity with Dy^{3+}-concentration in the Li$_4$Ca(BO$_3$)$_3$:0.01Ce^{3+},xDy^{3+} phosphor.

phosphors upon 350 nm excitation. The characteristic emission bands of Ce^{3+} (378 nm and 409 nm) and Dy^{3+} (488 nm and 577 nm) were observed. With the increasing Dy^{3+} doping concentrations, the Ce^{3+} emission intensity decreased noticeably, but the Dy^{3+} emission intensity increased initially and then decreased as the Dy^{3+} doping concentration reached beyond 0.3 mol% (Fig. 15**(b)**). The PL excitation spectra monitored at 577 nm emission of Dy^{3+} are shown in Fig. 17. The excitation spectra consist of the excitation bands of both Ce^{3+} and Dy^{3+} ions. These include the two broad excitation bands peaking at 283 nm and 343 nm due to 4f → 5d absorption of Ce^{3+} ions and one sharp band at 455 nm due to $^6H_{15/2}$ → $^4I_{15/2}$ of Dy^{3+} absorption. The absorption bands of Dy^{3+} ions are completely merged in the Ce^{3+} absorption between 300 nm to 400 nm. With the increasing concentration of Dy^{3+}, the Ce^{3+}

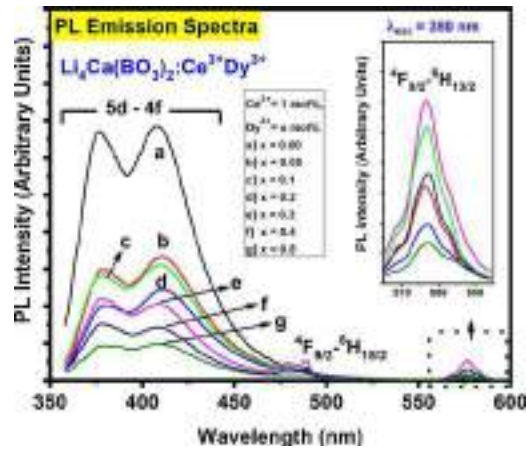**Fig. 16.** PL emission spectra of the $Li_4Ca(BO_3)_3$:0.01Ce^{3+},xDy^{3+} phosphor monitored at 350 nm excitation.
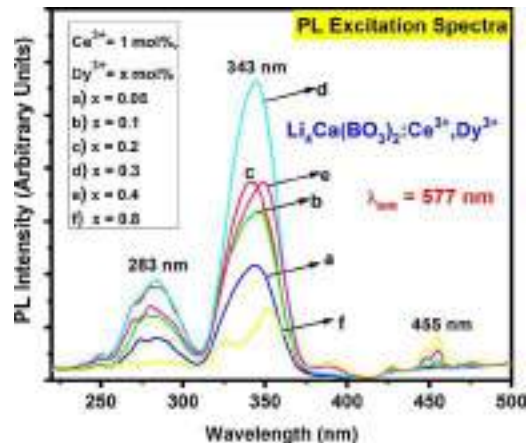
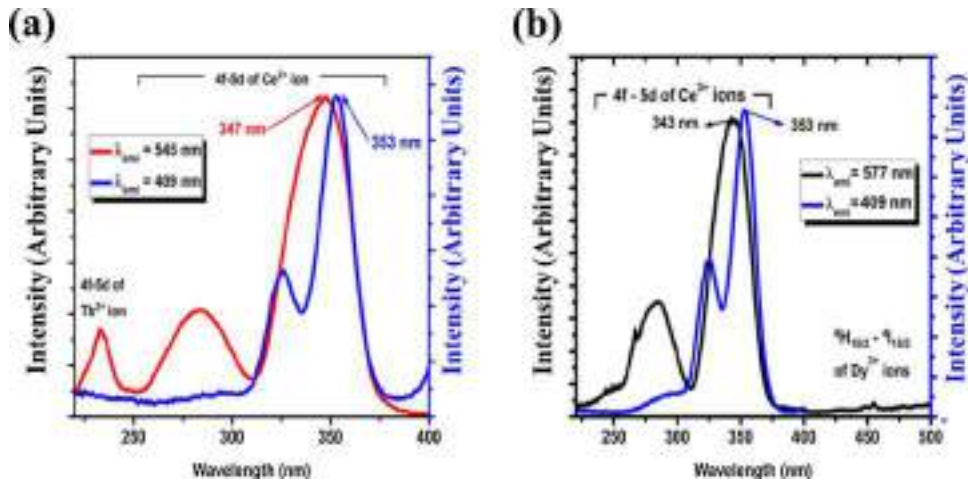**Fig. 17.** PL excitation spectra of the $Li_4Ca(BO_3)_3$:0.01Ce^{3+},xDy^{3+} phosphor monitored at 577 nm emission.

absorption cross-section weakened and led to the decrease in its emission intensity. The cross-relaxation between Dy^{3+} ions resulted in the decrease in both Ce^{3+} and Dy^{3+} emission intensities. Same as the excitation spectrum of the $Li_4Ca(BO_3)_2$:Ce^{3+},Tb^{3+}, the effective broad excitation spectrum of $Li_4Ca(BO_3)_2$:Ce^{3+},Dy^{3+} extends to 375 nm due to the energy transfer from Ce^{3+} to Dy^{3+} ions, and thereby, making the phosphor more suitable for wider applications. The results suggest the occurrence of energy transfer from Ce^{3+} to Dy^{3+}.

The comparison of the excitation spectra of Ce-Tb and Ce-Dy pairs monitored at 545 nm and 577 nm for Tb^{3+} and Dy^{3+}, respectively, with the 411 nm Ce^{3+} emission depict that there is a slight blue shift in the absorption peaks monitored for Tb^{3+} and Dy^{3+}. It can be seen in Fig. 18(a) and (b) that the excitation spectrum monitored for 545 nm (or 577 nm) of Tb^{3+} (or Dy^{3+}) emission is different for 409 nm of Ce^{3+} emission. In the excitation spectra, the Ce^{3+} absorption peak blue shift by about 6 nm (shifts from 353 nm to 347 nm) and 10 nm (shifts from 353 nm to 343 nm) when doped with Tb^{3+} and Dy^{3+} ions, respectively. This can be due to the presence of Tb^{3+}/Dy^{3+} ions in the vicinity of Ce^{3+} ions. During the transfer of energy from Ce to Tb (or Ce to Dy), absorption in the higher 5d states of Ce^{3+} ions increased and this resulted in the shifting of the excitation peaks to a higher energy region. Equation (4) was used to calculate the energy transfer efficiency from Ce^{3+} to Tb^{3+} and Dy^{3+} [22].

$$\eta_T = 1 - \frac{I_s}{I_{s0}}$$
(4)

Where, η_T is the energy transfer efficiency, I_s and I_{s0} are the luminescence intensites of the sensitizer (Ce^{3+}) in the absence and presence of an activator (Tb^{3+} or Dy^{3+}), respectively. The calculated energy transfer efficiencies are tabulated in Table. 1. It can be seen that with the increasing Tb^{3+} ion-concentration, the energy transfer efficiency increased; for intense green emission of Ce^{3+}(1 mol%)-Tb^{3+}(0.8 mol%) combination, it was found to be 79%. Above 0.8 mol% of Tb^{3+} ions, the energy transfer efficiency increased. But this did not result in further increase in thegreen emission due to the concentration quenching of Tb^{3+} ions (Fig. 15(a)). Similarly, for the intense yellow emission of Ce^{3+}(1 mol%)-Dy^{3+}(0.3 mol%) combination, energy the transfer efficiency was 69%. This indicated that the Ce^{3+} is an ideal sensitizer for both Tb^{3+} and Dy^{3+} ions.

The energy transfer between rare earth ions occur *via* exchange interaction or multipolar interaction [39]. To know the exact

Fig. 18. Comparison of the PL excitation spectra of: (a) $Li_4Ca(BO_3)_2$:0.01Ce^{3+}, 0.008Tb^{3+} phosphor monitored at 545 and 409 nm of Tb^{3+} and Ce^{3+} emission and (b) $Li_4Ca(BO_3)_2$:0.01Ce^{3+}, 0.003Dy^{3+} phosphor monitored at 577 and 409 nm of Dy^{3+} and Ce^{3+} emission, respectively.

Table 1
Energy transfer efficiency and color chromaticity coordinates.

Phosphor	Energy Transfer Efficiency, η_T (%)	Color Co-ordinates		Color
		x	y	
$Li_4Ca(BO_3)_2$:0.01Ce^{3+}	–	0.1715	0.0354	Violet
$Li_4Ca(BO_3)_2$:0.01Tb^{3+}	–	0.2781	0.5416	Green
$Li_4Ca(BO_3)_2$:0.01Dy^{3+}	–	0.3520	0.3820	White
$Li_4Ca(BO_3)_2$:0.01Ce^{3+},0.002Tb^{3+}	67	0.2324	0.3646	Bluish green
$Li_4Ca(BO_3)_2$:0.01Ce^{3+},0.004Tb^{3+}	80	0.2276	0.3600	Bluish green
$Li_4Ca(BO_3)_2$:0.01Ce^{3+},0.008Tb^{3+}	79	0.2223	0.3161	Bluish green
$Li_4Ca(BO_3)_2$:0.01Ce^{3+},0.012Tb^{3+}	86	0.2015	0.2150	Blue
$Li_4Ca(BO_3)_2$:0.01Ce^{3+},0.016Tb^{3+}	93	0.2050	0.1605	Blue
$Li_4Ca(BO_3)_2$:0.01Ce^{3+},0.0005Dy^{3+}	48	0.1708	0.0518	Violet
$Li_4Ca(BO_3)_2$:0.01Ce^{3+},0.001Dy^{3+}	52	0.1704	0.0516	Violet
$Li_4Ca(BO_3)_2$:0.01Ce^{3+},0.002Dy^{3+}	63	0.1698	0.0525	Violet
$Li_4Ca(BO_3)_2$:0.01Ce^{3+},0.003Dy^{3+}	69	0.2058	0.1082	Indigo
$Li_4Ca(BO_3)_2$:0.01Ce^{3+},0.004Dy^{3+}	80	0.2036	0.1065	Indigo
$Li_4Ca(BO_3)_2$:0.01Ce^{3+},0.008Dy^{3+}	85	0.1948	0.0937	Indigo

mechanism responsible for energy transfer, there must be the knowledge of the critical distance (R_c) between the sensitizer and activator and this can be calculated using the concentration quenching method. Blasse [40] has given the formula for R_c calculation as follows:

$$R_c = 2 \times (\frac{3V}{4\pi X_c N})^{1/3}$$

(5)

Where, V is the volume of the unit cell, X_c is the total concentration of Ce^{3+} and Tb^{3+} ions, at which the ET efficiency is about 50%, and N is the number of available sites for substitution of the dopant in the unit cell. Here, the values of V and N were 260.4298 Å^3 and 2, respectively. The value of X_c for Ce-Tb and Ce-Dy combinations were 0.012 and 0.011 mol, respectively. The calculated R_c values for Ce-Tb and Ce-Dy combinations were 27.47 Å and 28.28 Å, respectively. For the exchange interaction to occur, the critical distance must be of the order of 5 Å, and thus, the energy transfer in the present cases must not be occuring *via* exchange interaction. Therefore, the possible mechanism for energy transfer must be multipolar interaction. To figure out the type of multipolar interaction, Dexter's energy transfer formula of multipolar interaction and Reisfeld's approximation were used [41,42].

$$\frac{\eta_{S0}}{\eta_s} \propto C^{\frac{\alpha}{3}}$$

(6)

Where, η_{S0} and η_S represent the luminescence quantum efficiencies of sensitizer (Ce^{3+}) in the absence and presence of activators (Tb^{3+}/Dy^{3+}), C is the total concentration of Ce^{3+} and Tb^{3+}/Dy^{3+} ions, and the value of α = 6, 8 and 10 corresponds to the dipole–dipole, dipole–quadrupole and quadrupole–quadrupole interactions, respectively [43]. The ratio ($\frac{\eta_{S0}}{\eta_s}$) can be replaced by the ratio ($\frac{I_{S0}}{I_s}$), where, I_{S0} and I_S represent the luminescence emission intensity of sensitizer (Ce^{3+}) in the absence and presence of activators (Tb^{3+}/Dy^{3+}). Thus, the equation (6) can be written as
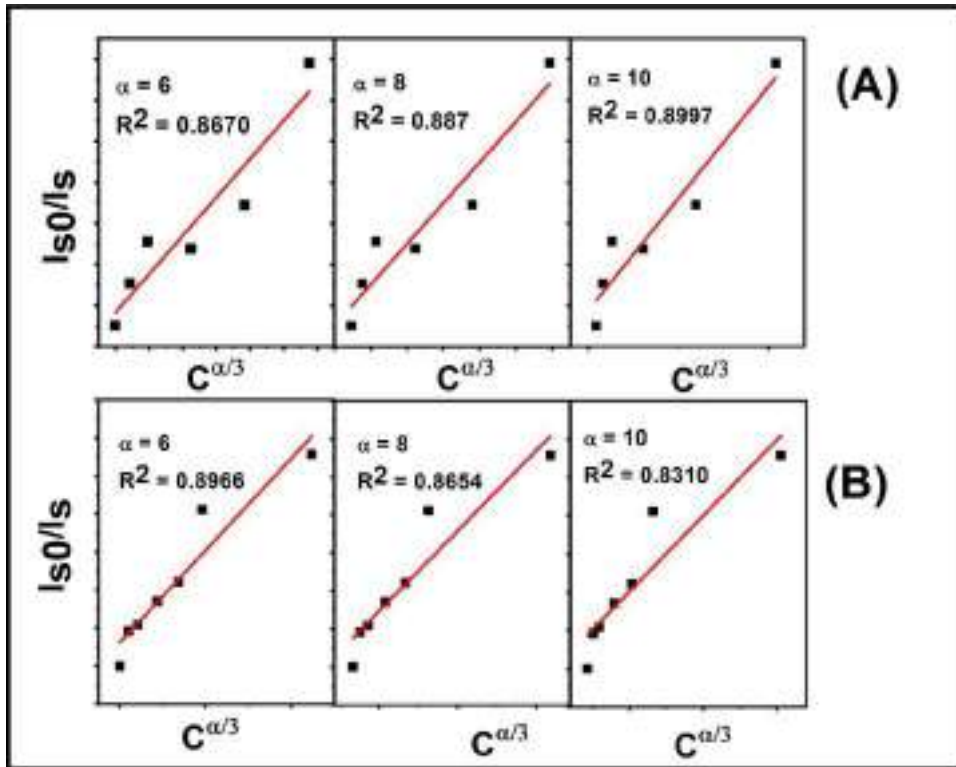
Fig. 19. The dependence between $\frac{I_{S0}}{I_S}$ and $C^{\frac{\alpha}{3}}$ for $\alpha = 6, 8, 10$ with linear fitting.

$$\frac{I_{S0}}{I_s} \propto C^{\frac{\alpha}{3}}$$

(7)

The dependence between $\frac{I_{S0}}{I_S}$ and $C^{\frac{\alpha}{3}}$ based on the above equation and the corresponding linear fitting results are illustrated in Fig. 19. For the Ce→Tb energy transfer, the best fit was observed for $\alpha = 10$ (Fig. 19(A)) and for Ce→Dy energy transfer the best fit was observed for $\alpha = 6$ (Fig. 19(B)). Thus, we may conclude that the Ce→Tb energy transfer occured *via* electric quadrupole–quadrupole interaction and Ce-Dy energy transfer occured *via* electric dipole–dipole interaction.

Fig. 20 illustrates the energy levels of the Ce^{3+}, Tb^{3+}, and Dy^{3+}. For Ce→Tb energy transfer, the photoluminescence process could be demonstrated as follow: Ce^{3+} is directly excited at 350 nm, then relaxed to the lowest 5d state. Some of the Ce^{3+} ions relaxed to the 4f state with photon emission, while some others transferred their energy to the excited level (namely $^5G_5$, and $^5D_3$) of the nearest Tb^{3+} ions. After relaxing to state $^5D_4$, Tb^{3+} ions transited to ^7FJ (J = 6, 5, 4, 3) with the emission of their corresponding photons. Similarly, for Ce→Dy energy transfer, after excitation by 350 nm, the electrons will be excited from the ground state of 4f to the 5d level of Ce^{3+}. In the excited state, some of these electrons relaxed to the lowest 5d crystal field splitting state and then returned to the ground state to produce emissions at 378 and 409 nm, while some others transfered the excitation energy to the neighboring Dy^{3+}. The $[^4I_{13/2} + {}^4F_{7/2}]$ level was populated by this energy transfer and then, the electrons non-radiatively relaxed to the $^4F_{9/2}$ level and the Dy^{3+} emissions were produced *via* radiative transitions of $^4F_{9/2} \rightarrow {}^6H_{15/2}$ and $^4F_{9/2} \rightarrow {}^6H_{13/2}$.

3.5. Photometry

The color chromaticity coordinates were determined using the color calculator software from radiant imaging on a CIE-1931 color chart. The CIE color coordinates (marked by ×) of the phosphors $Li_4Ca(BO_3)_2:Ce^{3+}$, $Li_4Ca(BO_3)_2:Tb^{3+}$, $Li_4Ca(BO_3)_2:Dy^{3+}$, $Li_4Ca(BO_3)_2:Ce^{3+},xTb^{3+}$ and $Li_4Ca(BO_3)_2:Ce^{3+},yDy^{3+}$, are presented in Fig. 21 and listed in Table 1. The color coordinates of $Li_4Ca(BO_3)_2:Ce^{3+}$, $Li_4Ca(BO_3)_2:Tb^{3+}$, $Li_4Ca(BO_3)_2:Dy^{3+}$, $Li_4Ca(BO_3)_2:Ce^{3+},xTb^{3+}$ and $Li_4Ca(BO_3)_2:Ce^{3+},yDy^{3+}$ are lying in the violet, green, white, green to bluish green and violet to indigo regions, respectively.

4. Conclusion

Different series of $Li_4Ca(BO_3)_2$ singly doped with Ce^{3+}, Tb^{3+} and Dy^{3+} as well as codoped with Ce^{3+}-Tb^{3+} and Ce^{3+}-Dy^{3+} pairs were successfully synthesized by the solid-state method. XRD results confirmed the pure phase formation of $Li_4Ca(BO_3)_2$. The FTIR analysis confirmed the vibration modes of the BO_3^{3-} group. The band gap using DRS was measured to be 4.98 eV. Under 350 nm excitation, $Li_4Ca(BO_3)_2:Ce^{3+}$ emitted broadband with two peaks centered at 378 and 409 nm due to 5d-4f ($^2F_{5/2,7/2}$) transition of the
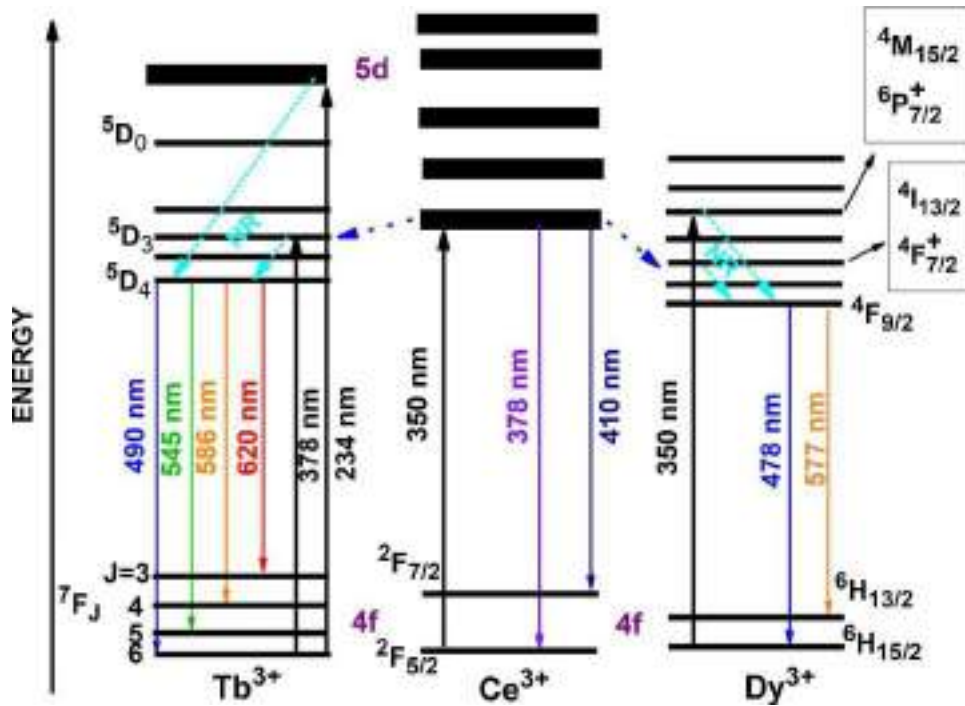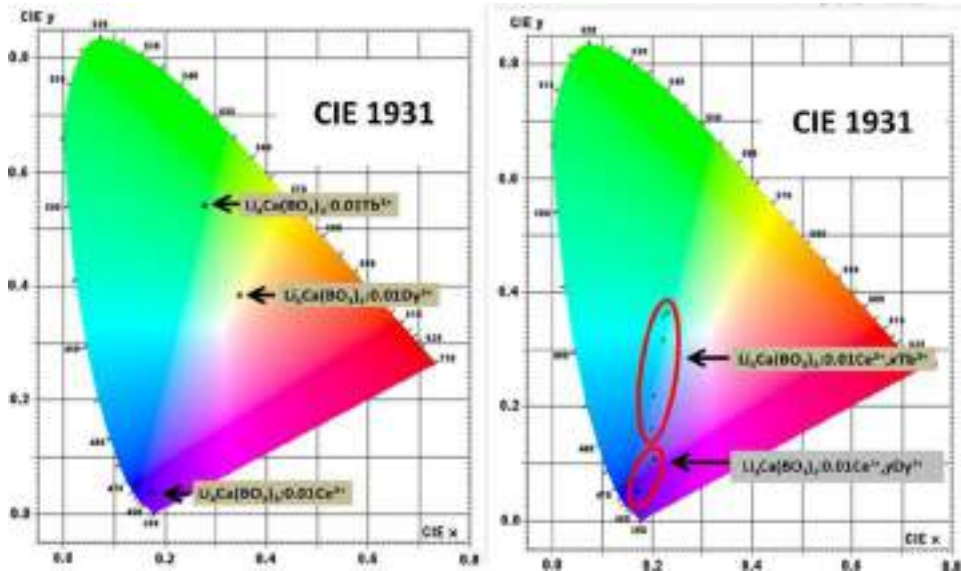
Fig. 20. Energy level diagram illustrating the Ce→Tb, Ce→Dy energy transfer process.

Fig. 21. CIE color chromaticity diagrams.

Ce^{3+} ions. The $Li_4Ca(BO_3)_2:Tb^{3+}$ phosphor excited by 378 nm emitted a dominant green peak at 545 nm. The $Li_4Ca(BO_3)_2:Dy^{3+}$ shows two characteristic peaks at 489 nm and 577 nm due to the transition from the $^4F_{9/2}$ excited state to the $^6H_{15/2}$ and $^6H_{13/2}$ states of the Dy^{3+} ions. When codoped with Ce^{3+}, the excitation spectrum of Tb^{3+} activated $Li_4Ca(BO_3)_2$ extended to 375 nm. The PL spectra demonstrated that Ce^{3+} ion absorbed UV photons *via* the allowed 4f-5d absorption and greatly enhanced the green emission of Tb^{3+} ions under the 350 nm excitation. Excitation spectra monitored under 545 nm emission of the $Li_4Ca(BO_3)_2:Ce^{3+},Tb^{3+}$ phosphor showed absorption bands of both Ce^{3+} ions and Tb^{3+} ions. Due to the occurrence of the energy transfer process, the emission hue of the phosphor eventually varied from blue (0.1715, 0.0354) to bluish green (0.2324, 0.3646) by varying the Tb^{3+} ion-concentration. The energy transfer from Ce^{3+} to Tb^{3+} ions was certified by the variation tendency of $Li_4Ca(BO_3)_2:0.01Ce^{3+},xTb^{3+}$ with different Tb^{3+} concentration and the major energy transfer mechanism was proved. Similarly, when codoped with Ce^{3+} ions,

$Li_4Ca(BO_3)_2$:Dy^{3+} greatly enhanced the Dy^{3+} emission. The excitation spectra monitored at 577 nm emission showed absorption due to both Ce^{3+} and Dy^{3+} ions, which proved that the energy was transferred from $Ce^{3+} \rightarrow Dy^{3+}$. As the Ce^{3+} emission in Ce-Dy codoped system remained dominant, the emission hue did not change significantly and emission remained in the violet region. The as-synthesized $Li_4Ca(BO_3)_2$:Ce^{3+},Tb^{3+} has potential applications as a green emitting phosphor in NUV converted WLEDs and displays.

Declaration of Competing Interest

The authors declare that they have no known competing financial interests or personal relationships that could have appeared to influence the work reported in this paper.

Acknowledgments

References

[1] P. Barpanda, D. Dwibedi, S. Ghosh, Y. Kee, S. Okada, Lithium metal borate (LiMBO$_3$) family of insertion materials for Li-ion batteries: a sneak peak, Ionics (Kiel) 21 (2015) 1801–1812, https://doi.org/10.1007/s11581-015-1463-6.

[2] Z. Fu, S. Pan, F. Yang, S. Gu, X. Lei, Y. Heng, G. Ren, M. Qi, Neutron detection properties of Li$_6$Y(BO$_3$)$_3$:Ce crystal, Radiat. Meas. 72 (2015) 39–43, https://doi.org/10.1016/j.radmeas.2014.11.010.

[3] M. Prokic, Lithium borate solid TL detectors, Radiat. Meas. 33 (2001) 393–396, https://doi.org/10.1016/S1350-4487(01)00039-7.

[4] P. Chen, M. Xia, R.K. Li, A terbium rich orthoborate LiSrTb$_2$(BO$_3$)$_3$ and its analogues, New J. Chem. 39 (2015) 9389–9395, https://doi.org/10.1039/C5NJ01913C.

[5] L. Wu, J.C. Sun, Y. Zhang, S.F. Jin, Y.F. Kong, J.J. Xu, Structure determination and relative properties of novel chiral orthoborate KMgBO$_3$, Inorg. Chem. 49 (2010) 2715–2720, https://doi.org/10.1021/ic901963t.

[6] U. Fawad, M. Oh, H. Park, S. Kim, H.J. Kim, Luminescent investigations of Li$_6$Lu(BO$_3$)$_3$:Tb^{3+}, Dy^{3+} phosphors, J. Alloys Compd. 610 (2014) 281–287, https://doi.org/10.1016/j.jallcom.2014.05.001.

[7] S. Tamboli, B. Rajeswari, S.J. Dhoble, Investigation of UV-emitting Gd^{3+} -doped LiCaBO$_3$ Phosphor, (2015), pp. 4–9, https://doi.org/10.1002/bio.2994.

[8] G.B. Nair, H.C. Swart, S.J. Dhoble, A review on the advancements in phosphor-converted light emitting diodes (pc-LEDs): phosphor synthesis, device fabrication and characterization, Prog. Mater. Sci. (2019) 100622, , https://doi.org/10.1016/j.pmatsci.2019.100622 in press.

[9] R.S. Kumar, V. Ponnusamy, V. Sivakumar, M.T. Jose, Role of monovalent co-dopants on the PL emission properties of YAl$_3$(BO$_3$)$_4$:Ce^{3+} phosphor, J. Rare Earths. 32 (2014) 927–932, https://doi.org/10.1016/S1002-0721(14)60164-2.

[10] R. Yu, S. Zhong, N. Xue, H. Li, H. Ma, Synthesis, structure, and peculiar green emission of NaBaBO$_3$:Ce^{3+} phosphors, Dalton Trans. 43 (2014) 10969–10976, https://doi.org/10.1039/c4dt00859f.

[11] J. Hou, W. Jiang, Y. Fang, F. Huang, Red, green and blue emissions coexistence in white-light-emitting Ca$_{11}$(SiO$_4$)$_4$(BO$_3$)$_2$:Ce^{3+},Eu^{2+},Eu^{3+} phosphor, J. Mater. Chem. C. 1 (2013) 5892, https://doi.org/10.1039/c3tc30933a.

[12] L. Yang, Y. Wan, Y. Huang, C. Chen, H.J. Seo, Development of YK$_3$B$_6$O$_{12}$:RE (RE = Eu^{3+}, Tb^{3+}, Ce^{3+}) tricolor phosphors under near-UV light excitation, J. Alloys Compd. 684 (2016) 40–46, https://doi.org/10.1016/j.jallcom.2016.04.052.

[13] D.-Y. Wang, Y.-C. Chen, C.-H. Huang, B.-M. Cheng, T.-M. Chen, Photoluminescence investigations on a novel green-emitting phosphor Ba$_3$Sc(BO$_3$)$_3$:Tb^{3+} using synchrotron vacuum ultraviolet radiation, J. Mater. Chem. 22 (2012) 9957–9962, https://doi.org/10.1039/c2jm16350k.

[14] R. Guo, S. Tang, F. Zheng, Z. Yang, D. Tan, Synthesis and luminescent properties of a new phosphor, La$_2$CaB$_8$O$_{16}$:RE^{3+} (RE=Eu, Tb), J. Alloys Compd. 550 (2013) 459–462, https://doi.org/10.1016/j.jallcom.2012.10.077.

[15] Z.S. Khan, N.B. Ingale, S.K. Omanwar, Synthesis and luminescence studies of NaSr$_4$(BO$_3$)$_3$:Dy^{3+} phosphors, Opt. – Int. J. Light Electron. Opt. 127 (2016) 6062–6065, https://doi.org/10.1016/j.ijleo.2016.04.006.

[16] İ. Pekgözlü, Photoluminescence properties of M$_2$Mg(BO$_3$)$_2$:Sm^{3+} (M:Sr and Ba), J. Lumin. 134 (2013) 8–13, https://doi.org/10.1016/j.jlumin.2012.09.031.

[17] M.M. Yawalkar, G.D. Zade, K.V. Dabre, S.J. Dhoble, Luminescence study of Eu^{3+} doped Li$_6$Y(BO$_3$)$_3$ phosphor for solid-state lighting, Luminescence 31 (2016) 1037–1042, https://doi.org/10.1002/bio.3006.

[18] L. Wu, C. Wang, X.L. Chen, X.Z. Li, Y.P. Xu, Y.G. Cao, Ab initio structure determination of new compound Li$_4$CaB$_2$O$_6$, J. Solid State Chem. 177 (2004) 1847–1851, https://doi.org/10.1016/j.jssc.2003.11.023.

[19] V.Kumar Neharika, V.K. Singh, J. Sharma, O.M. Ntwaeaborwa, H.C. Swart, Synthesis and photoluminescence study of a single dopant near white light emitting Li$_4$CaB$_2$O$_6$:Dy^{3+} nanophosphor, J. Alloys Compd. 688 (2016) 939–945, https://doi.org/10.1016/j.jallcom.2016.07.039.

[20] N. Wazir, V.K. Singh, J. Sharma, A.K. Bedyal, V. Kumar, H.C. Swart, Surface and spectral studies of Sm^{3+} doped Li$_4$Ca(BO$_3$)$_2$ phosphors for white light emitting diodes, J. Alloys Compd. 738 (2017) 97–103, https://doi.org/10.1016/j.jallcom.2017.12.118.

[21] Z. Leng, G. Yu, L. Li, Y. Liu, N. Zhang, S. Gan, Enhanced of Tb^{3+} emission in KSr$_4$(BO$_3$)$_3$:Dy^{3+}, Tb^{3+} phosphors via energy transfer from Dy^{3+}, J. Alloys Compd. 651 (2015) 679–684, https://doi.org/10.1016/j.jallcom.2015.08.184.

[22] Z. Cheng, J. Yu, Y. Zhang, N. Zou, Luminescence and energy transfer mechanism of α-Ba$_3$Y(BO$_3$)$_3$:Ce^{3+},Tb^{3+}, J. Lumin. 192 (2017) 1004–1009, https://doi.org/10.1016/j.jlumin.2017.08.041.

[23] X. Chen, Z. Xia, Synthesis and color-tunable luminescence of Ce^{3+}, Tb^{3+} codoped Sr$_6$YSc(BO$_3$)$_6$ phosphor, J. Solid State Light. 1 (2014) 4, https://doi.org/10.1186/2196-1107-1-4.

[24] M. Shi, C. Zhu, M. Zhang, M. Lu, J. Liu, NaCa$_4$(BO$_3$)$_3$: Ce, Dy, Eu phosphors for light emitting diode applications, Polyhedron 140 (2018) 19–24, https://doi.org/10.1016/j.poly.2017.10.021.

[25] H. Liu, Z. Guo, Ce^{3+} and Dy^{3+} doped Sr$_3$B$_2$O$_6$: solid state synthesis and tunable luminescence, J. luminescence 187 (2017) 181–185.

[26] G.B. Nair, S.J. Dhoble, White light emission through efficient energy transfer from Ce^{3+} to Dy^{3+} ions in Ca$_3$Mg$_3$(PO$_4$)$_4$ matrix aided by Li$^+$ charge compensator, J. Lumin. 192 (2017) 1157–1166, https://doi.org/10.1016/j.jlumin.2017.08.047.

[27] J. Rodríguez-Carvajal, Recent advances in magnetic structure determination by neutron powder diffraction, Phys. B Condens. Matter. 192 (1993) 55–69, https://doi.org/10.1016/0921-4526(93)90108-I.

[28] A. Rulmont, M. Almou, Vibrational spectra of metaborates with infinite chain structure: LiBO$_2$, CaB$_2$O$_4$, SrB$_2$O$_4$, Spectrochim. Acta Part A Mol. Spectrosc. 45 (1989) 603–610, https://doi.org/10.1016/0584-8539(89)80013-3.

[29] G. Kortüm, W. Braun, G. Herzog, Principles and techniques of diffuse-reflectance spectroscopy, Angew. Chemie Int. Ed. English 2 (1963) 333–341, https://doi.

org/10.1002/anie.196303331.

[30] N. Sangiorgi, L. Aversa, R. Tatti, R. Verucchi, A. Sanson, Spectrophotometric method for optical band gap and electronic transitions determination of semi-conductor materials, Opt. Mater. (Amst). 64 (2017) 18–25, https://doi.org/10.1016/j.optmat.2016.11.014.

[31] J. Tauc, Optical properties and electronic structure of amorphous Ge and Si, Mater. Res. Bull. 3 (1968) 37–46, https://doi.org/10.1016/0025-5408(68)90023-8.

[32] G.B. Nair, S.J.J. Dhoble, Highly enterprising calcium zirconium phosphate [CaZr$_4$(PO$_4$)$_6$:Dy^{3+}, Ce^{3+}] phosphor for white light emission, RSC Adv. 5 (2015) 49235–49247, https://doi.org/10.1039/C5RA07306E.

[33] E. Pavitra, G.S.R. Raju, Y.H. Ko, J.S. Yu, A novel strategy for controllable emissions from Eu^{3+} or Sm^{3+} ions co-doped SrY$_2$O$_4$:Tb^{3+} phosphors, Phys. Chem. Chem. Phys. 14 (2012) 11296, https://doi.org/10.1039/c2cp41722g.

[34] S. Liu, Y. Liang, M. Tong, D. Yu, Y. Zhu, X. Wu, C. Yan, Photoluminescence properties of novel white phosphor of Dy^{3+}-doped LaBSiO$_5$ glass, Mater. Sci. Semicond. Process. 38 (2015) 266–270, https://doi.org/10.1016/j.mssp.2015.04.009.

[35] S. Dutta, S. Som, S.K. Sharma, Luminescence and photometric characterization of K$^+$ compensated CaMoO$_4$:Dy^{3+} nanophosphors, Dalton Trans. 42 (2013) 9654–9661, https://doi.org/10.1039/c3dt50780g.

[36] G.B. Nair, S.J. Dhoble, White light emitting MZr$_4$(PO$_4$)$_6$:Dy^{3+}(M = Ca, Sr, Ba) phosphors for WLEDs, J. Fluoresc. 27 (2017) 575–585, https://doi.org/10.1007/s10895-016-1985-y.

[37] Y. Liu, Z. Yang, Q. Yu, X. Li, Y. Yang, P. Li, Luminescence properties of Ba$_2$LiB$_5$O$_{10}$:Dy^{3+} phosphor, Mater. Lett. 65 (2011) 1956–1958, https://doi.org/10.1016/j.matlet.2011.04.002.

[38] G.V. Lokeswara Reddy, L. Rama Moorthy, P. Packiyaraj, B.C. Jamalaiah, Optical characterization of YAl$_3$(BO$_3$)$_4$:Dy^{3+}–Tm^{3+} phosphors under near UV excitation, Opt. Mater. 35 (2013) 2138–2145, https://doi.org/10.1016/j.optmat.2013.05.038.

[39] D.L. Dexter, A theory of sensitized luminescence in solids, J. Chem. Phys. 21 (1953) 836, https://doi.org/10.1063/1.1699044.

[40] G. Blasse, Energy transfer in oxidic phosphors, Phys. Lett. A 28 (1968) 444–445, https://doi.org/10.1016/0375-9601(68)90486-6.

[41] D.L. Dexter, J.H. Schulman, Theory of concentration quenching in inorganic phosphors, J. Chem. Phys. 22 (1954) 1063, https://doi.org/10.1063/1.1740265.

[42] R. Reisfeld, E. Greenberg, R. Velapoldi, B. Barnett, Luminescence quantum efficiency of Gd and Tb in borate glasses and the mechanism of energy transfer between them, J. Chem. Phys. 56 (1972) 1698–1705, https://doi.org/10.1063/1.1677427.

[43] Z. Xia, Y. Liang, D. Yu, M. Zhang, W. Huang, M. Tong, J. Wu, J. Zhao, Photoluminescence properties and energy transfer in color tunable BaY2Si$_3$O$_{10}$:Ce,Tb phosphors, Opt. Laser Technol. 56 (2014) 387–392, https://doi.org/10.1016/j.optlastec.2013.09.014.
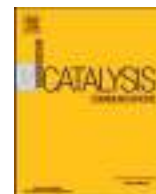
Short communication

Copper supported Mg−Al hydrotalcite derived oxide catalyst for enol carbamates synthesis via C−H bond activation of formamides

Rakhi Vishwakarma[a], Chandrakanth Gadipelly[a,c], Akhil Nakhate[a,b], Gunjan Deshmukh[a], Lakshmi Kantam Mannepalli[a,*]

[a] *Department of Chemical Engineering, Institute of Chemical Technology, Nathalal Parekh Marg, Matunga, Mumbai 400019, India*
[b] *Department of Chemistry, Bajaj College of Science, Wardha 442001, India*
[c] *The Wolfson Faculty of Chemical Engineering, Technion-Israel Institute of Technology, Haifa 3200003, Israel*

A B S T R A C T

A series of different copper supported Mg−Al−HT derived oxide catalysts have been synthesized by co-precipitation method followed by wet impregnation and calcination. The prepared catalysts were used for enol carbamate synthesis via C−H bond activation of dimethylformamide with ethyl acetoacetate. 15% Cu/Mg−Al−HT derived oxide was the best catalyst with 89% conversion towards ethyl acetoacetate at 100 °C using TBHP as an oxidizing agent. The fresh and spent catalysts have been characterized by XRD, SEM, physisorption, FTIR, TPR-TPD, and XPS. Cu/Mg−Al−HT derived oxide catalyst showed reusability without loss in catalytic activity for three cycles.

1. Introduction

Carbamates are of remarkable interest due to their wide application in various industries, for example in agrochemicals where they are utilized as herbicides, fungicides and pesticides, as drug intermediates in the pharmaceutical industry, for the production of polyurethanes in the polymer industries and in peptide synthesis [1]. Carbamates are used due to their chemical stability towards acids, bases, and hydrogenation. They contain excellent pharmaceutical properties such as antibacterial, neuroprotective, antineoplastic, and anti-filarial agents. There are various green alternative routes for carbamate synthesis like transesterification of substituted urea [2], oxidative carbonylation of amines [3], reductive carbonylation of nitro compounds [4], and methoxy carbonylation of amines [5,6]. A practical method is described for the synthesis of polyurea derivatives from CO_2 and diamines in the absence of the catalysts, and the resulted urea derivatives further reacted with dialkyl carbonates to afford N-substituted dicarbamates using MgO−ZnO catalyst [7]. Formamides are known to react differently under different reaction conditions, as summarized by Muzart in his review, that dimethylformamide is the most widely used derivative which can be a source of oxygen, CO, Me_2NCO, Me_2N and is vital in organometallic chemistry, catalysis and organic synthesis [8]. Not only it is an effective polar solvent, but due to its structure, it is also used as a multipurpose reagent in many reactions. Direct C−H bond activation of

formamides has been studied by aminocarbonylation of aryl halides using transition metal catalysts with DMF [9]. Metal-free C−H bond activation has been achieved by direct amidation of azoles with formamides using tertbutyl perbenzoate. Wang and coworkers achieved a possible synthesis of a free radical of dimethylformamide under peroxide conditions. [10] Direct coupling of β-dicarbonyl- or 2-carbonyl-substituted phenols with N, N′-disubstituted formamides under oxidative conditions is also used for carbamate synthesis [11]. Aromatic amides are produced by the coupling of formamides with aryl halides using palladium catalysts in the presence of phosphoryl chloride as an additive. [12] Earlier, we synthesized a series of HT-derived oxide catalysts (Cu−Al, Cu−Fe, Mg−Al, Mg−Fe, Ni−Fe and Ni−Al) from the parent HT–like material followed by calcination and studied their activity for the model reaction of the amidation of carboxylic acids with DMF using TBHP as an oxidant and also the amidation of substituted benzaldehydes [13].

Transition-metal-catalyzed cross-coupling reactions are considered as potent methods for carbon-heteroatom bond formation. Palladium complexes are recognized to be the efficient catalysts for this reaction. Therefore, taking this study forward, we evaluated other transition - metal catalysts, copper-based coupling reactions [14]. There are reports on the formation of aryl carbamates by the reaction of aryl boronic acids with potassium cyanate in the presence of alcohol using a copper catalyst.

The cost of homogeneous transition metal-catalyzed cross-coupling reactions and its single-use often restricts its usage. Therefore, heterogeneous catalytic systems have been gained importance for the synthesis of enol carbamates and amides [15,16]. Investigation of copper nanoparticles on charcoal for the synthesis of enol carbamates and amides by the oxidative coupling of N, N-dialkylformamides with 1,3-dicarbonyl compounds and amine hydrochloride salts with aromatic aldehydes, respectively was carried out [17].

Hydrotalcites ($Mg_6Al_2 (OH)_{16} CO_3.4H_2O$) are a class of solid bases which have been used widely for many organic reactions [18–21]. Mixed magnesium-aluminum oxides are formed with a large surface area consisting of acidic and basic sites when hydrotalcites are calcined at 500 °C. Acidic and basic properties can be adjusted by varying metal and metal composition [22].

We began this work with the synthesis of magnesium aluminum hydrotalcite (Mg−Al−HT) derived oxide as reported by Kantam et al. [23], which was further loaded with copper with varying amounts as per the procedure reported by Benito et al. [24] Then, we moved towards the anticipation of DMF activation under oxidative conditions to synthesize the coupled product with carbon nucleophiles using different copper loaded Mg−Al−HT derived oxides to determine the best catalyst for the reaction. For our preliminary experiments, ethyl acetoacetate was chosen as carbon nucleophile and treated with an excess of DMF and, in the presence of 15% Cu on Mg−Al−HT derived oxide catalyst and TBHP (70% in water) as an external oxidant (Scheme 1).

2. Experimental

Please See Supplementary Information.

3. Catalyst characterization

3.1. XRD analysis

The XRD of calcined Mg−Al−HT and copper supported Mg−Al−HT derived oxide catalysts (5% Cu/Mg−Al−HT, 10% Cu/Mg−Al−HT, 15% Cu/Mg−Al−HT, and 20% Cu/Mg−Al−HT) gives a crystalline structure as shown in Fig. SI-1 (Supplementary Information, Fig. 1). Calcined Mg−Al−HT shows reflections at 11°, 23°, 34°, 38°, 43°, and 62° and planes corresponding are (003), (006), (012), (015), (200) and (220), respectively Fig. SI-1a. Mixed oxides are formed from layered double hydroxides by the new broad deflections present at 43° and 62°, which correspond to (200) and (220) planes, respectively [25]. The lattice of MgO and Al_2O_3 were found to be as face-centered cubic and rhombohedral. Calcined Mg−Al−HT is compared with the supported copper Mg−Al−HT derived oxide catalysts made with the increasing concentration of copper in the range of 5, 10, 15, and 20% wt. loading respectively. The presence of copper oxide was in the form of base-centered monoclinic and was seen to increase in the XRD pattern by a sharp peak which goes descending with the increase in the concentration of copper as shown in the figure. Mg−Al−HT derived oxide showed newer peaks having 2θ values of 35°, 39°, 49°, 54°, 58°, 62°, 66°, 68°, 75° which correspond to the CuO phase in the material [26].)

3.2. FTIR studies

The FTIR of calcined Mg−Al−HT and copper supported Mg−Al−HT derived oxide catalysts (5% Cu/Mg−Al−HT, 10% Cu/Mg−Al−HT, 15%

Cu/Mg−Al−HT, and 20% Cu/Mg−Al−HT) are shown in Fig. SI-2 (Supplementary Information, Fig. 2). Hydrotalcite formation was confirmed by stretching of hydrogen bonding between the brucite layers with an absorption band at 3425 cm^{-1} as shown in Fig. SI-2a. The peak at 1367 cm^{-1} determines interlayer carbonates. The low-frequency band at 756 cm^{-1} and 623 cm^{-1} corresponds to Al−O and Mg−O. The double absorption band at 1049–997 cm^{-1} for samples (c), (d) and (e) was caused by the significant symmetry of CO_3^{2-}. This dual-band was less in the sample (c) than (d) and (e) [27].

3.3. Nitrogen adsorption-desorption isotherm

The Brunauer-Emmett-Teller (BET) surface area of calcined Mg−Al−HT derived oxide was measured to be 189.2 m^2/g, and the pore volume and pore size was 0.748 cc/g and 18.6 nm, respectively. Surface area analysis data for 5%, 10%, 15%, and 20% of Cu on Mg−Al−HT derived oxides are compared and illustrated in Fig. SI-3 (Supplementary Information, Fig. 3) below. The nitrogen adsorption-desorption isotherm for Mg−Al−HT derived oxide, and supported Cu/Mg−Al−HT found to be type IV with the characteristic of mesoporous material having a small plateau at high relative pressure. The BET surface area (SBET) along with the pore size and pore volume of Mg−Al−HT derived oxide, and the other Cu supported catalysts have been represented in Table SI-1 (Supplementary Information, Table SI-1). It is evident from the data that with an incremental copper loading there is decrease in the pore volume and surface area because of the regional pore-blocking due to the sintering/aggregation of copper species and/or collapse of the lamella due to the calcination temperature. [28,29] The most efficient catalyst 15% Cu supported Mg−Al−HT derived oxide showed a larger surface area compared to lower Cu supported catalyst which might be due to the formation of new surface adsorption sites facilitated from the high dispersion of Cu on the hydrotalcite surface. The decrease in surface area for catalyst with 20% copper loading may be due to aggregation of the copper species and is evident from the decrease in the pore size and pore volume. The copper is very well dispersed in the hydrotalcite materials is also observed in the elemental mapping and similar observation has been reported earlier. [13]

3.4. Microscopic analysis (SEM, EDS and HRTEM)

The surface morphology and elemental analysis of calcined Mg−Al−HT and copper supported Mg−Al−HT derived oxide catalysts was done by SEM and EDS, respectively. Fig. SI-4 (Supplementary Information, Fig. SI-4) shows the apparent difference in the morphology of Mg−Al−HT and copper supported Mg−Al−HT derived oxide analyzed by SEM. The calcined Mg−Al−HT shows an aggregate of a small particle with a smooth surface and in copper supported Mg−Al−HT derived oxide showed the rough surface with the agglomeration of copper nanoparticles. EDS was done for confirmation of aluminum, copper, and magnesium which remain constant in the synthesized catalyst. Furthermore the TEM analysis of calcined Mg−Al−HT and copper supported materials supports the observation of pore blockages due to deposition of copper into the Mg−Al−HT pores and surface Fig. SI-5a & 5b (Supplementary Information, Fig. SI-5) Also, the SAED pattern, (Fig. SI-5c & 5d) shows a perfect crystalline phase of the supported catalyst with array of the Mg−Al−HT catalyst having copper. Fig. SI-6 (Supplementary Information, Fig. SI-6) shows the elemental
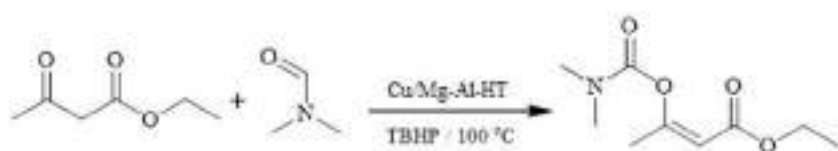
Scheme 1. Enol carbamate synthesis of ethylacetoacetate with formamide using Cu supported Mg−Al−HT derived oxide catalyst using TBHP as an oxidant at 100 ºC
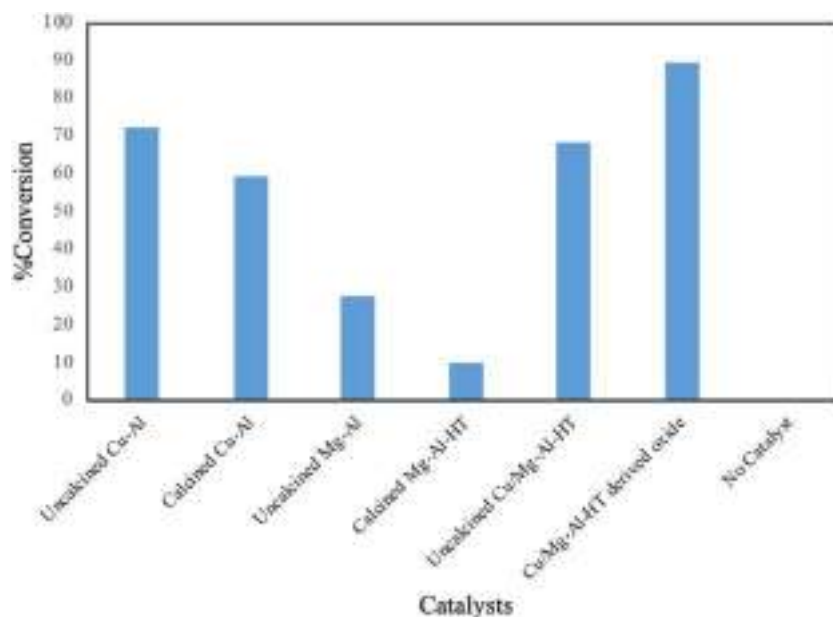
Fig. 1. Screening of various catalysts prepared for enol carbamate synthesis.
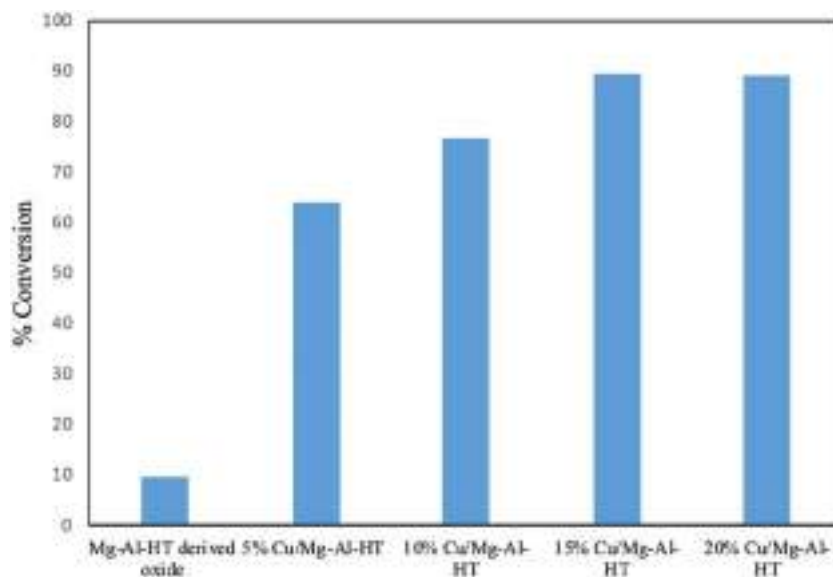

Fig. 2. Effect of copper loading on Cu supported Mg-Al-HT derived oxides [Reaction conditions: EAA (1 mmol.), Catalyst (10 wt% w.r.t. to EAA), DMF (2 mL), TBHP (1.5 equiv.), 100 °C, 12 h].

mapping image of the catalyst which shows an even distribution of copper species (white dots) over the Mg−Al−HT derived oxide. It can be concluded from the figure that the copper has evenly dispersed on the surface of hydrotalcite derived oxide.

3.5. XPS analysis

X-ray photoelectron spectroscopy (XPS) analysis was done to obtain the chemical state of the active metal copper present in the Cu/Mg-Al−HT derived oxide. The survey spectrum Fig. SI-7a (Supplementary Information, Fig. SI-7) clearly indicates the presence of Cu, Mg, and Al in the mixed metal oxide phase. The high-resolution scan of a fresh sample of the catalyst which indicates Cu 2p shown in Fig. SI-7b (Supplementary Information, Fig. SI-7) contains peak at binding energies of 934 eV (Cu 2p$_{3/2}$) and 954 eV (Cu 2p$_{1/2}$) which concludes the presence of copper in +2 oxidation state. Al 2p core level spectra exhibit a single component and the Al 2p binding energy was

observed at 74.48 eV, which is the characteristic photoemission peak of alumina phase Presence of shake up satellite peaks of the Cu 2p core level at 942.5 and 962.6 eV, respectively confirmed the formation of Cu^{2+} on the surface The XPS data of the catalyst after the reaction was also studied to understand the stability of the catalyst. There is no significant change observed seen in the high-resolution scan of used catalyst as shown in Fig. SI-7c & d (Supplementary Information, Fig. SI-7). [27]

3.6. TPR and TPD studies

Temperature programmed reduction studies with H$_2$ were performed for Mg−Al−HT derived oxides and their subsequent Cu supported Mg−Al−HT derived oxides showed reduction of copper moiety in the temperature range from 200 °C to 340 °C with two sharp peaks at 210 °C and 315 °C showing maximum consumption of hydrogen [30], which signifies the reduction of Cu^{2+} to Cu^0 in two stages. The first
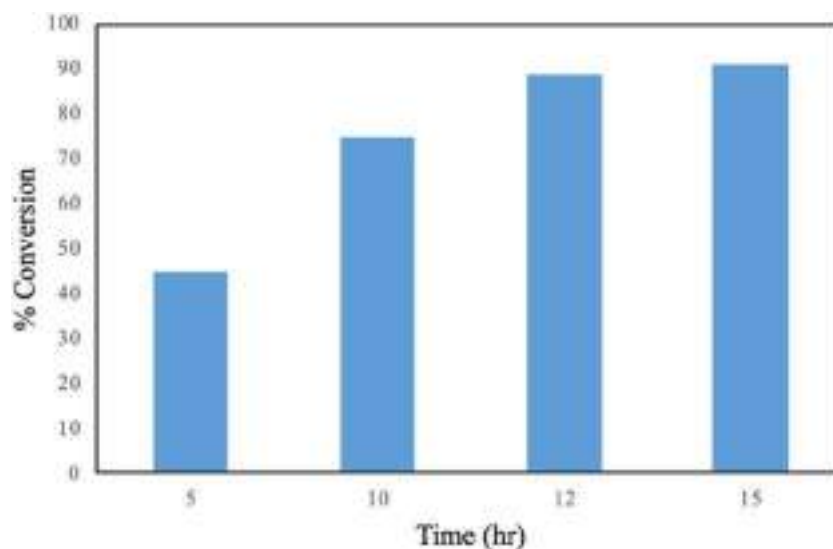
Fig. 3. Effect of reaction time [Reaction conditions: EAA (1 mmol.), Catalyst (10 wt% w.r.t. to EAA), DMF (2 mL), TBHP (1.5 equiv.), 100 ℃].

Table 1

Screening of various as-synthesized catalyst for enol carbamate reaction[a].

Sr. No	Catalyst	% Yield
1	Uncalcined Cu−Al	72
2	Calcined Cu−Al	59
3	Uncalcined Mg−Al	28
4	Calcined Mg−Al−HT	10
5	Uncalcined Cu/Mg−Al−HT	68
6	Cu/Mg−Al−HT derived oxide	89

[a] Reaction condition: EAA (1 mmol.), Catalyst (15%), DMF 2 mL, TBHP (1.5 equiv.) 100 ℃ 12 h.

peak at 210 ℃ is attributed to the reduction of the highly dispersed Cu phase from Cu^{2+} to Cu^{+} phase and the second sharp peak if the final reduction of Cu^{+} to Cu^{0} phase. The amount of hydrogen consumed per gram and per meter square is presented in Table SI-2 (Supplementary Information, Table SI-2). As the copper concentration increased, there was an increase in hydrogen consumption. This also points to the strong interaction of the copper species to the hydrotalcite support. [26,31]

CO_2 temperature-programmed desorption studies of the catalysts were carried to understand the strength and concentration of basic sites present on the surface. In all the catalysts analyzed, three types of desorption bands were observed, which attributed to the weak, medium, and strong basic strength during desorption in the temperature range from 100 to 600 ℃. In all cases, a broad desorption band is observed between 100 ℃ and 460 ℃, which can be deconvoluted into three contributions at about 165 ℃ (weak basic strength), 200 ℃ (medium basic strength) and 255 ℃ (high basic strength). The low-temperature desorption peak corresponds to basic surface OH^{-} groups. The medium temperature peak can be ascribed to $Mg^{2+}-O^{2-}$, $Al^{3+}-O^{2-}$ and $Cu^{2+}-O^{2-}$ acid-base pairs. The high-temperature peak is usually attributed to the strong basic sites associated with low coordinated O^{2-} anions. The amount of CO_2 desorbed represented by these features allows estimating the number of basic sites of the samples. In calcined Mg−Al−HT derived oxide, the basicity was observed to be significantly higher (total basic site density: 5.21 mmol CO_2/g) as compared to copper loaded Mg−Al−HT derived oxides. It is reported that calcination of as-synthesized hydrotalcite gives a well-dispersed mixture of Mg and Al mixed oxides having strong Lewis (isolated O^{2-} anions) and weaker Brønsted (OH^{-} groups) basic sites [31]. The basicity of the catalytic material decreased on copper loading to the Mg−Al−HT derived oxide, and there was no substantial change in the basicity observed with an increase in the copper concentration.

4. Catalytic activity

Initially, screening of different calcined and uncalcined hydrotalcite was carried out under the same reaction conditions, Ethyl acetoacetate [EAA] (1 mmol, limiting reagent), catalyst (15% w.r.t. limiting reagent), dimethyl formamide [DMF] (2 mL), tert-Butyl hydrogen peroxide [TBHP] (1.5 equiv.) at 100 ℃ 12 h. The influence of different hydrotalcite on the yield of enol carbamate was comparatively analyzed.

The reaction was carried out with calcined and uncalcined Mg−Al−HT with and without copper support, along with other copper-aluminum catalysts prepared by co-precipitation techniques for comparison and understanding the role of copper. As mentioned in Table 1 and Fig. 1, Cu/Mg−Al−HT derived oxide was found to be the best for enol carbamate synthesis, whereas no product formation was seen without the catalyst. Cu−Al catalyst (calcined or uncalcined) also showed lower conversions in comparison to the HT based catalyst as in the former Cu species are in bulk form whereas in later the copper species are very well dispersed into the hydrotalcite structure making the Cu ions more accessible. Also, in the catalyst preparation method, catalyst synthesized by wet-impregnation of copper species in alcoholic medium was found to be more efficient as compared to impregnation in aqueous medium which gave 79% conversion only. This is due to the excellent dispersion of copper ions in the HT support in alcoholic medium as the metal species diffuse very well as compared to aqueous medium. [32] So, we can conclude that basic supports (hydrotalcite and its derived mixed oxide) are found to be suitable for copper to promote its catalytic activity for C−H bond activation for enol carbamate synthesis.

With Cu supported Mg−Al−HT derived oxide catalyst as the best suited material for enol carbamate synthesis, further screening was studied to understand the effect of copper loading on the catalytic activity. No conversion was seen when native Mg−Al−HT derived oxide was used, and an increase in conversion was observed with an increase in the percentage of copper concentration on the support as shown in Fig. 2. The catalytic yield for 15 wt% and 20 wt% Cu supported Mg−Al−HT derived oxide showed no significant change with both showing conversions of 89% respectively. Thus, 15 wt% Cu supported Mg−Al−HT derived oxide was considered to be an efficient catalyst and used for further optimizations. In order to study the role of oxidant, we used 1.5 equiv. of TBPB (tert-butyl peroxy benzoate) as an oxidant, 5% conversion was observed. Whereas, we observed no product formation when TBHP in 5.0 M decane was used as an oxidant without catalyst.
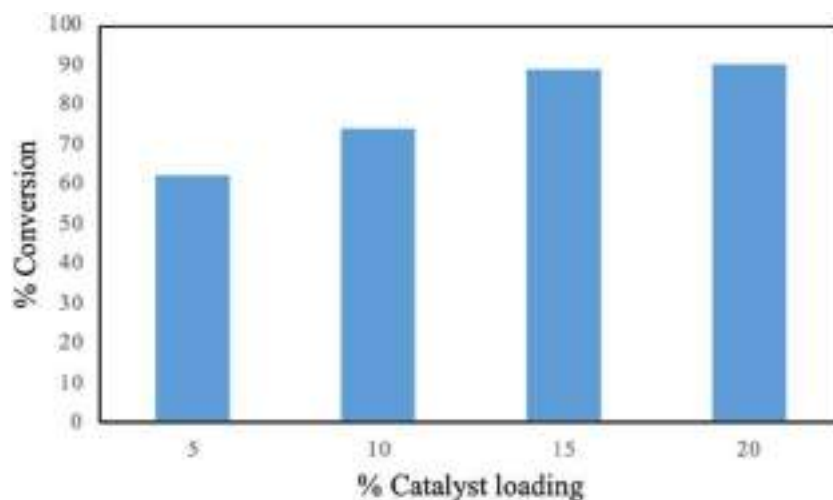
Fig. 4. Effect of catalyst loading. [Reaction conditions: EAA (1 mmol.), DMF (2 mL), TBHP (1.5 equiv.), 100 °C, 12 h].

We determined that TBHP proved to be the best oxidant to synthesize enol carbamates, which is consistent with our previous studies of C—H activation [33].

Further, optimization of the reaction time was monitored from 5 to 15 h. The conversion obtained at different time intervals is shown in Fig. 3. It can be observed that the conversion increases with an increase in reaction time up to 12 h. Further increase in reaction time to 15 h, did not result in any significant increase in conversion, and therefore, 12 h was optimized for further reactions. Different experiments were carried out by varying the reaction temperature from 80 to 100 °C, for studying the temperature effect on oxidative coupling over Cu/Mg—Al—HT derived oxide as shown in Fig. SI-8 (Supplementary Information, Fig. SI-8) Increase in conversion was observed with the increase in temperature and reached a maximum of 89% at 100 °C.

The effect of catalyst loading was studied further and presented in Fig. 4, which shows the varying percent of catalyst used for the reaction from 5 wt% - 20 wt% catalyst with respect to limiting reagent. It was observed that the conversion of limiting reagent increased with increase in catalyst loading. There was no significant conversion observed beyond 15% catalyst loading. The results show that the highest conversion 89% was obtained at 15 wt% of catalyst loading, and the lowest 62% at 5 wt% of 15% Cu/Mg—Al—HT derived oxide catalyst.

4.1. Substrate scope of enol-carbamate

With the reaction conditions optimized, substrate with structural diversity were studied using 15% Cu/Mg—Al—HT derived oxide catalyst at 100 °C with 2 mL of dimethylformamide and diethylformamide as a solvent and TBHP as the external oxidant. Various β-ketoesters were used as substrates under standard reaction conditions for the formation of enol carbamate, as shown in Table SI-3 (Supplementary Information, Table SI-3) We observed that all β-ketoesters were transformed into their corresponding enol carbamates. Excellent conversions were found by using dimethylformamide with various substituted β-ketoesters. However, the active methylene group did not participate in the reaction in the case of 1, 3-cyclohexanedione, which showed lower conversions in comparison to other substrates. Cyclic and bulky formamides provided slightly lower yields, suggesting the negative effect of steric hindrance on the reaction.

Mechanistically, the dicarbonyl functionalities in the β-ketoesters possess the tendency of forming coordination complexes with transition metals as shown in the mechanism, Fig. SI-9 (Supplementary Information, Fig. SI-9). The copper complex then decomposes TBHP to form respective radicals which can further abstract hydrogen from the formamide, generating the corresponding radical. This radical then further reacts with the copper complex to give the desired carbamate [34]. The similar reaction pathway has also been reported by Barve et al. [35]

4.2. Recyclability of the catalyst

After the reaction, the catalyst was filtered and refluxed with 10 mL of methanol and washed with 15 mL methanol to remove any adsorbed material from catalytic surface and pores and then dried at 120 °C. It was also calcined at 450 °C for 8 h and then cooled to room temperature and weighed. Overall there was no loss of catalyst during centrifugation and separation. The same procedure was followed in subsequent experiments. The catalyst was reused for three times without loss in activity, and results are shown in Table SI-4 (Supplementary Information, Table SI-4). Thus, the stability of the synthesized material was confirmed w.r.t. activity. The XRD of the recycled catalyst was compared with the fresh catalyst, and there was no significant change in the catalyst which confirmed the stability of the catalyst. (Supplementary Information, Fig. SI-10).

Also, the catalyst was subjected to hot-filtration method to check for the leaching of the active metals from the catalyst. After the reaction, the reaction vial was opened in the hot condition and filtered quickly using a filter paper. The filtrate collected was diluted with 10 mL of DMF. The prepared sample was given for ICP-OES and copper was not detected in the solution indicating no leaching of copper ions from the catalyst. The yield after removing the catalyst was 89%, which was consistent with the results obtained during the recyclability studies.

5. Conclusion

A simple and efficient procedure was developed for the synthesis of carbamate derivatives over Cu/Mg—Al—HT derived oxide catalysts. Cu/Mg—Al—HT derived oxide catalyst (5%, 10%, 15% and 20% copper loading) is synthesized and characterized by various analytical techniques such as XRD, FTIR, SEM, and N_2 adsorption-desorption. Among all the catalysts, 15% Cu/Mg—Al—HT derived oxide catalyst was found to be active for the synthesis of enol derivatives. Broad substrate study has been done for the synthesis of enol carbamates. The catalyst was recycled up to three cycles and found to be active without any significant loss in activity.

Declaration of Competing Interest

The authors declare that they have no known competing financial interests or personal relationships that could have appeared to

influence the work reported in this paper.

Acknowledgment

Appendix A. Supplementary data

Supplementary data to this article can be found online at https://doi.org/10.1016/j.catcom.2020.106150.

References

[1] A.R. Modarresi-Alam, M. Rostamizahed, P. Najafi, Solvent-free preparation of primary carbamates, Turkish J. Chem. 30 (2006) 269–276.

[2] P. Wang, Y. Fei, Q. Li, Y. Deng, Effective synthesis of dimethylhexane-1,6-dicarbamate from 1,6-hexanediamine and dimethyl carbonate using 3-amino-1,2,4-triazole potassium as a solid base catalyst at ambient temperature, Green Chem. 18 (2016) 6681–6686, https://doi.org/10.1039/c6gc02509a.

[3] B. Chen, S.S.C. Chuang, CuCl2 and PdCl2 catalysts for oxidative carbonylation of aniline with methanol, J. Mol. Catal. A Chem. 195 (2003) 37–45, https://doi.org/10.1016/S1381-1169(02)00550-2.

[4] F. Ragaini, M. Gasperini, S. Cenini, Phosphorus acids as highly efficient promoters for the palladium- phenanthroline catalyzed carbonylation of nitrobenzene to methyl phenylcarbamate, Adv. Synth. Catal. 346 (2004) 63–71, https://doi.org/10.1002/adsc.200303143.

[5] Y. Ono, Catalysis in the production and reactions of dimethyl carbonate, an environmentally benign building block, Appl. Catal. A. Gen. 155 (1997) 133–166, https://doi.org/10.1016/S0926-860X(96)00402-4.

[6] N. Lucas, A.P. Amrute, K. Palraj, G.V. Shanbhag, A. Vinu, S.B. Halligudi, Non-phosgene route for the synthesis of methyl phenyl carbamate using ordered AlSBA-15 catalyst, J. Mol. Catal. A Chem. 295 (2008) 29–33, https://doi.org/10.1016/j.molcata.2008.08.009.

[7] J. Shang, S. Liu, X. Ma, L. Lu, Y. Deng, A new route of CO2 catalytic activation: Syntheses of N-substituted carbamates from dialkyl carbonates and polyureas, Green Chem. 14 (2012) 2899–2906, https://doi.org/10.1039/c2gc36043h.

[8] J. Muzart, N,N-Dimethylformamide: Much more than a solvent, Tetrahedron. 65 (2009) 8313–8323, https://doi.org/10.1016/j.tet.2009.06.091.

[9] J. Ju, M. Jeong, J. Moon, M.J. Hyun, S. Lee, Aminocarbonylation of aryl halides using a nickel phosphite catalytic system, Org. Lett. 9 (2007) 4615–4618, https://doi.org/10.1021/ol702058e.

[10] T. He, H. Li, P. Li, L. Wang, Direct amidation of azoles with formamides via metal-free C-H activation in the presence of tert-butyl perbenzoate, Chem. Commun. 47 (2011) 8946–8948, https://doi.org/10.1039/c1cc13086b.

[11] G.S. Kumar, C.U. Maheswari, R.A. Kumar, M.L. Kantam, K.R. Reddy, Copper-catalyzed oxidative C-O coupling by direct C-H bond activation of formamides: synthesis of enol carbamates and 2-carbonyl-substituted phenol carbamates, Angew. Chem. Int. Ed. 50 (2011) 11748–11751, https://doi.org/10.1002/anie.201105020.

[12] K. Hosoi, K. Nozaki, T. Hiyama, Carbon monoxide free aminocarbonylation of aryl and alkenyl iodides using DMF as an amide source, Org. Lett. 4 (2002) 2849–2851, https://doi.org/10.1021/ol026236k.

[13] P.S. Samudrala, A.V. Nakhate, S.S.R. Gupta, K.B. Rasal, G.P. Deshmukh, C.R. Gadipelly, S. Theegala, D.K. Dumbre, S. Periasamy, V.R.C. Komandur, et al., Oxidative coupling of carboxylic acids or benzaldehydes with DMF using hydrotalcite-derived oxide catalysts, Appl. Catal. Environ. 240 (2019) 348–357.

[14] E. Kianmehr, M.H. Baghersad, Copper-catalyzed coupling of arylboronic acids with potassium cyanate: A new approach to the synthesis of aryl carbamates, Adv. Synth. Catal. 353 (2011) 2599–2603, https://doi.org/10.1002/adsc.201100153.

[15] D. Saberi, A. Heydari, Oxidative amidation of aromatic aldehydes with amine hydrochloride salts catalyzed by silica-coated magnetic carbon nanotubes (MagCNTs@SiO 2)-immobilized imine-Cu(I), Appl. Organomet. Chem. 28 (2014) 101–108, https://doi.org/10.1002/aoc.3087.

[16] S. Ghosh, A. Bhaumik, J. Mondal, A. Mallik, S. Sengupta, C. Mukhopadhyay, Direct

[17] amide bond formation from carboxylic acids and amines using activated alumina balls as a new, convenient, clean, reusable and low cost heterogeneous catalyst, Green Chem. 14 (2012) 3220–3229, https://doi.org/10.1039/c2gc35880h.

[17] D. Saberi, S. Mansoori, E. Ghaderi, K. Niknam, Copper nanoparticles on charcoal: An effective nanocatalyst for the synthesis of enol carbamates and amides via an oxidative coupling route, Tetrahedron Lett. 57 (2016) 95–99, https://doi.org/10.1016/j.tetlet.2015.11.072.

[18] G.D. Yadav, G.P. Fernandes, Selective synthesis of natural benzaldehyde by hydrolysis of cinnamaldehyde using novel hydrotalcite catalyst, Catal. Today 207 (2013) 162–169, https://doi.org/10.1016/j.cattod.2012.04.052.

[19] P. Liu, K. You, R. Deng, Z. Chen, J. Jian, F. Zhao, P. Liu, Q. Ai, H. Luo, Hydrotalcite-derived Co-MgAlO mixed metal oxides as efficient and stable catalyst for the solvent-free selective oxidation of cyclohexane with molecular oxygen, Mol. Catal. 466 (2019) 130–137, https://doi.org/10.1016/j.mcat.2019.01.019.

[20] A. López, J.A. Aragón, J.G. Hernández-Cortez, M.L. Mosqueira, R. Martínez-Palou, Study of hydrotalcite-supported transition metals as catalysts for crude glycerol hydrogenolysis, Mol. Catal. 468 (2019) 9–18, https://doi.org/10.1016/j.mcat.2019.02.008.

[21] M.S. Maru, S. Ram, R.S. Shukla, N.H. Khan, Ruthenium-hydrotalcite (Ru-HT) as an effective heterogeneous catalyst for the selective hydrogenation of CO2 to formic acid, Mol. Catal. 446 (2018) 23–30, https://doi.org/10.1016/j.mcat.2017.12.005.

[22] D.P. Debecker, E.M. Gaigneaux, G. Busca, Exploring, tuning, and exploiting the basicity of hydrotalcites for applications in heterogeneous catalysis, Chem. - A Eur. J. 15 (2009) 3920–3935, https://doi.org/10.1002/chem.200900060.

[23] B.M. Choudary, M. Lakshmi Kantam, C. Venkat Reddy, K. Koteswara Rao, et al., Henry reactions catalysed by modified Mg–Al hydrotalcite:. an efficient reusable solid base for selective synthesis of $β$-nitroalkanols, Green Chem. 1 (1999) 187–189.

[24] P. Benito, A. Vaccari, C. Antonetti, D. Licursi, N. Schiarioli, E. Rodriguez-Castellón, A.M. Raspolli Galletti, Tunable copper-hydrotalcite derived mixed oxides for sustainable ethanol condensation to n-butanol in liquid phase, J. Clean. Prod. 209 (2019) 1614–1623, https://doi.org/10.1016/j.jclepro.2018.11.150.

[25] S.L. Bhanawase, G.D. Yadav, Activity and selectivity of different base catalysts in synthesis of guaifenesin from guaiacol and glycidol of biomass origin, Catal. Today 291 (2017) 213–222, https://doi.org/10.1016/j.cattod.2016.12.008.

[26] N. Blanch-Raga, A.E. Palomares, J. Martínez-Triguero, G. Fetter, P. Bosch, Cu mixed oxides based on hydrotalcite-like compounds for the oxidation of trichloroethylene, Ind. Eng. Chem. Res. 52 (2013) 15772–15779, https://doi.org/10.1021/ie4024935.

[27] A.V. Nakhate, G.D. Yadav, Hydrothermal synthesis of CuFe2O4 magnetic nanoparticles as active and robust catalyst for N-arylation of indole and imidazole with aryl halide, ChemistrySelect. 2 (2017) 2395–2405, https://doi.org/10.1002/slct.201601846.

[28] M. Peymani, S.M. Alavi, H. Arandiyan, M. Rezaei, Rational design of high surface area mesoporous Ni/CeO2 for partial oxidation of propane, Catalysts. 8 (2018), https://doi.org/10.3390/catal8090388.

[29] E.M. Fuentes, A. Da Costa Faro, T. De Freitas Silva, J.M. Assaf, M.D.C. Rangel, A comparison between copper and nickel-based catalysts obtained from hydrotalcite-like precursors for WGSR, Catal. Today 171 (2011) 290–296, https://doi.org/10.1016/j.cattod.2011.03.082.

[30] J.S. Valente, J. Hernandez-Cortez, M.S. Cantu, G. Ferrat, E. López-Salinas, Calcined layered double hydroxides Mg-Me-Al (Me: Cu, Fe, Ni, Zn) as bifunctional catalysts, Catal. Today 150 (2010) 340–345, https://doi.org/10.1016/j.cattod.2009.08.020.

[31] M. Dixit, M. Mishra, P.A. Joshi, D.O. Shah, Physico-chemical and catalytic properties of Mg-Al hydrotalcite and Mg-Al mixed oxide supported copper catalysts, J. Ind. Eng. Chem. 19 (2013) 458–468, https://doi.org/10.1016/j.jiec.2012.08.028.

[32] J. De Waele, V.V. Galvita, H. Poelman, C. Detavernier, J.W. Thybaut, PdZn nanoparticle catalyst formation for ethanol dehydrogenation: active metal impregnation vs incorporation, Appl. Catal. A. Gen. 555 (2018) 12–19, https://doi.org/10.1016/j.apcata.2018.02.005.

[33] P.S. Samudrala, A.V. Nakhate, S.S.R. Gupta, K.B. Rasal, G.P. Deshmukh, C.R. Gadipelly, S. Theegala, D.K. Dumbre, S. Periasamy, V.R.C. Komandur, S.K. Bhargava, L.K. Mannepalli, Oxidative coupling of carboxylic acids or benzaldehydes with DMF using hydrotalicite-derived oxide catalysts, Appl. Catal. Environ. 240 (2019) 348–357, https://doi.org/10.1016/j.apcatb.2017.12.058.

[34] D. Saberi, S. Poorsadeghi, Nickel-catalyzed oxidative esterification of formamides with 1,3-dicarbonyl compounds under mild reaction conditions, Appl. Organomet. Chem. 31 (e3855) (2017), https://doi.org/10.1002/aoc.3855.

[35] B.D. Barve, Y. Wu, M. El-Shazly, D. Chuang, Y.-M. Chung, Y.-H. Tsai, S.-F. Wu, M. Korinek, Y.-C. Du, C. Hsieh, J. Wang, F. Chang, Synthesis of carbamates by direct C-H bond activation of Formamides, Eur J. Org. Chem. 2012 (2012) 6760–6766, https://doi.org/10.1002/ejoc.201201160.

Molecular docking and antioxidant activity of *Cleome simplicifolia* assisted synthesis of cerium oxide nanoparticles

Ratiram Gomaji Chaudhary [a],*, Prashant B. Chouke [a,b],*, Rina D. Bagade [c], Ajay K. Potbhare [a], Kanhaiya M. Dadure [d],*

[a] Post Graduate Department of Chemistry, Seth Kesarimal Porwal College, Kamptee 441 001, India
[b] Department of Chemistry, Government Polytechnic, Bramhapuri 441 206, India
[c] Post Graduate Teaching Department of Chemistry, Rashtrasant Tukadoji Maharaj Nagpur University, Nagpur 440033, India
[d] Department of Chemistry, J. B. Science College, Wardha 442001, India

A B S T R A C T

Bio-motivated CeO_2 NPs were fabricated using plant extract of *Cleome simplicifolia*. The chemicals present in the plant extracts played pivotal role in the fabrication of CeO_2 NPs. Initially, fabricated CeO_2 nanoparticles were authenticate by using the XRD pattern which resembles a cubic structure. UV–Visible data estimated the band gap of CeO_2 around 3.50 eV. SEM images revealed nearly monodisperse spherical shapes due to agglomerization of CeO_2 NPs. DPPH assay of CeO_2 NPs exhibited an excellent antioxidant property. Moreover, molecular docking of CeO_2 NPs was investigated by new protein molecule.

© 2020 Elsevier Ltd. All rights reserved.
Selection and peer-review under responsibility of the scientific committee of the International Conference on Advanced Functional Materials (Innovations in Chemical, Physical and Biological Sciences).

1. Introduction

Nowadays, a synthesis of bio-coherent metal/metal oxide nanoparticles and semiconductor nano-structure is a significant part in the field of science and technology. Recently, cerium oxide nanoparticles (CeO_2 NPs) have been immensely utilized as semiconducting materials with wide band gap energy 3.50 eV. CeO_2 NPs are capable in showing the applications in various fields viz. drug delivery, agriculture, pharmaceuticals and biosensor [1–5]. Earlier, a variety of synthesis techniques has been employed to fabricate the CeO_2 NPs such as sol–gel [6], co-precipitation [7], microwave [8], hydrothermal [9], flame spray pyrolysis [10], and sonochemical [11]. However, the applied methods are compact with several negative aspects such as very expensive, use hazardous chemical, toxicity, complicated, time-consuming and harmful to perform [12]. In response, researchers are searching for alternatives to conventional methods. "Green approach" has a

capacity to minimize the elimination of harmful gases and chemicals during the formation of NPs [13]. The green method possesses abundant benefits such as low-cost, eco-friendly, large scale production on a commercial basis and a lot of biomedical applications [14,15].

Therefore, we referred the various kinds of literatures concerning cerium oxide NPs and found that, cerium is the first rare earth metal of lanthanide series in the periodic table. Cerium can be present in both 3^+ and 4^+ states. Therefore, in a bulk condition cerium oxide can be in existence as both CeO_2 and Ce_2O_3. At nanoscale, cerium oxide reveals a mix of cerium in the 3^+ and 4^+ states on the surface of the nanoparticles [16]. As a result, CeO_2 NPs are being extensively used in nanotechnology due to their helpful applications as catalysts, fuel cells, and antioxidants in biological systems [17–21]. Hence, CeO_2 NPs have been synthesized by using many bio- components such as fungal extracellular, honey and white egg. These bio-components, behaving like stabilizing and anti-oxidizing agents cause to manufacture crystalline structure of NPs with different shape, size, and morphology. Such observed things inspired us to do something new. Thus, we have adopted a green approach to synthesize CeO_2 NPs by using plant extracts of *Cleome simplicifolia* and its antioxidant properties have been reported for the first time here.

* Corresponding authors at: Post Graduate Department of Chemistry, Seth Kesarimal Porwal College, Kamptee 441 001, India (P.B. Chouke).

E-mail addresses: chaudhary_rati@yahoo.com (R. Gomaji Chaudhary), prashant_bchouke@rediffmail.com (P.B. Chouke), kmdadure@gmail.com (K.M. Dadure).

The *Cleome simplicifolia* existed in *Cleomaceae* family. The plant is about 15 to 60 cm tall, annual herb and native of Asia. This plant can be observed in the parts of Andhra Pradesh, Chhattisgarh, Goa, Gujarat, Karnataka, and prominently found in the part of Maharashtra. The plant is collected from the western part of Nagpur. Every part of the plant has been used in medicine. The plant is being used as a traditional medicine by the tribal's. Earlier, many researchers reported the bioinspired synthesis of CeO_2 nanoparticles using *Curvularia lunata* [22], *Olea europaea* [23], *Aloe arbadensis* [24], and *Hibiscus Sabdariffa* [25].

In the present study, we have carried out bio-assisted synthesized CeO_2 NPs using plant extract of *Cleome simplicifolia.* After fabrication, CeO_2 NPs were confirmed by different microscopic techniques. On the other hand, we have studied the antioxidant property of fabricated CeO_2 NPs. Similarly, we have also studied how protein (enzyme) interacts with a molecule (Ligand) of synthesised CeO_2 NPs under molecular docking. This is the first report on *Cleome simplicifolia* assisted green synthesis of CeO_2 NPs.

2. Materials and methods

2.1. Chemicals reagents

Cerium nitrate hexahydrate $Ce(NO_3)_3 \cdot 6H_2O$ with purity 99%, procured from Merck, where as 1-Diphenyl-2-picrylhydrazyl (DPPH) was purchased from Himedia laboratories. Without any purification all chemicals were used to carry out the experiments.

2.2. Fabrication of leaves extract

In the present work, *Cleome simplicifolia* was collected from Gorewada National Park, Nagpur, India. The plant was recognized with the support of taxonomists. The plant was cleaned several times using potable water, again with sterilised water to eliminate the surface contamination and soil present on the plant. Subsequently cleaned plant pieces were shadow dried for 5 to 6 days, then the dehydrated plant was cut into fine particles and make a powdered with the help of mortar and pistol. An aqueous solution of the plant was prepared by mixing 20 g of sterile fine particles of plant in 300 mL distilled water, boiled at 60 °C for 30 min and later the solution was cleaned by Whatman filter paper No.42 to take away the undesirable materials. Then, the solution was centrifuged at 3000 rpm for 3 min whereas the supernatant was used for fabrication of nanoparticles.

2.3. Bioinspired synthesis of cerium oxide NPs (CeO_2 NPs)

0.86 g of cerium nitrate hexahydrate ($Ce(NO_3)_3 \cdot 6H_2O$) was suspended in 200 mL water, where 20 mL extract was added dropwise and stirred the mixture for half an hour by using a magnetic stirrer. Green colour precipitate in a conical flask at the bottom was obtained. The volume of supernatant liquid was removed from the conical flask to concentrate the obtained product as a precipitant. The obtained precipitant was washed thoroughly with sterilised water repeatedly, followed by alcohol and later dried it in an oven at 80 °C to acquire the very well particles of CeO_2 NPs. Further, the dried precipitate was calcinated at 800 °C for 2 h (Scheme 1).

2.4. Spectroscopic instrumentation for CeO_2 NPs

The intense peak of CeO_2 NPs was investigated with the help of lambda 35 UV–Visible Spectroscopy. JASCO 460 PLUS FTIR spectrometer was used to determine the IR spectra in the region of 4000–400 cm^{-1}. Cu Kα radiation ($\lambda = 1.54060$ Å) with nickel monochromator was used to record the XRD pattern of fabricated NPs in the region of 2θ from 10° to 80°. Scherrer's formula [$D = 0.9\lambda / \beta \cos \theta$] was employed to determine the standard crystallite size of material. The morphology of material was examined by JEOL JSM-7100 F instruments.

2.5. Antioxidant activity

The reducing capability of the CeO_2 nanoparticles was examined by a DPPH free radical scavenging technique according to our previous work [26]. Near about 10 to 50 μg of CeO_2 nanoparticles was mixed to 100 μL of DPPH solution. Afterwards the reaction mixture was incubated for 30 min at room temperature where the absorbance (*A*) was recorded at 517 nm using a spectrophotometer. This procedure was repeated for three times. Here, ascorbic acid was employed as a standard material. At last scavenging measurement of free radicals was calculated as % inhibition according to the standard formula.

2.6. Docking study

The 2-D and 3-D structures of these molecules were designed by using Chem Office software 12. The process of 2D and 3D design is elaborately explained in the user manual of the Chem Office and was used here without any modifications. CHIMERA and PYMOL tools were used to visualize the docked site.

3. Results and discussion

3.1. X-ray diffraction and infrared spectroscopy of CeO_2 NPs

A Fig. 1a shows the crystalline structure of fabricated CeO_2 NPs. The 2θ values of diffraction peaks were observed at 47.42, 28.51, and 33.06 matched with (2 2 0), (1 1 1), and (2 0 0) planes of the material. Correspondingly, erstwhile peaks were obtained at 2θ values of 78.99, 76.57, 69.00, 59.09, and 56.30 are analogous to (4 2 0), (3 3 1), (4 0 0), (2 2 2), and (3 1 1) planes of CeO_2 material. Off course, CeO_2 materials perfectly matched with JCPDS card no. 34-0394 and revealed a face centre cubic structure [27]. The recorded full width at half maxima of these peaks which are interpreted to determine the average crystalline size of synthesised NPs by using standard equation. An average crystalline size of CeO_2 NPs was found as 33.31 nm.

Moreover, the material was recorded by FT-IR spectroscopy (Fig. 1b) to authenticate the chemical bonding. The strong band was obtained at 3425 and 1498 cm^{-1} because of the O–H vibrational frequency of hydration molecules contaminated during analysis [28–29]. A peak obtained at 1455 cm^{-1} equivalent to the in-plane and out-of-plane pending of O–H bond exists in absorbed water molecule. The peak obtained at 1151 cm^{-1} was responsible for the overtone bond for trace of the Ce-OH. The peaks were obtained at 862 and 957 cm^{-1} were perfectly matched with bending vibrations of the Ce-O species. Finally, the peak achieved at below 862 cm^{-1} indicated formation of the Ce-O bond [30].

3.2. Raman and UV–visible spectroscopy of CeO_2 NPs

Raman spectrum of material has been displayed in Fig. 2a. A cubic structure of cerium oxide nanoparticles was also confirmed by Raman spectroscopy. The stretching vibrational peak obtained at 463 cm^{-1} due to the oxygen atoms. This renders the vibration very sensitive to micro-structural changes such as oxygen sub lattice disorder and non-stoichiometric [31]. A broaden and asymmetric peak obtained at 463 cm^{-1} as the oxygen vacancy concentration increases, and the T_2g mode structure shifts to lower frequency. These changes may also be accompanied by the appear-
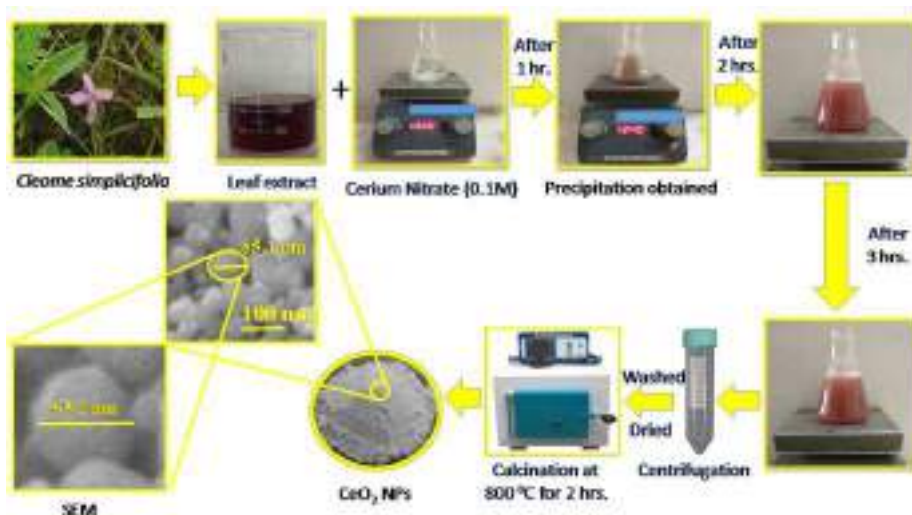
Scheme 1. Fabrication of CeO$_2$ NPs.
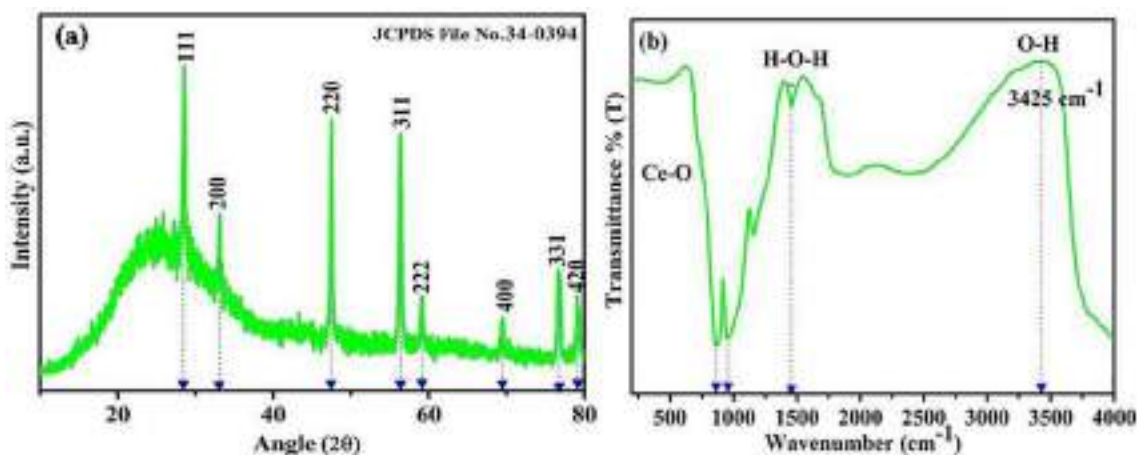
Fig. 1. (a) XRD and (b) FT-IR patterns of synthesized CeO$_2$ NPs.
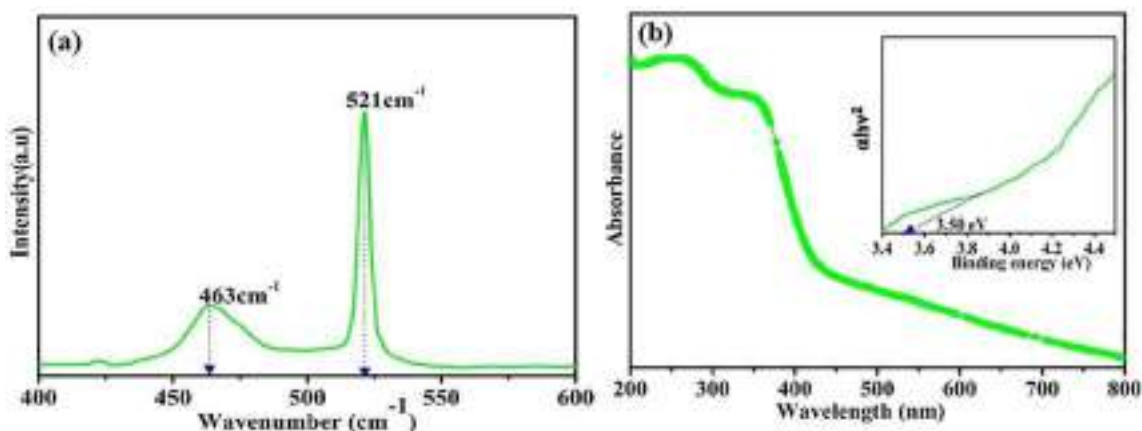
Fig. 2. (a) Raman and (b) UV–visible spectrum of synthesized CeO$_2$ NPs.

ance of a strong longer peak at 521 cm^{-1} which were attributed due to the O vacancies [31].

UV–visible spectroscopy was performed to understand the electronic structure and to estimate the optical band gap of material. The spectrum data of CeO$_2$ NPs have been shown in Fig. 2b. A strong absorption band obtained at 370 nm was authenticated to the formation of desired material. Besides, in support of the present material a literature survey revealed that similar bands were observed in the earlier report [32]. A peak located at around 300–600 nm shifted towards shorter wave-length, which clearly

indicated that it might be due to the blue shift. Further, by using UV–visible data, band gap energy of material estimated around 3.50 eV. The band gap energy was estimated by plotting $(\alpha h\upsilon)^2$ of the micro-crystalline materials against the photon energy $(h\upsilon)$. UV-absorption edge provided accountable guess of the band gap of any system.

3.3. Surface morphology of CeO$_2$ NPs

Morphological study of synthesized CeO$_2$ NPs was investigated by using SEM (Fig. 3). The study shows that high homogeneity emerged in the surface of the sample occur because of increasing the annealing temperature. The morphology of fabricated CeO$_2$ material shows spherical in shape at calcined 800 °C temperature. Also, data reveal nearly uniformity in spherical shapes with average diameter of each 60–85.1 nm (inset image in Fig. 3). Nearly uniform microspheres are shown in Fig. 3. In fact, these uniform microspheres emerged by aggregation of numerous nearly monodisperse nanospheres. Hence, the process of aggregation to spherical morphology caused by aging time, orientation, interaction, nucleation and extended heating at the higher temperature and fusion of nanoparticles, which lead to agglomeration that serves as crystal seed to grow the microspheres [33–35].

3.4. Antioxidant activity

In the past years, CeO$_2$ nanoparticles showed ROS scavenging capabilities that defence in gastrointestinal epithelium and human breast line models. A thorough study certainly shows that CeO$_2$ NPs with low Ce^{3+}/Ce^{4+} surface ratios function as proficient antioxidant catalyse idiophone [36]. The DPPH scavenger radical method was broadly drawn to determine the proton donating capacity of synthesised CeO$_2$ NPs and to prevent the formation of free radicals. The DPPH scavenger radical method was utilized according to our previous work [37,38]. The scavenger free radical DPPH absorption plot was articulated to the green synthesized CeO$_2$ NPs from the extract contrasted with ascorbic acid as a positive control. We observed that CeO$_2$ NPs have the ability to remove DPPH free radicals as shown in Fig. 4. DPPH scavenger free radical activity was as concentration-dependent; as a result, the antioxidant property of synthesised NPs was increased when the concentration of NPs in a solution increased [39,40]. Also, the study showed CeO$_2$ NPs was more efficient than ascorbic acid.

3.5. Docking assay of CeO$_2$ NPs

3.5.1. Selection of inhibitor

Here our main aim is to develop an efficient inhibitor (material) against drug-resistant bacteria, therefore, we are working here to identify and develop inhibitors of essential biological pathways
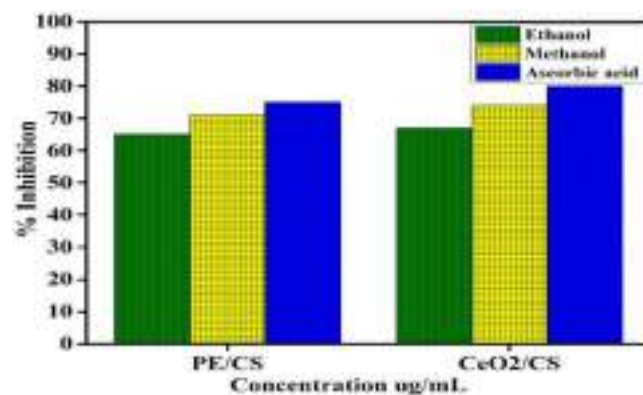

Fig. 4. Antioxidant property of plant extract (PE) and synthesized CeO$_2$ NPs.

that are not targeted by current therapies. A clinically pertinent antibacterial agent can be leaded by the fatty acid biosynthesis pathway [41,42]. Several small molecules were identified through a combination of high-throughput, besides, fragment screening was co-crystallized with β-ketoacyl-acyl carrier protein syntheses III from *Escherichia coli* and *Streptococcus pneumonia*. Structural-based drug design provided a new class of inhibitors. After optimization for gram-negative enzyme, inhibitory potency to study inhibition of an enzyme crystal structure of PDB ID 4Z8D which were targeted by inhibitor *trans*-4-[({[(2-chlorobenzyl) oxy] carbonyl} amino) methyl] cyclohexane carboxylic acid are listed in Fig. 5a [43]. The finalized 3D structures of the molecule were tested for global minima by ascertaining the minimum energy value of the molecule which was calculated as −9.65284 kcal/mole, and the same was replaced with the synthesized CeO$_2$ nanoparticles.

3.5.2. Molecular docking analysis

The interaction of nanoparticles with cells, DNA and protein has extensively acquired an immense interest in the field of bio-nanosciences. Fig. 6a shows the molecular docking of material. Fig. 6b-c exhibits the docking results of CeO$_2$ NPs with a size of 1.5 and 1 nm (PDB ID 4Z8D) correspondingly. An energy values for larger and smaller CeO$_2$ NPs clusters was calculated in the form of binding energies which were found as −651.85 and −540.90 kcal/mol respectively. The molecular docking study demonstrated the superior binding affinity for bigger clusters. The docked images of CeO$_2$ NPs are displayed in Fig. 6 (a-f) respectively and CeO$_2$ NPs of 1.5 nm with interacting close amino acid residues 247 ASN, with close distances of 1.201482, 1.449510, 2.118387, 1.984162, and 1.20254 in A (Armstrong) are shown in Fig. 6c. The molecular docking study of synthesized CeO$_2$ NPs was explored with a fine harmony and the plot of accessible surface area and experimental data.
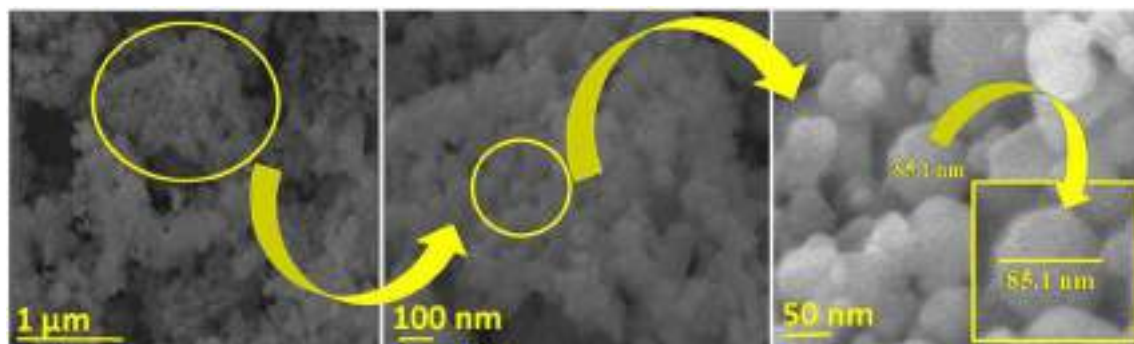
Fig. 3. SEM image of synthesized CeO$_2$ NPs.
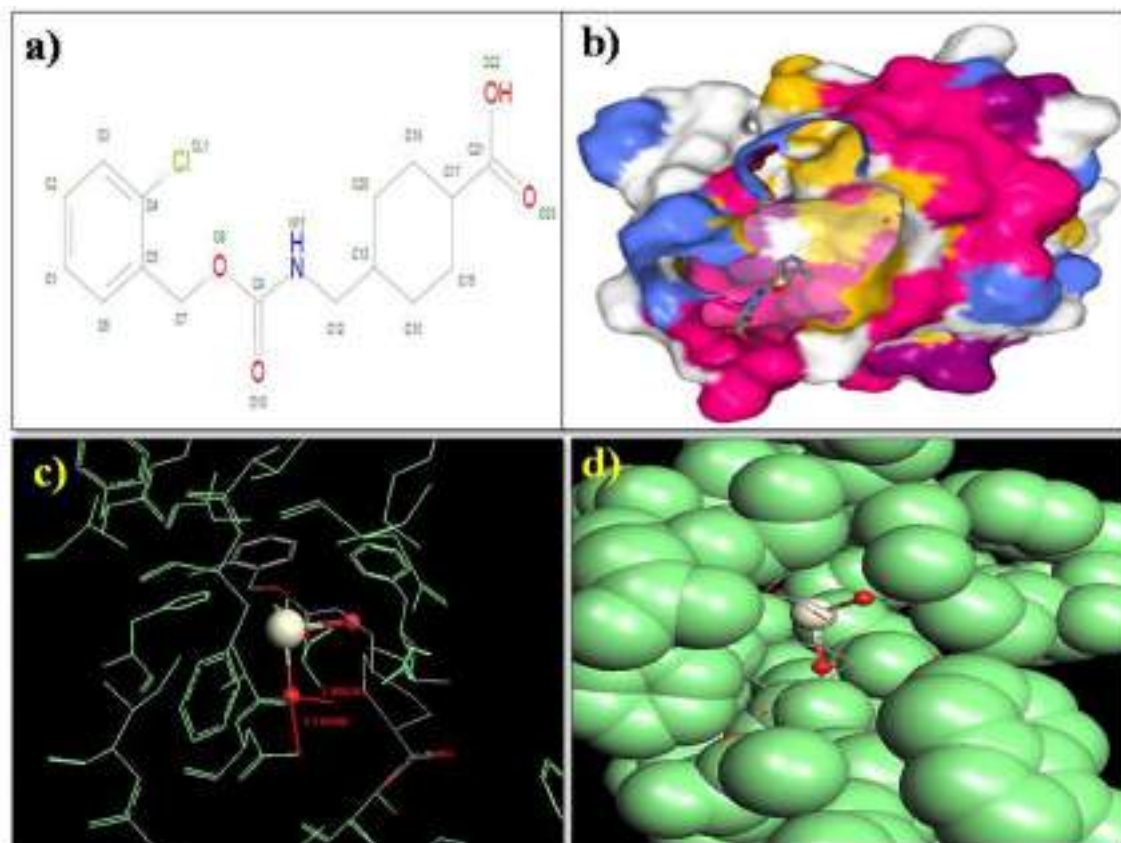
Fig. 5. (a) *trans*-4-[({[(2-chlorobenzyl)oxy]carbonyl}amino)methyl]cyclohexanecarboxylic acid; (b) 3-D Interaction of protein crystal structure PDB ID 4Z8D Natural inhibitor ligand code 4LBin center ball and stick surface mode; (c) 3-D ball and stick model of CeO2 Nanoparticle fit in wireframe binding site, and (d) 3-D CeO$_2$ ball and stick mode fit in center CPK bonding site [43].
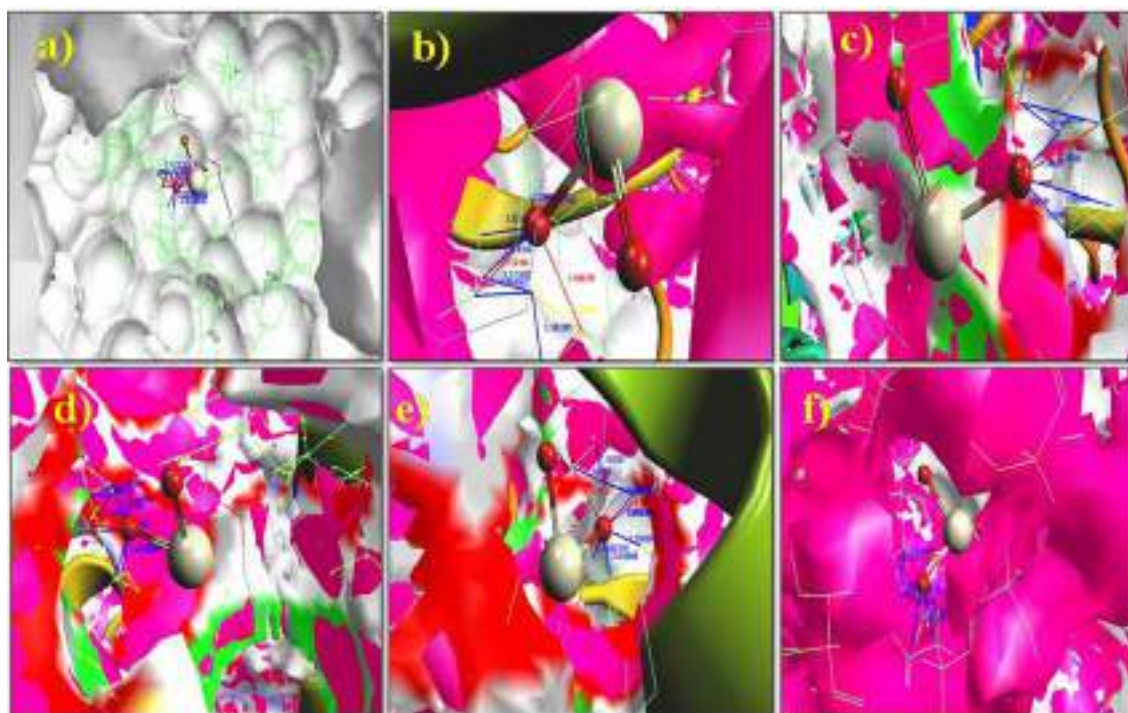
Fig. 6. (a-f) Protein crystal structures of PDB ID 4Z8D complex with CeO$_2$ as inhibitor red in centre ball and stick mode. Hydrogen bonds (2.5–3.5 Å) are depicted as blue, red lines in translucent surface carton mode binding site show specific mode of interaction with selected amino acids residues. (For interpretation of the references to colour in this figure legend, the reader is referred to the web version of this article.)

4. Conclusion

In short, the *Cleome simplicifolia* assisted CeO_2 NPs which is authenticated by the XRD technique and resembles to a cubic structure. The crystallite size of CeO_2 NPs is estimated around 33.31 nm by Scherer equation. The morphology investigation of material has revealed spherical shapes with nearly monodisperse having average diameter of each 60–85.1 nm. Antioxidant activity of CeO_2 nonmaterial has demonstrated a more effective and an excellent activity against ascorbic acid. Moreover, the molecular docking study of material has shown an outstanding result with high binding energies −651.85 and −540.90 kcal/mol, and has revealed a greater binding affinity towards big clusters.

CRediT authorship contribution statement

Prashant B. Chouke: Investigation, Writing. **Rina D. Bagade:** Investigation, Writing. **Ajay K. Potbhare:** Methodology, Data Analysis. **Kanhaiya K. Dadurre:** Methodology, Data Analysis. **Ratiram Gomaji Chaudhary:** Conceptualization.

Declaration of Competing Interest

The authors declare that they have no known competing financial interests or personal relationships that could have appeared to influence the work reported in this paper.

Acknowledgements

References

[1] J.A. Vassie, J.M. Whitelock, M.S. Lord, Mol. Pharm. 15 (2018) 994–1004.
[2] Z. Cao, C. Stowers, L. Rossi, W. Zhang, L. Lombardini, X. Ma, Environ. Sci. Nano. 4 (2017) 1086–1094.
[3] S. Das, J.M. Dowding, K.E. Klump, J.F. McGinnis, W. Self, S. Seal, Nanomed. 8 (2013) 1483–1508.
[4] K.M. Poole, C.E. Nelson, R.V. Joshi, J.R. Martin, M.K. Gupta, S.C. Haws, T.E. Kavanaugh, M.C. Skala, C.L. Duval, Biomaterial. 41 (2015) 166–175.
[5] M.S. Gul, S. Ahmad, A. Naqvi, R. Hussain, A.A. Wali, I.A. Farooqi, J. Appl. Biol. Biotechnol. 5 (2017) 072–085.
[6] H. Li, G. Lu, D. Qiao, Y. Wang, Y. Guo, Y. Guo, Catal. Lett. 141 (2011) 452–458.
[7] M. Farahmandjou, M. Zarinkamar, T.P. Firoozabadi, Rev. Mex. Fis. 62 (2016) 496–499.
[8] V.D. Araujo, W. Avansi, H.B. deCarvalho, M.L. Moreira, E. Longo, C. Ribeiro, M.I. B. Bernardi, Cryst. Eng. Comm. 14 (2012) 1150–1154.
[9] T. Masui, H. Hirai, N. Imanaka, G. Adachi, T. Sakata, H. Mori, J. Mater. Sci. Lett. 21 (2002) 489–491.
[10] S. Shao-Ju, B. Konstantin, Li-Jr. Borisenko, Yi-C. Chin, J. Nano. Res. 12 (2010) 1553–1559.
[11] D.V. Pinjari, A.B. Pandit, Ultrason. Sonochem. 18 (2011) 1118–1123.
[12] M. Darroudi, M.B. Ahmad, A.H. Abdullah, N.A. Ibrahim, Int. J. Nanomed. 6 (2011) 569–574.
[13] P. Raveendran, J. Fu, S.L. Wallen, Am. Chem. Soc. 125 (2003) 13940–13941.
[14] A.K. Potbhare, R.G. Chaudhary, P.B. Chouke, S. Yerpude, A. Mondal, V.N. Sonkusare, A.R. Rai, H.D. Juneja, Mater. Sci. Eng. C. 99 (2019) 783–793.
[15] S. Narayanan, B.N. Sathy, U. Mony, M. Koyakutty, S.V. Nair, D. Menon, ACS Appl. Mater. Interface. 4 (2012) 251–260.
[16] A.S. Karakoti, S.V. Kuchibhatla, K.S. Babu, J. Phys. Chem. C. 111 (2007) 17232–17240.
[17] J. Gagnon, K.M. Fromm, Eur. J. Inorg. Chem. 27 (2015) 4510–4517.
[18] Z. Tian, J. Li, Z. Zhang, W. Gao, X. Zhou, Y. Qu, Biomaterials. 59 (2015) 116–124.
[19] A. Arya, A. Gangwar, S.K. Singh, Int. J. Nanomed. 11 (2016) 1159–1173.
[20] X. Beaudoux, M. Virot, T. Chave, G. Durand, G. Leturcq, S.I. Nikitenko, Green Chem. 18 (2016) 3656–3668.
[21] M.B. Gawande, V.B. Bonifacio, R.S. Varma, Green Chem. 15 (2013) 1226–1231.
[22] S. Munusamy, K. Bhakyaraj, L. Vijayalakshmi, A. Stephen, V. Narayanan, Int. J. Innov. Res. Sci. Eng. 2 (2014) 318–323.
[23] Q. Maqbool, M. Nazar, S. Naz, et al., Int. J. Nanomed. 11 (2016) 5015–5025.
[24] G.S. Priya, A. Kanneganti, K.A. Kumar, K.V. Rao, S. Bykkam, Int. J. Sci. Res. Publ. 4 (6) (2014) 1–4.
[25] N. Thovhogi, A. Diallo, A. Gurib-Fakim, M. Maaza, J. Alloys Compd. 647 (2015) 392–396.
[26] A.R. Bagade, R.G. Chaudhary, A. Potbhare, A. Mondal, M. Desimone, K. Dadure, R. Mishra, H. Juneja, Chem. Select. 4 (2019) 6233–6244.
[27] T.K. Mishra, A. Kumar, S.K. Sinha, B. Gupta, Mater. Today: Proc. 5 (2018) 27786–27794.
[28] J. Tanna, R.G. Chaudhary, N. Gandhare, A. Mondal, H. Juneja, J. Chin. Adv. Mater. Soc. 5 (2017) 103–117.
[29] V.N. Sonkusare, R.G. Chaudhary, G.S. Bhusari, A. Mondal, A.K. Potbhare, R.K. Mishra, H.D. Juneja, A.A. Abdala, ACS Omega. 5 (2020) 7823–7835.
[30] S. Sebastiammal, A. Mariappan, K. Neyvasagam, A. Lesly Fathima, Mater. Today: Proc. 9 (2019) 627–632.
[31] D.W. Wheeler, I. Khan, Vib. Spectrosc. 70 (2014) 200–206.
[32] M.M. Ali, H.S. Mahdi, A. Parveen, A. Azam, AIP Conf. Proc. 1953 (2018) 030044-1-030044-4.
[33] R.G. Chaudhary, V. Sonkusare, G. Bhusari, A. Mondal, D. Shaik, H. Juneja, Res. Chem. Intermed. 44 (2017) 2039–2060.
[34] J. Tanna, R.G. Chaudhary, N. Gandhare, A. Rai, S. Yerpude, H. Juneja, J. Expt. Nanosci. 11 (2016) 884–900.
[35] V. Sonkusare, R.G. Chaudhary, G. Bhusari, A. Rai, H. Juneja, Nano-Struct. Nano-Obj. 13 (2018) 121–131.
[36] T. Pirmohamed, J.M. Dowding, S. Singh, B. Wasserman, E. Heckert, A.S. Karakoti, J.E. King, S. Seal, W.T. Self, Chem. Comm. 46 (2010) 2736–2738.
[37] P.B. Chouke, A.K. Potbhare, G.S. Bhusari, S. Somkuwar, D.P.M.D. Shaik, R.K. Mishra, R.G. Chaudhary, Adv. Mater. Lett. 10 (2019) 355–360.
[38] A.K. Potbhare, P.B. Chouke, S. Zahra, V. Sonkusare, R. Bagade, M. Ummekar, R.G. Chaudhary, Mater. Today: Process. 15 (2019) 454–463.
[39] F. Pagliari, C. Mandoli, G. Forte, ACS Nano. 6 (2012) 3767–3775.
[40] S.S. Lee, W. Song, M. Cho, ACS Nano. 26 (2013) 9693–9703.
[41] X.Y. Lu, J. Tang, Z. Zhang, K. Ding, Curr. Med. Chem. 22 (2015) 651–667.
[42] V. Gerusz, Annu. Rep. Med. Chem. 45 (2010) 295–311.
[43] D.C. McKinney et al., ACS Infect. 2 (7) (2016) 456–464.

Role of Ajan Vruksha/Khandu Chakka Plant (*Ehretia Laevis Roxb.*) in Covid-19 Pandemic

Rushikesh Thakre*1, Ketaki Harne2, Pradip Tekade2, Shweta Parve3

1Department of Samhita & Siddhant, Mahatma Gandhi Ayurved College, Hospital and Research Centre, Salod(Hi), Wardha, Datta Meghe Institute of Medical Sciences (DU), Nagpur, Maharashtra, India
2Department of Chemistry, Bajaj College of Science (Formerly known as Jankidevi Bajaj College of Science), Wardha (MS), Rashtrasant Tukadoji Maharaj Nagpur University, Nagpur(MS), India
3Department of Panchakarma, Mahatma Gandhi Ayurved College, Hospital and Research Centre, Salod(Hi), Wardha, Datta Meghe Institute of Medical Sciences (DU), Nagpur, Maharashtra, India

ABSTRACT

Ehretia Laevis Roxb. plant has many compounds useful in wound healing, fractures, UTI, aphrodisiac, headache, antihelminthics, diuretic, demulcent, expectorant, RTI, fever, fungal infections, hepato-protective , cytotoxic, insecticidal, anti-inflammatory, anti-apoptotic, anti-carcinogenic, weight gain, diabetes , muscles wasting, anti viral activity, preventing viral mutations, blood clotting, reduce the serum lipid level, immunity booster, promotes neural crest cell survival, sedation , anti-Alzheimer, antinociceptive , thyroid uptake promotion, anticoagulant, antiplatelet aggregatory, peptic ulcer, antiasthmatic, antiosteoporotic & antiosteopenic , anticataract & ophthalmic effect, decongestant, skin protective, nephroprotective, anti fatigue effect, protection of human sperm, protection of testicular tissue , larvicidal, antimalarial, antiretroviral, cosmetics product, atopic dermatitis, anti fatigue, neuroprotective, retinoprotective, lung tissue protection, heart protection , prevention of splenocyte apoptosis, relieve stress and improve sleep, hepatic encephalopathy , anti-secretory, neurotransmitter, myelin sheath maintenance, gastric acid secretion & regulation, metal ions chelator, anemia, psychiatric disorders, collagen formation, reduce the recurrence, severity, healing period of herpes simplex virus infections, calcium absorption , muscle protein, post surgery recovery, sports injuries, hormones , aging, used in psychotropic drugs.

*Corresponding Author

Name: Rushikesh Thakre
Phone: 9765404039
Email: dr.rushu@gmail.com

INTRODUCTION

Corona Virus Disease (COVID-19) is a contagious disease caused by virus. It causes respiratory symptoms such as a dry cough, high fever, sore throat and, difficulty breathing in severe cases. It spreads by coughing, sneezing, personal contact, infected material, mass gatherings; one can avoid infection by regular hand wash, covering of mouth and by maintaining social distance. Cases were reported in Wohan city, Hubei province of china in the month of December 2019. On 7th January 2020 they have confirmed COVID-19 as a causative virus. And on 30th January 2020 WHO authorities declared that the outbreak constitutes a public health emergency of interna-

tional concerns (PHEIC).

No promising medicine is available for treatment and prevention till. Lot of studies is going on for treatment and prevention. In word near about 1,39,5136 cases are confirmed, 81580 confirmed deaths till 9th of April 2020 (WHO, 2020) . In India 5095 are active cases, 472 cured and 166 total death till 9th April 2020 (WHO, 2020). Lots of efforts are being taken by government for prevention and to stop spread of infections. Traditional medicines are very famous in China and used for COVID-19. Indian government also published advisory by AYUSH department for COVID-19

As Ayurved is Science of life and lots of majors are mentioned in Ayurveda for controlling this Janapadadwansa like Dincharya, Ritucharya, majors for building good immune system and medicines to cure diseases. In Maharashtra state of India *Ehretia Laevis Roxb.* plant is being used for many diseases traditionally. Also this is very spiritual plant as Santa Ghynaneshwar Maharaj from Alandi Pune has taken Samadhi at the base of this plant (Admuthe, 2016). In this herbal plant, many phytochemicals are available which shows antimicrobial activities including anti viral activities. Also they have antioxidant properties which are useful for building immunity to fight viral infections.

REVIEW OF LITERATURE

Ehretia laevis Roxb. also known as Khandu Chakka and Ajan Vruksha plant has many medicinal useful chemical compoundsTable 1.
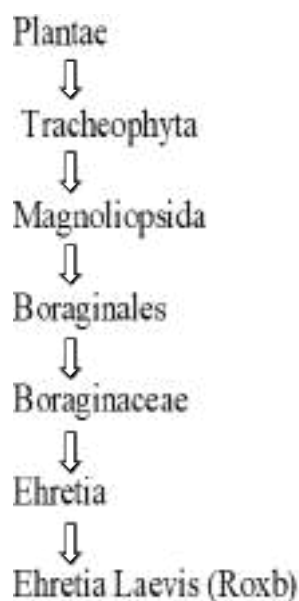
Figure 1: Plant Description

Ehretia laevis is Commonly known as: ovate-leaved ivory wood, Gujarati: Vadhavaradi, Sanskrut:-

Charma Vruksha Hindi: Bhairi, chamror, Konkani: kalo gamdo, Malayalam: Caranti, Marathi:, Datrangi (As it colors teeth in red), Ajan Vruksha (Sant Dnyaneshwar from Alandi Maharashtra India took Samadhi near the base of this tree). leaves ,fruits and flowers are shown in Figures 2, 3 and 4. Native to: India, Pakistan, Laos, Myanmar, Vietnam, China, Bhutan. In Ayurvedic literature this plant mentioned as Charma Vruksha and useful for *Prameha (*Diabetics) and *Vishaghna* (Anti-Venom) (Moorthy, 2002; Acharya, 2001) . This plant is commonly used in joints pain, wound healing, minor fractures by local peoples (Thakre, 2016).

Figure 2: Leaves of *Ehretia Laevis Roxb*

Figure 3: Fruits of *Ehretia Laevis Roxb*

Ajan Vruksha

This is the sacred tree. It is a myth that the root of a plant was touching Gnyaneshwar Maharaj's throat and was removed by Shree Eknath Maharaj . Pilgrims practice Gnyaneshwari Parayan under Ajan Vruksha plant.

Eknath Maharaj visited to Alandi which is Samadhi place of Sant Gnyaneshwar . Sant Gnyaneshwar Maharaj asked him in his dream to remove the roots of Ajan tree from his neck. Eknath Maharaj located the Samadhi of Sant Gnyaneshwar Maharaj and spotted the Ajan tree near the Samadhi of Sant

Figure 4: Flowers of *Ehretia Laevis Roxb*

Gnyaneshwar Maharaj. He went inside the Samadhi place & removed the root (sadgurus-saints sages, 2020).

Its medicinal properties are used in syphilis and diphtheria, eczema, as an aphrodisiac. Leaves are used to cure ulcers and in headache, anti-helminthics, diuretic, demulcent, expectorant, urine infection, diseases of lungs and decoction of bark is used for gargle in throat infections. Malaria, fever, in fungal infections and has hepato-protective properties (Thakre, 2016) .

Drug has aphrodisiac property like Rasayan and Vajikaran properties mentioned in the ayurveda. Such drugs are always useful for building immunity and acts as an antioxidant. This property of plant may be useful for fighting viral infections and other complications. Also studies shows that maximum deaths are in vulnerable patients. In vulnerable patients we can use this plant for Rasayan and Vajikaran therapy.

Local peoples are using this plant for diphtheria, head ache, demulcent and expectorant and diseases of lungs (Thakre, 2016). This property of this plant can be useful for infection of respiratory tracts and symptoms of viral infections. As decoction is used for gargles in throat infection hence it can be used for sore throat. Sore throat is one of symptoms in viral infection.

It has very good pain relief activity (Thakre, 2016). Peoples can use plant leaves with oil for pain relief. It is very beneficial for old peoples suffering from joint pains. It will save the side effects of pain killer medicines and save the money of general public, as income sources are restricted due to lock down.

This plant is also used in malaria and fever (Thakre, 2016). Recent studies shows that anti malarial drugs are effective in the treatment of COVID-19. This plant may be used for fever in viral infections.

As per Ayurvedic literature this plant is used in

Prameha (Moorthy, 2002; Acharya, 2001) . Diabetes is considered as one of the co morbidity in COVID-19. Hence this plant may be used to decrease co morbidity in viral infections. This plant has anti oxidant property (Velappan and Thangaraj, 2013). This property is very useful for boosting immunity to fight infections.

Its Hepato protective property will be useful in the side effects of drugs on liver during the treatment of viral infections. Its wound healing property is proven on scientific basis and can be used in wounds to avoids untoward effects of antibiotics (Thakre, 2016) . *Ehretia Laevis Roxb*.plant shows anti microbial activity on S. aureus, E. Coli (Thakre and Harne, 2019). Pseudomonas aeruginos ,salivary microflora (Deshpandea *et al.*, 2015) B.subtilis (Jyothirmai *et al.*, 2016). This antimicrobial property can be used for secondary infection and associated infections in viral treatment and to maintain general hygiene.

This plant contains many chemicals like,

Naphthoquinone derivative named lewisone, n-octatricontane, baurenol acetate, baurenol, ursolic acid (Thapliyal and Aggarwal, 2011) . Proteins, Lipids, Amino acids, Minerals such as Ca,NH3, Mg, Na, Fe, Mn, , P, Zn, K, Cu and Si, Gallic acid, tannins, rutin ,Vit C, decanoic acids, phenylephrine, acontanes ,phthalic acid, phytol, α and β amyrin, piperazine (Velappan and Thangaraj, 2013).

Benzoquinones

Benzoquinones- 1,4naphthoquinone lewisone, Bauerenol ,Bauerenol acetate, α-amyrin, Betulin, Lupeol, Betulinic acid, β-sitosterol (Li *et al.*, 2010). Dodecane, Tridecene , Tetradecane , n Octylcyclohexane,Tridecanol ,Hexadecane ,Decyl cyclohexane ,Heptadecane ,Nonadecane , Tetratetracontane (Rangnathrao and Shanmugasundaram, 2019), Di – n octyl phthalate (Ibrahim *et al.*, 2012). Amino acid- Butyric acid, Ornithine, Cysteine, Histidine, Arginine, Serine, Hydroxy proline, Glutamic acid, Proline, Lysine, Tryptamine having various therapeutic properties (Torane *et al.*, 2009) .

2(4H)-Benzofuranone, 5,6,7,7a-tetrahydro-4,4,7a-trimethyl ; Ppropiolicacid,3-(1-hydroxy-2-isopropyl-5*methylcyclohexyl) ; 3,7,11,15-Tetramethyl-2-hexadecen-1-ol ; Hexadecanoic acid, 15-methyl-, methyl ester ; Tridecanoic acid ; 12,15-Octadecadienoic acid, methyl ester ; Methyl 2-hydroxy-octadeca-9,12,15-trienoate; 1,2-15,16-Diepoxyhexadecane ; 8,11-Octadecadienoic acid, methyl ester ; Methyl 8,11,14-heptadecatrienoate; 5-Chloro-3beta-hydroxy-6beta-nitro-5alpha-androstan-17-one.

Propane, 1,2-dichloro-2-methyl, 1-Chloro-2-ethoxy-2-methoxy-propane, 4-Chloro-2,4-dimethylhexane, Cyclohexasiloxane, dodecamethyl, Cycloheptasiloxane, tetradecamethyl, Phenol, 2,4-bis(1,1-dimethylethyl) ; Cyclooctasiloxane, hexadecamethyl ; 9,10-Dimethyltricyclo[4.2.1.1(2,5)]decane-9,10-diol ; 1,1,3,3,5,5,7,7,9,9,11,11,13,13,15,15-hexadecamethyloctasiloxane ; 3,7,11,15-Tetramethyl-2-hexadecen-1-ol ; 9-Eicosyne; 1,2-Benzenedicarboxylic acid, butyloctyl ester ; Phthalic acid, isobutyl octadecyl ester ; Oxirane, hexadecyl-; Methyl 6,10-octadecadienoate ; 9,12,15-Octadecatrienoic acid, (Z,Z,Z)- ; Phthalic acid, octyl 2-propylpentyl ester.

Benzoic acid, 2,6-bis [[(trimethylsilyl)oxy]-trimethylsilyl ester ; Silane(pregn-5-ene-3á,11á,17,20á-tetrayltetraoxy)tetrakis[trimethy; (5á)Pregnane-3,20á-diol ; 2-Trimethylsiloxy-6-hexadecenoic acid, methyl ester; 4-(Dimethylaminomethyl-5-hydroxybenzofuran-3-yl)(4-methoxyphenyl)methanone ; Chromone, 5-hydroxy-6,7,8-trimethoxy-2,3-dimethyl- ; 6,7-Epoxypregn-4-ene-9,11,18-triol-3,20-dione ; 3,9-Epoxypregn-16-ene-14-18-diol-20-one, 7,11-diacetoxy-3-methoxy- ; 5,8,11,14-Eicosatetraynoic acid, trimethylsilyl ester ; 2,7-Diphenyl-1,6-dioxopyridazino[4,5:2',3']pyrrol o[4',5'-d]pyridazine ; 2,15-Heptadecadiene, 9-(ethoxymethyl) ; Ethyl iso-allocholate; 4-Methoxyphenoxyformamide N-methyl-N-[4-(1-pyrrolidinyl)-2-butynyl] ; Hexadecanoic acid, 14-methyl-, methyl ester; Phthalic acid, butyl oct-3-yl ester; Methyl 9,12-epithio-9,11-octadecanoate ; Methyl 4,7,10,13,16,19-docosahexaenoate; Z,Z-4,16-Octadecadien-1-ol acetate ; 2,7-Diphenyl-1,6-dioxopyridazino[4,5:2',3'] pyrrolo [4',5'-d] pyridazine (Joshi and Wagh, 2018).

The medicinal uses of above chemicals are mentioned in Table 1.

RESULTS AND DISCUSSION

This Ajan Vruksha plant also known as Khandu Chakka herbal plant, may be useful as antiviral drug and useful in symptom like fever and other associated infections in COVID-19 complications.

This plant has major characteristic of Analgesic, anti arthritic and antinociceptive which is useful in severe body ache, inflammation in viral infection. It has chemical which has antioxidant & anti-apoptotic property which is useful to built immunity in viral infection.

Plant has many such chemicals which are useful in malignancy, obesity, blood sugar, cardio vascular diseases, blood pressure and lipids and muscle wasting to minimise the risk in viral infection, because maximum death in COVID-19 are associated with secondary complications.

Plant has a property to fight infections of fungus and bacteria which may associate with viral infections. This herbal plant has chemicals which have very good effect on neural diseases like brain ischemia, and useful for promotion of neural crest cell survival, sedative, anticonvulsant, anti-Alzheimer, Anti-seizure , antidepressant , stroke (Rushikesh et al., 2012).

Plant has thyroid uptake promotion property which will be useful for thyroid patients. Anticoagulant, antiplatelet property is useful in old age patients and bedridden patients, also this will reduce the risk in heart patients. Beneficial chemicals to treat the peptic ulcer and cataract are available in this plant. This will help for prevention of diseases (Rushikesh et al., 2016).

Antiasthmatic property may be used for common cold one of the symptom in COVID-19. Antiosteo-porotic and antiosteopenic properties are useful for old age patients and rural people as their movements are restricted due to lock down and limited resources.

Chemicals present in this plant act as diuretic, has protective effect on human sperm, protection to testicular tissue, reproduction, useful for kidney and reproductive organs diseases (Santos et al., 2013).

Plant chemical has a property of larvicidal which is useful in malaria. And useful in cosmetics and skin care product, atopic dermatitis, increase immunity, Anti fatigue activity.

Rutin from this plant is responsible for Neuroprotective activity, Retinoprotective, Protective effect on lung tissue hence this will be useful in COVID-19 pandemic. Also it has Cardioprotective , Hepatoprotective, Nephroprotective, Protective effect on blood vasculature, Wound healing property , Radio modulatory effects and help in prevention of splenocyte apoptosis. These properties can be used in associated conditions of the patient.

A chemical from plant is useful in Asthma and can be used in bronchodilator in chest infection. It has antidepressive activity. As many people are in lock down from many days hence there may be chance for depression. To overcome depression this property may be used.

To protect other organs in infection or for maintenance of proper health by its gastro &hepato protective, antipancreatitic, anticholytic, anti diabetic & hypolipidemic effects are very useful. It contains

---

Table 1: The medicinal uses of present chemicals

S No	Name of chemical	Medicinal uses
1	Naphthoquinone derivative	antibacterial, antifungal, antiviral, insecticidal, cytotoxic, anti-inflammatory, antipyretic, anti parasite (Babula et al., 2007)
2	1,4-naphthoquinone lewisone	NA
3	n-octatricontane	NA
4	Baurenol acetate	NA
5	Baurenol	analgesic, in swellings (Villaseñor et al., 2004)
6	Ursolic acid	anti-inflammatory, anti-oxidant, anti-apoptotic, cytotoxic, obesity, diabetes mellitus, heart disease, brain & liver disease, muscle wasting (Seo et al., 2018)
7	Minerals such as Na, NH3, Fe, Mn, K, P, Zn, Cu, Si, Mg, Ca,	immune system, antioxidants, antiviral activity, preventing viral mutations (Chaturvedi et al., 2004)
8	Gallic acid	antiviral property (Balachandar et al., 2020)
9	Tannic acid	bacteria ,fungi, yeasts, viruses growth is prohibited by tannins. Clotting of blood, reduce hyper tension, control lipid level, causes liver necrosis, and improve immune responses (Chung et al., 1998)
10	Rutin	anticancer, neuroprotective effect on brain ischemia, improve neural crest cell survival, anticonvulsant, anti-alzheimer, antidepressant , stroke, sedative, analgesic and antiarthritic , analgesic and antinociceptive , Antiarthritic , antifungal, antidiabetic, antihypercholesterolemic, thyroid uptake promotion, hypertension, anticoagulant, antiplatelet aggregatory, peptic ulcer, antiasthmatic, antiosteoporotic and antiosteopenic , anticataract and ophthalmic effect Diuretic, protection of human sperm, protection of testicular tissue, anticancer, antibacterial, antifungal, antimycobacterial, larvicidal, antimalarial, antiretroviral, antiviral, anti-apoptotic, cosmetics and skin care product, atopic dermatitis, increase immunity, Anti fatigue activity, neuroprotective activity, retinoprotective, protective of lung tissue, protection of heart , prevention of splenocyte apoptosis, hepatoprotective, nephroprotective, protective effect on blood vasculature, Wound healing, Radio modulatory effects. (Ganeshpurkar and Saluja, 2017)
11	Vitamin C -ascorbic acid	Improve immune system (Wintergerst et al., 2006)
12	Acontanes	NA
13	Decanoic acids	antiseizure (Sills et al., 1986) ,Larvicidal activity (Santos et al., 2017)
14	Phthalic acid	NA

Continued on next page

Table 1 continued

S No	Name of chemical	Medicinal uses
15	Phytol	antinociceptive and Antioxidant (Santos *et al.*, 2017) ,anticancer and immune-enhancing effects, inhibit cellular senescence (Jeong, 2018) ,arthritis, asthma, mosquito repellent, useful for malaria (Okiei *et al.*, 2009)
16	α and β amyrin	antinociceptive, anticonvulsant, analgesic, in inflammation, depression, hepatic & pancreatic diseases, anticholytic, gastroprotective, anti diabetic & hypolipidemic Oliveira *et al.* (2005) microbial, fungal, and viral infections, cancer cells (Rao, 2012)
17	Piperazine	anti-helmintic , antiviral (Aggarwal *et al.*, 2017)
18	Phenylephrine	decongestant (Vardanyan and Hruby, 2006)
19	Betulin & Betulinic acid	antitumor, anti viral, antibacterial, anti-inflammatory, antimalarial (Alakurtti *et al.*, 2006)
20	Lupeol	antiprotozoal, antimicrobial, anti-inflammatory, antitumor and chemo preventive properties (Gallo and Sarachine, 2009). anti-diabetic, cardioprotective, anti-inflammatory, skin protective, hepatoprotective, nephroprotective (Siddique and Saleem, 2011)
21	β-sitosterol	antibacterial, anti-inflammatory, cytotoxic, antifertility, angiogenic, antioxidant, immunity enhancer, antidiabetic, antinociceptive (Ambavade *et al.*, 2014)
22	Dodecane	NA
23	Tridecene	NA
24	Tetradecane	NA
25	Tridecanol	NA
26	Hexadecane	NA
27	Decyl cyclohexane	NA
28	Heptadecane	NA
29	Nonadecane	NA
30	Di – n octyl phthalate	anti venom (Ibrahim *et al.*, 2012)
31	Butyric acid	NA
32	Ornithine	decrease stress and enhance sleep quality related to fatigue (Miyake *et al.*, 2014) Hepatic Encephalopathy (Li *et al.*, 2018)
33	Cysteine	wound healing, antitumor Salas *et al.* (2008) ,Antioxidant, skin-whitening (Sakamoto *et al.*, 2017)

Table 1 continued

S No	Name of chemical	Medicinal uses
34	Histidine	Precursor for several hormones, anti-inflammatory, anti-oxidant, and anti-secretory functions within the body, neurotransmitter, maintenance of the myelin sheath, gastric acid secretion and regulation, chelator of metal ions like copper, zinc, manganese, and cobalt, anemia (Kessler and Purich, 2019)
35	Serine	psychiatric disorders (de Koning *et al.*, 2003)
36	Hydroxy proline	promotes collagen which maintains the structure and strength of connective tissue like bones, cartilage, blood vessels & skin (Li and Wu, 2018)
37	Glutamic acid	proper metabolism & nervous tissue functions Weil-Malherbe (1950)
38	Lysine	Reduce the recurrence, severity, and healing period of herpes simplex virus infections (Chen *et al.*, 2011) . Treatment for schizophrenia Wass *et al.* (2011) Absorption of calcium, building of muscle protein, post surgery recovery ,sports injuries , production of hormones, enzymes, & antibodies, osteoporosis, anxiety and mood disturbances, migraine, alzheimer's dementia, loss of hairs, shingles, malignancy, heart diseases and aging (Singh *et al.*, 2011)
39	Tryptamine	hallucinations, used in psychotropic drugs (Araújo *et al.*, 2015)
40	Hexadecanoic acid	anti-inflammatory (Aparna *et al.*, 2012) , Cytotoxic Ravi and Krishnan (2016)
41	12,15-Octadecadienoic acid, methyl ester	Antifungal, Antibacterial, Antimicrobial, Emulsifier, Perfumery Industry (Arora *et al.*, 2017)
42	Cyclohexasiloxane	Cosmetic ingredients (Johnson *et al.*, 2011)
43	Benzoic acid	Expectorant, analgesic, and antiseptic (Lillard, 1904)
44	Ethyl Iso-allocholate	Antimicrobial (Malathi *et al.*, 2016)
45	5,8,11,14-Eicosatetraynoic acid-(Arachidonic acid is an omega-6 fatty acid)	Essential for all cells functions, especially for nervous system, skeletal muscle, & immune system, brain & muscles functions, protection from *Schistosoma mansoni* and *S. haematobium* infection , tumor initiation, development, metastasis, swelling & wound healing, heart diseases (Tallima and Ridi, 2018)

piperazine it may be used as Anti-helmintic. Deworming of population is very important to maintain proper health to fight infection. Phenylephrine is available in this plant; hence this plant may be used as a decongestant in flu like symptoms.

This plant contains Lupeol which is skin protective, hence can be used as cosmetic purpose. In Ayurveda this plant is mentioned as Vishagna i.e. anti venom also this plant contains Di – n octyl phthalate which shows anti venom property. Ornithine from this plant may help to decrease stress and enhance sleep quality in the panic situation of COVID-19 pandemic. Hydroxy proline from this plant may help for formation of collagen which is important for normal structure and connective tissue & blood vessels in lack of exercise in lock down situation.

Plant contains Lysine which reduce the recurrence, severity, and healing period of herpes simplex virus infections hence can be used in other viral infection (Sivasankari *et al.*, 2013). Also this is useful in treatment for schizophrenia, absorption of calcium, muscle protein, post surgery recovery, sports injuries, production of hormones, enzymes, antibodies, osteoporosis, anxiety and disturbances of mood, migraine, Alzheimer's dementia, loss of hairs, shingles, malignancy, heart diseases and aging. Tryptamine from this plant causes Hallucinations, used in psychotropic drugs and can be used for needy patients under medical supervision. These properties of Ajan Vruksha also known as Khandu Chakka plant may be useful for the patients in various medical conditions to overcome from COVID-19 pandemic crises, when there is lock down and limited recourses are available nationally and internationally. As this plant shows activity against pathogens and has many chemicals which can be used against pathogens, hence one can do further study to make hand wash as a sanitizer for prevention of disease. This will give employment to the peoples when there are lack of opportunities due to lock down and economical crises.

CONCLUSIONS

Hence to tackle such situation this herbal plant which is also considered very spiritual plant may help in this critical condition of COVID-19 pandemic by its Anti Viral activity and other medicinal useful activities for co morbidity conditions. These medicinal activities of plant will open the door for further research and will provide good opportunities for employment and farming to strengthen the economy of world. This spiritual plant may pave the way for humanity.

REFERENCES

Acharya, V. Y. T. 2001. Charak Samhita of Agnivesa Elaborated by Charaka and Dridhbala with the Ayurved Dipika Commentary by Chakrapani. *Chaukhambha Sanskrit Sansthaan*.

Admuthe, N. B. 2016. Micropropagation for Ehretia laevis Roxb. A rare Indian medicinal plant. *International Journal of Advanced Scientific and Technical Research*, 3(6):411–422.

Aggarwal, M., Kaur, R., Saha, A., Mudgal, R., Yadav, R., Dash, P. K., Parida, M., Kumar, P., Tomar, S. 2017. Evaluation of antiviral activity of piperazine against Chikungunya virus targeting hydrophobic pocket of alphavirus capsid protein. *Antiviral Research*, 146:102–111.

Alakurtti, S., Mäkelä, T., Koskimies, S., Yli-Kauhaluoma, J. 2006. Pharmacological properties of the ubiquitous natural product betulin. *European Journal of Pharmaceutical Sciences*, 29(1):1–13.

Ambavade, S. D., Misar, A. V., Ambavade, P. D. 2014. Pharmacological, nutritional, and analytical aspects of β-sitosterol: a review. *Oriental Pharmacy and Experimental Medicine*, 14(3):193–211.

Aparna, V., Dileep, K. V., Mandal, P. K., Karthe, P., Sadasivan, C., Haridas, M. 2012. Anti-Inflammatory Property of n-Hexadecanoic Acid: Structural Evidence and Kinetic Assessment. *Chemical Biology & Drug Design*, 80(3):434–439.

Araújo, A. M., Carvalho, F., de Lourdes Bastos, M., de Pinho, P. G., Carvalho, M. 2015. The hallucinogenic world of tryptamines: an updated review. *Archives of Toxicology*, 89(8):1151–1173.

Arora, S., Kumar, G., Meena, S. 2017. Screening and Evaluation of Bioactive Components of Cenchrus Ciliaris L. By GC-MS Analysis. *International Research Journal of Pharmacy*, 8(6):69–76.

Babula, P., Adam, V., Havel, L., Kizek, R. 2007. Naphthoquinones and their pharmacological properties. *Ceska a Slovenska farmacie: casopis Ceske farmaceuticke spolecnosti a Slovenske farmaceuticke spolecnosti*, 56:114–120.

Balachandar, V., Mahalaxmi, I., Kaavya, J., Vivekanandhan, G., Ajithkumar, S., Arul, N., Singaravelu, G., Kumar, N. S., Devi, S. M. 2020. COVID-19: emerging protective measures. *European Review for Medical and Pharmacological Sciences*, 24(6):3422–3425.

Chaturvedi, U. C., Shrivastava, R., Upreti, R. K. 2004. Viral infections and trace elements: a complex interaction. *Current science*, (11):1536–1554.

Chen, F., Kan, H., Castranova, V. 2011. Methylation of lysine 9 of histone H3: role of heterochromatin modulation and tumorigenesis. *Handbook of Epigenetics*, pages 149–157.

Chung, K. T., Wong, T. Y., Wei, C. I., Huang, Y. W., Lin, Y. 1998. Tannins and Human Health: A Review. *Critical Reviews in Food Science and Nutrition*, 38(6):421–464.

de Koning, T. J., Snell, K., Duran, M., Berger, R., Poll-The, B.-T., Surtees, R. 2003. l-Serine in disease and development. *Biochemical Journal*, 371(3):653–661.

Deshpandea, R. R., Kamatha, A., Shepa, S., Muthaa, M., Methaa, B., Patila, D., Toraneb, R., Deshpandeb, N. 2015. Comparative Evaluation of Antimicrobial Properties of Active Extracts of Morinda pubescens and Ehretia laevis against Salivary Microflora. *The Journal for Dentistry*.

Gallo, M. B., Sarachine, M. J. 2009. Biological activities of lupeol. *Int J Biomed Pharm Sci*, 3(1):46–66.

Ganeshpurkar, A., Saluja, A. K. 2017. The Pharmacological Potential of Rutin. *Saudi Pharmaceutical Journal*, 25(2):149–164.

Ibrahim, S., Nok, J. A., Abubakar, M. S., Sarkiyayi, S. 2012. Efficacy of Di-n-octyl Phthalate Anti Venom Isolated from" Ceiba pentandra" Leaves Extract in Neutralization of" Echis ocellatus" Venom. *Research Journal of Applied Sciences, Engineering and Technology*, 4(15):2382–2387.

Jeong, S. H. 2018. Inhibitory effect of phytol on cellular senescence. *Biomedical Dermatology*, 2(1):13–13.

Johnson, W., Bergfeld, W. F., Belsito, D. V., Hill, R. A., Klaassen, C. D., Liebler, D. C., Marks, J. G., Shank, R. C., Slaga, T. J., Snyder, P. W., Andersen, F. A. 2011. Safety Assessment of Cyclomethicone, Cyclotetrasiloxane, Cyclopentasiloxane, Cyclohexasiloxane, and Cycloheptasiloxane. *International Journal of Toxicology*, 30(6_suppl):149S–227S.

Joshi, U. P., Wagh, R. D. 2018. GC-MS Analysis of Phytochemical Compounds present in the bark extracts of Ehretia laevis Roxb. *International Journal of Research and Development in Pharmacy & Life Sciences*, 7(6):3150–3154.

Jyothirmai, N., Nagaraju, B., Kumar, J. S. 2016. Evaluation of anti-inflammatory and anti-bacterial activities of different solvent extracts of Ehretia laevis Roxb. *Journal of Pharmaceutical Sciences and Research*, 8(8):715–715.

Kessler, A. T., Purich, D. L. 2019. Biochemistry, Histidine. In StatPearls . Stat Pearls Publishing.

Li, H. W. C., Naidas, M. A. L. M., Mondragon, K. A. M., Maralit, R. M. 2018. The role of L-ornithine-L-aspartate in the Management of Minimal Hepatic Encephalopathy among Patients with Liver cirrhosis: a Systemic review and Meta-analysis. *Acta Medica Philippina*, 52(1):94–94.

Li, L. I., Peng, Y., Yao, X., Xu, L. J., Wulan, T. N., Liu, Y., Shi, R., Xiao, P. 2010. Chemical constituents and biological activities of plants from the genus Ehretia Linn. *Chinese Herb Med*, 2:106–117.

Li, P., Wu, G. 2018. Roles of dietary glycine, proline, and hydroxyproline in collagen synthesis and animal growth. *Amino Acids*, 50(1):29–38.

Lillard, B. 1904. Practical druggist and pharmaceutical review of reviews . volume 13. Lillard & Company.

Malathi, K., Anbarasu, A., Ramaiah, S. 2016. Ethyl Iso-allocholate from a Medicinal Rice Karungkavuni Inhibits Dihydropteroate Synthase in Escherichia coli: A Molecular Docking and Dynamics Study. *Indian Journal of Pharmaceutical Sciences*, 78(6):780–788.

Miyake, M., Kirisako, T., Kokubo, T., Miura, Y., Morishita, K., Okamura, H., Tsuda, A. 2014. Randomised controlled trial of the effects of L-ornithine on stress markers and sleep quality in healthy workers. *Nutrition Journal*, 13(1).

Moorthy, S. 2002. *Sushruta Samhita with English translation*. Chaukhambha Orientalia Varanasi.

Okiei, W., Ogunlesi, M., Ofor, E., Osibote, E. A. S. 2009. Analysis of Essential Oil Constituents in Hydro-Distillates of Calotropis procera (Ait.) R.Br.

Oliveira, F. A., Chaves, M. H., Almeida, F. R., Lima, R. C., Silva, R. M., Maia, J. L., Brito, G. A. A., Santos, F. A., Rao, V. S. 2005. Protective effect of α- and β-amyrin, a triterpene mixture from Protium heptaphyllum (Aubl.) March. trunk wood resin, against acetaminophen-induced liver injury in mice. *Journal of Ethnopharmacology*, 98(1-2):103–108.

Rangnathrao, T. S., Shanmugasundaram, P. 2019. Antioxidant and Hepatoprotective activity of Ehretia laevis Roxb against paracetamol induced acute Hepatotoxicityin wistar rats. *Research Journal of Pharmacy and Technology*, 12(12):6143–6143.

Rao, V. 2012. Phytochemicals: a global perspective

of their role in nutrition and health. *BoD-Books on Demand*.

Ravi, L., Krishnan, K. 2016. Cytotoxic Potential of N-hexadecanoic Acid Extracted from Kigelia pinnata Leaves. *Asian Journal of Cell Biology*, 12(1):20–27.

Rushikesh, T., Bhutada, S., Chouragade, B., Khobragade, P., Ketaki, H. 2012. Evaluating the systematic position of Ehretia asperula Zoll. & Moritzi based on ITS1, matK and trnL-trnF DNA sequences. *International Journal of Research in Ayurveda and Pharmacy*, 36(2):93–102.

Rushikesh, T., Bhutada, S., Chouragade, B., Khobragde, P., Ketaki, H. 2016. Ethano Botanical Properties of Unexplored Plant Khandu Chakka (Ehretia Laevis Roxb.). *International Journal of Ayurveda and Pharma Research*, 4(7):68–73.

sadgurus-saints sages 2020. History of saint Eknath Maharaj [online] sadgurus-saints sages.

Sakamoto, K., Lochhead, R., Maibach, H., Yamashita 2017. Cosmetic science and technology: theoretical principles and applications.

Salas, C. E., Gomes, M. T., Hernandez, M., Lopes, M. T. 2008. Plant cysteine proteinases: Evaluation of the pharmacological activity. *Phytochemistry*, 69(12):2263–2269.

Santos, C. C., De, M. P., Salvadori, M. S., Mota, V. G., Costa, L. M., Almeida, A. A. C. D., Oliveira, G. A. L. D., Costa, J. P., Sousa, D. P. D., Freitas, R. M. D., Almeida, R. N. D. 2013. Antinociceptive and Antioxidant Activities of Phytol In Vivo and In Vitro Models. *Neuroscience Journal*, pages 1–9.

Santos, L. M. M., Nascimento, J. S., Santos, M. A. G., Marriel, N. B., Bezerra-Silva, P. C., Rocha, S. K. L., Silva, A. G., Correia, M. T. S., Paiva, P. M. G., Martins, G. F., Navarro, D. M. A. F., Silva, M. V., Napoleão, T. H. 2017. Fatty acid-rich volatile oil from Syagrus coronata seeds has larvicidal and oviposition-deterrent activities against Aedes aegypti. *Physiological and Molecular Plant Pathology*, 100:35–40.

Seo, D. Y., Lee, S. R., Heo, J. W., No, M. H., Rhee, B. D., Ko, K. S., Kwak, H. B., Han, J. 2018. Ursolic acid in health and disease. *The Korean Journal of Physiology & Pharmacology*, 22(3).

Siddique, H. R., Saleem, M. 2011. Beneficial health effects of lupeol triterpene: A review of preclinical studies. *Life Sciences*, 88(7-8):285–293.

Sills, M. A., Forsythe, W. I., Haidukewych, D. 1986. Role of octanoic and decanoic acids in the control of seizures. *Archives of Disease in Childhood*, 61(12):1173–1177.

Singh, M., Rao, D. M., Pande, S., Battu, S., Dutt, K. R., Ramesh, M. 2011. Medicinal uses of L-lysine: past

and future. *International Journal of Research in Pharmaceutical Sciences*, 2(4):637–642.

Sivasankari, V., Revathi, P., Parimelazhagan, T. 2013. Evaluation of In Vitro Antioxidant Activity In Edible Fruits of Ehretia Laevis Roxb. *The Journal for Dentistry*, 4(3):B 847–B 857.

Tallima, H., Ridi, R. E. 2018. Arachidonic acid: Physiological roles and potential health benefits – A review. *Journal of Advanced Research*, 11:33–41.

Thakre, R. 2016. Anti microbial activity of Ehretia Laevis Roxb. *Khandu Chakka) plant, wjpls, 4*, pages 112–116.

Thakre, R., Harne, K. 2019. Comparative Antimicrobial Study of Polar and Non Polar Extracts of Ehretia Laevis Roxb.(Khandu Chakka) Plant. *wjpls*, 6(10):7–9.

Thapliyal, P. C., Aggarwal, L. K. 2011. A New Quinone From Aerial Parts of Ehretia Laevis.

Torane, R. C., Ruikar, A. D., Chandrachood, P. S., Deshpande, N. R. 2009. Study of amino acids and carbohydrates from the leaves of Ehretia laevis. *Asian Journal of Chemistry*, 21(2):1636–1638.

Vardanyan, R., Hruby, V. 2006. Synthesis of essential drugs.

Velappan, S., Thangaraj, P. 2013. Phytochemical Constituents and Antiarthritic Activity ofEhretia laevisRoxb. *Journal of Food Biochemistry*, 38(4).

Villaseñor, I. M., Canlas, A. P., Faustino, K. M., Plana, K. G. 2004. Evaluation of the bioactivity of triterpene mixture isolated from Carmona retusa (Vahl.) Masam leaves. *Journal of Ethnopharmacology*, 92(1):53–56.

Wass, C., Klamer, D., Katsarogiannis, E., Pålsson, E., Svensson, L., Fejgin, K., Bogren, I.-B., Engel, J. A., Rembeck, B. 2011. L-lysine as adjunctive treatment in patients with schizophrenia: a single-blinded, randomized, cross-over pilot study. *BMC Medicine*, 9(1):40–40.

Weil-Malherbe, H. 1950. Significance of Glutamic Acid for the Metabolism of Nervous Tissue. *Physiological Reviews*, 30(4):549–568.

WHO 2020. Corona virus disease (COVID-19) outbreak situation.

Wintergerst, E. S., Maggini, S., Hornig, D. H. 2006. Immune-Enhancing Role of Vitamin C and Zinc and Effect on Clinical Conditions. *Annals of Nutrition and Metabolism*, 50(2):85–94.

Study of Excess Parameters and Partial Molar Volume for the Molecular Interactions of an aqueous 2-(tert-butylamino)-1-(3-chlorophenyl) Propan-1-one and NaCl Solution at Different Temperatures

Nita P. Mohabansi[*]

Department of Chemistry, Bajaj College of Science, Jamanalal Bajaj Marg, Civil Lines, Wardha, India.
nitamohabansi15@gmail.com

Abstract: **Density(ρ),Viscosity(η),Ultrasonic Velocity(U) and Surface Tension(γ) of an aqueous-consolute, NaCl solution of 2-(tert-butylamino)-1-(3-chlorophenyl)Propan-1-one (0.0201, 0.0402, 0.0804,0.1608 mol/kg)were measured at 293, 303 and 313K. These data were used to calculate various acoustical parameters viz., adiabatic compressibility(β), acoustic impedance (Z), relative association(RA), molar Compressibility (W), Rao's Constant (R), free volume(V_f^E), Intermolecular free length (L_f), and partial molar volume which provides valuable information regarding drug-electrolyte (NaCl) interaction. The excess parameters viz. excess adiabatic compressibility (β_E), excess inter molecular free length (L_f^E) and excess free volume (V_f^E) were also calculated. These calculations help in predicting the intermolecular interactions.**

Index Terms: **Acoustical parameters, Excess parameters, Inter molecular interaction, Partial molar volume.**

I. INTRODUCTION

Recently ultrasonic studies in aqueous solution of various drugs yield a piece of essential information about the strength of the intermolecular interactions and physical nature (Baluja, Solanki & Kacchadia, 2007; Murshed, Castro, Lourenco, Lopes & Santos, 2011). The interpretation of the nature of molecular interactions depends upon knowledge of the basics of different experimental aspects of the binary fluid system and the hypothetical analysis of ultrasonic velocity. There is thus much practical use to study and understand the experimental aspects of certain aqueous electrolytic solution through the exposure of

them to the ultrasound (Blandamer, 1973; Hwrzfeld & Litovitz, 1959). Extended applications can be found in the ultrasonic studies as the ultrasounic velocity in liquids and mixtures are closely related to several parameters which determine the physicochemical behavior of liquid and liquid soltions. Mixtures of solvents are extremely important in most chemical and industrial processes rather than single pure liquids because they give ample information of more component mixtures and it ensures that the derived characteristics of the medium can be continually adjusted. Relevant information on pharmaceutical and medicinal chemistry is provided through physicochemical behavior and inter-molecular interaction of the drug with an electrolyte. Multiple authors have examined interactions in between the molecules of various binary liquid mixtures with an electrolyte at varying temperatures. NaCl has specialized property like low melting but a high boiling point(Begaum, Sandhya, Karunakumar & Rambabu, 2013).These electrolytes are insoluble in ether but soluble in water (Begaum, Sandhya, Karunakumar & Rambabu, 2013; Gurung & Roy, 2006; ; Kharat, 2008; Nain, 2008; Thanuja, Kanagam, Sreedevi, 2011;Thirumaran & Sabu, 2012]. The interactions of the molecules of the drug and electrolytic solvent and its dependence on the temperature play a key role in understanding drug action (Dhondge, Zodape & Parwate, 2012a; Dhondge, Paliwal, Bhave & Pandhurnekar, 2012b; Syal, Chauhan & Chauhan, 2005; Thakur & Chauhan, 2011) Therefore, it can be fascinating to analyze the deviation of these parameters with temperature to understand drug-electrolytic solvent mechanisms (Baluja, Solanki & Kachhadia, 2007; Baragi & Maganur, 2013;

---

[*] Corresponding Author

Sonar & Pawar, 2010; Yadav & Yadav, 2005;) Thermodynamic studies of the binary solution with an electrolyte have attracted much attention. These experimental data from various scientist for the different systems can now be assessed and published (Ali &Navi, 2008; Chauhan, Singh, Kumar, Neelakantan et. al , 2016; Nain, 2007).

In the present study, an effort has been made to study the interaction between the drug, 2-(tert-butylamino)-1-(3-chlorophenyl) propan-1-one and the aqueous NaCl solution to determine the nature of the molecular environment. This drug is used as an anti-depressant drug (Fig.1)

II. EXPERIMENTAL METHODS AND MATERIALS

The solutions of different concentration (mol/kg) of 2-(tert-butylamino)-1-(3-chlorophenyl) propan-1-one (2-TBP) (Molar mass = 276.201 g/mol) were prepared in double distilled water (DW) as the solvent. The densities (ρ) of these binary solutions were determined accurately using 25 ml density bottle in an electronic balance with ±0.01mg accuracy. The basic parameter ultrasonic velocity (U) had been measured on Digital Ultrasonic Pulse Echo Velocity Meter (Vi Microsystems Pvt. Ltd. Model VCT-70 with single frequency of 2 MHz having an accuracy of 0.1%. Ostwald's viscometer calibrated with doubly distilled water was used to determine the viscosities (η) of the solutions with an accuracy of ±0.001 Pa.sec. Stalagmometer was used to determine the surface tension of the solutions. These basic parameter U, η and ρ of various solutions of drug viz.,0.0201,0.0402, 0.0804, 0.1608mol/kg were measured at 293, 303 and 313 K. Thermostatically controlled water circulation system is used to maintain the temperature with an accuracy of 0.05^0C. For all studied solutions and pure components, measurements were repeated thrice. The various acoustical parameters were evaluated from U, η and ρ values by using following formulae.

1. Adiabatic compressibility (β) $= \frac{1}{U^2\rho}$ $Kg^{-1}ms^2$

   U= velocity; ρ= Density of liquid

2. Specific Acoustic impedance (Z)=U*ρ $Kg^{-1}ms^{-3}$

3. Relative association (RA) = $[\frac{\rho}{\rho 0}][\frac{U0}{U}]^{1/3}$

Where ρ and ρ_0 are the densities of solution and solvent respectively. U and U_0 are the ultrasonic velocities of solution and solvent respectively.

4. Molar compressibility (W) $= \frac{(M.\beta)^{\frac{1}{7}}}{\rho}$

   Where ρ =density, M=Molecular weight,

   β = adiabatic compressibility

5. Rao's constant (R) $= \frac{M}{\rho} . [U]^{\frac{1}{2}}$

   Where, M = Molecular Weight,

ρ = density

6. Free volume (V_f) $= [M_{eff}.\frac{U}{K\eta}]^{1/2}$ m^3,

   Where M_{eff}= effective molecular weight,

   K-temperature independent constant

   K = 4.28 x10^9 for all liquid) (Nori, Babavali & Srinivasu, 2019).

7. Intermolecular Free Length (L_f) =KT x $\sqrt{\beta}$

   Where, Jacobson's Constant,

   KT = (93.875 + 0.375 x T)

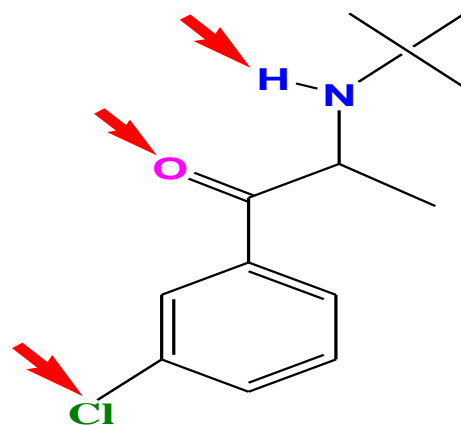8. Surface Tension: γ=(S/6.3 X$10^{-4}\rho$)$^{2/3}$ N/m

Fig.1-Structure of 2-(tert-butylamino)-1-(3- chlorophenyl) propan-1-one (arrow shows the interacting sites)

III. RESULT AND DISSCUSSION

The experimental data of density (ρ), viscosity(η), ultrasonic velocity (U) and Surface tension (γ) and the derived acoustic parameters of the aqueous 2-(tert-butylamino)-1-(3-chlorophenyl) propan-1-one (2-TBP)-NaCl solution at various studied concentrations at different temperature are reported in the table 1-6 .

Density, ultrasonic velocity, viscosity and surface tension are the essential parameters to know the strength of intermolecular interactions. Increase in these parameters with increased concentration shows that there is strong interaction between the drug and solvent and these interaction found to increase with the increase in temperature. Cohesive strength and thus molecular association in the solution is often dependable for observed values of unionized solute particles. It is also clearly observed that density, ultrasonic velocity, surface tension and viscosity rise with the increase in the aqueous co solute NaCl solution. This is may be due to the association of the aqueous co solute solution with the drug in consequence of dipole interaction between the Na^+ and Cl^- ions and the polar solvent.

Acoustic Impedance (Z) increases with an increase of drug concentration and the co solute, NaCl concentration. But Z was found to be decrease with the increase in the temperature which may be due to decrease in the interaction between the co-solute and solvent. Adiabatic compressibility (β) is measure of an inter-molecular association or dissociation measurement. The structure of the molecules affects their adiabatic compressibility and it also determines their orientation around the liquid molecules. Decrease in the adiabatic compressibility with the increase in the temperature and the increase in the co solute concentration concludes the structural changes in the drug- polar solvent interaction reflecting the system reduces compressibility. Relative association (RA) increases with concentration indicate that the solvation of the solute is existing over the breakdown of 2-TBP-aqueous solution aggregates (Table 6). The values of molar compressibility (W) and Rao's Constant (R) observed in the entire system are growing with increasing concentration at any temperature indicating that there are more components available in the region, thereby enhancing the medium's interactions in close packaging. Free Volume (V_f) is easily determined and is fundamental to the distinctly different interactions in the solution. The gradual raise in the free volume with the rise in the drug co solute NaCl mole fraction confirms the structural interaction between Na^+ and Cl^- ions and solvent.

The free length (L_f) of the neighboring molecules is the distance between them. The deviation of the ultrasonic speed in a solution depends on the mixing intermolecular free length. In the current study L_f decreases with a concentration of an aqueous drug solution signify that the extensive interaction between drug and solvent molecules. But the reduce in free length in the aqueous 2-TBP- co solute NaCl solution reveals the structural promoting behaviour between co solute and the drug.

Partial molar volume of an aqueous drug solution and 2-TBP-NaCl solutions were calculated by using the equation(Deosarkar, Tawde & Kalyankar, 2018; Arsule, Sawale & Deosarkar, 2019)-

$$\text{Partial molar volume} = \frac{M}{\rho} - \frac{\rho - \rho_0}{m \, \rho \, \rho_0}$$

Where, ρ and ρ_0 are the density of solvent and solution (kg.m^{-3}), m is the molality of solution (mol·kg^{-1}). M is the molar mass of drug (kg·mol^{-1}). Fig 2-3 shows the plot of partial molar volume against the concentration of the drug and the effect of co-solute NaCl.
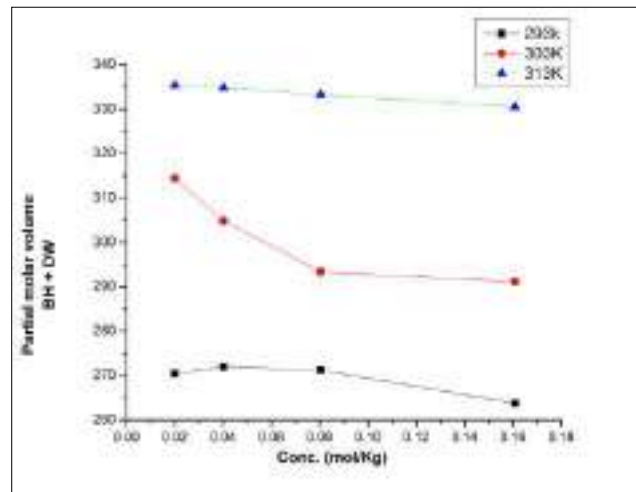

Fig. 2- Partial molar volume of 2-TBP + DW at different temperature.

Table 1:- Density (ρ), ultrasonic velocity (U) and Viscosity (η) and surface tension of drug at 293K, 303K and 313K in distilled water

Molar Conc.	Density(ρ) Kg.m^{-3}			Velocity(U) m.s^{-1}			Viscosity(η) N.s.m^{-2}			Surface tension (σ) X 10^5 N/m		
Temp.	293K	303K	313K	293K	303K	313K	293K	303K	313K	293K	303K	313K
0.0201	1.0804	0.954	0.9034	1218.2	1212.4	1202.2	7.7175	5.958	6.040	6.1522	5.3556	4.9447
0.0402	1.1024	0.994	0.9125	1228.6	1216.9	1210.6	7.9331	6.279	6.114	6.4394	5.6446	5.1000
0.0804	1.1208	1.040	0.9213	1235.9	1221.2	1222.4	7.9269	6.589	6.265	6.6645	5.9685	5.3012
0.1604	1.1604	1.054	0.9312	1241.3	1225.2	1226.3	8.3094	6.708	6.352	6.9917	6.1062	5.4094

Table 2:- Acoustic impedance (Z) Adiabatic compressibility (β) and free length (L_f) and Wada's constant (W) of drug at 293K , 303K and 313K in distilled water.

Molar Conc.	Acoustic impedance(z) x10^4 g/s/m^{-2}			Adiabatic compressibility (βad)x10^{-7} m ^{2} s^{-2}			Free path length (L_f) x10^{-7}			Wada's constant (W)		
Temp.	293K	303K	313K	293K	303 K	313K	293K	303K	313K	293K	303K	313K
0.0201	1316.1	1156.6	1086.1	6.2373	7.1323	7.8476	6.4376	7.3564	8.0313	1.7924	1.6593	1.6256
0.0402	1354.4	1210.8	1104.7	6.0095	6.7945	7.4864	6.2028	7.0723	7.8613	1.7832	1.6682	1.6408
0.0804	1385.2	1270.5	1126.2	5.8415	6.4594	7.2695	6.0291	6.7119	7.6323	1.7943	1.6884	1.6812
0.1604	1440.4	1291.3	1141.9	5.5929	6.3243	7.1454	5.7728	6.5894	7.5945	1.7348	1.7018	1.6956

Table 3 :- Rao's constant (R), free volume (Vf) and Relatively association of drug at 293K , 303K and 313K in distilled water.

Molar Conc.	Rao's constant (R) x101m$^{10/3}$s$^{-1/3}$Mol^{-1}			Free volume (V$_f$) x 10^{-8}			Relatively Association (R$_A$)		
Temp	293K	303K	313K	293K	303K	313K	293K	303K	313K
0.0201	442503.7	498825.1	522304.3	4.7382	3.6445	3.6696	0.04262	0.03782	0.03612
0.0402	437492.9	480335.3	520702.9	4.9121	3.8594	3.7378	0.04312	0.03927	0.03723
0.0804	432894.8	460720.5	520762.2	4.9375	4.0616	3.8616	0.04359	0.04095	0.03822
0.1608	419843.4	456264.9	516886.5	5.1984	4.1419	3.9315	0.04493	0.04135	0.0395

Table 4:- Density (ρ), ultrasonic velocity (U), Viscosity (η) and surface tension(γ) of drug at 293K, 303K and 313K in aq. NaCl solution

Molar Conc.	Density(ρ) Kg.m^{-3}			Velocity(U) m.s^{-1}			Viscosity(η) N.s.m^{-2}			Surface tension (σ) X 10^5 N/m		
Temp.	293K	303K	313K	293K	303K	313K	293K	303K	313K	293K	303K	313K
0.0201	1.3856	1.3244	1.3228	1210.3	1214.2	1216.4	9.9466	7.8821	7.6268	9.9466	7.8821	7.6268
0.0402	1.4356	1.3832	1.3748	1215.9	1219.2	1223.2	10.282	8.4190	8.0431	10.2802	8.4190	8.0438
0.0804	1.4636	1.4272	1.4023	1218.6	1222.3	1225.3	10.853	8.8634	8.5043	10.8513	8.8634	8.5048
0.1608	1.5072	1.4748	1.4488	1220.3	1224.5	1230.2	10.970	8.3455	8.3735	10.9704	8.3455	8.3455

Table 5:- Acoustic impedance(Z) Adiabatic compressibility (β) and free length (L$_f$) and Wada's constant (W) of drug at 293K, 303K and 313K in NaCl.

Molar Conc.	Acoustic impedance(z) x10^{4}g/s/m^{-2}			Adiabatic compressibility (β$_{ad}$)x10^{10}10^{3}Kg^{-1}ms^{-2}			Free path length (L$_f$) x10^{-7} m			Wada's constant (W)		
Temp.	293K	303K	313K	293K	303K	313K	293K	303K	313K	293K	303K	313K
0.0201	1676.9	1620.0	1600.0	4.92694	5.1204	5.1234	5.0213	5.3334	5.3723	1.6238	1.6593	1.6654
0.0402	1745.5	1686.3	1640.6	4.71162	4.8634	4.8607	4.8631	5.0713	5.1163	1.7308	1.6782	1.6848
0.0804	1783.5	1744.4	1717.8	4.60103	4.6984	4.7507	4.749E	4.8893	4.9934	1.7328	1.6884	1.6832
0.1608	1839.2	1805.8	1782.3	4.45557	4.5234	4.5627	4.5988	4.7133	4.7947	1.7624	1.6813	1.7343

Table 6:- Rao's constant (R), free volume (V$_f$) and Relatively association of drug at 293K, 303K and 313K in aq. NaCl.

Molar Conc.	Rao's constant (R) x10^{1}m$^{10/3}$s-$^{1/3}$Mol^{-1}			Free volume (V$_f$) x 10^{-8}			Relatively association (R$_A$)		
Temp	293K	303K	313K	293K	303K	313K	293K	303K	313K
0.0201	3428	359850.2	360938.3	6.0671E+16	4.83E+16	4.67E+16	0.055	0.052	0.052
0.0402	3324	345971.8	349227.7	6.2996E+16	5.19E+16	4.94E+16	0.056	0.054	0.054
0.0804	3268	336158.2	343040.3	6.6644E+16	5.47E+16	5.20E+16	0.057	0.056	0.054
0.1608	3177	325883.2	333286.7	6.7469E+16	5.38E+16	5.15E+16	0.059	0.057	0.056

Table 7:- The Redlich –Kister coefficients of the calculated Excess parameters of the BH+DW+ NaCl solutions at 293K, 303K and 313K.

Excess Parameters	Coefficients	Temperature		
		293 K	303K	313K
` Excess free volume (V$_f^E$) X 10^{-7}m^3/mol	A$_0$	5.4729	8.1156	8.4977
	A$_1$	-1.4735	-1.6174	-1.4003
	A$_2$	1.2101	1.7866	1.5350
	A$_3$	-3.0169	-2.9170	-2.8133

	A_4	1.3901	1.2135	1.1974
	A_5	5.4729	8.1156	8.4977
Excess intermolecular free length (L_f^E) $\times 10^{-2}$ A^0	A_0	-1.1595	0.4124	6.1833
	A_1	-1.2524	-1.9753	-7.8452
	A_2	-9.6057	-1.4549	-2.0016
	A_3	2.8377	5.3632	1.1361
	A_4	-2.8193	-5.5252	-1.2973
	A_5	8.9856	1.7272	4.3866
Excess adiabatic compressibility $\times 10^{-11} m^2/N$	A_0	-1.4735	-1.6174	-1.4003
	A_1	-1.9155	-3.2341	-4.1245
	A_2	2.9072	5.9135	7.2749
	A_3	-3.6933	-7.1228	-9.352
	A_4	1.3588	2.4863	3.3714
	A_5	0.07297	0.1394	0.2123

The dipole interaction between the co solute ions and the solvent may be the reason for the rise in the partial molar volume of the drug -co solute NaCl than in the aq. drug concentration. These interactions were found to increase with the rise in the temperature.
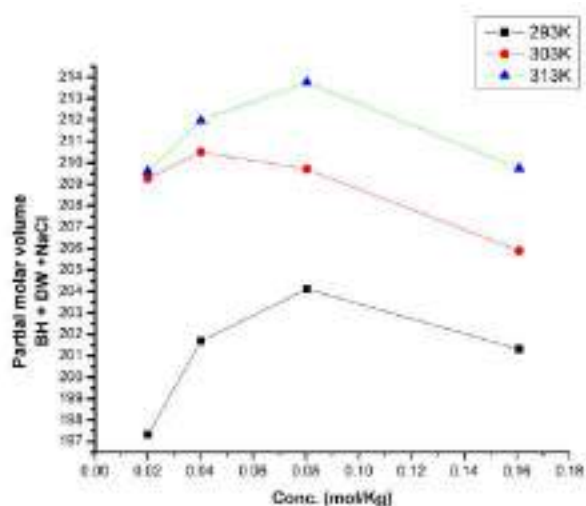

Fig.3- Partial molar volume of 2-TBP+ DW+ NaCl at different temperature.

The divergence between the experientially measured values and the ideal values at the particular thermodynamic stage are called as the excess properties. These properties are dependent on molecular size as well as shape and the mixture-component interactions. The various excess molar properties for studied solutions were evaluated using the relation given below- (Deosarkar, Tawde& Kalyankar, 2018).

$$Y^E = Y_{Exp} - (x_1 Y_1 + x_2 Y_2) \text{----------------------------(1)}$$

Where, Y^E is the excess thermoacoustical parameter. Mole fraction of solute and solvent are given by x_1 and x_2 respectively. Y_{Exp} is experimentally determined parameter.

Molecular interactions among the components were discussed by using these calculated excess parameters. These excess parameters are built-in to the Redlich-Kister polynomial given below (Redlich & Kister, 1948).

$$Y^E = x1(1-x_1) \sum_{i=1}^{n} A_i (2x_i - 1)^{i-1} \text{--------------------(2)}$$

Y^E is the excess thermoacoustical parameter. are the Mole fraction of solute and solvent are given by x_1 and x_2 respectivelly. The regression analysis method was used to calculate the values of the coefficients A_i. These values are summarized in Table 7.

The variations of excess free volume (V_f^E) with the concentration of 2-TBP and electrolyte in the aqueous solution are represented in Fig.4. For the studied mole fraction range the values of V_f^E are negative for the given concentrations of 2-TBP. Thus it is concluded from these observations that these component molecules are more close proximity in the liquid mixture than in pure liquids. This reflects the strong dipole–dipole interactions between component molecules. The values of the excess free volume depend on the temperature. From Fig.4 it is also observed that the temperature effect is not uniform. With the initial 10K rise in the temperature from 293 to 303K there is no considerable change in the excess free volume but with further rise of 10K shows measurable change in the its values. This implies that the decreases in the interaction with increase in temperature, which is credited to more aggressive thermal movement and the decline in the solvation of solute ions (Chauhan, Singh, Kumar, Neelakantan & Kumar, 2016; Roy, Jha & Dey.2001)

From Fig. 5, excess intermolecular free length (L_f^E) values are observed to be negative for the full mole fraction range of binary liquid mixutre. The negative trend of L_f^E indicates the sturdy interactions between liquid mixtures and this is supported by the Kerr effect as well (Deosarkar, Tawde& Kalyankar, 2018).

Furthermore, L_f^E values shows negative trend with temperature reveals that as the temperature rise interaction decreases.
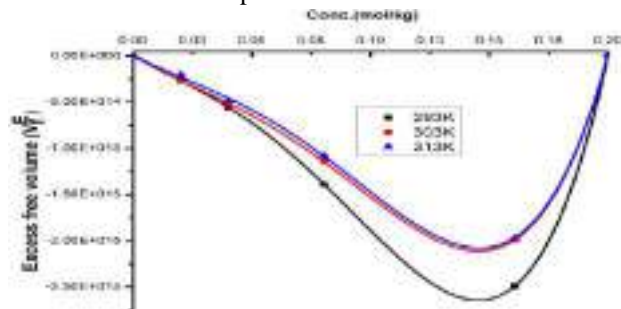

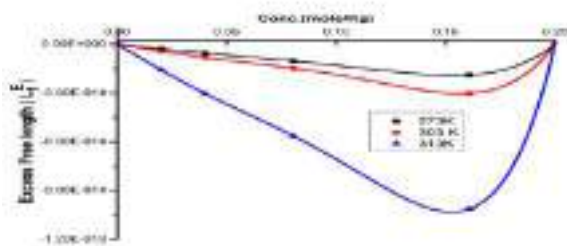Fig.4- Excess free volume (V_f^E) of an aqueous 2-TBP +NaCl at different temperature.

Fig. 5- Excess free length (L_f^E) of an aqueous 2-TBP + NaCl solution at studied temperature

Fig. 6 shows that over the entire concentration range, the β_E values for aqueous temperature range were found to be negative. This shows that the intermolecular attraction between the component molecules is a stronger indication of strong hetero-molecular interaction in the liquid mixtures. Excess compression of both the liquid mixtures is negative in the present study. It is also found that with the rise in temperatures interactions become weak, β_E values decrease negatively.
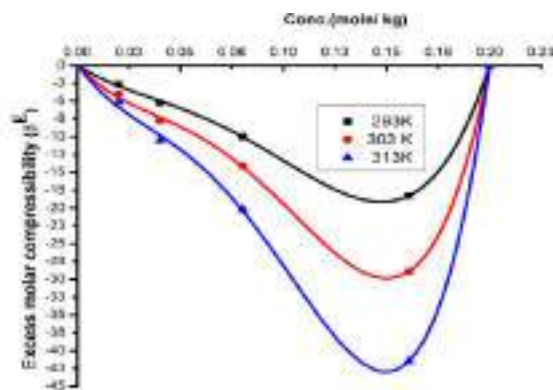

Fig. 6- Excess adiabatic compressibility (β^E) of an aqueous 2-TBP +NaCl solution at different temperatures.

CONCLUSION

In an aqueous 2-TBP and co solute NaCl solution, ultra-sonic velocity, density, viscosity and surface tension are measured at 293, 303 and 313K. The excess thermo-acoustic parameters, such as excess freely intermolecular (L_f^E), excess adiabatic compressibility (β_E) and excess free volume (V_f^E), are calculated for the whole mole fraction range. An interpretation of these data shows that the interaction between drug and solvent dominate over interaction between the solute-solute (Deosarkar, Tawde, Kalyankar, 2018). Thus it may be concluded that the hydration sphere of the drug releases water molecules due to the electrolyte NaCl and solvent interactions. 2-TBP has multiple interacting sites viz., secondary amine, carbonyl, cholo-phenyl group, shown by the red headed arrows (Fig.1). The deviation of the various studied parameters of an aq. NaCl solution of drug may be due to the intermolecular interactions at these sites. The anomalous relationship is observed in different excess parameters due to the characteristic property that strong dipolar interactions and directional interactions between the component molecules simultaneously act. Also in the aqueous co solute NaCl solutions the strength of intermolecular interactions is observed to decline with temperature.

CONFLICT OF INTERESTS

Authors declare that there is no conflict of interest regarding the publication of present research article.

REFERENCES

Anwar Ali, Firdosa Navi, (2008).Volumetric, ultrasonic and viscometric behavior of binary mixtures of styrene with ethyl alcohol and chloro benzene at different temperatures. Journal of Molecular Liquids, 143(2-3), 141-146.

Arsule,A. D. , Sawale, R.T.& Deosarkar, S.D.,(2019). Temperature-dependent volumetric and ultraacoustic studies of α-amino acids in aqueous acetylsalicylic acid drug solutions, Journal of Molecular Liquids, 275(1) 478-490.

Baluja, S., Solanki, A., & Kacchadia, N., (2007). An ultrasonic study of some drugs in solutions. Russian Journal Of Physical Chemistry A, 81(5), 742-746.

Baragi J. G., Maganur, S., (2013). Excess molar volumes and refractive indices of binary liquid mixtures of acetyl acetone with n-Nonane, n-Decane and n-Dodecane at (298.15, 303.15, and 308.15) K. Journal of Molecular Liquid, 178, 175-177.

Begaum Z., Sandhya P.B., Karunakumar D. B. ,&Rambabu C. (2013). Thermodynamic, ultrasonic and FT-IR studies on binary liquid mixtures of anisaldehyde and alkoxyethanols at different temperatures, Journal of Molecular Liquids, 178, 99-112.

Blandamer, M. J. (1973). Introduction to Chemical Ultrasonics, Academic Press, Landon.

Chauhan, S., Singh, K., Kumar, K., Neelakantan S. C. and Kumar, G. J. , (2016). Drug−Amino Acid Interactions in Aqueous Medium: Volumetric, Compressibility, and Viscometric Studies.Chem. Eng. Data, 61 (2), 788–79.

Deosarkar, S. D. Tawde, P. D. Kalyankar T. M., (2018). Partial molar volumes and compressibilities of metformin hydrochloride in aqueous-NaCl/sucrose solutions at 30 °C. Journal of Molecular Liquids, 251, 40-44.

Dhondge, S. S., Zodape S. P. & Parwate, D. V. (2012). Volumetric and viscometric studies of some drugs in aqueous solutions at different temperatures J. Chem. Thermodynamics, 48, 207-212.

Dhondge, S. S., Paliwal, R. L., Bhave N. S. & Pandhurnekar, C.P., (2012). Study of thermodynamic properties of aqueous binary mixtures of glycine, l-alanine and β-alanine at low temperatures (T= 275.15, 279.15, and 283.15) K. J. Chem Thermodynamics, 45, 114-121.

Fakruddin Babavali S. K., Shakira, P., Rambabu, K. Narendra, K. & Srinivasu, C., (2016). Excess thermo-acoustical parameters in the study of molecular interactions in binary liquid mixtures containing quinoline with arenes (benzene and toluene) at temperatures T = (303.15, 308.15, 313.15 and 318.15) K, Journal of Molecular Liquids, 220, 113–119.

Gurung, B.B., & Roy, M. N., (2006). Study of densities, viscosities and ultrasonic speeds of binary mixtures containing 1, 2-dimethoxyethane and an alkan-l-ol at 298.15 K, Journal of Solution Chemistry, 35, 1587-1606.

Hwrzfeld, K. F., & Litovitz, T. A., (1959). Absorption and Dispersion Of Ultrasonic Waves. Academic Press, Landon.

Kharat, S. J. (2008). International Journal of Appl. Chem, Sept, Saravazyan A P, Ann Rev Biophys Chem, 1991, 20,1321.

Nain, A. K., (2007). Ultrasonic and viscometric study of molecular interactions in binary mixtures of aniline with 1-propanol, 2-propanol, 2-methyl-1-propanol, and 2-methyl-2-propanol at different temperatures. Fluid phase equilibrium, 259, 218-227.

Nain, A.K., (2008) Molecular interactions in binary mixtures of formamide with 1-butanol, 2-butanol, 1,3-butanediol and 1,4-butanediol at different temperatures: An ultrasonic and viscometric study. Journal of Fluid Phase Equilibria, 265(1-2), 46-56.

Nori, T. S., Babavali, S. K ., Srinivasu C. (2019) Characteristic IR-acoustical analysis and surface tension variations in organic liquid mixtures at different temperatures", Materials Today: Proceedings.

Murshed, S. M. S., Nietode Casstro, C. A., (2011) Lourenco, M. J.V.,Lopes M. L. M. & Santos, F. J. V., Renew.Sust.Energ.Rev.15, 2342,DOI:10.5772/13920.

Redlich, O. Kister, A.T. (1948). Algebraic Representation of Thermodynamic Properties and the Classification of Solutions Ind. Eng. Chem. 40, 345-348.

Roy, M. N., Jha, A. and Dey, R., (2001). Study of Ion-Solvent Interactions of Some Alkali Metal Chlorides in Tetrahydrofuran + Water mixture at Different Temperatures. J. Chem. Eng. Data 46, 1327–1334.

Sonar A. N. and Pawar, N. S., (2010). Ultrasonic velocity, density, and viscosity measurement of substituted heterocyclic drugs in 1, 4-dioxane at 303 K. Rasayan J. Chem., 3(1), 38-43.

Syal, V. K., Chauhan A. and Chauhan, S., (2005). Ultrasonic velocity, viscosity and density studies of poly (ethylene glycols)(PEG - 8,000, PEG - 20,000) in acetonitrile (AN) and water (H$_2$O) mixtures at 250C. J Pure Appl. Ultrasonics, 27, 61-69.

Thakur S. K. and Chauhan, S. (2011). Ultrasonic Velocity and allied parameters of drug Colimax in aqueous 1-propanol at 298.15K Journal Chem. Pharm. Research, 3, 657-664.

Thanuja, B., Kanagam, C., Sreedevi S. (2011). Studies on intermolecular interaction on binary mixtures of methyl orange–water system: Excess molar functions of ultrasonic parameters at different concentrations and at different temperatures. Journal of Ultrasonics Sonochemistry, 18, 1274–1278.

Thirumaran S. & Sabu J. K., (2012). Ultrasonic studies of interactions of some alkali halides in aqueous d-glucose solutions at varying molalities and temperature. Journal Exp. Sci., 3 33-39.

Yadav, S. S. Yadav, A., (2005).Ultrasonic study on binary liquid mixtures between some bromoalkanes and hydrocarbons. Journal of Ultrasonics, 43, 732–735.

***